Low-frequency Absorbing Acoustic Metasurfaces : Deep-learning Approach and Experimental Demonstration

Krupali Donda

INSTITUT JEAN LAMOUR
UNIVERSITÉ DE LORRAINE

Doctoral School **Chemistry-Mechanics-Materials-Physics**

University Department **Institut Jean Lamour**

Thesis defended by **Krupali Donda**

on **December 15, 2021**

In order to become Doctor from Université de Lorraine

Academic Field **Physics**

Speciality **Acoustics**

Low-frequency Absorbing Acoustic Metasurfaces: Deep-learning Approach and Experimental Demonstration

Thesis Supervised by M. Badreddine Assouar

Committee Members

President of Jury	M. Nico Declercq	Professeur, Georgia Tech Lorraine
Referees	M. Abdelkrim Khelif	Directeur de Recherche CNRS, Université de Franche–Comté
	M. Yan Pennec	Professeur, Université de Lille
Examiners	Mme. Agnes Maurel	Directrice de Recherche CNRS, ESPCI Paris
	M. Jean-François Ganghoffer	Professeur, Université de Lorraine
Supervisor	M. Badreddine Assouar	Directeur de Recherche CNRS

Keywords: acoustic metasurfaces and metamaterials, low-frequency absorption, deep learning, convolutional neural network, conditional generative adversarial network, inverse design.

Mots clés : métasurface et métamatériaux acoustiques, absorption basse fréquence, deep-learning, réseaux de neurones convolutifs, réseaux adverses génératifs conditionnels, problème inverse.

I humbly and affectionately dedicate this work to
my beloved husband Hardik Joshi and my both families.

Thank you for your unconditional and everlasting support and love.

Acknowledgments

Only slowly I begin to realize that it's done: I am a doctor now! Years of hard work towards a successful defense has never felt better! I would like to thank all the people who contributed in their particular way to the achievement of this doctoral thesis. Foremost, my greatest gratitude for the work presented in this thesis goes to my thesis director Prof. Badreddine Assouar for entrusting me with this opportunity and for his help, advice, and continuous guidance over the last three years. I gratefully acknowledge his suggestions and comments on my thesis, which are invaluable to the quality of this dissertation. I hope to emulate his integrity, work ethic, and passion in my research career. I would like to express my sincere gratitude to my jury members Prof. Abdelkrim Khelif, Prof. Yan Pennec, Prof. Agnes Maurel, Prof. Nico Declercq, and Prof. Jean-François Gangauffer for their thoughtful feedback and scholarly conversation during the defense. Despite all the restrictions due to the ongoing pandemic and roller coaster periods, it was a fantastic event at the end of an ambitious and exciting research journey.

I would like to especially thank Dr. Yifan Zhu for continuously helping me from the very beginning to the end of my Ph.D. thesis. You were always there to fix any problem and I could not have asked for one better. I would also like to thank Prof. Aurélien Merkel for his valuable suggestions and deep insight into Physics which helped me a lot to improve my work. Many many thanks to all my colleagues (Team 407) who also grew to be good friends over time. Thank you Liyun, Sheng, Shi-wang, and Yi for sharing your knowledge and skills with me. I will forever remember our collaborative efforts and mutual help. I also owe a big thanks to my friends from the lab with whom I have had countless funny moments and cups of coffee. Thank you so much Mengxi, Cécile, Abir, Prince, Jérémy, Danny, Spencerh, and Baptiste.

Coming to Nancy 3 years ago, with no knowledge of the French language and little exposure to the culture, I found myself in a sea of unfamiliarity. Over time, I started loving this beautiful town and I feel it my home now. Thank you Elizabeth Aubrun who is now a good friend also for all the support you offered, especially during the first wave of the Covid. I enjoyed the time we discussed different cultures and our travel experiences. Friends played an important part in both keeping my sanity and uplifting it during all these years. They were like my second family, and without these friends, these years would not have been so eventful and

memorable. I would like to thank Priyanka, Shoaib, Tulika, Rahul, Asma, Anil, Yasmeen, Parul, Aswin, Aman, and Harshad for making these years beautiful in Nancy. I have to thank all my friends and colleagues from India who always pushed me to achieve more. I am falling short of words how lucky I am to have you my seniors Priyanka Tyagi and Vishal Vashishtha. I apologize that I cannot mention everyone here but you were and still are an important part of my life. I am so thankful to my friends Tulika Bose, Hardik Jain, Aman Sinha, and Param Rajpura for their time to teach me and fruitful discussion on deep learning concepts.

I would like to express my sincere gratitude to all my previous teachers and supervisors, whose hard work played a significant role in shaping my research interest. Thank you, Dr. Hitesh Pandya, Mr. Ravinder Kumar (ITER-India, Institute for Plasma Research), and Prof. Ravi Hegde (Indian Institute of Technology, Gandhinagar) for building the foundation for this research journey and continuous support over the years. I would like to thank my both family, for their invaluable patience, trust, and encouragement during this thesis. I would certainly not be where I stand today without the unconditional and everlasting support and love from my husband, Hardik. You have been there for me consistently through all good and bad times. Words cannot express how grateful I am to my hard-working parents for all of the sacrifices that they have made on my behalf. I would also like to thank my younger brother, Nirav. Prayers of my family for me were what sustained me thus far.

Finally, I gratefully acknowledge the funding received towards my Ph.D. from the Air Force Office of Scientific Research (FA9550-18-1-7021). I would also acknowledge the support from la Région Grand Est.

Contents

List of Tables

List of Figures

General Introduction

Owing to the steep rise in the urban population, noise pollution has become a major issue in our daily lives and adversely impacts health and the quality of the life. In particular, the existence of high levels of manmade low-frequency noise has been reported in many environments. In the urban soundscape, the major sources of such noises are transportation, compressors, turbines, amplified music, etc. There are several reports showing many hazardous impacts of low-frequency noise on human health. In 2011, the World Health Organization (WHO) considered noise as one of the most crucial factors that negatively affect public health. In this perspective, it is essential to find efficient means to control the noise effectively.

To reduce the noise level, a variety of traditional materials such as natural fibers (wool, kenaf, natural cotton, etc.), granular materials, synthetic cellular materials, etc. are used. These materials can be used for developing systems and structures for high-frequency noise absorption. Despite being simple, the approaches to control noise with materials readily found in nature come with drastic restrictions, especially for the low-frequency absorption because of its high penetrative power. Based on the mass-density law, the absorption spectra can be only adjusted by changing the thickness, for a given dense classical material, which results in bulky absorbers. To absorb the low-frequency sound, many composite structures have been proposed such as gradient index materials, absorbers based on microperforated panels, porous materials, etc. Such structures are capable of attenuating noise in the mid-to-high frequency range. However, the attenuation of low-frequency sound is still challenging due to the weak intrinsic dissipation of traditional homogenous materials in the low-frequency regime.

Within a span of 20 years, the advent of acoustic metamaterials/metasurfaces has overturned conventional means in all aspects of sound propagation and manipulation. Especifically, it has offered an unprecedented expansion of our ability to attenuate sound beyond the mass-density law. Over the past few years, we have witnessed tremendous progress in developing various concepts based on acoustic metasurfaces to absorb low-frequency sound waves with deep subwavelength features, which will be the main aspect discussed in this dissertation. The demonstrations are mainly based on the impedance matching metasurfaces with hybrid resonances or coiling-up space geometries. Due to the flexibility to be made of any

acoustically rigid material, the implementation of coiled-up metasurface absorbers is straightforward. However, it is still remaining a challenge to achieve extreme low-frequency (<100Hz) absorption as, in these designs, the absorption is controlled by the length of the coiled channel, creating difficulties in adjusting the resonance frequency.

For acoustic metasurface absorber designs, structural designs play a key role. These design approaches, to date, are relied on expertise in acoustics to implement the theoretical models or to guide the progression of numerical simulations based on the finite element method (FEM). The theoretical approaches include physics-based methods like impedance analysis, complex frequency plane, etc. Although these approaches provide useful guidelines, finding the right structures to realize the desired acoustic response is not an easy task, especially in the case of complex geometries in a multi-constrained problem. In such cases, we rely on numerical simulations. Starting from the initial condition and setting up proper boundary conditions, the solution can be obtained by solving the linearized Navier-Stokes equations. With sufficient meshes and many iterations, and accurate acoustic response can be derived for a given structure. Nevertheless, it is frequently needed to fine-tune the geometry and run simulations iteratively to approach the desired acoustic response. Similar to the theoretical approaches, this procedure also requires past experience and knowledge in acoustics. Due to computational power and time constraints, this approach allows exploring only limited design space to find the best structure. In this dissertation, we identify solutions to circumvent these conventional design approaches using modern deep learning architectures.

The main aim of this dissertation is to design ultrathin acoustic metasurface absorbers for an extreme low-frequency regime (<100Hz). For this, we first have proposed the concept of multicoiled metasurface absorber (MCM) that allows us to achieve low-frequency limits of the previously implemented concepts. To establish the deep learning-based framework, we adopt deep learning architectures based on convolutional neural networks (CNNs) and conditional generative adversarial network (CGAN) for the forward and inverse designs, respectively. In the context of the inverse acoustic designs, a CNN-based forward simulator helps to accelerate the simulation process, resulting in faster convergence during the optimization process. Based on the two essential properties of the latent space: compactness and continuity, the CGAN can identify topologies more efficiently as compared to the traditional search algorithms, and can also produce the metasurface structure which is not in the dataset. As such, the implemented inverse design scheme represents an efficient and automated way for the design of acoustic metasurface absorbers for oblique wave incidence with subwavelength features.

The thesis begins with chapter 1, which provides a brief state of art and literature review on acoustic metamaterials and metasurfaces. It reviews some relevant works of literature on acoustic metasurface design for very low-frequency absorption. In the second part of chapter 1, the fundamental equations of acoustics are outlined. The importance of the thermodynamic properties of the sound propagation medium, especifically, the presence of viscous and thermal boundary layers on the interface between fluid and a rigid boundary is discussed.

In chapter 2, a detailed overview of the important methodologies used throughout the thesis work is presented. First, numerical simulation using the finite element method which is used to analyze all the designs throughout the thesis work is discussed. When the sound propagates through the narrow regions of the structure, the losses occur in the boundary layers near the walls which need to be considered to build the accurate model. For this, the simulation models are implemented using the Thermoviscous Acoustics interface which is explained. For the measurements, multiple experimental samples have been fabricated using 3D printing that will be discussed, following that the two-microphone method for the acoustic absorption measurement is presented with the associated calibration process. In the later part of the chapter, machine learning methods used to design the metasurface absorbers are discussed. First, the discriminator and generator type neural networks are discussed along with their training process. A brief explanation of classical machine learning techniques like k-nearest neighbor (KNN), random forest (RF), support vector machine (SVM) used to compare the performance of the implemented deep learning network is provided. Several techniques that mitigate the reliability of large training datasets and dimensionality reduction is also discussed.

In chapter 3, the concept of the multicoiled metasurface absorber for extreme low-frequency absorption is demonstrated. The analytical derivation, numerical simulation, and experimental demonstrations are provided and the associated physical mechanism is discussed. In contrast to the state of the art, this original conceived multi-coiled metasurface offers additional degrees of freedom to tune the acoustic impedance effectively without increasing the total thickness. Furthermore, based on the same conceptual approach, the supercell approach is presented to broaden the bandwidth by coupling unit cells exhibiting different properties. In the last part, the effect of the temperature on the performance of MCM is investigated via numerical and theoretical approaches.

In chapter 4, a convolutional neural network-based framework for the forward design of acoustic metasurface absorber is introduced. We have implemented customized CNN architecture with two convolution layers and two pooling layers. The efficacy of the

implemented network is demonstrated through a few examples. To compare the performance of the 2D CNN, three classical machine learning algorithms: KNN, RF, and SVM are implemented and trained on the same dataset. Furthermore, the efficacy and reliability of this design strategy are confirmed through experimental validations. The proposed forward design strategy based on deep learning can be generically utilized for fast and accurate modeling of acoustic metasurface devices with minimum human intervention.

In chapter 5, the forward and inverse designs of metasurface absorber for oblique wave incidences are presented based on a two-dimensional convolutional neural network (2D CNN) and conditional generative adversarial network, respectively. The proposed forward deep learning network is capable of simulating a metasurface absorber for very low-frequency absorption using 2D images of the structure concatenating with other geometric properties (height, angle of incidence, etc.). The data is preprocessed using several data transformation strategies like data normalization, principal component analysis (PCA), etc. which are discussed. We also introduced the data augmentation concept to increase the diversity in the dataset. For the complex acoustic structures, the training data is normally generated by the simulation, and the size of such dataset is smaller as compared to the number of parameters in the modern deep learning network architectures (usually in the order of millions). In such a case, the model tends to be overfitted. Thus, data augmentation significantly reduces this problem and makes the model more robust. Further, we propose the CGAN for the inverse design. The idea of inverse design is to generate a metasurface structure directly from the desired acoustic absorption spectra, eliminating the need for lengthy parameter scans or trial-and-error methods.

Finally, a summary of the acoustic metasurface absorbers designs and implemented deep learning strategies in this dissertation are presented. Challenges of acoustic metasurface absorber design for low-frequency applications and future research directions using the deep learning approaches are also discussed.

Chapter 1

State of the Art

In this chapter, the underlying theory, as well as a brief state of the art relevant to this thesis is presented. First, the concept of acoustic metamaterials and metasurfaces for wave manipulation is sufficiently reviewed and presented. Following this, various concepts of acoustic metasurface absorber design for low-frequency absorption are discussed. The thermal and viscous losses play an important role in the attenuation of the acoustic waves when passing through narrow cavities, these loss mechanisms are presented in the second part of the chapter.

1.1 Acoustic Metamaterials and Metasurfaces

Controlling sound propagation has been desired for centuries. Since the years, many techniques are used to enhance or to absorb sound waves in auditoriums or public places. However, it is not always easy to control the nonreciprocal wave with the materials available in nature [1]. In the last two decades, artificial materials with more complex properties, known as metamaterials [2–5] have been introduced and designed to tailor functionalities to deal with wave propagation in unprecedented ways. Metamaterials are artificial composite structures made of meta-atoms that act like a continuum with 'on-demand' effective properties. The field of the wave propagating in the artificial structures for the wave control started with photonics [6] and phononics [7].

Acoustic metamaterials (AMMs) [8–14], as a counterpart of the electromagnetic metamaterials, provide a leap towards an effective medium description [15]. They are used to control airborne sound, which is the simplest and most ubiquitous form of classical waves. In the absence of the source, the governing equation of the pressure wave propagation inside a homogenous linear fluid can be given by [16],

$$\nabla^2 P(r) - \frac{\rho}{B}\frac{\partial^2 P(r)}{\partial t^2} = 0 \tag{1.1}$$

Where P is the acoustic pressure, B is the bulk modulus, and, ρ is the mass density. For the natural materials, the value of B and ρ are strictly positive. On the contrary, the aim of the

AMMs is to develop structures having an extreme range of values (including negative values) of the bulk modulus and mass density. This is what enables the AMMs to support a variety of physical phenomena that can be used to control sound propagation in unprecedented ways. The bulk modulus and the mass density can be defined as below [17],

$$B = -V\frac{dP}{dV} \tag{1.2}$$

$$\rho = \frac{dP}{dV}\frac{F}{V} \tag{1.3}$$

Where V is the volume, and F is the applied force. dP/dV indicates the variation in the pressure with respect to the change in volume. The index of refraction can be defined as,

$$n^2 = \frac{B_0}{B}\frac{\rho}{\rho_0} \tag{1.4}$$

For the natural materials, the volume decreases when positive pressure is applied. Therefore, dV is negative which leads to positive B. In contrast, the volume of the material with negative bulk modulus increases under the positive applied pressure, resulting in the volume difference, dV=V_2-V_1 which is illustrated in Fig.1.1(a). As shown in Fig.1.1(b), a material having negative ρ indicates that the acceleration, a of the material is opposite to the exerting force F.

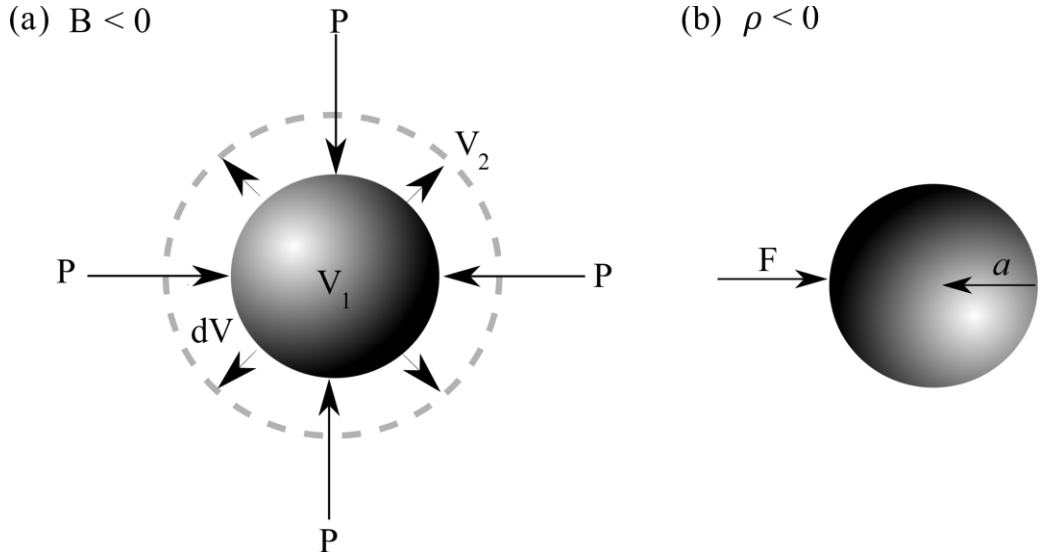

Figure 1.1- Schematic illustration of negative (a) bulk modulus, B and (b) mass density, ρ.

Initially, AMMs have been designed for sound-attenuation applications. The first acoustic metamaterial consisted of rubber-coated lead spheres arranged in a simple cubic structure [18]. This system is analogous to a mass-spring system as the solid sphere acts as a mass while the rubber acts as the spring. Figure 1.2(a) shows the cross-section of the coated lead sphere. The coated spheres are arranged in a simple cubic crystal which is shown in Fig. 1.2(b). The lattice constant is 1.55cm which is much smaller than the operation wavelength. The transmission was measured (frequency range=250Hz-1600Hz) for a sonic layer crystal with four layers. Figure 1.2(c) shows the ratio of the amplitude measured at the center to the incident wave. The plot shows two dips with a peak after each dip. The locally resonant and sub-wavelength nature of this metamaterial forms an unconventional band structure having flat dispersion curves as shown in Fig.1.2(d). The effective bulk modulus turned negative at frequencies close to resonance. It can be observed from Eq.(1.4), for the negative value of the bulk modulus the refractive index *n* becomes complex. The imaginary component of *n* indicates the wave decays exponentially as it enters the material and the bandgaps form.

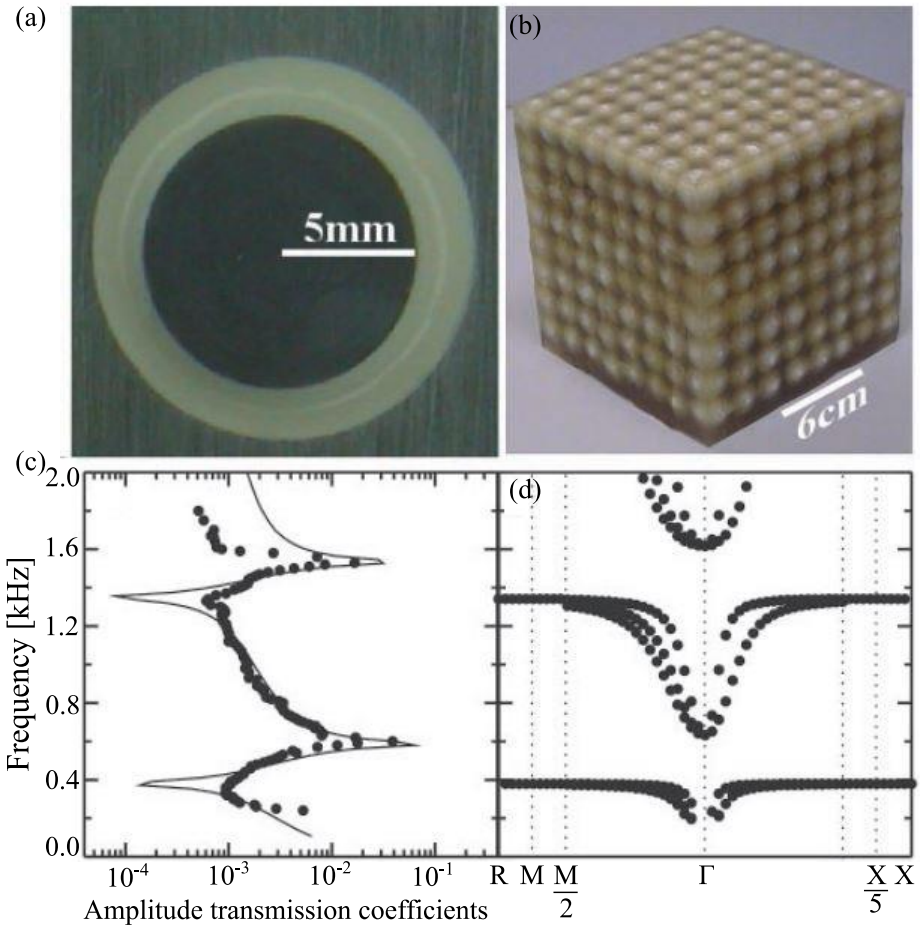

Figure 1.2- (a) Cross-section of a coated lead sphere to forms the metamaterial structure (b) for a sonic crystal made of 8 × 8 × 8 units. (c) Transmission coefficients obtained via theory (solid line) and measurements (dots). (d) The band structure for a simple cubic array of the coated spheres [18].

Other important structures of AMMs include the pipe segments and resonators consist of open and close cavities. Figure 1.3 illustrates the parameter space for AMMs for four combinations of the values of both density and bulk modulus. The top-right quadrant (Quad. I) is quite a familiar space in acoustics that includes natural materials for which B and ρ are strictly positive. The second quadrant includes the acoustic metamaterials with $B > 0$ and $\rho < 0$. The negative mass density can be obtained when the fluid segment accelerates out of phase with respect to the acoustic driving force. Membranes fixed at the rims of a tube or the array of the holes as shown in Fig.1.3 can be used to generate such acoustic response [9,19,20]. It is possible to alter the resonance over a spectral range by changing the size of the membranes or loading with a mass. The fourth quadrant (Quad. IV) includes the metamaterials with $B < 0$ and $\rho > 0$ which can be obtained using the array of the Helmholtz resonator. An array of Helmholtz resonators connected to a waveguide in series through a narrow propagation channel is shown in Fig.1.3. A low-frequency stopband is created at their collective resonance frequency. Any change in the volume of the cavity results in a change in the resonance frequency. The resonance can be shifted to a very low frequency by attaching a series of open-side branches to the waveguide. The wave completely reflects up to the frequency at which the sign of B changes [9]. The entire panel of such open-side branches can be used to design acoustic double fishnet structures for broadband sound blockage [21].

Quadrant III represents double negative acoustic metamaterials ($B<0$ and $\rho<0$). For the locally resonant AMMs, it has been demonstrated that the spatial symmetries of the relevant resonant modes can be used as mark if the mass density or bulk modulus of the composite structure becomes dispersive [16]. Theoretically, it is proven that monopolar resonance creates a dispersive bulk modulus, whereas dipolar resonance creates an effective negative density [22]. Therefore, there is a range of frequency where both, monopolar and dipolar resonances overlap and artificial media whose effective bulk modulus and density both are dispersive, and can become negative for a range of the same frequency. Using the simple labyrinthine architectures as shown in Fig.1.3, the sound propagation phase can be delayed in such a way that band folding with negative dispersion ($\rho<0$, $K<0$) is compressed towards the long-wavelength regime [23–25]. Another method for achieving negative refraction is to stack several holey plates together to create an anisotropic structure with hyperbolic dispersion. Sound refraction can occur at negative angles for almost any direction of incident sound due to the hyperbolic shape of the dispersion contours [26,27]. AMMs with negative properties have shown fascinating capabilities in unconventional wave manipulation enabling promising applications in super-

focusing [28–30], subwavelength imaging [31–33], cloaking [34–36], reverse Doppler effect [37,38], and many more [39,40]. When both bulk modulus and mass density approach zero (regions close to the axes marked a green dot), the phase velocity becomes extremely large, leading to a quasi-static spatial distribution for time-harmonic fields [16]. Such exotic behavior has the potential to be used in a variety of exciting applications, including total reflection and cloaking [41] and tailoring radiation phase patterns [42].

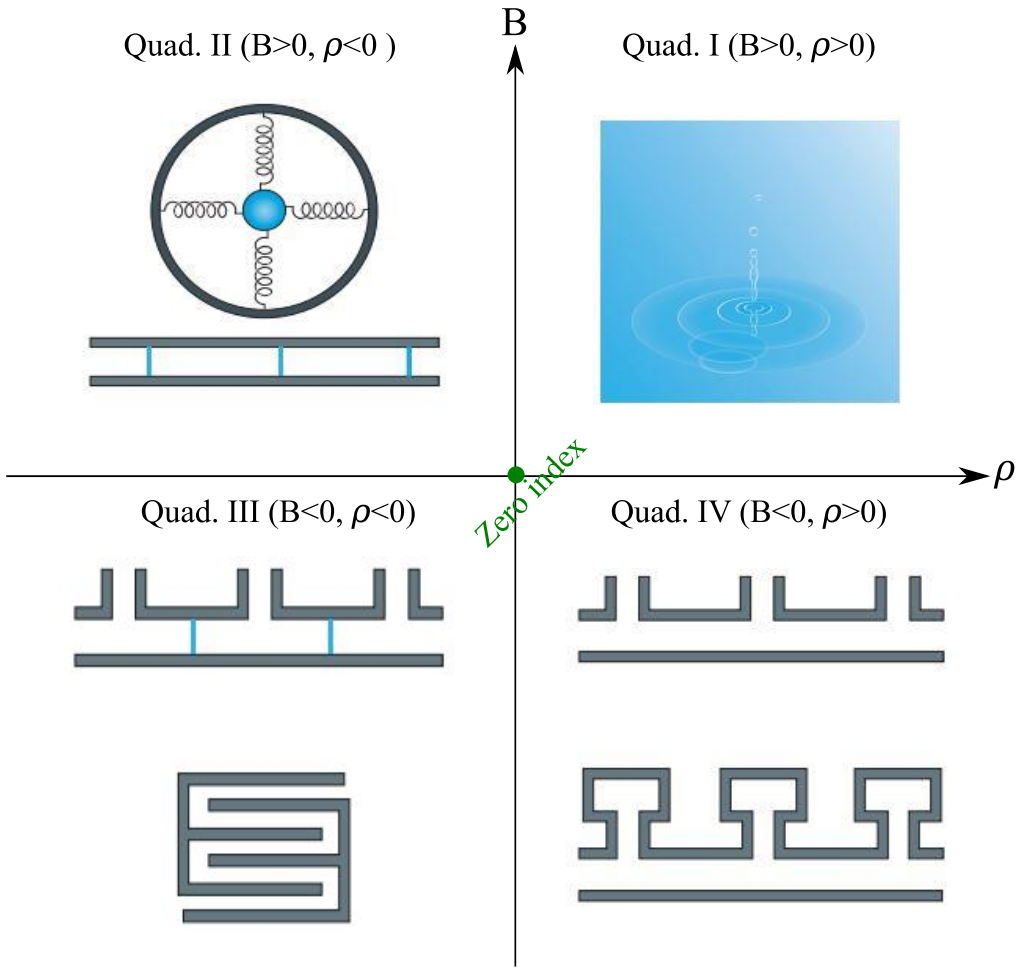

Figure 1.3- Acoustic metamaterials with extreme constitutive parameters. The top-right quadrant (Quad. I) is the space known in acoustics. It represents natural materials for which B and ρ are strictly positive (B>0, ρ>0) [10]. Metamaterials (Quad. II) with B>0 and ρ<0 can be obtained with membranes and coated bead structures [18,19]. Quadrant III represents double-negative (B<0 and ρ<0) AMMs which can be obtained with space-coiling or coupled filter element structures [23–25]. Metamaterials with B<0 and ρ>0 (Quad. IV) can be obtained using open and closed cavity resonators [43,44].

The Acoustic metasurfaces are a kind of 2D configuration of acoustic metamaterials with a subwavelength thickness that provide nontrivial local phase shift or extraordinary sound absorption [45]. This tailored surface is capable of manipulating sound waves in many ways and allows the design of devices of extremely compact size. The concept of the acoustic

metasurface is based on an array of subwavelength units which can include Helmholtz resonators [46], coiling up space structure [47,48], and membranes [49]. The metasurface design with such units has shown unprecedented capabilities to realize wavefront engineering features like perfect absorption [47,50], reflection [51], asymmetric transmission [52,53], artificial Mie resonance [54], etc. However, designing an acoustic metasurface as a counterpart of the electromagnetic metasurface is challenging mainly due to the mechanical and distinct properties of the acoustic waves, for example, the difficulty of coupling acoustic waves with very thin structures.

The general concept of metasurfaces was initiated and introduced by the use of generalized Snell's law that governs wave propagation at the interface of two homogenous media [55]. Snell's law can be extended theoretically to define the phase at the interface to achieve desired sound wave reflection or refraction. Such control on sound waves can be achieved by introducing abrupt phase shifts in the acoustic path by incorporating periodic structures on a planar interface on subwavelength scales. Figure 1.4 illustrates an acoustic plane wave incident on an artificially engineered interface which introduces an additional phase shift to the acoustic waves transmitted or reflected from the interface. Considering that the interface is located in the plane of z=0, then it creates a phase discontinuity as φ(x). A detailed explanation is given in Ref. [45]. Governed by the generalized Snell's law of reflection, the nonlinear relationship between the angle of incidence, θ_i and angle of reflection, θ_r can be expressed as,

$$\sin\theta_r - \sin\theta_i = \frac{\lambda_0}{2\pi}\frac{d\varphi(x)}{dx} \tag{1.5}$$

Practically, such manually introduced phase distributions, which can define phase discontinuities on the propagating waves, can be implemented using a layer of individual phase shift elements, known as acoustic metasurface. Acoustic metasurfaces are empowered with physics and distinct from bulk metamaterials, enabling then new applications, thanks to their extended wave-steering functionalities at reduced dimensions. Even though acoustic and optical metasurfaces obey Snell's law, the translation from optical to acoustic metasurfaces is not straightforward due to the inherent differences between acoustic and electromagnetic waves. For example, in acoustics, there is no direct counterpart of plasmonic resonance induced by metallic antennas in acoustics, which is essential for optical metasurfaces to provide 0 to 2π phase shift [56]. On the other hand, the thermoviscous losses are well-known phenomena in acoustic systems, but it is not found in optical ones. The theory of the thermoviscous losses is discussed in detail in section 1.3 of this chapter.

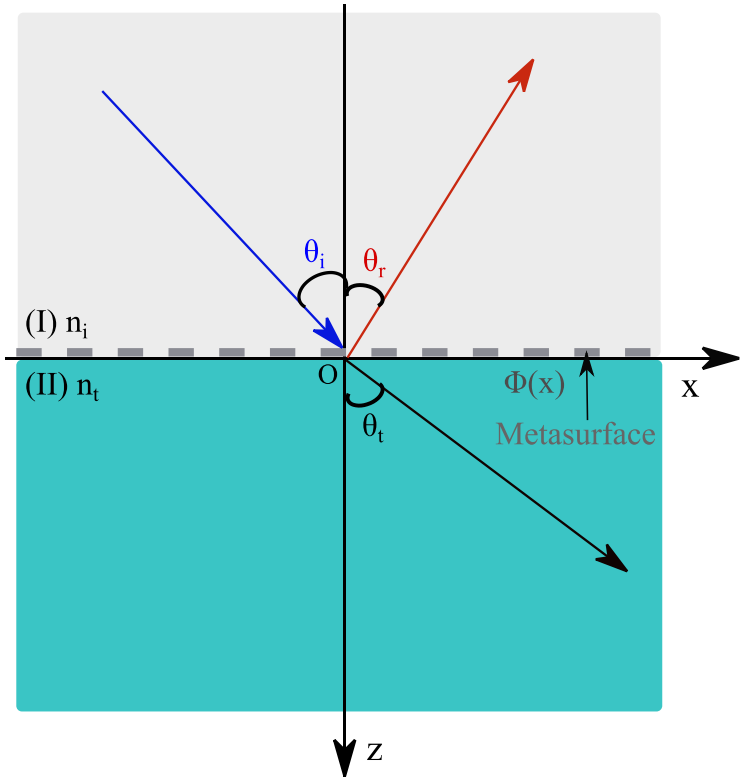

Figure 1.4- Schematic illustration of generalized Snell's law and acoustic metasurface. Using an artificially engineered interface, an abrupt phase shift along the interface is introduced. The interface is located at $z = 0$ [45].

The major types of acoustic metasurface designs include coiling up space structure [47,48], array of the Helmholtz resonators [46], coiling structure with a perforated plate [47], and membrane type structure [49]. When discussing acoustic wave manipulation, two important parameters should be considered, one is the phase for tailored wavefront and the other is the amplitude of the reflected or transmitted waves. The phase of the reflected waves can be tuned by the coiling up structure shown in Fig. 1.5(a). Such structures elongate the effective propagating path along with the coiling structure which is longer than the geometrical dimensions of the structure. The key benefit of the coiling up structure is that it can control the refractive index of the acoustic metasurface by controlling the path length to various degrees as per the requirement. Because of the longer path length, reflected waves can be modulated and the reflected phase shift can be tailored within the entire 0–2π range. The coiling path, on the other hand, must be designed to avoid excessive thermoviscous losses [45]. As shown in Fig.1.5(b), the local resonance of the HR element can also introduce sufficient phase shits of reflected waves.

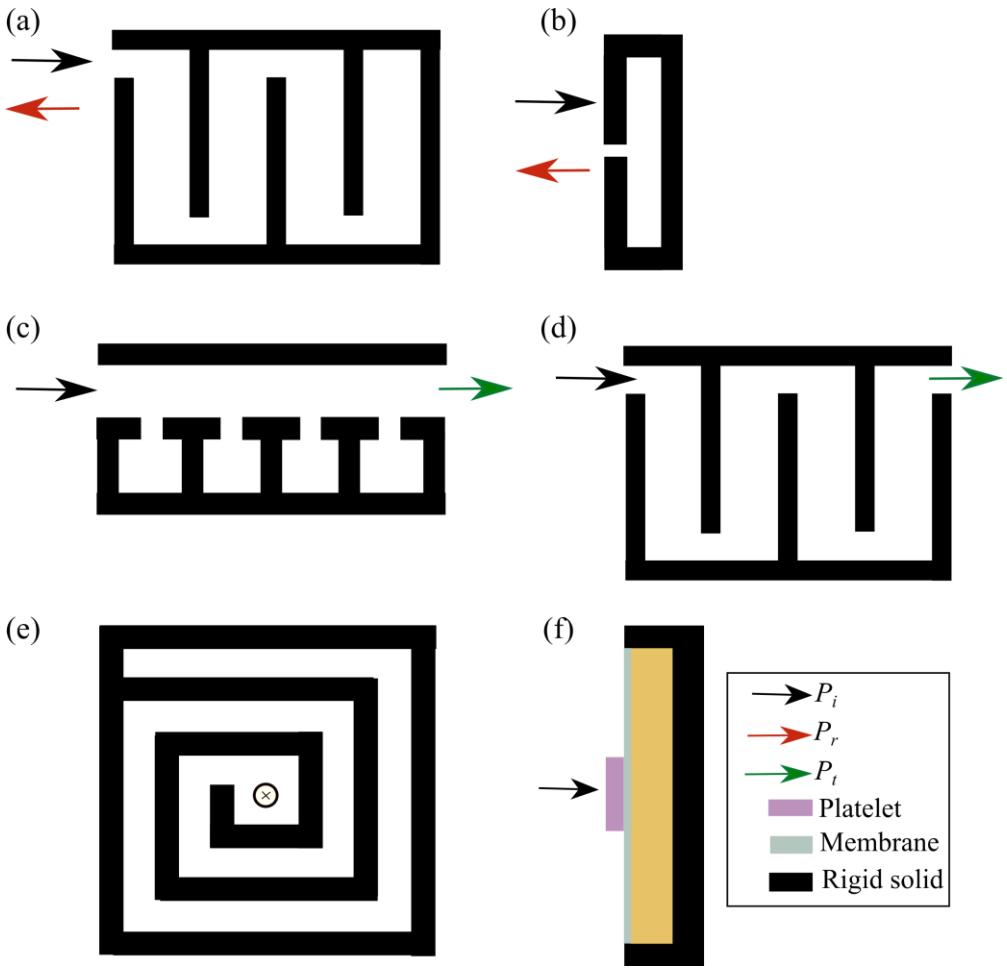

Figure 1.5 – Schematic illustration of the major designs of the acoustic metasurface. (a) Space coiling type structure using labyrinth elements, and (b) Helmholtz resonator for phase shift in reflected wave manipulation. (c) An array of four HRs with a connecting pipe, and (d) coiling-up-space element for transmitted wave control. (e) Spiral-shaped coiling structure with a perforated plate, and (f) decorated membrane with hybrid resonance for the acoustic absorption.

To achieve a high refractive index and high transmission at the same time, a metasurface structure was proposed using an array of four HRs and a connecting pipe connected at the open side of the HRs as illustrated in Fig.1.5(c) [57]. Here, the series of HRs contributes to cover a full range of phase 0-2π and the connected pipe contributes to achieving hybrid resonance that compensates the impedance mismatch with the surrounding medium. Using a straight pipe with the length of λ/2, effective impedance matching was obtained, which is based on Fabry-Parrot resonance [58]. The resulting metasurface had a tunable phase velocity and a transmission efficiency that is close to unity with a deep-subwavelength width of the structure.

In another approach, spatially varied coiling-slit subunits are used as shown in Fig.1.5(d). In this design, a couple of verticals and some horizontal bars are used that forms the zigzag path which effectively elongates the propagation distance of the wave [59]. There are many structure

parameters, i.e. number and geometry of bars which can be tailored to obtain the required amplitude and phase response. A supercell of eight units was constructed for a working frequency of 2550Hz with the same thickness but different numbers of rigid bars. Using these eight units, the full phase 2π range is covered as the phase shift increase with a step approximately $\pi/4$ among the nearest neighbors. The efficient transmission can be achieved by properly configuring geometrical parameters to minimize the dissipation that arises due to the thermoviscous effects. However, in the case of the acoustic absorption, it should be reversed, i.e. all the acoustic energy should be dissipated within the structure. For example, consider a space-coiled-up based spiral structure with a perforated plate shown in Fig.1.5(e). Here, an acoustic wave enters into the structure through the perforated hole and propagates inside the spiral structure, and gets absorb due to the thermoviscous loss [47]. Using this structure perfect absorption can be achieved in the very low-frequency range with a subwavelength thickness of the structure. Another approach is to use a structure composed of a decorated membrane and a reflecting surface as shown in Fig.1.5(f). In such a design, perfect absorption can be realized by adding an extra impedance to the decorated membrane resonator to hybridize the two resonances [49]. Using the resulting metasurface, the perfect absorption is achieved at a frequency close to the anti-resonance despite having a deep-subwavelength thickness. Figure 1.5 provides an overview of the major designs used to achieve controllable reflection, transmission, and absorption for various applications. From these designs, many transformative structures are recently derived to construct the metasurface to achieve desired functionalities [48-50].

1.2 Acoustic Metasurface for Low-frequency Absorption

In this 21st century, noise has become an integral part of a domestic and industrial environment that significantly affects the quality of life and also leads to health issues. In 2011, noise pollution was identified as one of the most important factors by the World Health Organization having a direct negative impact on public health. Traditionally, natural fibers (cotton and wool), porous material [60,61], synthetic cellular materials [62], etc. have been broadly used to absorb low-frequency noise. They normally result in poor impedance matching to the incoming acoustic waves. Also, these designs require to have the thickness comparable to the working wavelength which hinders their application for a low-frequency regime. Efficient low-frequency absorption can be achieved using a microperforated panel with a back cavity but, it still has a large thickness [63]. Acoustic absorption and attenuation in the low-frequency regime

(50-500Hz) has been and still is a real challenge due to the weak intrinsic dissipation of conventional materials in the low-frequency region [12]. The major drawback of the conventional acoustic absorbers is that they are bulky for low-frequency applications. The emergence of acoustic metamaterials/metasurfaces has shown promising ways for their application to the absorption and mitigation of acoustic waves [7,10,18,45]. In recent years, many promising schemes have been proposed and implemented to design efficient metasurface absorbers at very low frequencies [47-50,64–67].

One interesting way to achieve total absorption at a very low frequency is to use an ultra-thin decorated membrane. Membrane-type acoustic metasurface composed of different forms of decorated membrane resonators (DMRs) has been previously explored [49]. Different studies demonstrate that using such structures various functionalities can be realized like near-unity transmission at the resonant frequencies, total reflection at the anti-resonant frequencies, negative refraction index. Moreover, based on the hybrid resonances, perfect absorption at lower frequencies can also realize with an ultra-thin membrane [49]. Figure 1.6(a) shows the geometry of the unit cell consists of a DMR, a reflective surface (an aluminum backplate), and a thin sealed gas (Sulphur hexafluoride) layer in between. The boundary of the membrane is fixed on a rigid frame. The DMR is composed of a uniform stretched elastic membrane and is decorated by a platelet. As shown in Fig.1.6(b), two eigen modes characterized the DMR: one mode is related to the oscillation of the platelet obtained at 112Hz and the second is related to the oscillation of the elastic membrane (the platelet being nearly stationary) obtained at 888Hz. The reflective surface and the sealed gas add an extra impedance in series to the DMR which results in the change into the resonance conditions. The DMR's resonances are forced to hybridize, resulting in new resonant hybrid modes that satisfy the absorption conditions. Figure 1.6(c) shows the absorption spectra as a function of frequency obtained via theory and measurements. Nearly perfect absorption is achieved at 152Hz, indicating a perfect impedance matching with the air. Remarkably, this result is achieved with the ultra-small cell thickness of $\lambda/133$. From Fig.1.6(c), it can be observed that the absorption peak does not coincide with the DMR's eigenfrequency but, it is obtained near the vicinity of its anti-resonance. However, the narrow width of the absorption peak (1.2Hz) and fragility resulting from the sealed gas layer and the thin membrane limit the practical application of such metasurface.

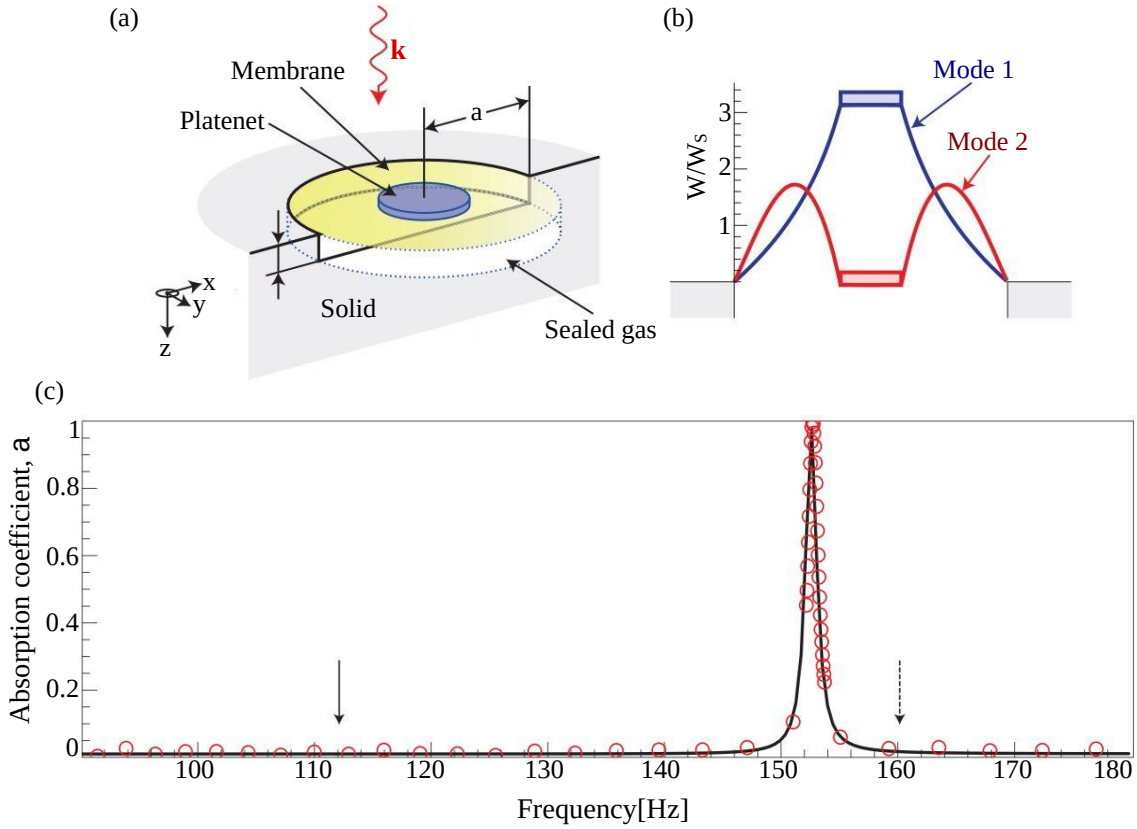

Figure 1.6- (a) Schematic illustration of acoustic metasurface composed of a DMR (radius *a*) and reflecting surface, between which gas is sealed in a cell (depth *s*). Here, **k** denotes the wave vector. (b) Cross-sectional illustration of the lowest eigen modes of a DMR. Here, W is the normal displacement of the membrane which is normalized to the amplitude of the incident sound waves, W_s. (c) Comparison of the absorption coefficients obtained via theory (black curve) and experiments (red circles). Nearly perfect absorption is achieved at 152Hz [49].

Another approach to achieve perfect absorption is using the mechanism of critical coupling condition [68]. Figure 1.7(a) shows asymmetric Fabry-Perot cavity (length L) with two different mirrors, i.e., the resonant scatterer. Because of the sub-wavelength size and the rigid backing, it can be considered as a point-scatterer. As the desired frequency range is well below the first cut-off frequency of the higher propagative modes in the waveguide, the problem can be considered as one-dimensional. The absorption of the presented system can be expressed as, $\alpha = 1 - |r|^2$, where r is the complex reflection coefficient. Considering the inherent losses of this configuration, a perfect absorption condition is fulfilled when the reflection coefficient is zero. Figure 1.7(b) shows the set-up used for the single resonant scatterer with the HR (L_n=2cm, R_n=1cm, R_R=2.15cm) connected to a closed waveguide (R=2.5cm, L=15cm). Both a complex wave vector and a complex impedance characterize the thermoviscous losses at the waveguide and resonator walls. Figure 1.7(c) shows the trajectory (black dashed line) of the zero of the reflection coefficients in the complex frequency plane by changing the L_R from 0 to

15cm. It is produced by a hybrid resonance due to the interaction of the resonance of the HR and the resonance of the back cavity. As the L_R increases, the zero moves to lower real frequencies. Now, considering the thermoviscous losses in the system, it can be observed that the trajectory of the zero down-shifts (black continuous line) as compared to the lossless case. The condition of the critical coupling is fulfilled at the frequency at which the trajectory crosses the real frequency axis. There are two crossing points, i.e., two different configurations produce perfect absorption which corresponds to L_R=8.3 cm (f=484.5 Hz) and L_R=3.9 cm (f=647 Hz). The corresponding absorption curves are shown in Fig.1.7(d). Red continuous line (with open red circles) and green dotted lines (with open green squares) present the absorption coefficients, α for the L_R=8.3 cm (f=484.5 Hz) and L_R=3.9 cm (f=647 Hz), respectively. Results show very good agreement between the theoretical approach and measurements.

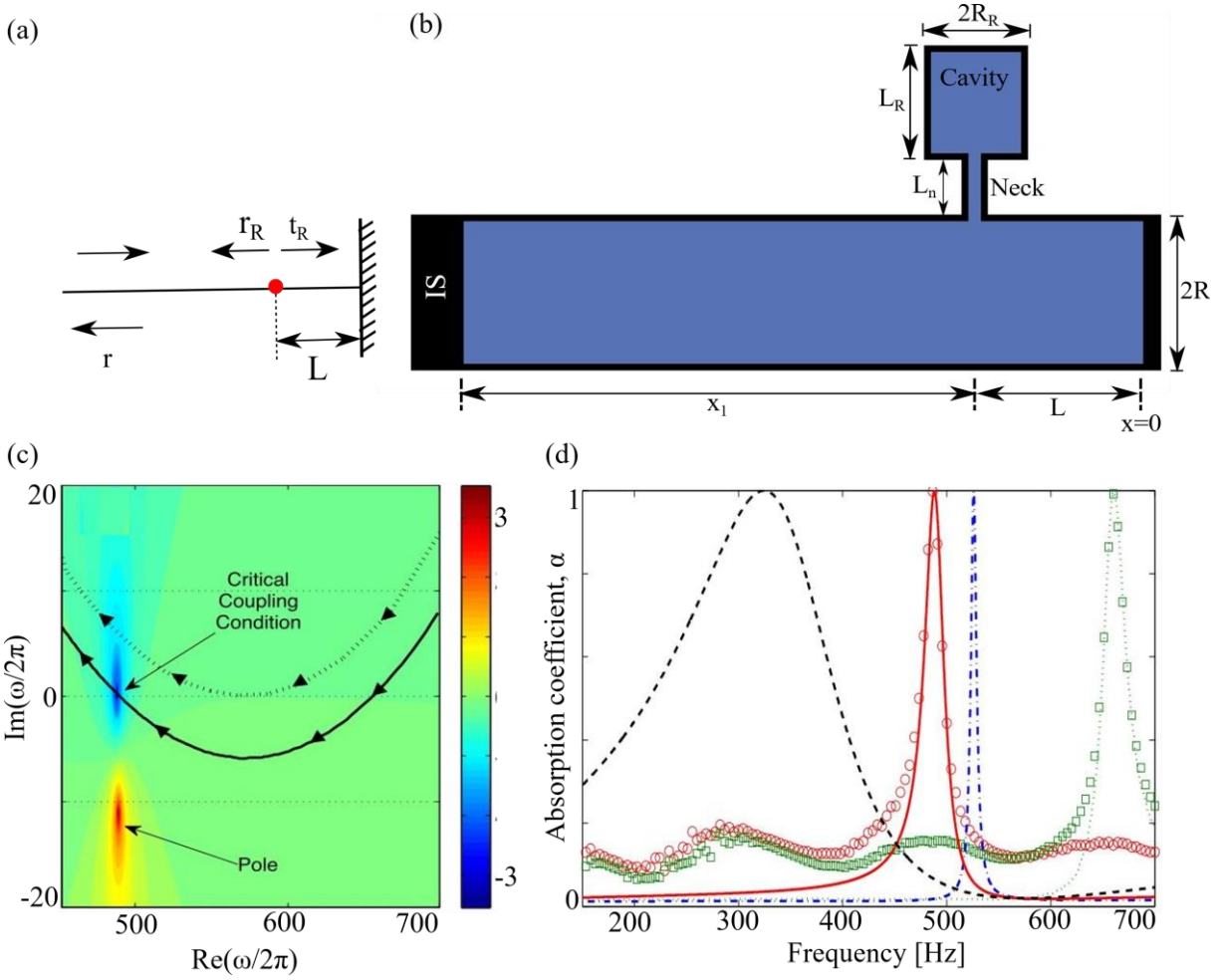

Figure 1.7- (a) Asymmetric Fabry-Pérot resonator consists of a resonant element (red point) and a rigid back. (b) Set up for single resonator scatterer. An impedance sensor (IS) is used for the measurements. (c) Representations of the reflection coefficients in the complex frequency plane with L_R=8.3cm. Black dashed and the continuous line represents the trajectory of the zero for the lossless and lossy case, respectively with the increase in L_R. (d) The absorption coefficients, α obtained via theory (measurements) for the configuration (L_R, f_{CC}) = (8.3 cm, 484.5 Hz) and (L_R, f_{CC}) = (3.9 cm, 647 Hz) is

shown by the red continuous (open red circles) and green dotted lines (open green squares), respectively [68].

Another intriguing approach to realize the perfect absorption at a very low frequency with the ultrathin structure is to introduce a high refractive index. Such a high index medium can be realized by using the concept of coiled-up space through curled channels, for example- a labyrinth, zigzags, or spiral [47,69,70] . This concept has gained widespread interest over the past few years due to its ability to shrink the bulky structures to the deep-subwavelength scale. The implementation of such coiling metasurface absorbers is very simple and flexible to be made of any rigid material. A prototype of metasurface-based absorbers consist of a perforated plate and a coiled coplanar chamber is shown in Fig.1.8(a). Here, the acoustic wave penetrates the coiled chamber (width and thickness *w*) through the perforated hole (diameter *d*, thickness *t*) [47]. The coplanar air chamber is formed using some solid beams (width *b*, thickness *h*). This structure is designed to simultaneously satisfy two conditions to obtain the perfect absorption: (i) resonant state, and (ii) impedance matching with the surrounding medium viz air in this case. Upon satisfying these two conditions, all the acoustic energy transfer into the coiled chamber, rather than reflecting. It finally gets absorbed within the perforated hole due to the thermoviscous losses. The acoustic wave propagates through the coiled channel, which increases the total propagation path length of the wave, resulting in a low sound velocity and high refractive index.

Figure 1.8(b) presents the absorption spectra of the given metasurface as a function of the frequency with an absorption peak at 125.8Hz. The absorption coefficients obtained using the impedance analysis are also shown for comparison with the simulation result. The absorption coefficients obtained from the impedance analysis method with diameter d=3.5mm shows excellent agreement with the simulation result (d=3.3mm). The inset plot shows the comparison for the same diameter value, d=3.5mm. The slight difference of the absorption is because the thermal conduction equation is omitted in the theoretical calculations for simplifying the derivation of the special acoustic impedance while it is considered in the numerical simulations. The normalized specific reactance, y_s (red curve) and resistance, x_s (blue curve) of the presented system in shown in Fig.1.8(c). It can be observed that the curve of the y_s crosses the 0 at 125.8Hz which indicates the resonant state. The coiled channel provides an extra reactance, y_c to compensate for the acoustic reactance provided by the hole, y_h which is a prerequisite to obtain perfect absorption. At the same frequency, x_s reaches 1, which indicates

the perfect impedance matching between the metasurface and air. With these two conditions satisfied simultaneously, the total absorption is achieved at 125.8Hz. Here, it is worth noting that the total thickness of the system is $t+w$=12.2mm which is only 1/223 of the working wavelength. However, in this concept, the reactance of the structure determines the absorption performance, and thus, the channel length of the coil is strictly required to be a quarter wavelength for the full absorption. In other words, the channel length cannot be tuned to realize perfect absorption at the desired frequency. It creates difficulties in the realization of the tunable acoustic absorber.

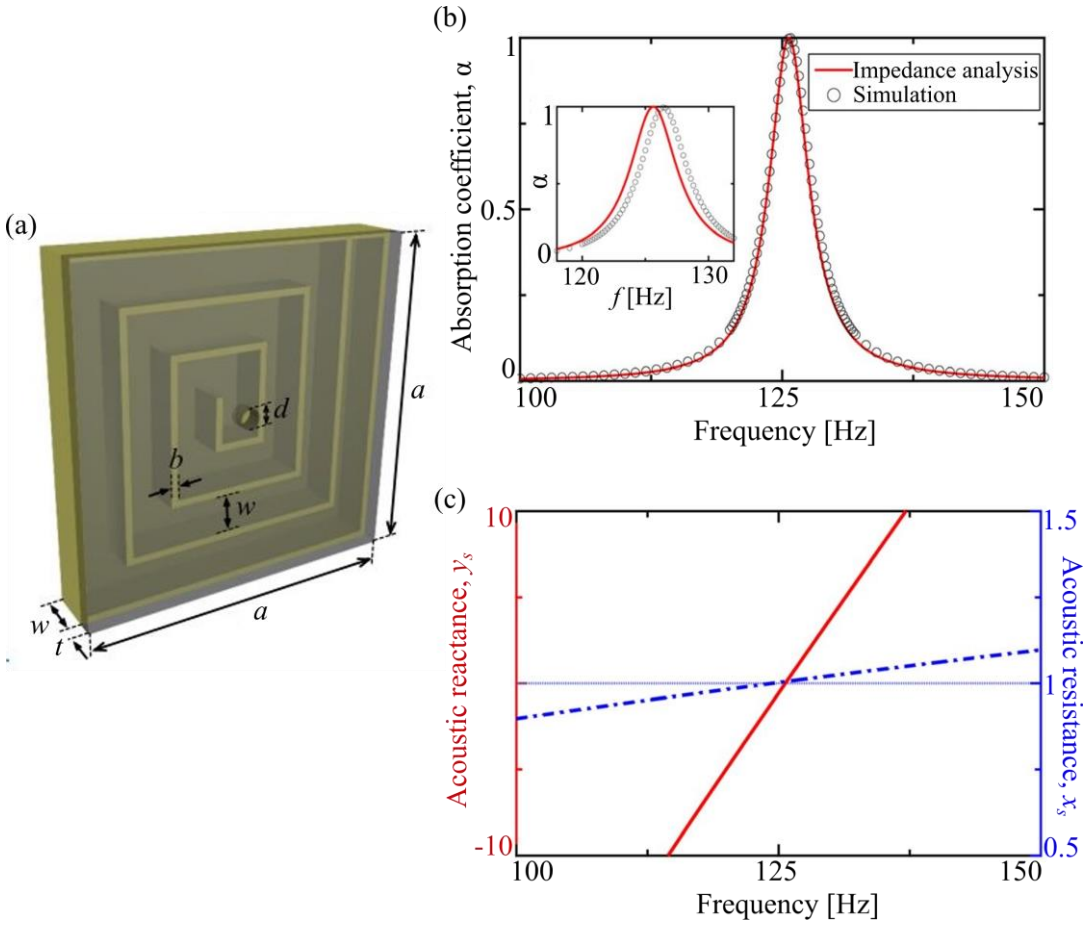

Figure 1.8- (a) The spiral metasurface (width a and total thickness=$w+t$) based on the coiling up space structure. It consists of a perforated plate (thickness t) with a hole (diameter d) in the center. (b) Comparison of the absorption coefficients, α obtained via numerical simulation (black circles) and theory (red curve) for the presented metasurface with geometrical parameters, d=3.3mm, t=0.2mm, a=100mm, b=1mm. The perfect absorption is obtained at 125.8Hz. (c) The normalized specific acoustic reactance, y_s (red curve) and the resistance, x_s (blue dotted line) of the presented metasurface [47].

A number of studies have shown that incorporating an array of extended tubes into a panel can improve low-frequency absorption [71–73]. A recent study has shown that using a number of parallel long elastic open necks, a thin (~λ/25) and highly efficient acoustic absorber

can be designed [73]. To overcome the limitation of quarter wavelength channel length to achieve the perfect absorption, one interesting way is to introduce an aperture into the system that adds an extra degree of freedom to tune the impedance powerfully [48]. Figure 1.9(a) and (b) shows the proposed spiral metasurface composed of a coplanar coiling channel with a circular aperture embedded at the opening of the channel.

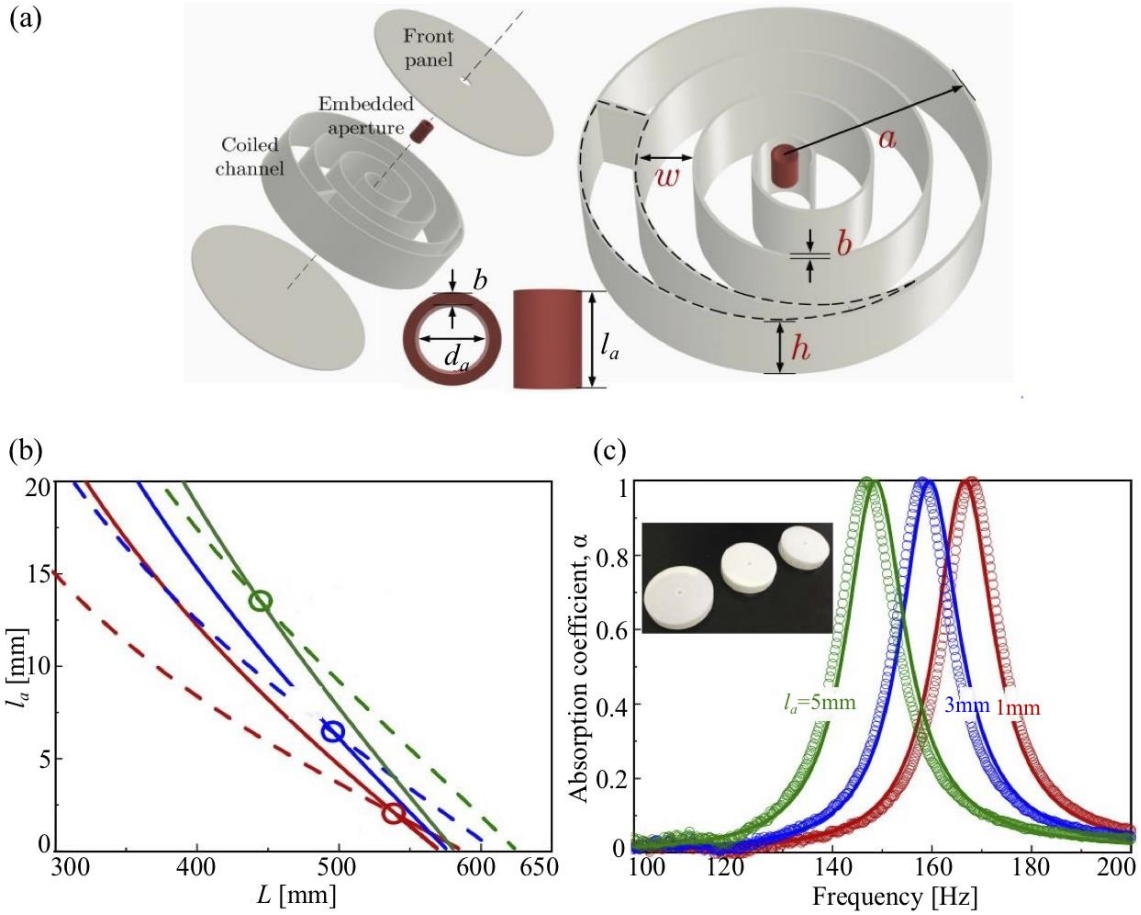

Figure 1.9- (a) Schematic illustration of a spiral metasurface (radius *a*) composed of a coiled channel (width *w*, height *h*) and a circular aperture (length l_a, diameter d_a). The left sketch shows a detailed view of the system. The right sketch illustrates the structural assembly of the embedded aperture and the coiled channel. (b) Impedance matching diagram as functions of the length of the coiled channel, *L*, and the length of the aperture, l_a. (c) The absorption coefficient of the presented systems (shown in the inset photo) with perfect absorption. The diameter and the length of embedded apertures are d_a=6mm and l_a= 5mm, 3mm, and 1mm [48].

Figure 1.9(b) shows the impedance matching plot of the presented system. The solid lines present the acoustic reactance matching and the dashed lines present the resistance matching condition. The perfect absorption condition is satisfied at the intersections between the solid and dashed lines. It can be observed that as the height of the aperture increases, the resonance frequency shifts to the lower frequency (137.5Hz), which cannot be achieved only

with the coiling structure for the same parameters. For instance, to obtain the perfect absorption at 137.5Hz using the coiling channels, the length of the coiled channel, L, must be 614mm. By introducing an aperture with a diameter of 6mm and a length of 13.5mm, the required length of the channel reduces to 440mm. Figure 1.9(c) shows the absorption coefficients obtained via theoretical calculation and experiments as a function of frequency for the different heights of the aperture, l_a. Corresponding fabricated samples are shown in the inset photo. The results show that the increasing height of the aperture shifts the resonance curves towards lower frequency without increasing the total thickness of the system, demonstrating a tunable performance in designing these ultrathin acoustic absorbers.

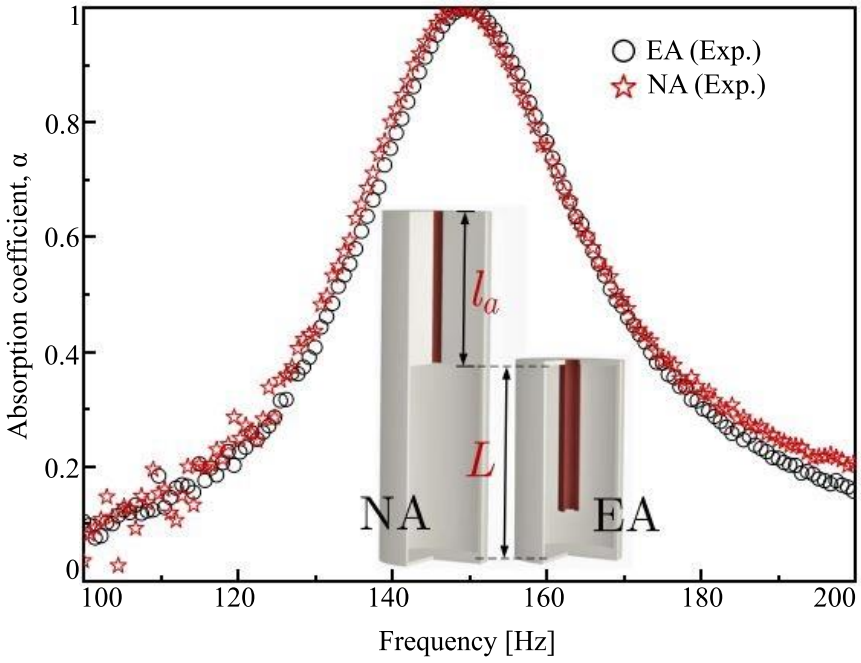

Figure 1.10- Experimentally measured absorption coefficients as a function of frequency for two perfect absorbers: a normal aperture (red pentagrams) and with an embedded aperture (black circles). The inset shows the fabricated HRs a normal aperture (NA) and an embedded aperture (EA) [50].

In addition to the coiled-space configurations, the embedded aperture can also enable the tunable performance of the HR while preserving the full absorption and the constant external shape [50]. Figure 1.10 shows the absorption coefficients obtained via an experiment for the two cases: (1) a normal HR without aperture (NA), represented by red pentagrams, (2) with an embedded circular aperture (EA), represented by black circles. The samples are shown in the inset. From the results, it can be observed that the thickness of the structure can be significantly decreased by embedding an aperture. The absorption performance for this case remains almost

the same (in terms of both resonant frequency and absorption bandwidth) as in the case of a normal HR.

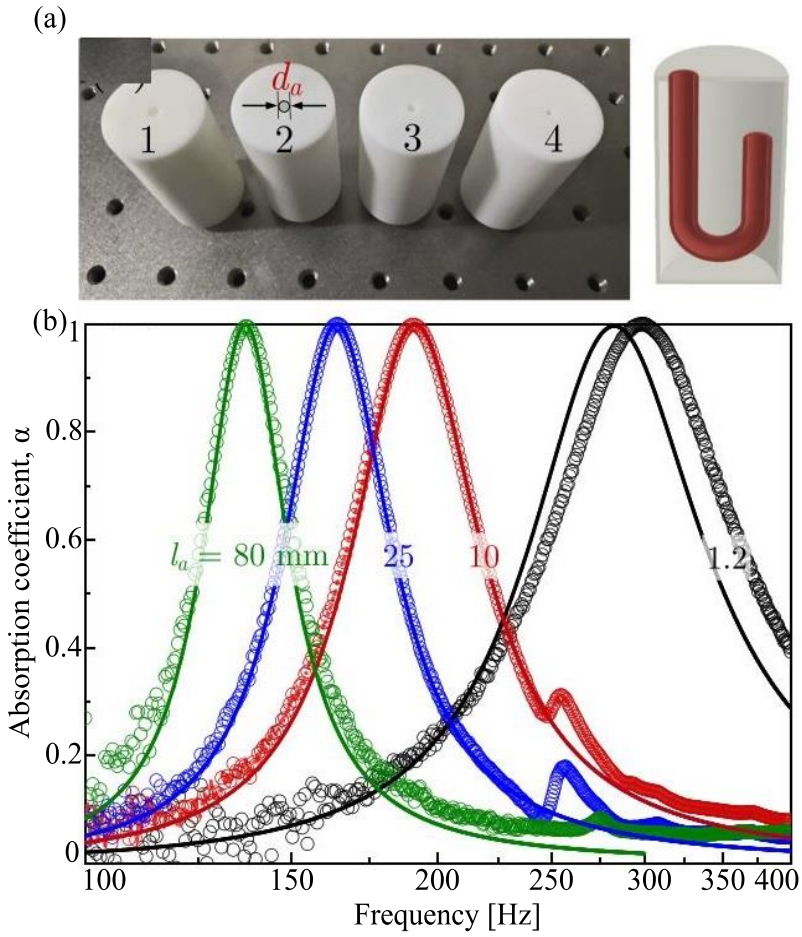

Figure 1.11- (a) Photographs of four experimental samples with different length and diameters of the aperture. Sample no. 1 is curled shape with longer aperture length than the total thickness of the structure. (b) The absorption coefficients of four samples obtained via theoretical calculations (solid lines) and the experiments (circles) [50].

To further evaluate the tunable performance of this system, four different samples with the same thickness were considered as illustrated in Fig.1.11(a). The first sample was fabricated having the curled shape aperture (l_a=80mm) as shown in the right inset. This approach allows designing the system with a longer aperture than the thickness of the structure which further improves the capacity to manipulated the impedance. The geometrical parameters of the fabricated samples are, sample 1: l_a=80mm, d_a=4.4mm, sample 2: l_a=25mm, d_a=3.1mm, sample 3: l_a=10mm, d_a=2.4mm, and sample 4: l_a=1.2mm, d_a=1.6mm. Figure 1.11(b) shows the absorption performance of these four samples. They all exhibit perfect absorption at different frequencies showing the superior impedance manipulation capability of the embedded aperture. With the curled shape aperture, the perfect absorption is achieved with the thickness of the

structure only λ/48. It can be also observed that the bandwidth in the all cases (No.1-No.4) are different ranges from 22.6% (f_r=137 Hz), 26.2% (f_r=164 Hz), 31.7% (f_r=190.75 Hz), and 46.5% (f_r=299 Hz), respectively [50]. Under the constraints of perfect absorption and constant external shape, a lower frequency resonance is achieved with a narrower absorption band. This behavior can be explained by the *Q*-factor which can be defined as, $1/Q = \Delta f_r/f_r = [1 + Re(Z)/(\rho_0 c_0)]2\pi L f_r/c_0$. It indicates that for the perfect absorbers with a constant thickness, the *Q*-factor are only determined by the frequency of the resonance (f_r). The quality factor increases when the resonance frequency decreases and the absorption bandwidth would also decrease.

Under the condition of impedance matching, above discussed designs can achieve the perfect absorption with a thin structure. However, there is a trade-off between the structure thickness and the absorption bandwidth. As discussed before, lower absorption frequency leads to narrower bandwidth. In some approaches, the bandwidth of a single or identical resonator is improved by tailoring the damping, i.e., by increasing the intrinsic material damping [74] or by using heavily overdamped condition [75]. However, these designs can hardly apply for airborne sound absorption without scarifying the thickness. One promising way to obtain broadband performance is to use supercells composed of several unit-cells having different geometrical parameters which determine the position of the absorption peak. To increase the bandwidth of the absorption curve, many designs based on coupled resonators [76–78] are proposed. Their corresponding thicknesses along the propagating direction, on the other hand, are either thick or have room for improvement. As a result, it's reasonable to wonder how much room for improvement remains. What is the minimum sample thickness required for a target absorption spectrum? To answer these questions, recently, the direct relationship between the absorption spectrum and the structure thickness has been discussed in relation to sound-absorbing structures based on the causality constraint [79].

1.3 Background Theory

When the acoustic wave passes through narrow channels, all acoustic energy converts into random thermal energy. The source of such dissipation is mainly categorized as (1) one intrinsic to the medium, and (2) one related to the boundary of medium [80]. The losses related to the medium can be further divided into heat conduction loss, loss related to the internal molecular process, and viscous loss. Heat conduction loss occurs near the rigid boundary or in the bulk of the medium, as a result of the conduction of energy from higher temperature to lower

temperature region. The internal molecular process leads to absorption which includes the conversion of the energy of the molecules in the form of rotational energy, vibration energy, or potential energy [80]. These processes depend on the chemical structure of the fluid and the related explanation is out of the scope of this thesis work.

Viscous losses occur at the interface of rigid walls, arising from relative motion between the contiguous regions of the fluid that causes the shear. The designed metasurface absorber structures in this thesis consist of narrow cavities and regions through which the acoustic wave passes. Here, as the propagation medium is in contact with a rigid boundary, complex viscous and thermal boundary layer effects come into play which requires a more thorough investigation to evaluate how it affects the acoustic systems in order to design them accurately. To understand these mechanisms, the fundamental equations of acoustics are outlined in this section which is followed by the explanation of the thermal and viscous losses.

1.3.1 Equation of State

To completely describe the behavior of the acoustic wave, it is necessary to define a set of relevant variables which can describe the physical mechanism behind the wave propagation in the given medium. Thermodynamics variables, pressure P, density ρ, and the absolute temperature (T) can be related by the equation of state, $P = P(\rho, T)$. In the case of an ideal gas (sufficient to describe most acoustics [80,81]), the equation of state can be expressed as,

$$\frac{P}{\rho} = RT \tag{1.6}$$

Where R is the individual gas constant (for air, R=286.9K kg^{-1}) [82]. Therefore, if any two thermodynamics variables are known then the gas can be fully described using Eq. (1.6). Once the thermodynamic state is obtained, the velocity $\vec{v}$ of the gas molecules is all that is needed to fully define the acoustic field. This solution can be obtained from the conservation of mass, conservation of energy, and conservation of momentum.

The equation of state defined by Eq. (1.6) arise in part from the conservation of energy is sufficient to describe the sound propagation in an unbound gas considering the adiabatic process. However, it is not complete. When the acoustic wave propagates through the air, it experiences losses due to thermal dissipation of the energy, even if it is very small. A more complete equation of state is needed to consider these losses. When the acoustic wave

propagates, the heat transfer that occurs between regions of high and low density needed to be considered. Therefore, the energy equation can be given by [83],

$$\Delta\rho C_p\left(\frac{\partial T}{\partial t}\right) = -\vec{\nabla}\cdot\left(-k\vec{\nabla}T\right) - \frac{1}{\rho}\frac{\partial\rho}{\partial T}\Big|_P T\frac{\partial P}{\partial t} \tag{1.7}$$

Here, *k* is the thermal conductivity of the fluid. In the right-hand side of the equation, the first term is a form of diffusion equation which measures the conduction of the heat through the gas while the second term is the measurement of the thermal expansion of the gas in high pressure regions.

1.3.2 Conservation of Mass

Consider a volume element of the fluid with mass being allowed to flow in or out. According to the conservation of matter, net flow into or out for the volume element must be equal to the gain or loss of fluid within it. The conservation of mass can be expressed by the continuity equation, a statement of the conservation of mass for compressible fluid flow [80,81],

$$\frac{\partial\rho}{\partial t} - \vec{\nabla}\cdot(\rho\vec{v}) = 0 \tag{1.8}$$

where, $\vec{\nabla} = \frac{\partial}{\partial x}\hat{x} + \frac{\partial}{\partial y}\hat{y} + \frac{\partial}{\partial z}\hat{z}$ is the gradient operator.

1.3.3 Conservation of Momentum

Describing the force acting on a particle within a fluid leads to Newton's second law which states that the rate of change of momentum of an object is directly proportional to the force applied. In many cases, this law can be simplified by neglecting the viscous forces as they are negligible for the short sound propagation distance. This simplification can be applied to derive the loss-free acoustic wave equation. However, in presence of the rigid boundary, the viscous force can be significant and needs to be considered.

For a particle moving in the velocity field, $\vec{v}(x, y, z, t)$, the acceleration term can be given by,

$$\vec{a} = \frac{D\vec{v}}{Dt} \tag{1.9}$$

Where D/Dt is the advective (or convective) derivation which is often used in fluid mechanics and classical mechanics which can be given by,

$$\frac{D}{Dt} = \frac{\partial}{\partial x} + \frac{dx}{dt}\frac{\partial}{\partial x} + \frac{dy}{dt}\frac{\partial}{\partial y} + \frac{dz}{dt}\frac{\partial}{\partial z} \tag{1.10}$$

where, D/Dt represents the time derivation with respect to moving coordinates system. Summing up all the forces $d\vec{F}$ acts on a fluid volume element dV which includes (1) gravity g, (2) surface normal force due to pressure, σ_{mm}, (3) surface tangential force due to shear, τ_{mn}. Here, m and n indicate the direction of axis, and both are expressed in terms of force per unit area. Considering only *x* direction for the simplification, Sum of all these forces can be expressed as,

$$dF_x = \left(\rho g_x + \frac{\partial \sigma_{xx}}{\partial x} + \frac{\partial \tau_{yx}}{\partial y} + \frac{\partial \tau_{zx}}{\partial z}\right) dxdydz \tag{1.11}$$

According to Newton's second law,

$$d\vec{F} = dm\vec{a} = \rho dV \frac{D\vec{v}}{Dt} \tag{1.12}$$

From Eq. (1.10) and Eq. (1.11),

$$\rho g_x + \frac{\partial \sigma_{xx}}{\partial x} + \frac{\partial \tau_{yx}}{\partial y} + \frac{\partial \tau_{zx}}{\partial z} = \rho\left(\frac{\partial v_x}{\partial x} + \frac{dx}{dt}\frac{\partial v_x}{\partial x} + \frac{dy}{dt}\frac{\partial v_x}{\partial y} + \frac{dz}{dt}\frac{\partial v_x}{\partial z}\right) \tag{1.13}$$

Assuming that the stress due to viscosity is proportional to the rate of angular deformation, σ_{xx} and τ_{yx} in terms of velocity gradients and the coefficients of shear viscosity can be expressed as,

$$\sigma_{xx} = -\Delta p - \frac{2}{3}\eta \vec{\nabla} \cdot \vec{v} + 2\eta \frac{\partial v_x}{\partial x} \tag{1.14}$$

$$\tau_{yx} = \eta\left(\frac{\partial v_y}{\partial x} + \frac{\partial v_x}{\partial y}\right) \tag{1.15}$$

When substitute Eq. (1.14) and Eq. (1.15) in Eq. (1.13), and solving it results in Navier-Stokes equation which is discussed in the next section.

1.3.4 The Navier-Stokes Equation

The Navier-Stokes equations govern the motion of fluids and can be thought as Newton's second law of motion for fluids. Combining force equation (Eq.(1.13)) with tensor equations (Eq. (1.8) and Eq. (1.9)) results into the well-known Navier-Stokes equation [83],

$$\Delta\rho\left(\frac{\partial\vec{v}}{\partial t}+(\vec{v}\cdot\vec{\nabla})\vec{v}\right)=-\vec{\nabla}\Delta p+\left(\frac{4}{3}\eta+\eta_B\right)\vec{\nabla}(\vec{\nabla}\cdot\vec{v})-\eta\vec{\nabla}\times\vec{\nabla}\times\vec{v} \qquad (1.16)$$

Where η is the dynamic viscosity, and η_B is the bulk velocity of the fluid which is concerned with energy dissipation through internal molecular processes. Different terms in Eq. (1.16) indicates different types of loss mechanisms. The second term on the right-hand side, $\left(\frac{4}{3}\eta+\eta_B\right)$ describes viscous losses which occur in the fluid bulk. The last term is $\eta\vec{\nabla}\times\vec{\nabla}\times\vec{v}$ which is 'vorticity' term which deals with viscous losses occur due to complex non-linear effects near a rigid boundary. Using more robust energy equation given by Eq. (1.7) and force equation given by Eq. (1.16), the internal viscous and thermal losses can be considered.

1.3.5 Thermal and Viscous Losses

When an acoustic wave propagates through a fluid medium with a normal incidence on a solid wall, the impedance mismatch is very large so that the wall can be treated as acoustically perfect rigid. It means that the sound cannot penetrate the wall and get totally reflected. As illustrated in Fig. 1.12, consider a lossless plane wave propagating along the *x*-direction. A wall is placed at *z*=0. According to the 'no-slip' boundary condition, the component of the velocity, v_x parallel to the wall must equal zero at the boundary.

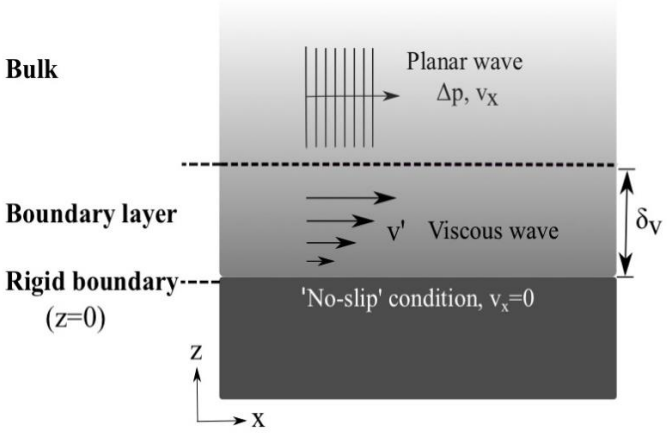

Figure 1.12- Schematic illustration of the viscous boundary layer formation. The thickness of the viscous boundary layer is given by δ_v [83].

Now, as moving away from the wall, the value of v_x must be back to its free space value. The velocity filed over which this change takes place is described as secondary viscous wave. It has its own particle velocity, v'. From the vorticity term in Eq. (1.16), the diffusion equation for v' can be given as,

$$\frac{\partial v'}{\partial t} = \frac{\eta}{\rho_0}\frac{\partial^2 v'}{\partial z^2} \tag{1.17}$$

Applying the boundary condition ($v_0 = -v^x$) when z=0, the solution of Eq. (1.17) using the method of separation of variables can be derived as (assuming a frequency dependence of e^{iwt}),

$$v' = -v_x e^{-(1+i)\frac{z}{\delta_v}} \tag{1.18}$$

Here, δ_v is the thickness of the viscous layer. It can be defined as measure of the size of thickness of the region over which particle velocity decay is zero. The thickness of the viscous boundary layer, δ_v as a function of the incident frequency can be written as [85],

$$\delta_v = \sqrt{\frac{2\eta}{\rho_0 \omega}} = \sqrt{\frac{v}{\pi f}} \tag{1.19}$$

Where v is the kinematic viscosity.

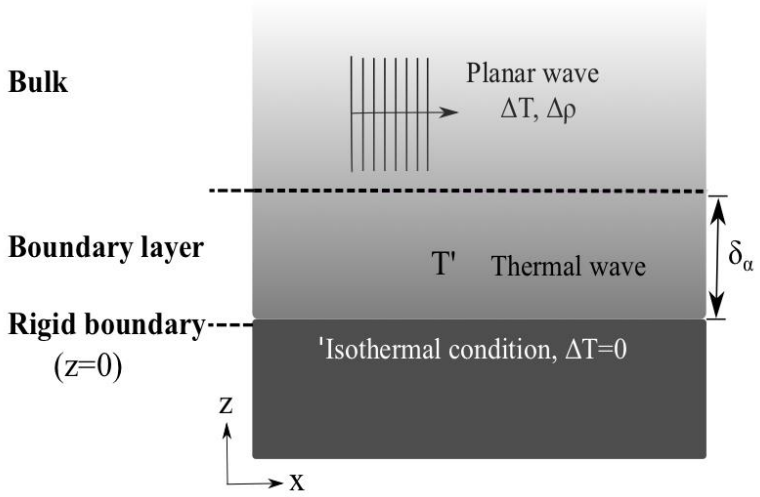

Figure 1.13- Schematic illustration of the viscous boundary layer formation. The thickness of the viscous boundary layer is given by δ_α [83].

Another important loss to be considered is thermal loss which is induced by the rigid-wall boundary. The rigid wall can be assumed as an infinite heat-sink that is at thermal equilibrium T_0 with the surrounding medium. In other words, the rigid wall acts as an isothermal boundary condition. To understand the thermal loss mechanism, consider the same case "plane-wave-perpendicular-to-wall" which is developed to understand the viscous loss. The thermal loss mechanism can be explained from Fig.1.13. In the case of the free space propagation of a plane wave of pressure amplitude *P*, the excess temperature that is generated by the density fluctuations can be given by [80],

$$\Delta T = T_0 + T_0(\gamma - 1)\left(\frac{P}{\rho_0 c^2}\right)e^{i(wt-kx)} \tag{1.20}$$

This temperature fluctuations can be treated as they are in the lossless case in the region far from the wall: very slow and insignificant in magnitude to be conducted to surrounding regions of the fluid which can be regarded as an adiabatic process. However, this excess temperature immediately conducts into the wall in close proximity to the rigid boundary. This process signifies that the acoustic process is switched from the adiabatic to the isothermal. A secondary thermal wave T' is created as a result of the evolving of the acoustic wave propagation near the wall to the free space. This process can be thought similar to the formation of the secondary viscous wave *v'* resulted from the tangential particle velocity being forced to zero. The full mathematical description of this process in explained in Ref. [80,81,86,87]. Similar to the Eq. (1.17), applying the boundary conditions (considering a frequency dependence of $e^{i\omega t}$), a total thermal field of the primary and the secondary temperature wave, *ΔT-T'* can be obtained as,

$$\Delta T - T_0 = (1 - e^{-(1+i)\frac{z}{\delta_\alpha}})T_0(\gamma - 1)(\frac{P}{\rho_0 c^2})e^{i(\omega t-kx)} \tag{1.21}$$

Here, *P* is the pressure amplitude of the plane wave and δ_α is the thickness of the thermal boundary layer which can be given by,

$$\delta_\alpha = \sqrt{\frac{\alpha}{\pi f}} \tag{1.22}$$

Both the viscous and thermal boundary layer thickness can be related by dimensionless Prandtl number, P_r given by,

$$P_r = \frac{\delta_v^2}{\delta_\alpha^2} \tag{1.23}$$

which shows a measure of the ratio between the viscous losses and the thermal losses in a given system. For the air, this value is 0.7, while it is around 7.1 for the water. Both the thermal and viscous effects are almost equally important in air, while for the case of water (or for most of the fluid), the thermal losses play a more minor role.

The study of the viscous and boundary layers was first explored by Kirchhoff [88] and expanded by Rayleigh [89]. Also, there are many studies on the effects of the thermal and viscous boundary layers in acoustics [90-93]. Molerón et al. [93] emphasized the importance of including thermoviscous effects on the acoustic propagation through metamaterials made up of rigid slabs with subwavelength slits embedded in air. Their results show that when the thermoviscous effect is considered, 100% reflection occurs. However, for the same case, the perfect transmission was predicted without considering the losses. The effect of these boundary layers has been also studied for the porous media [94].

1.4 Conclusions

The state of art and literature review on acoustic metamaterials and metasurfaces is presented in this chapter. We reviewed the most relevant works of literature on acoustic metasurface design for very low-frequency absorption. In the second part, the fundamental equations of acoustics are outlined to support the discussion of viscous and thermal losses. The importance of the thermodynamic properties of the sound propagation medium, specifically, the presence of viscous and thermal boundary layers on the interface between fluid and a rigid boundary is also discussed in this chapter.

Chapter 2
Methods

In this chapter, all the theoretical, experimental, and numerical methods which are used throughout this thesis work are presented. First, the numerical modeling and simulation steps using the finite element method are discussed. Specifically, we use thermoviscous acoustic interface to consider the effect of the thermoviscous losses in the narrow cavities. Modeling steps like geometry construction, mesh to resolve the viscous and thermal boundary layers are discussed. For the measurements, multiple experimental samples and structures have been fabricated using 3D printing that will be presented. Further, the experimental measurement using the two-microphone method is explained with the associated calibration process. In the later part of the chapter, machine learning methods used to design the metasurface absorbers are described and discussed. Regarding this part, the training of deep learning and the loss functions used for the training of the networks are explained. In the subsequent section, the discriminator and generator neural networks are discussed. Specifically, we use a convolutional neural network for the forward design and a conditional generative adversarial network (a type of generator neural network) for the inverse design. A summary of classical machine learning techniques (KNN, RF, and SVM) used to compare the performance of the implemented deep learning network is provided. Fundamental machine learning concepts framed within the context of this thesis are also discussed which includes data augmentation and dimensionality reduction.

2.1 Numerical Modeling- The Finite Element Method

Throughout this thesis, theoretical and experimental results are compared with the numerical simulations performed using the finite element method. We have used commercially available FEM-based software COMSOL Multiphysics for this purpose. The FEM is a powerful numerical analysis technique for obtaining approximate solutions of partial differential equations (PDEs) arising in physics and engineering [95]. For the vast majority of geometric problems, partial differential equations (PDEs) cannot be solved with analytical methods. Instead, approximate equations are constructed based on various discretization by using

numerical model equations to approximate the PDE which is then solved using numerical methods [96]. The FEM is used to compute such approximations. For example, consider that a function u is defined to be a dependent variable in a PDE (i.e., pressure, temperature, volume, etc.). It is possible to approximate the function $u \approx u_h$ using linear combinations of basis functions,

$$u_h = \sum_i u_i \psi_i \tag{2.1}$$

where u_i is the coefficient of the functions that approximate u with u_h and ψ_i is the basis function. An example to illustrate this for a 1D problem is shown in Fig.2.1. The function u (blue line) is approximated by u_h (red line) consists of 8 basis functions. Here, the value of the linear basis functions is 1 at their respective nodes and 0 at other nodes. This discretization depends on the solution required, not necessarily to be linear. Distribution of the basis function is used to resolve parts of the function where a higher resolution is needed. In COMSOL Multiphysics, this discretization is defined by mesh elements. A geometry is divided into a large number of mesh elements and a system of equations is solved in each element which combines to produce the final result.

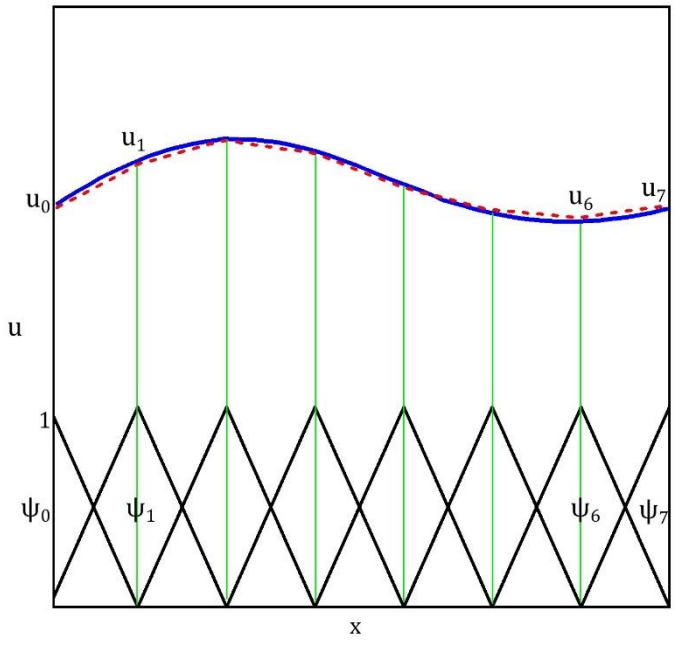

Figure 2.1 - The function u (blue line) is approximated with the function u_v (red dashed line), which is a linear combination of linear basis function, ψ_i (black solid line). $u_0 - u_7$ represents the coefficients [97].

Using such simulations, many things can be achieved. First, a purely numerical experiment can be conducted to test different conditions, such as what would happen if the temperature is changed, or what happens if we change the material of the structure. It offers a high degree of flexibility; numerical experiments can be performed by turning particular terms on or off, isolating particular physical effects, or by altering input parameters, boundaries, or initial conditions. New experiments that would be too costly to test on the spur of the moment can be conceived this way. Another thing, for the complex systems (such as metasurface structures designed in chapters 4 and 5), it is difficult to find a solution using the theoretical method. Numerical modeling is preferable in such cases to solve the system and post-processing steps such as to study acoustic pressure distribution, temperature variations, etc. The following discussion explains the construction of the simulation models, the used boundary conditions, and how we solve wave propagation equations for a typical acoustic structure.

The numerical simulation in COMSOL Multiphysics involves building a model of the experimental environment one wishes to test. This starts with creating basic geometry and then assigning materials properties to the different parts. In our simulations, solid is considered perfectly rigid so, it is only needed to model the propagation medium, i.e. air. Though this assumption was verified using Polylactic Acid (PLA) material for the multicoiled metasurface structure with the structural mechanics module. PLA was modeled with the following physical parameters: density=1250kg/m^3, young modulus=3.2×10^9, and poisson ratio=0.35. The next step is to choose the proper conditions at the geometry's many boundaries. We use solid hard boundary conditions at the air-solid interface due to the large impedance mismatch between air and solid. On the sound hard boundary, the normal component of the acceleration is zero since no motion is possible,

$$-n \cdot \left(-\frac{1}{\rho_c} (\nabla P - q_d) \right) = 0 \tag{2.2}$$

where ρ_c is fluid density, and P is acoustic pressure. With the boundary conditions determined, the set of equations to be solved are chosen. For solving acoustic structures, two systems are used. Where thermodynamics effects are not significant, the 'Pressure-Acoustics' (PA) module is used. This module solves the basic loss-free acoustic equation in the form of the Helmholtz equation. It is computationally cheap, as it is used for regions of linear acoustics described only by a scalar pressure variable. It allows for some basic modeling of loss. Where necessary, for example in narrow cavities, the 'Thermoviscous-Acoustic' module must be used. It solves the

linearized Navier-Stokes equation for fluid flow (given by Eq.(1.16)), and a detailed form of the equation of state (Eq.(1.7)). This system of equations has many more degrees of freedom than the Pressure-Acoustics module which increases the computation time. Also, this module uses finer mesh compared to the PA module since there are so many small-scale mechanisms particularly in the confined spaces such as narrow acoustic spaces/cavities, where the complex interaction of the sound with the viscous and thermal boundary layers must be accounted for. In the modeling of the structures in this work, we have defined the boundary layers thickness using Eq.(1.19).

The next important step is to define mesh which determines where to solve the relevant equations. Denser mesh provides better accuracy but, this accuracy comes with computation cost and memory. So, a smart way is to optimize the mesh quantity. There is vast literature available regarding the dedicated optimization process of mesh [98,99] but, it is not in the scope of this thesis work. The thumb rule is that the maximum mesh size should not exceed the five elements of the shortest wavelength of interest. COMSOL Multiphysics simulates the model with a finer mesh and compares the respective result to the one obtained with previous mesh density, by subtracting the field at each point. If the magnitude of the result of the subtraction is below the given tolerance level, such as 1×10^{-5}, then the model has converged and the mesh is assumed to be sufficient. In modeling all the structures in this thesis, we have done a quick test with different maximum mesh element sizes and choose the smallest optimized mesh for each case. An example of such meshing is shown in Fig.2.2(a), which shows the meshing near the transition region between the acoustic cavity section and the free space. A thermoacoustic interface is applied at the narrow opening of an acoustic cavity. The mesh in the thermoacoustic region is denser than in the pressure region since the equations are simpler in the PA and the unbound fields do not vary significantly. Also, special mesh refinement by defining the boundary layer mesh is shown near boundaries. At the rigid wall of the cavity, the thermoviscous boundary layers exist which affects the sound propagation even though they are very small. Figure 2.2(b) shows the thickness of viscous and thermal layer as a function of frequency. The boundary layer mesh is applied in this region which allows increasing the resolution in these particular layers, without slowing down the rest of the model. We have used 10 layers of the boundary layer mesh with a growth factor of 1.2 between each layer. Finally, the system of equations can now be solved to find specific answers. We use a direct solver, which is the default solver in most physics interface. It is efficient and robust for all medium

problems. In the 'frequency sweep', the desired frequency range is set to determine the absorption spectra.

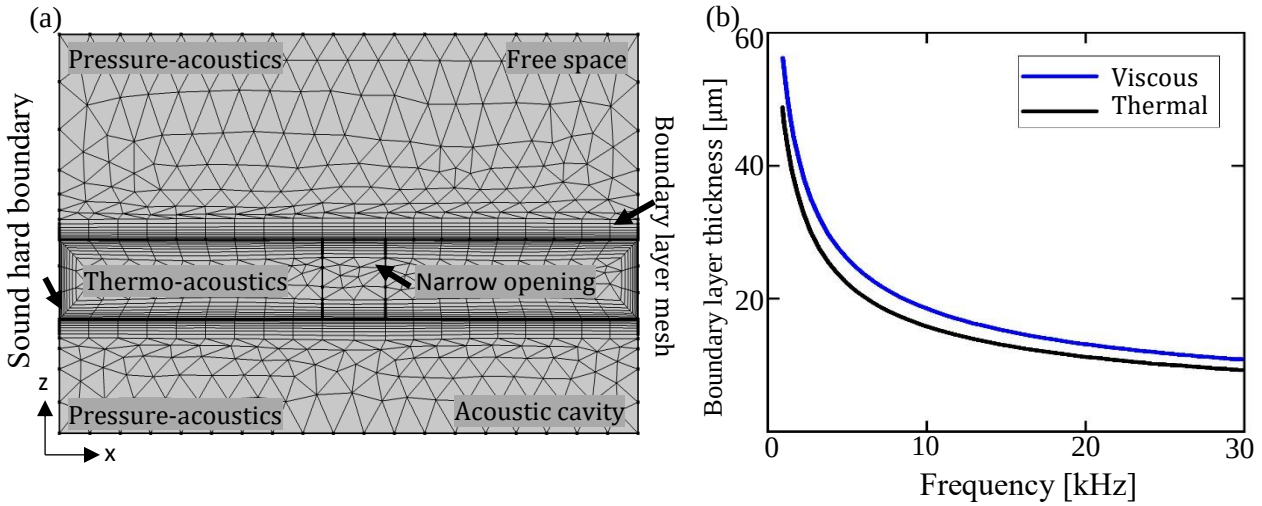

Figure 2.2 – (a) Cross section of COMSOL model set up for simulating an acoustic cavity with narrow opening. (b) Viscous and thermal boundary layer thickness in air as a function of frequency.

2.2 Complex Frequency Plane Analysis

We use the concept of the zeros and the poles of the reflection coefficient in the complex frequency plane for the study of the temperature effect on the multicoiled metasurface absorber (chapter 3). This concept has been widely used as an efficient tool to study and design the broadband and metasurface absorbers in the low-frequency regime [67,68]. Using this method, the reflection coefficients of the whole system can be evaluated in the complex frequency plane in which the real part of the frequency is represented in the abscissas, and the corresponding imaginary part is represented on ordinates.

This concept can be explained by considering the simple example of a slot with a quarter wavelength resonance [68] that is related to the concept of coiling up space for designing subwavelength acoustic metamaterials. As the interest lies in low frequency absorption, attention is paid to the frequency range smaller than the cutoff frequency of the waveguide and therefore the problem can be considered as 1D. The structure of interest is shown in Fig.2.3(a). It is equivalent to an incident wave on a slot having length l_b and section B_2 at the end of a waveguide of section B_1 or to a wave normally incident on a wall with periodic slots. Considering that a plane wave is incident from the left direction such that a standing wave is formed in $y < 0$ which can be written as,

$$p = e^{iky} + Re^{-iky} \tag{2.3}$$

Where k is the wave number, c is the speed of wave, and r is the reflection coefficient. For the rigid wall at the end of the slot, $p'(l_b) = 0$ and $\frac{p'(0^+)}{p(0^+)} = k\tan(kl_b)$. Here, the prime indicates the differentiation with respect to y.

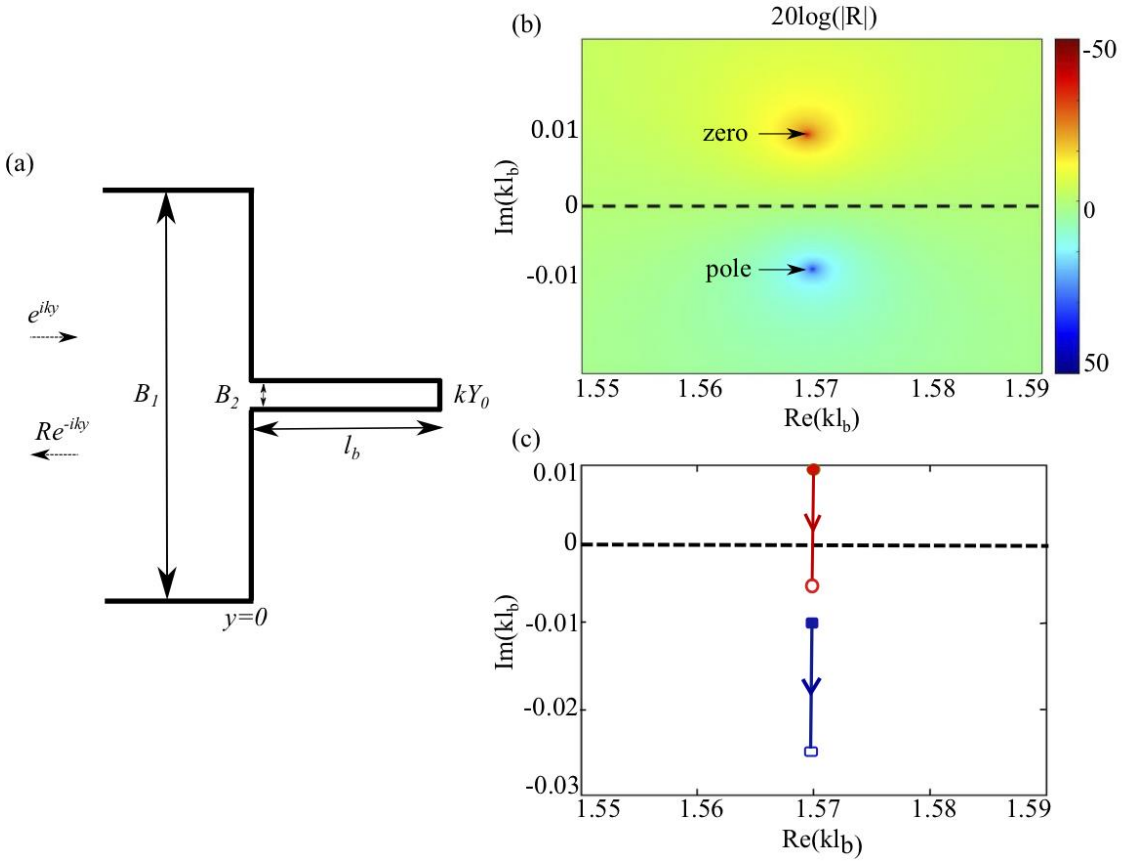

Figure 2.3- The complex frequency plane analysis for a slot resonator. (a) Schematic of the slot with $l_b = 25cm$ and $B_2/B_1 = 0.1$. (b) Complex frequency representation of $20\log(|R|)$ for the lossless case. The pole-zero pair obtained using Eq.(2.5) and Eq.(2.6) is located in the plane. (c) Down-shifting of the pole (blue line) and zero (red line) when the losses are added to the system. Arrows show the direction of shifting as the losses increase. The lossless case is represented by filled symbols, while the lossy case is represented by open symbols [68].

As one mode approximation is assumed, the continuity conditions can be written as $p(0^-) = p(0^+)$ and $B_1 p'(0^-) = B_2 p'(0^+)$. From this, the reflection coefficient can be defined as [68],

$$R = \frac{\cot(kl_b) + i(B_2/B_1)}{\cot(kl_b) - i(B_2/B_1)} \tag{2.4}$$

From Eq. (2.4), zero corresponds to numerator, $\cot(kl_b) + i(B_2/B_1) = 0$ and the pole corresponds to denominator, $\cot(kl_b) - i(B_2/B_1) = 0$. With the assumption $(B_2/B_1) << 1$, the equations of the first pole-zero pair can be written as,

$$(kl_b)_{pole} = \frac{\pi}{2} - i\frac{B_2}{B_1} \tag{2.5}$$

$$(kl_b)_{zero} = \frac{\pi}{2} + i\frac{B_2}{B_1} \tag{2.6}$$

Here, the imaginary part (B_2/B_1) signifies the leakage caused by radiation at the open end of the slot towards the slot's exterior. Figure 2.3(b) shows the representation of |R| in the complex frequency plane for the lossless case. Generally, for the lossless case, one finds the poles and zeros of the reflection coefficient symmetrically distributed around the real axis. The zeros are in the positive imaginary frequency plane and the poles are in the negative imaginary plane. Now, considering the loss is introduced to the system by adding a thin lossy coating at the end of slot such that $p'(l_b) = kY_0p(l_b)$ with $Im(Y_0) > 0$. Using $\frac{p'(0^+)}{p(0^+)} = (k\tan(kl_b) + p'(l_b)/p(l_b))(1 - \tan(kl_b)/k \times p'(l_b)/p(l_b))$, Eq.(2.4) can be rewrite as [68],

$$R = \frac{\cot(kl_b) - Y_0 + \dfrac{iB_2}{B_1(1 + Y_0\cot(kl_b))}}{\cot(kl_b) - Y_0 - \dfrac{iB_2}{B_1(1 + Y_0\cot(kl_b))}} \tag{2.7}$$

Here, $|R| < 1$ for real frequency k due to loss. Also, the pole-zero pair shifts into the complex plane k as compared to the lossless case. Assuming that the slot is thin and coating is small, the pole-zero pair for the lossy case can be written as,

$$(kl_b)_{pole} = \frac{\pi}{2} - i\frac{B_2}{B_1} - Y_0 \tag{2.8}$$

$$(kl_b)_{zero} = \frac{\pi}{2} + i\frac{B_2}{B_1} - Y_0 \tag{2.9}$$

Equation (2.8) and (2.9) indicates that the pole-zero pair is down-shifted by Y_0 which is shown in Fig.2.3(c). The zero of R coincides with the real axis when $\frac{B_2}{B_1} = Im(Y_0)$. This signifies the critical coupling condition is fulfilled (the leakage (B_2/B_1) is balanced by the loss, $Im(Y_0)$) and full absorption ($\alpha = 1$) is achieved for the real frequency. Here, the distance between pole and zero.

2.3 Sample Fabrication

Within this thesis, multiple experimental samples have been fabricated in our lab using 3D printing technology based on fused filament fabrication (FFF) as shown in Fig.2.4. Presently, in this work, the complex properties of sound when traveling through solid objects are not of concern. Any acoustically rigid material can be used, and in practice, almost all solids can be treated as perfectly rigid as compared to air because the impedance mismatch is so large. Here, PLA (density, ρ=2700kg/m^3) is used as the structural material. It is a biodegradable and rigid polymer and the main advantage of it is how easy it is to use in 3D printing and the good results it delivers [100].

For 3D printing, the FFF is the most commonly used technology nowadays due to its ease of use, lack of reliance on harsh chemicals, and cost-effectiveness. During the process, the filament is extruded through a heated nozzle. The nozzle (diameter 0.4mm) is mounted on a motion system that moves it around a build area. The melted filament from the nozzle is deposited onto a build plate as shown in Fig.2.4(a), where it cools and solidifies to form the desired layer. This process is repeated until the complete object is formed.

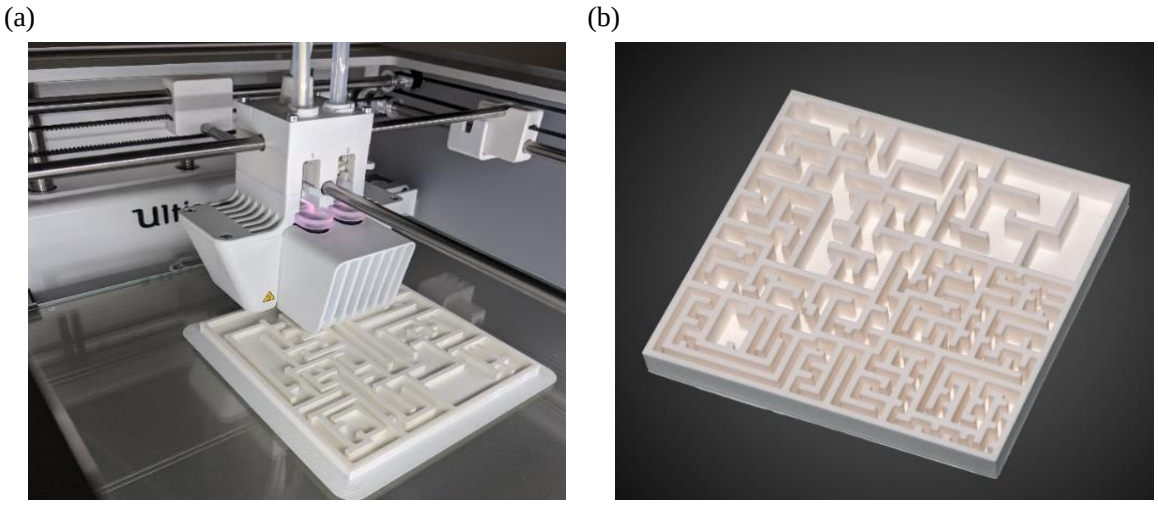

Figure 2.4- (a) Sample fabrication using the FFP based 3D printing process. (b) Fabricated sample without the perforated plate.

During the 3D printing process, some parts may require support structures. For example, the fabrication of the perforated plate and circular aperture in the samples designed in this thesis is a bit challenging as it needs to use dedicated support material. One solution is to use water

dissolvable polyvinyl alcohol (PVA). It can be easily removed after the printing process. The use of a dedicated support material ensures that the final printed structure has a smooth surface finish. In our case, it is difficult to remove the dissolved part of the material from the labyrinthine structure through a small hole. As a substitute, the labyrinthine structure and the perforated plate were fabricated separately and then carefully attached with the glue from the sides and this method worked well.

2.4 Acoustic Absorption Measurement

For the acoustic absorption measurement of the designed metasurface, we use two microphone method which is discussed in the subsequent section. The experimental apparatus consists of an impedance tube (inner size is of $10 \times 10\, cm^2$), two Bruel & Kjær 1/4-in.-diameter microphones (M_1 and M_2), and Bruel & Kjær measuring module "Acoustic Material Testing" are used to measure the absorption of the metasurface [101]. Two fixed microphones are flush mounted on the wall of a normal incidence acoustic impedance tube. The thickness of the waveguide wall is 6mm.

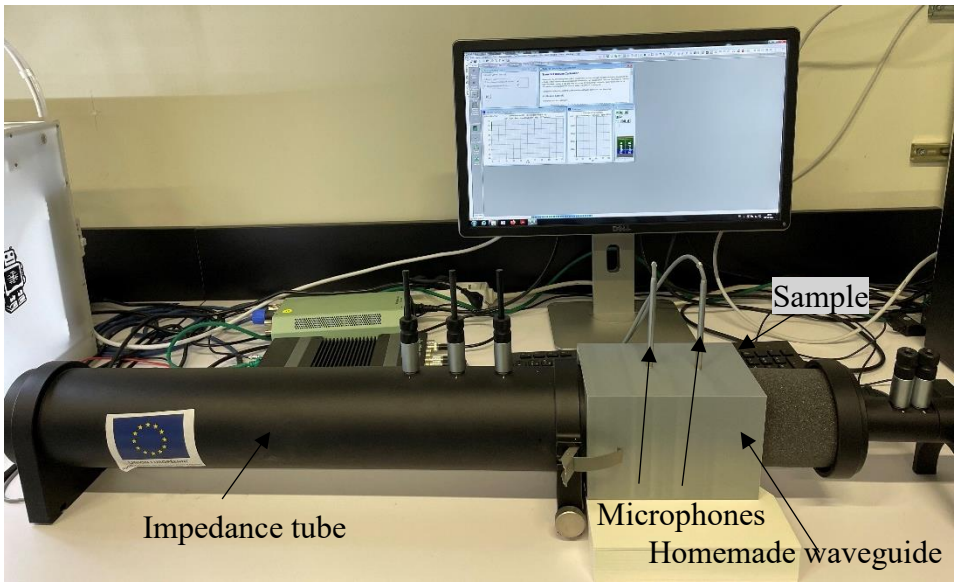

Figure 2.5 – Experimental setup to measure the absorption of the sample using two microphone methods.

We fabricate homemade waveguide to fix the sample at the end of the tube as shown in Fig.2.5; the absorption spectra can be measured for the corresponding metasurface. On the other end, a sound source is connected to an amplifier which is connected to a waveform generator that generates the broadband signal. It is important to note that this method requires very precise

transfer function measurements, which require accurate amplitude and phase calibrations for the microphones. Before each absorption measurement, the calibration procedure was carried out which is explained in section 2.4.2. Since the rear of the wall is a hard wall condition, it can be assumed that there is no transmission. A digital signal (white noise) powered by the amplifier is sent to the loudspeaker. The absorption coefficient was obtained by analyzing the signal by two microphones. Each experiment was repeated multiple times to validate its reproducibility.

2.4.1 The Two-Microphone Method

To measure the acoustic absorption, the two-microphone method includes the decomposition of the source generating broadband stationary random signal into its incident (P_i) and reflected (P_r) components [101]. These components are determined from the relationship between the acoustic pressure measured by microphones (M_1 and M_2) at two locations on the wall of the tube as shown in Fig.2.6.

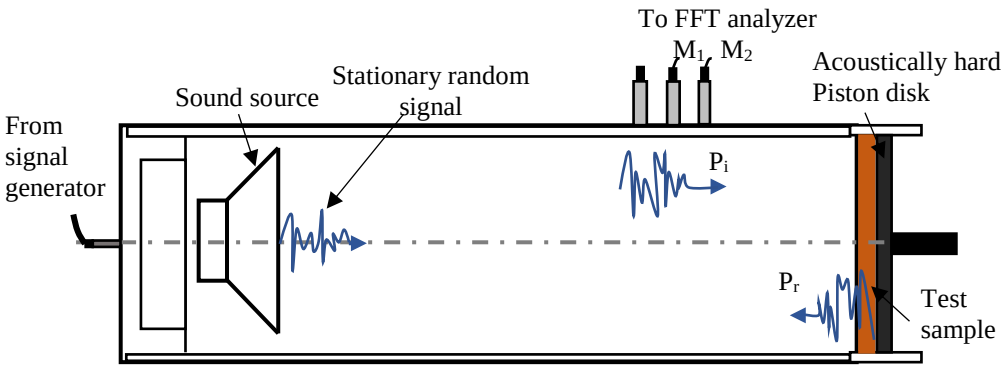

Figure 2.6 - 2D cross-section of impedance measurement tube that shows the incident (P_i) and reflected (P_r) components of the stationary random signal.

Using the incident and reflected components of the sound wave at the two microphone locations, three frequency response functions are calculated,

- H_1, the frequency response function
- H_i, the frequency response function related to the incident component (P_i)
- H_r, the frequency response function related to the reflected component (P_r)

From these three values, the complex reflection coefficient (R) is calculated by,

$$R = \left(\frac{H_1 - H_i}{H_r - H_1}\right) e^{j2k(l+s)} \tag{2.10}$$

where, k is the wave number, l is the distance between the first microphone (M_2) location and the front of the sample, and s is the distance between the two microphones (in mm). Using this value for the reflection coefficient, the normalized impedance ratio ($z/\rho c$) and the sound absorption coefficient, α can be derived as,

$$\frac{z}{\rho c} = \frac{1+R}{1-R} \tag{2.11}$$

$$\alpha = 1 - |R|^2 \tag{2.12}$$

Here, plane-wave propagation is assumed with no mean flow and no losses due to absorption at the tube wall. The design of the type 4187 protection grid and the microphone positions assures that the absorption at the wall of the impedance measurement tube is kept to a minimum.

2.4.2 Calibration Process

Before starting the measurements, the calibration procedure must be carried out with the sample mounted in the sample holder. During this procedure, the frequency response functions are calculated by interchanging the position of the two microphones and again in their original positions. The calibration frequency response functions for the standard positions (H_{C1}) of microphone and the interchanged positions (H_{C2}) can be calculated by [101],

$$H_{C1} = |H_{C1}|e^{j\Phi_1} \tag{2.13}$$

$$H_{C2} = |H_{C2}|e^{j\Phi_1} \tag{2.14}$$

Here, $\emptyset_1$ and $\emptyset_2$ are the phase of the functions H_{C1} and H_{C2} respectively. Using these values, the calibration factor, H_c is calculated as,

$$H_C = |H_C|e^{j\Phi_1} \tag{2.15}$$

Where,

$$|H_C| = \sqrt{H_{C1}H_{C2}} \tag{2.16}$$

$$\phi_C = (\phi_1 + \phi_2) \tag{2.17}$$

The calibration factor can now be added to any response function that is calculated using the tube setup. It gives a value that is not affected by any amplitude or phase mismatches between the microphones.

2.5 Machine Learning Algorithms

In the second part of this thesis, machine learning techniques are implemented as a practical tool to design acoustic absorbing metasurfaces for low-frequency applications. It includes deep learning-based algorithms such as convolutional neural network, conditional generative adversarial network, and classical machine learning algorithms (KNN, SVM, RF) which are discussed in brief in subsequent section.

Acoustic systems are usually studied in terms of two problems: (1) Forward problem: given an acoustic structure what is the acoustic response? (2) Inverse problem: given a prescribed acoustic response, how to conceive and design the suitable acoustic structure and geometry? The first problem is straightforward and can be solved using various theoretical or numerical simulation methods. While numerical simulation provides accurate device response predictions evaluating Navier-Stokes equations, it is severely time-consuming when evaluating large batches of simulations. It makes difficult to explore the whole parameter space. This is a major concern especially for the low-frequency three-dimensional (3D) calculations because, at low frequencies (<50Hz), the narrow bandwidth requires sufficiently high resolution to sweep the frequencies for accurate calculations. Another approach is to develop analytical models using theoretical methods [47,48,50,67,68,102,103] where acoustic wave theory is the design basis, and the designers are required to have a strong background in this field, which prevents layman users from device design according to actual demands. Also, it may be difficult to develop a theoretical model for complex systems such as the metasurface absorber designed in chapters 4 and 5. For the inverse designs, approaches used to solve this problem in acoustic device design include evolutionary [104], simulated annealing [105], adjoint variable algorithms [106], etc. While great paces have been made in solving the inverse problems, it still remains a challenge to identify the best device design for the given desired objectives and constraints.

To overcome these obstacles, a data-driven approach based on machine learning (ML) methods is considered in this dissertation. Such methods have provided a promising platform to learn the intrinsic relation between various structural parameters and their spectral responses

in an intelligent manner. Once the training phase is over, it offers a solution to significantly reduce time-consuming calculations with limited computational resources. Also, such methods are broadly accessible. Open-source software ranging from TensorFlow [107] to PyTorch [108] are freely available to implement and train the network. Among all ML methods, deep learning has emerged as a very promising method especially, to solve non-institutional problems and has turned out to be very efficient at discovering intricate structures in high-dimensional data . It offers a fresh perspective to solve forward and inverse problems due to its ability to mimic nonlinear physics-based relationship between a large number of interdependent variables, such as those between acoustic structure and its spectral response. Also, it is now possible to design and train deeper neural networks that can exploit larger datasets with higher performance thanks to the introduction of novel training and regularization techniques such as 'ReLU' (rectified linear units) activation function [109], dropout [110], and batch normalization [111]. The rapid development in this field enables researchers to efficiently solve numerous scientific problems including photonics structures [112,113], optical metasurface [114,115], quantum physics problem [116], acoustic cloak design [117], and other complex problems [118,119]. Despite of such significant advancement in the field of MLs, the reported studies to the date mostly focused on solving forward and inverse problems of electromagnetics and optics while there are only few robust deep learning models developed for inverse acoustic scattering problems [117, 120–122].

For the dataset generation, a few thousand simulations are performed using COMSOL Multiphysics in batch mode without the graphical user interface on three servers working in parallel. For the automatic data extraction, a batch job (to extract the absorption coefficients) is defined under job configurations in the solver sequence. After setting the job, the models were set to run automatically in batch mode using the command lines. All the proposed models are built under the windows 10 operating system in our simulation lab. The configuration of the computer is Intel(R) Core (TM) i5-3470 CPU @ 3.19GHz. It is realized on the Anaconda platform with Python version 3.6. Keras framework with a TensorFlow backend is also used to set up the model.

2.5.1 Discriminative and Generative Neural Networks

To understand the discriminative and generative neural networks, consider the acoustic metasurface which can be described by two types of labels as shown in Fig.2.7(a). The first

type includes physical variables such as geometrical parameters. Here, they are labeled by x. The second type comprises the physical response corresponding to the given spectral range which is labeled by the variables. Normally, physical responses can be expressed as a single-valued function of the physical variables means that given an input value maps a single value of y in the output. For example, an acoustic absorbing metasurface having a fixed geometrical configuration produces a single absorption spectrum. However, the opposite is not true, a given input physical response y can map to multiple xs. For example, the same absorption spectrum can be generated using the different combination of physical variables too. Depending on the type of device labels, different neural networks can be implemented. The most commonly used neural network classes in electromagnetism and acoustics are based on discriminative and generative networks [117,118,120,121].

Discriminator neural network can interpolate complex and nonlinear input-output relationship by modeling $y = f(x)$ and solve the forward problem as shown in Fig.2.7(b). This input-output mapping is single valued function which supports one-to-one or many-to-one mappings. Discriminator neural network can be generically utilized for fast and accurate modeling of acoustic metasurface devices with minimum human intervention. Because it uses the same deep-network concepts as discriminative neural networks, generative neural networks appear deceptively similar to discriminative neural networks architecture [113]. However, there is a main difference between both the networks. One of the inputs to the generative network is a latent variable, z, which is a random variable to the neural network. Here, 'latent' mention that variable, z does not have an explicit physical meaning. Either uniform or Gaussian distribution is used to sample the latent variables. A single instance of sampling z maps to a single network output and continuum of z samplings maps to a distribution of outputs of network. In the vast majority of cases, generative networks are used to generate a distribution of device layouts, as shown in Fig.2.7(c). The inputs to the network include a z and θ which represents the set of the label. This type of networks is known as 'conditional' as the output distributions can be considered as probability distributions conditioned on the set of the labels, θ. The network learns from a training set that consists of a collection of discretely labeled devices, also called as samples from the distribution $P(x \mid \theta)$. Once properly trained with enough data, the network outputs a device distribution $\hat{P}(x \mid \theta)$ that matches $P(x \mid \theta)$. For the unconditional network, there is only one input, latent variable, z. Similar to the conditional networks, such kind of network can also be trained and it produces devices. However, there is no control over modes of the data to be generated. The stochastic nature of generative neural

networks distinguishes them from discriminative neural networks. Based on the given input θ, generative network can execute one-to-many mappings.

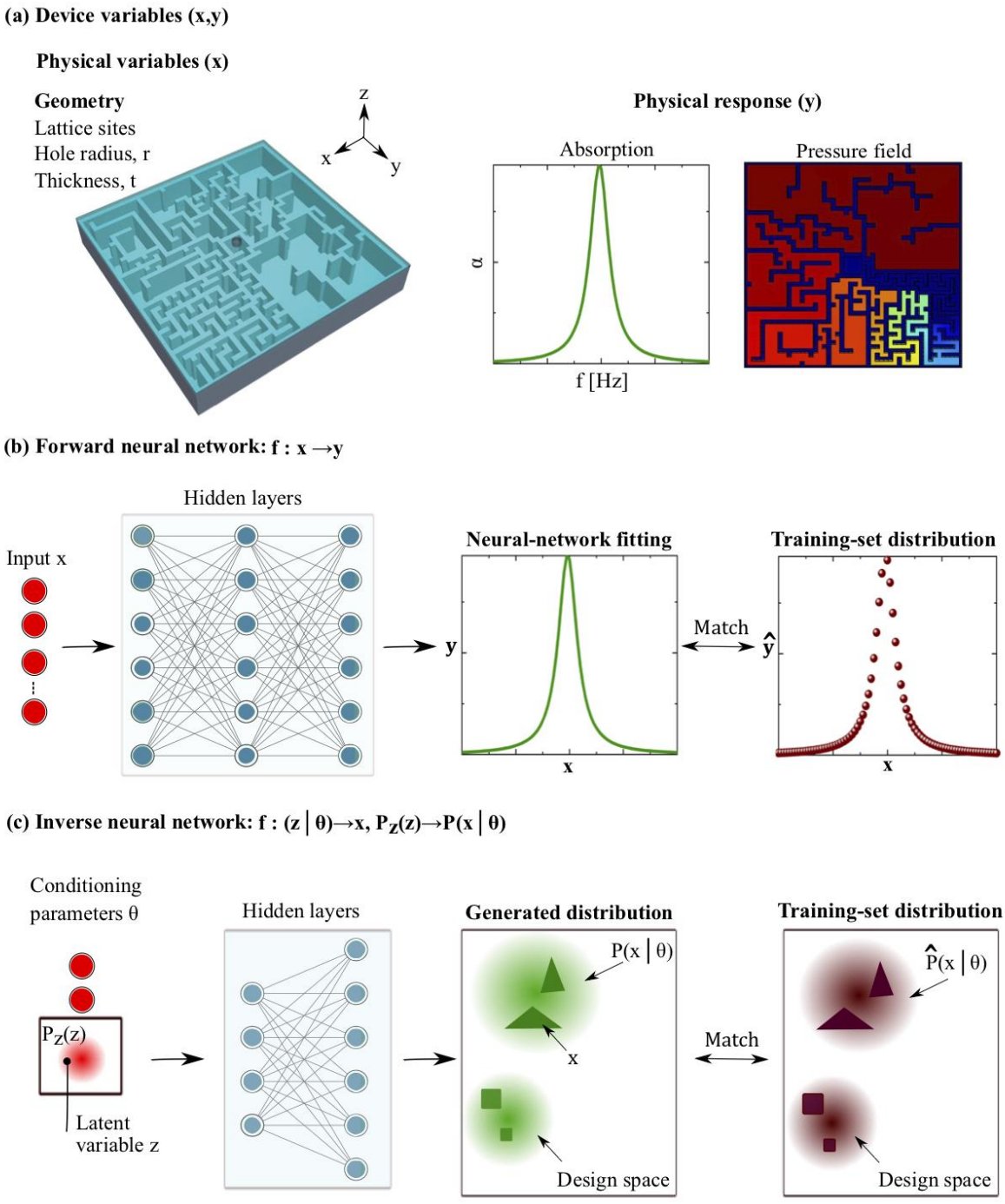

Figure 2.7- (a) Acoustic devices can be presented with two types of labels, physical variables x and physical responses y. (b) Discriminative neural networks: built the relationship $y = f(x)$ which matches with the training set values $(x, \hat{y})$. (c) Generative neural networks: maps the latent variables, z and condition labels, θ, to a distribution of device, $P(x|\theta)$. The trained network matches $P(x|\theta)$ with the training set distribution, $\hat{P}(x \mid \theta)$.

2.5.1.1 Principle of the Neural Network

Deep learning is a powerful class of ML algorithms that models extremely nonlinear data relationships by serially stacking nonlinear processing layers. Such networks consist of a series of many hidden layers of the artificial neurons through which the network can learn complex pattern. A neuron can be considered as a mathematical function that takes one or more inputs which are multiplied by a value called 'weights' and added together, resulting in a single output value. For example, consider a network that receives an input vector $x = \{x_1, x_2, x_3\}$ and in output, it gives a scalar value y. As shown in Fig.2.8(a), the neuron executes two operations: a weighted sum and nonlinear mapping [113]. The weighted sum, s can be expressed as, $s = \sum w_i x_i + b = w^T x + b$ where, w is the trainable weight vector having the similar dimension as x. Here, b represents trainable bias value. A set of weights is used to initialize a neural network when it is trained on the training set. During the training phase, theses weights are optimized. Next, nonlinear mapping is performed on a weighted sum, s using a nonlinear activation function f, such that the output of the neuron is $y = f(s)$. The neurons in a network can be connected in a various way to design the network. The most commonly used network design to solve physics related problems are fully connected (FC) and convolution layers [112,114,115,117,118,121,124]. As shown in Fig.2.8(a), FC layers consist of a vector of neurons. Each neuron in a layer receives its inputs from the preceding layer's output values. For different layers, the number of neurons may be varied. When a large number of layers are stacked in a sequence, data features with higher degrees of abstraction are recorded from lower-level features. Each layer has a nonlinear activation function f applied to it, ensuring that stacking various FC layers adds computational complexity that can't be represented using only one layer.

In physics, there are a variety of data structures that may be used to represent a wide range of phenomena. It can be in form of vectors that describe parameters or images that describe devices. Geometric and material qualities for relatively simple acoustic setups can be defined by a vector of discrete parameters. Some of these parameters include the height, width and the periodicity of a device geometry, material properties like mass density and bulk modulus, and the frequency and angle of incidence wave. Such data structures naturally interface with the fully connected neural networks as shown in Fig.2.8(a). A deep fully connected network architecture will usually suffice if the purpose of the network is to locate discrete input and output data structures. Many devices have freeform geometries that are best described by two- or three-dimensional images and cannot be parameterized with a few

variables. For such cases, convolutional neural network can more effectively process the data using a set of convolution layers in series (Fig.2.8(b)) that extract and process spatial features. A CNN with simply convolution layers can be used if the goal of the network is to output an image data structure, such as field distribution within a device. If the aim of the network is to output a discrete structure, such as the spectral response, device efficiency, etc., feature maps from a series of convolution layers can be extended to combine with FC layers. It converges to the proper data structure.

As shown in Fig.2.8(b), convolution layers are specifically used to process image-based data structure though they can be applied to matrices and tensor data structures. Taking the advantage of the local spatial features within data, networks using convolution layers are proven to be more efficient as compared to the FC network in the field of image recognition [123,124]. In chapter 4, the CNN is trained with the data in matrices format while in chapter 5, images are used to train the network. For the convolution layer operation, a kernel is used to extract the features of the input image by spatially displaced over the width and height of it. The kernel is nothing but a matrix with trainable weights. A single value in the output matrix is computed at each kernel position using a dot product between the input image elements and the kernel filter, and then nonlinear activation is performed. The output matrix is commonly known as a 'feature map' since each value in it is derived from a small region of the input image. It highlights the features in the image with kernel-like features. Normally, an input image is processed by a number of kernels, each of which produces a distinct feature map. To create an output tensor, these feature maps are stacked together.

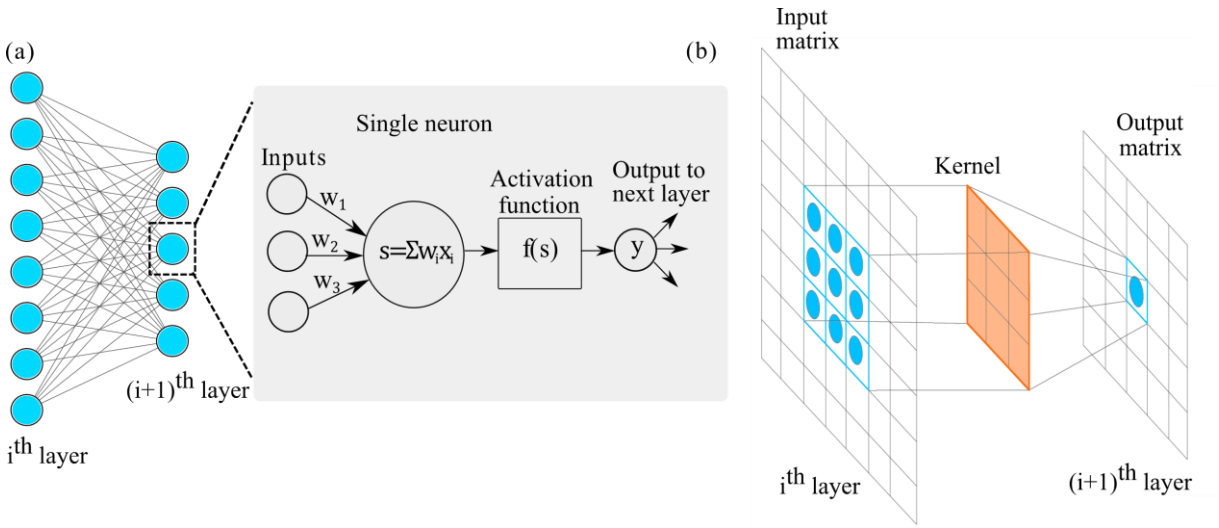

Figure 2.8- Schematic diagram of (a) Fully connected layers and, (b) convolution layers [113].

During the initial stage, weights assigned to all neurons are random. To capture the desired network input-output relations, these weights are iteratively modified to push this relationship according to the training set. The goal of the network is to minimization of the loss function. The loss function estimates the difference between the output value predicted by the neural network and the ground truth values from the training dataset. For a discriminative network performing regression task, consider terms from the training set $(x, \hat{y})$ where the x is given network inputs and the corresponding output is y. The loss function mean squared error (MSE) can be defined as [113],

$$L(y, \hat{y}) = \frac{1}{N}\sum_{n=1}^{N}\left(y^{(n)} - \hat{y}^{(n)}\right)^2 \tag{2.18}$$

where N is the batch size. Because this training method gives a decent approximation of the gradient calculated using the whole training set while balancing the computing cost of network training, it is commonly employed in practice.

For the generative network, the training set and generated devices must be treated in the subject of probability distributions. The training set devices $\{x_i\}$ are samples from the intended probability distribution across the design space, S, which is represented by $\hat{P}(x)$. The probability of selecting device x from the design space, S, denoted by P, is represented by this distribution. Such distribution shows the probability of selecting the device x upon a random sampling of a device from the design space, S, denoted by $P(x)$. Similarly, the generative network's device distribution can be thought of as a probability distribution spanning the design space, denoted as $\hat{P}(x)$. It is the probability that the network will generate device x by sampling the input latent random variable. Here, the aim of the training process is to match $P(x)$ and $\hat{P}(x)$. The loss function should be able to measure the dissimilarity between $P(x)$ and $\hat{P}(x)$ in order to achieve this goal. One approach is to use Kullback-Leibler (KL) divergence [125]. It is a measure of the dissimilarities between two probability distributions and can be defined as,

$$D_{KL}(\hat{P}||P) = \int \hat{P}(x)\, log\frac{\hat{P}(x)}{P(x)}dx \tag{2.19}$$

Another way is to use Jensen-Shannon (JS) divergence function, also known as information radius (IRad) [126]. It is defined by the average KL divergence of $P(x)$ and $\hat{P}(x)$ and their average distribution $(\hat{P}(x) + P(x))/2$,

$$D_{JS}(\hat{P}, P) = \frac{1}{2} D_{KL}\left(\hat{P} || \frac{\hat{P} + P}{2}\right) + \frac{1}{2} D_{KL}\left(P || \frac{\hat{P} + P}{2}\right) \tag{2.20}$$

When $P(x)$ and $\hat{P}(x)$ are equal, both functions are minimized, and using either as a network loss function achieves the training goal.

To successfully train the network, a significant amount of data points in the training set is necessary to capture the accurate mapping between the entire design and response space. A brute force sampling technique is computationally expensive but amenable for devices in a relatively low-dimensional design space. For example, for devices having only a few geometrical parameters, the training set can be generated by a few thousand simulations. However, as the dimension of the design space grows, the problem becomes increasingly intractable. For the free form devices which are normally represented by images with hundreds or thousands of voxels, a brute force sampling strategy needs billions of training set devices. Such an approach is impractical. To solve this problem, many preprocessing techniques are implemented which represent a device from a high to low dimensional space without losing important information. The list includes Fourier transformations, principal component analysis (PCA), non-negative matrix factorization, autoencoder, kernel PCA. In this thesis, PCA is used to reduce the dimensionality of data. With the smaller dataset, PCA helps the neural network to learn the metasurface absorber patterns more easily.

The principal component analysis is a statistical process of calculating the principal component in which a set of device parameters in a high dimensional space is projected to a low dimensional subspace [127]. For this, the first step is to identify a new orthogonal basis for the parameters in the high dimensional space. It is decided by specifying the sequential specification of basis vectors with the highest component scores which indicates the amount of information preserved when the device parameters are projected to the corresponding basis vector. A subset of such basis vectors with the highest component scores is then chosen to determine the low dimension subspace. The salient features of high-dimensional device data structures projected to such a subspace will be preserved with minimum distortion.

2.5.1.2 Convolutional Neural Network

Convolutional neural networks or *convnets*, for short – are special case of feed-forward neural network that use convolution in place of general matrix multiplication in at least one of its

layers. They are very similar to regular neural networks. The key difference is that the CNN architecture makes the implicit assumption that the input is image-like, which allows to encode certain properties. In particular, convolutions capture translation invariance. This, in turns greatly reduces the number of parameters which makes the network easier to optimize and less dependent on the size of data. Such architecture is more efficient candidate to process data represented in high-dimensional spaces, such as acoustic device patterns represented as images, and spectral responses of given devices.

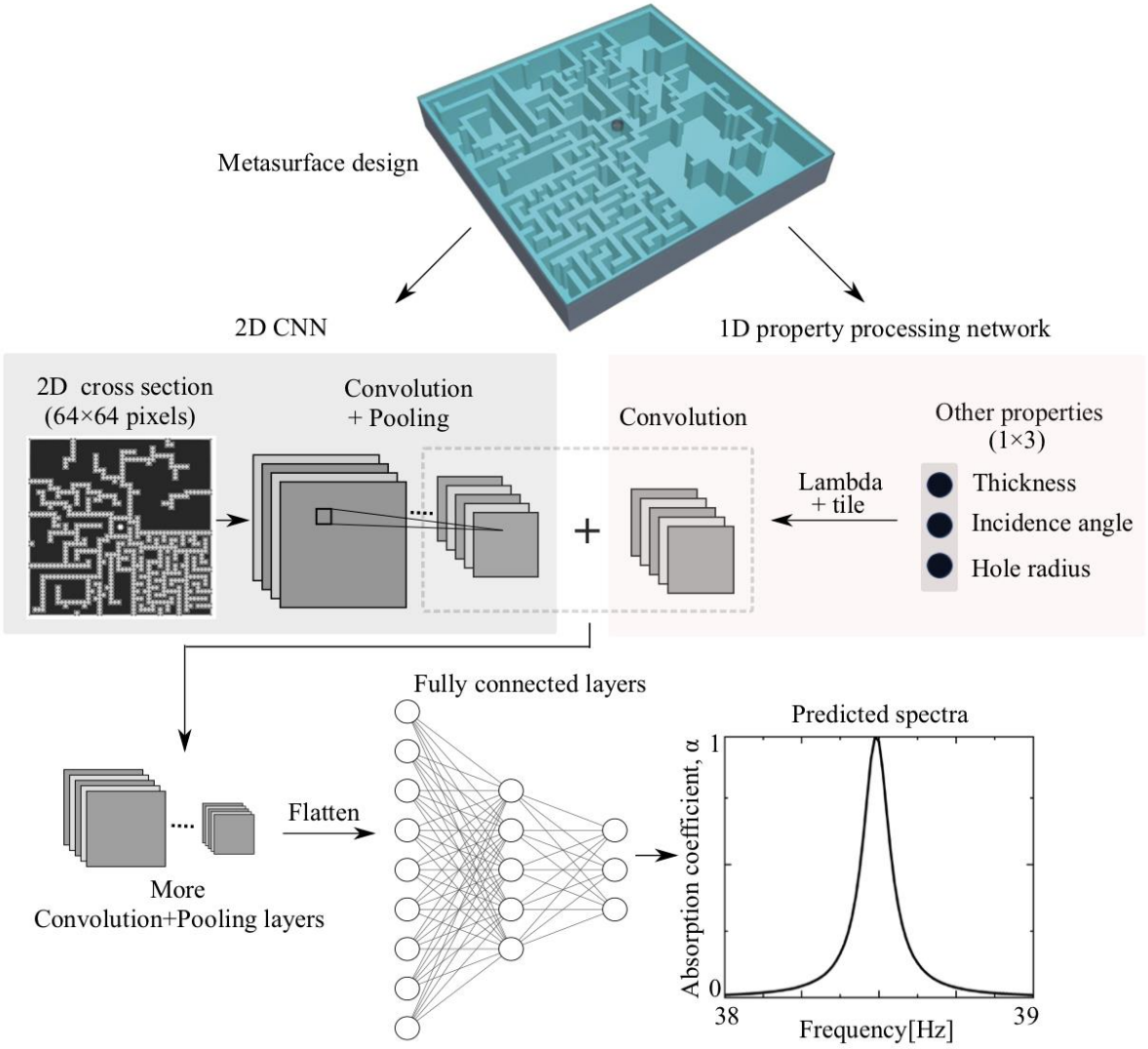

Figure 2.9 – An illustration of the CNN architecture for the metasurface absorber design. Design parameters are processed through separate neural networks: 2D image processing network and 1D property processing network. 2D images are processed with a set of convolution layer and then combined with the 1D design properties. Combined results are further processed with convolution and pooling layers then flattened into a 1D array before feeding to the FCLs. After being processed, the absorption spectra over the given frequency range is ready for evaluation.

The 2D CNN architecture and its application to simulate an acoustic metasurface absorber is explained in Fig. 2.9 to understand the role of each layer. Here, the network aims to uncover hidden relationship between metasurface absorbers and their absorption response, and thus accurately predict responses for given metasurface structure over a given frequency range. Here, each metasurface is decomposed into a 2D pattern, thickness, angle of incidence, hole radius and all are combined as an input of the CNN. They are processed through separate input networks to reconcile the huge dimension mismatch. Both are later combined and passed through the rest of the network to obtain the output spectra. The 2D CNN consists of a sequence of convolution and pooling layers, where every layer transforms the output of the previous layer through another differentiable function. These layers are like feature extractors and dimensionality reduction, respectively.

During the forward operation, a filter, *w* of the first convolution layer slides across the input volume and computes the its activation map at that particular point. It can be computed by the pointwise product of each value and adding these to obtain the activation at the point. The sliding filter is implemented by a convolution operator. Intuitively, this means that during the training of CNN, the network will learn from filters that capture some kind of visual information such as an edge, orientation, and eventually, the entire pattern in a higher layer of the network. For each convolution layer, there is a set of such filters, each of which produces separate activation map which are stacked to obtain the output map of that layer. Mathematically, the convolution of function *x* and *w* is defined as [123],

$$(x * w)(a) = \int x(t)w(a-t)da \tag{2.21}$$

Where $a \in R^n$ for any $n \gg 1$, and the integral is replaced by its higher-dimensional variant. Here input and kernel are continuous function. In practice, it is more realistic to assume that parameter *t* is discrete. In that case, the discrete convolution can be defined as [123],

$$(x * w)(a) = \sum_{a} x(t)w(a-t) \tag{2.22}$$

Where, *a* runs over all values in the space. Next important layer is the pooling layer that produces a summary statistic of its input and reduces the spatial dimensions of the feature map (hopefully without losing important information). There are two types of pooling: max-pooling and average pooling. In the case of max-pooling, the kernel moving across the matrix considers the maximum value for each position and puts it in the corresponding position of the output matrix, while the average pooling reports the average value. Commonly, the max-pooling layer

uses stride 2 together with the kernel size 2, which divides the feature map spatially into a rectangular grid of squares with side 2.

Architecting a deep CNN stands for designing an appropriate succession of convolutional, pooling, and fully connected layers, as well as their hyperparameters. Hyperparameter tuning is one of the important features in CNN. Manually tuning these hyperparameters is difficult and also impractical. Vast literature is available on various techniques for the optimization of these hyperparameters like Bayesian optimization [128], tree-structured parzen estimators (TPE) [129], random search, grid search [130]. However, further discussion about these methods is beyond the scope of this thesis. We have simply used the grid search method to choose the optimum parameter values. The important hyperparameters of CNN can be listed as below,

- **Number of hidden layers:** It is usually good to add more convolution and pooling layers until the test error no longer improves. It is computationally expensive to train the network but, a small number of layers may lead to underfitting.
- **Activation function:** It adds nonlinearity in the model which allows CNN to learn nonlinear prediction boundaries. Rectifier activation function (ReLU) is used in the CNN models in this thesis.
- **Network weight initialization:** It is used to define the initial values for the parameters in CNN before training the models on a dataset. We have used random uniform weight initialization.
- **Batch size:** Mini-batch is usually preferable in the learning process of CNN.
- **Learning rates:** It controls how much to update the weight in the optimization algorithm.
- **Number of epochs:** The number of epochs is the number of times the entire training set pass through the network. It should be increased until the gap between the training and testing error is very small.
- **Momentum:** It is used to know the direction of the next step based on the knowledge of the previous steps. Typically, its value is chosen between 0.5 to 0.9.
- **Dropout:** Introduced in Ref.[110], dropout is a powerful regularization technique to avoid overfitting in the network. It simply drops out units in network based on the desired probability, $p \in (0,1)$. A default value $p = 0.5$ is considered as a good choice to test with.

2.5.1.3 Conditional Generative Adversarial Network

For the inverse design of metasurface absorbers, we consider Generative Adversarial Networks (GANs) in chapter 5. These networks have been introduced in 2014 as a novel way to train a generative neural network [131]. Such networks are pair of two 'adversarial' networks: a generative network *G* which captures the data distribution, and a discriminative network *D* which determines the probability that the sample is from the training set rather than from the *G*. Here, *D* and *G* both can be non-linear mapping function, e.g. multi-layer perceptron. The generative network builds a mapping function from a prior noise distribution $p_z(z)$ to data space as $G(z;\theta_g)$ that helps to learn a generator distribution p_g over data x. The discriminative network generates a single scalar that represents the probability that x is from training data rather than from p_g. We use convolution neural network as a discriminative network. The training of both *G* and *D* goes simultaneously. The parameters for G are adjusted such a way that it minimizes $\log(1 - D(G(z)))$ and the parameters for *D* are adjusted such a way that it minimizes $logD(X)$. The training is framed as if they are following the two-player min-max game with value function $V(G, D)$ [132],

$$\min_G \max_D V(D,G) = E_{x\sim p_{data}(x)}[\log D(x)] + E_{z\sim p_z(z)}\left[\log\left(1 - D\big(G(z)\big)\right)\right] \qquad (2.23)$$

GANs can be extended to a conditional network if both adversial networks are conditioned on some extra information *y*. The conditioning can be performed by feeding *y* into both networks as input layer. In the next step, the input noise $p_z(z)$ and *y* are combined in the generator. x and y are inputs in the discriminator and the objective function of a two-player minimax game can be written as [132],

$$\min_G \max_D V(D,G) = E_{x\sim p_{data}(x|y)}[\log D(x|y)] + E_{z\sim p_z(z)}\left[\log\left(1 - D\big(G(z|y)\big)\right)\right] \qquad (2.24)$$

2.5.2 Classical Machine Learning Methods

In chapter 4, we have implemented classical machine learning algorithms i.e. K-Nearest Neighbors, Random Forest, and Support Vector Machine to compare the performance of the deep learning methods. It is well known that when the number of input features for any ML algorithms increases, the number of calculations performed increases, which leads to an increase in both the computation time as well as the required computational resources. To overcome this issue, PCA was implemented to reduce the dimensionality. Before training the

machine learning algorithms, data preprocessing is performed using the MinMaxScaler function defined in the sci-kit learn library, the input data is scaled to be within the provided input range (default feature range = {0,1}). Data preprocessing is an integral step as any ML algorithm performs better and converges faster when features are on a relatively similar scale and close to normally distributed. A brief description of all these three methods and hyperparameters that have to be tuned is given below.

K-Nearest Neighbors (KNN): KNN is one of the fundamental algorithms in machine learning which can be used to solve both classification and regression problems [133]. This method assigns a predicted value to a new observation based on the mean of its K "Nearest Neighbors" in the training set. It is very simple to implement no need to tune several parameters or make additional assumptions. To select the right value of K, one has to run the algorithm several times with different values of K and the value should be select that reduce the error. Also, one has to make sure it maintains the algorithm's ability to accurately predict for data it hasn't seen before.

Random forest (RF): RF is a quite popular algorithm in machine learning because of its simplicity and diversity. It is an ensemble learning method that operates by constructing a multitude of decision trees at the training time that is the mean/average prediction of the individual trees [134]. Here, the hyperparameters include the number of decision trees in the forest and the number of features considered by each tree. One can use the set of default hyperparameters value which was implemented for all the models. But, it does not guarantee to give the optimal solution for a problem. We use the grid search technique to find an optimal combination of hypermeters.

Support vector machine (SVM): SVM is a highly preferred technique in machine learning as it gives significant accuracy with less computation power and relatively simpler hyperparameter tuning [135]. It tries to find a hyperplane (multidimensional space) that separates these two classes. Then it classifies the new point depending on whether it lies on the positive or negative side of the hyperplane depends on the classes to predict. The important hyperparameters are (1) C that controls the tradeoff between smooth decision boundary and classifying training points correctly, and (2) Gamma that decides that how much curvature we want in a decision boundary.

2.5.3. Note on Data Augmentation

All the machine learning methods described in the above section are data-driven. It needs a large amount of training data to build an efficient and robust model especially in the case of deep learning networks. Models trained on a small number of datasets tend to overfit and produce inaccurate results. We use COMSOL Multiphysics to generate the dataset which includes input structures and corresponding absorption spectra. To simulate the absorption spectra at very low frequencies is time taking process as the frequency step size has to be kept very small due to very narrow bandwidth. Due to this reason, the dataset generation process is very slow.

To overcome the problem of a small dataset, it is a practice to artificially increase the existing datasets by adding data to it in a process called data augmentation [136–139]. It can be train-time augmentation or the test-time augmentation. In the test-time augmentation, the aim is to improve test-time performance of the given model. For a given test sample $x \in R^d$ of the predictive model f, one computes the model predictions $f(x), f(T_1 x), \dots, f(T_n x)$ for different augmenting transformations and sum up these predictions in a certain way like by averaging soft-max output from the classification layer. The other one is the train-time data augmentation which is implemented in chapter 5 for designing oblique angle metasurface absorber. The aim is to provide a larger training dataset to the algorithm. In supervised learning, a dataset D consisting of pairs (x_i, y_i) of a training sample $x_j \epsilon R^j$ and corresponding label y_j is given. For the given dataset D, the transformation $T_1, T_2, T_3, \dots, T_n: R_d \rightarrow R_d$ should be designed which are label-preserving in a way that for each sample $(x_i, y_i) \epsilon D$ and each transformation T_i the resulting vector $T_i x_j$ still looks like a sample from D with label y_j. The resulting new samples are added to the training dataset with their labels assigned and the optimization as usual is performed. In general, the choice of the augmentation transformation depends on the dataset. Few common strategies used for data augmentation in imaging tasks are flipping, random cropping and scaling, rotation, gamma transformation, and color augmentations.

In chapter 5, the train-time augmentation is introduced using the rotation of input sample images for the normal incidence cases. For the normal incidence of a sound wave, if the structure is rotated with reference to the incidence axis, the output absorption should be invariant. So, the metasurface structure can be rotated at any angle to generate transformations of a sample. This process does not only increase the dataset but also, helps to increase the diversity of the dataset which helps to build a robust network and prevent it from overfitting.

2.6 Conclusions

In this chapter, the important techniques that are used in this thesis were outlined. First, the finite element method which is used to design and post-processing of all the metasurface absorber designs is discussed. 3D Sample fabrication process using FFF is briefly discussed, next followed by an explanation of the experiment measurement set up and the principle of the two-microphone method. In chapter 4, deep learning methods based on convolution neural network and classical machine learning methods (i.e. KNN, SVM, RF) are implemented to design the acoustic metasurface absorber which is discussed. For the oblique wave incidence metasurface absorber design in chapter 5, we proposed forward and inverse designs using two-dimensional convolutional neural networks and conditional generative adversarial network, respectively which are presented. This includes the explanation of each layer in the network architecture and the important hyperparameters. As the training dataset is generated by the numerical simulation, its size is smaller. To increase the diversity in the dataset and to avoid network overfitting issues, we use the data augmentation technique which was discussed in brief.

Chapter 3

Multi-coiled Metasurface for Extreme Low-frequency Absorption

In this chapter, we introduce the concept of multi-coiled acoustic metasurface (MCM) for extreme low-frequency absorption. The proposed metasurface structure is composed of a perforated plate, a coplanar coiled chamber with an aperture, and labyrinthine passages. In contrast to the state of the art, this original conceived multi-coiled metasurface offers additional degrees of freedom to tune the acoustic impedance effectively without increasing the total thickness. It provides a quasi-perfect absorption (reaching 99.99% in experiments) at an extremely low-frequency of 50Hz, and simultaneously featuring an ultrathin thickness down to $\lambda/527$ (1.3cm). We provide analytical derivation, numerical simulation, and experimental demonstrations for this unique absorber concept, and discuss its physical mechanism which breaks the quarter-wavelength resonator theory. Furthermore, based on the same conceptual approach, we propose a broadband low-frequency metasurface absorber by coupling metasurface unit cells exhibiting different properties. Our findings could pave the way for the development of thin and light acoustic absorbers to address the extreme low-frequency absorption challenges. We have also investigated here as reported in the latter part of the chapter, the effect of temperature on the performance of the MCM for practical applications. We have developed numerical and theoretical approaches to understand this effect and we can take it into account in the “absorption equation”.

3.1 Introduction

The perfect absorption of sound at low-frequency (<100 Hz) is always a scientific challenge due to the weak intrinsic dissipation of conventional materials in the low-frequency regime [12]. To enhance the dissipation, it is necessary to increase the energy density inside the relevant material by some means like by introducing resonant structures. It is a challenge to achieve resonance at a very low frequency with a deep-subwavelength thickness structure. As discussed in chapter 1, the explosion of interest in developing artificial resonant structures like acoustic

metamaterials [8–14] and metasurfaces [40,41,45,140,141,142] is drastically increased owing to their exotic capabilities of manipulating sound waves and their deep subwavelength thickness. In related researches, perfect metasurface absorbers [64–67,141,142] have received considerable attention, and a variety of acoustic metasurface designs have been designed for the applications in noise control at a low-frequency regime which could be used in aircraft, locomotives, automobiles, machines, and buildings.

Ultrathin acoustic absorber metasurface is generally based on a single or hybrid resonant system. The hybrid resonant system usually has a broader bandwidth than a single resonant one. Various design approaches to design acoustic metasurface absorbers are discusses in chapter 1, section 1.2. Among all reported structures, one promising concept is to introduce a medium with a high refractive index. It can be realized by using the coiled-up space geometry [47,48]. Such coiled structures provide a more direct way to drastically shrink the thickness of the absorber system. A prototype of such a metasurface was proposed by Li. et al. [47] with the structural thickness being $\lambda/223$, showing the ultra-thin property of coiled acoustic metasurface. This system could present a limitation in the sense that the absorption depends on the length of the coiled channel and strictly requires a quarter wavelength channel length for the full absorption, creating difficulties in adjusting the absorption frequency and bandwidth. To improve this design, Huang et al. [48] reported a spiral metasurface (thickness being $\lambda/100$) with adding an aperture with the coiled structure to have an additional degree of freedom to tune the absorption frequency. This approach provides a tunable perfect absorption (in terms of resonant frequency and bandwidth) with the same length of the coiled channel. However, with these designs, it is still a challenge to achieve the total absorption at an extremely low frequency (<100Hz) with the constant metasurface thickness.

To overcome these limitations in terms of both absorption frequency and associated metasurface thickness, in this chapter, we introduce an original absorbing physical mechanism enabling the simultaneous achievement of extreme low-frequency absorption with ultra-subwavelength metasurface thickness. Unlike the conventional mechanism based on a quarter wavelength resonator by which we can shrink a meta-structure to make it thin while conserving the same operating frequency, our proposed mechanism breaks this physics limitation by introducing a novel concept based on a multi-coiled metasurface [143]. This achieved concept is composed of a perforated plate, a coplanar coiled chamber with an aperture, and labyrinthine passages. The multi-coiled geometry is formed by adding the labyrinthine passages inside the coiled chamber. The advantages of this concept are first, to fully use the space inside the coiled

chamber, and second to have an additional degree of freedom which helps to shift the resonance towards extreme low-frequency without increasing the total thickness of the metasurface. It also weakens the dependence of the resonance frequency on the total channel length. As we will demonstrate, absorbing metasurface operating at 50Hz with a total thickness down to an unprecedented λ/527 is achieved. We first implement a numerical simulation model based on the finite element model. Then, we provide an analytical model based on the equivalent circuit method to derivate the absorption coefficient and discussed it against the numerical simulation. Finally, we conduct experimental fabrication, measurement, and analysis of the conceived metasurfaces to provide a proof-of-concept of our finding. We present the first demonstration of an extreme low-frequency perfect absorber operating at 50Hz and having only 1.3cm thickness. Then, we provide a second demonstration of a broadband absorber of the same thickness, exhibiting a high absorption over 85%.

In the later part of the chapter, we theoretically and numerically present an investigation of the temperature effect on the absorption performance of the MCM. Temperature changes have a significant impact on the absorption coefficient which is rarely studied [144–146]. In fact, in practical applications, room temperature is uncommon for acoustic absorbers, the working temperature can be instead higher. The temperature inside the aircraft, voltage transformer, submarines, combustion chamber of the gas turbines, and other engineering services can significantly be higher than room temperature [146–149]. As a result, when designing acoustic metamaterials/metasurfaces, it is necessary to comprehend the impact of high temperature on sound absorption performance. However, reported studies on high-temperature effects are primarily focused on fibrous materials and metal foams [144,150,151], with insufficient studies involving acoustic metamaterials and metasurfaces [145,146,152], especially in the low-frequency regime. To get a better insight, we first implemented a numerical simulation model to study the temperature effect on MCM, and then we theoretically analyzed it by introducing the temperature-dependent parameters for better understanding.

3.2 Coiled Metasurface Absorber

A direct approach to design an acoustic metasurface absorber for the low-frequency absorption based on coiling-up space geometry has been reported by Li and Assouar in their study [47], where they proposed a structure composed of a perforated plate and a coiled chamber as shown in Fig.1.8 in chapter 1. Using this structure, perfect sound absorption is achieved at a very low frequency of 125.8Hz with the thickness down to a deep subwavelength scale (~λ/223). To go

a step forward, we numerically investigate two-coiled and three-coiled metasurface absorbers in the subsequent sections to further achieve extreme low-frequency (<100Hz) absorption with an ultrathin thickness. Next, we demonstrate the design and results from the analysis of the multi-coiled metasurface absorber.

3.2.1 Two-coiled Metasurface Absorber

As shown in Fig.3.1, the two-coiled metasurface absorber consists of two coiling structures with two holes in the perforated plate (in the center of each coil). The thickness of the perforated plate is *t*. Here, an incident acoustic wave propagates normally along the *z*-direction and penetrates the holes (diameters d_1 and d_2, thickness *t*) to the coiling structure (thickness *h*, width *w*). The coiling chamber is made up of several solid beams (wall thickness *g*). The propagation channel of both the coiled structures is connected from the back to back. We impose the transparent effect on the perforated plate to clearly display the coiling chambers in the back. The coiled chambers and the perforated plates are combined which forms the whole system (total thickness=*h*+*t*). The cross-area of the structure is *a*×*b* where, *a* is the length and *b* is the width of the structure.

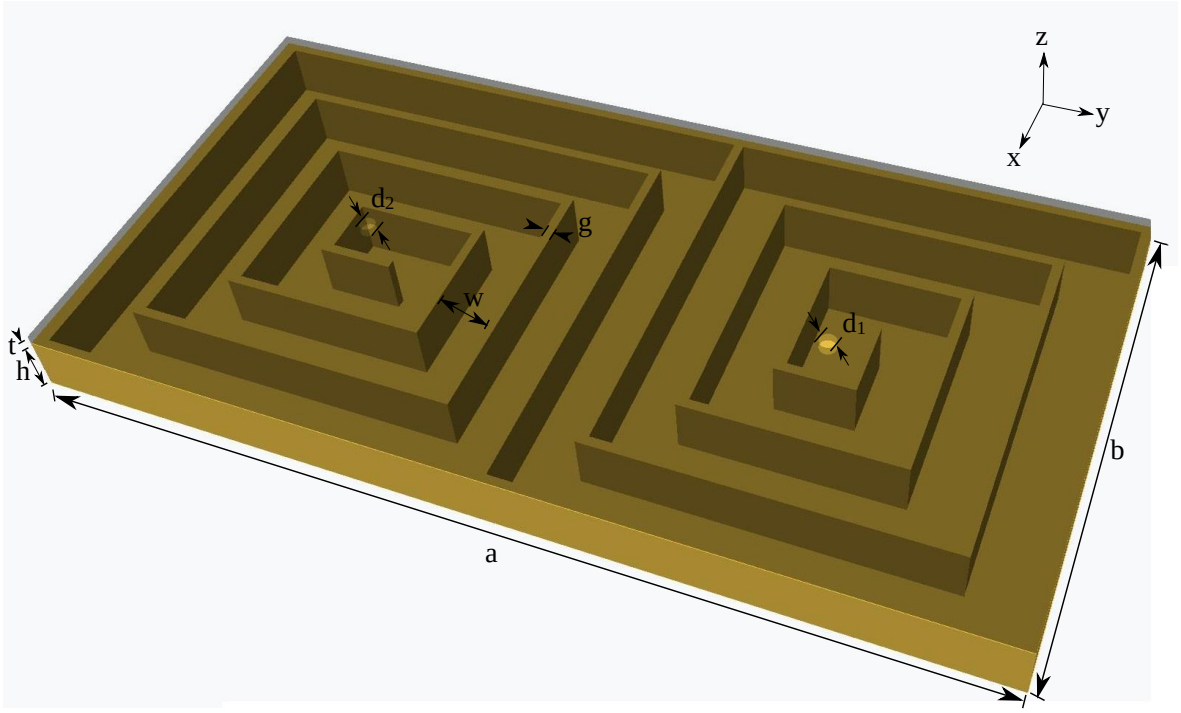

Figure 3.1- Schematic illustration of two-coiled metasurface absorber (cross area $a \times b$, total thickness $h+t$) composed of two coiled channels (channel thickness *h*, width *w*) (yellow color) connected and perforated plate (thickness *t*) with two holes (diameters d_1 and d_2, thickness *t*) (transparent black color). The perforated plate is combined with the coiling chambers to make the full system. The normal incidence wave propagates along the *z*-axis enters into the system through the perforated holes and

penetrates the coiling chambers. The perforated plate is given a transparent effect to display the details of the coiling chamber in the back.

As a result of the energy dissipation, the sound energy can be highly absorbed at the resonance frequency. As the geometrical size of the perforated holes is comparable to the viscous boundary layer, the viscous friction on the wall of holes contributes to the energy dissipation in this absorber system. We conduct numerical calculations using commercial software of COMSOL Multiphysics v5.4. The Acoustic-Thermoviscous Acoustic Interaction module (frequency domain) is used to consider the viscous friction effect as the geometric parameters of the holes are comparable to the viscous boundary layer thickness. The background medium is air with the properties: density ρ=1.21 kg/m^3, sound speed c=343 m/s, and dynamic viscosity μ=1.56×10^{-5} Pa s. Hard boundaries are imposed on the air-structure interfaces due to the large impedance mismatch between both. The absorption coefficient, α is expressed as $\alpha = 1-|r|^2$ with the reflection coefficient $r = (Z-1)/(Z+1)$ to calculate the absorption spectrum for the given frequency range.

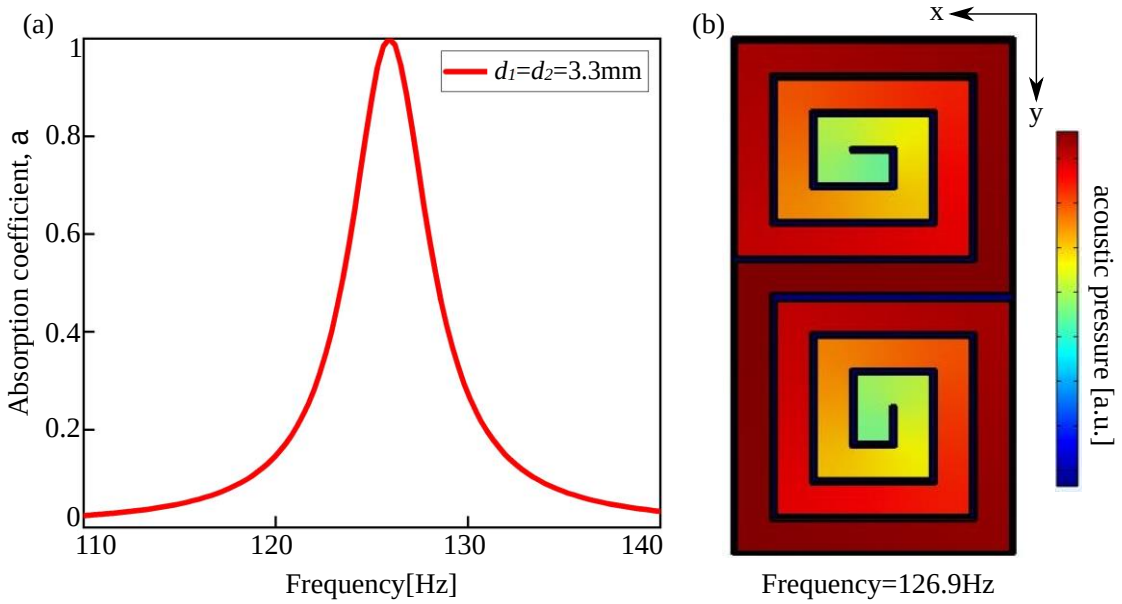

Figure 3.2- (a) Numerically obtained absorption spectrum of the two-coiled metasurface absorber with the geometrical parameters, d_1=d_2=3.3mm, t=0.2mm, a=200mm, b=100mm, h=12mm, w=12mm, g=2mm. Total absorption is achieved at 125.9Hz. (b) Acoustic pressure profile of two-coiled metasurface absorber at 125.9Hz.

Figure 3.2(a) shows the numerically obtained absorption spectrum of the two-coiled metasurface absorber with the same diameters of both holes, d_1=d_2=3.3mm. The other geometrical parameters are kept constant as, a=200mm, b=100mm, t=0.2mm, h=12mm, g=2mm. The result shows that the perfect absorption is achieved at 125.9Hz which is very close

to the resonance frequency for the perfect absorption observed in the single-coil structure with the same geometrical parameters [47]. Figure 3.2(b) shows the acoustic pressure distribution inside the two-coiled structure at the resonant frequency, 125.9Hz. It can be observed that the acoustic pressure is higher in the deeper regions inside both the coils as compared to the opening of the coils, whose distribution is similar to previous design with gradient channels [142]. When the acoustic wave passes through the channel at the coupling resonant frequency, it gets attenuated and absorbed due to thermoviscous loss and finally gets dissipated in form of heat.

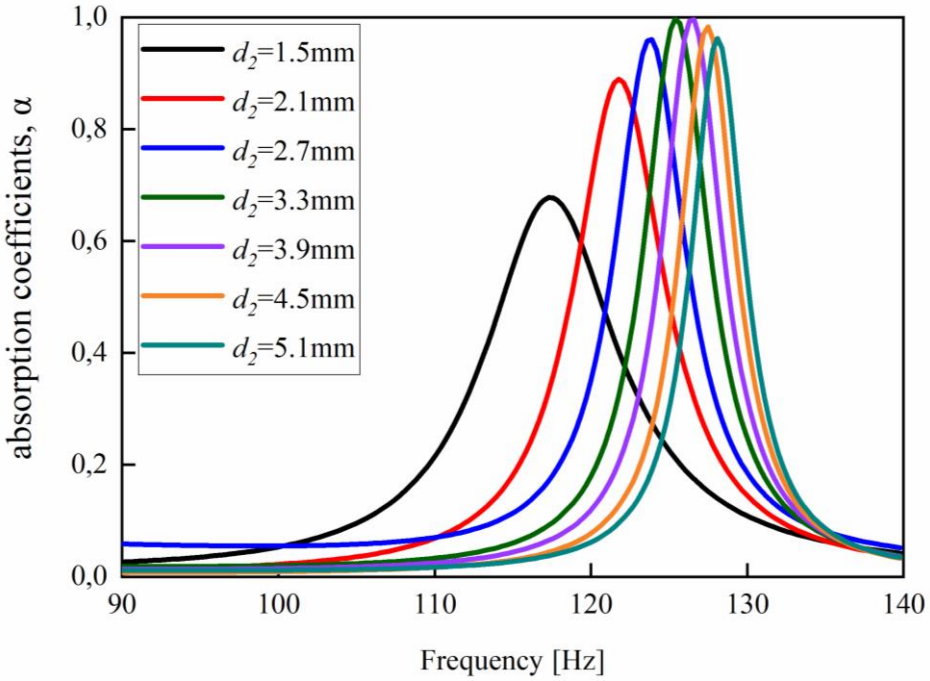

Figure 3.3- The absorption spectrum of the two-coiled metasurface as a function of the diameter d_2 with the fixed parameters (d_1=3.3mm, t=0.2mm, a=200mm, b=100mm, h=12mm, w=12mm, g=2mm).

In addition, we investigate the absorption coefficients when diameters of the both holes are different. As shown in Fig.3.2(a), full absorption is achieved when d_1=d_2=3.3mm. Next, we fix d_1=3.3mm and vary d_2, keeping the other geometrical parameters constant. Figure 3.3 shows the absorption spectrum as a function of d_2. As the value of d_2 decreases from 3.3mm to 1.5mm, the resonance frequency also decreases. We also observe a decrease in the amplitude of the absorption curves with the decrease in the diameter d_2 which shows impedance mismatching with the background air. Also, increasing the diameter d_2>3.3mm shifts the resonance frequency beyond 125.9Hz. We did not observe any improvement in resonance frequency for the total absorption in a double coiled design with two holes as compared to the single coiled structure. It has been previously reported that the longer propagation channel may favorably

influence the resonance frequency. Consequently, we adopt an approach where we remove one hole from the two-coiled system and investigate its effect on the absorption performance.

Figure 3.4(a) shows the schematic representation of a two-coiled absorber with a single hole (diameter d_2). Numerically, the perfect absorption with the single hole is achieved by tuning the diameter to d_2=4.5mm which is presented in Fig.3.4(b). The result shows that the absorption peak is shifted to 65Hz. To theoretically calculate the absorption coefficients, we use the impedance analysis method. An acoustic absorbing system, in general, can be considered as an artificial boundary with normalized acoustic special impedance, $z_s = r_s + ix_s$ [47]. Here, r_s and x_s are acoustic special resistance and reactance, respectively. They are normalized to the impedance of the air, $z_a = \rho_0 c_0 / A$ where ρ_0 and c_0 are mass density and sound speed in the air, and A is the cross-section area of the absorber. The absorption coefficient of such system can be expressed by [47],

$$\alpha = \frac{4r_s}{(1 + r_s)^2 + (x_s)^2} \tag{3.1}$$

From, Eq. (3.1), it can be observed that the perfect absorption can be achieved when two conditions are satisfied: (1) $x_s = 0$ indicating a resonant state, and (2) $r_s = 1$ revealing impedance matching with the surrounding medium viz air in our case. It results that sound energy is totally dissipated by the resistance, r_s. Normalized acoustic special resistance, R_{h_2} and reactance, X_{h_2} of the hole (diameter d_2) represents this energy dissipation which can be expressed as [153],

$$R_{h_2} = \frac{32\mu t}{pcd_2^2}\left(\sqrt{1 + \frac{K^2}{32}} + \frac{\sqrt{2}Kd_2}{8t}\right) \tag{3.2}$$

$$X_{h_2} = \frac{\omega t}{pc}\left(1 + \frac{1}{\sqrt{9 + \frac{K^2}{2}}} + 0.85\frac{d_2}{t}\right) \tag{3.3}$$

Where,

$$K = \frac{d_2}{2}\sqrt{\frac{\omega}{\mu}} \tag{3.4}$$

$$p = \frac{\pi d_2^2}{4A} \tag{3.5}$$

Here, p is the porosity of the perforated plate and A is the cross-section area. The function of the coiled channel is to provide an extra reactance, X_c to compensate the hole reactance X_h

which is a necessary condition for achieving complete absorption. The reactance of the coil can be written as [47],

$$X_c = -i\,A/A' \cot\frac{\omega l}{c_0} \tag{3.6}$$

Where, l is the length of coiling channel, and $A' = w^2$. In our case, the normalized acoustic special impedance of the two-coiled system with a single hole is given by,

$$Z_s = R_{h_2} + i\left(X_{h_2} + X_{c_1} + X_{c_2}\right) \tag{3.7}$$

Where, R_{h_2}, and X_{h_2} are the acoustic special resistance, and reactance of the hole, respectively. The absorption coefficient, α for the whole system can be given by,

$$\alpha = \frac{4R_{h_2}}{\left(1 + R_{h_2}\right)^2 + \left(X_{h_2} + X_{c_1} + X_{c_2}\right)^2} \tag{3.8}$$

Equation (3.8) shows that the total absorption can be achieved when $R_{h_2} = 1$ and $X_{h_2} + X_{c_1} + X_{c_2} = 0$. By substituting the geometrical parameters in this equation, the absorption spectrum based on the impedance analysis method can be obtained.

Comparison of theoretically and numerically obtained absorption curves is shown in Fig.3.4(b) for the geometric parameters: *a*=200mm, *b*=100mm, *d*=4.5mm, *t*=0.2mm, *h*=12mm, *g*=2mm. Perfect absorption is achieved at 65Hz in the case of the numerical simulation, and at 64.7Hz in theoretical calculations. Little mismatch in absorption peaks can be explained by the fact that the thermal conduction equation is used in the numerical simulations but not in the impedance analysis to make the derivation of the special acoustic impedance easier [47]. From, Eq.(3.6), it can be observed that the length of the propagation channel, l in the cotangent function, plays a major role in determining the resonant frequency. Here, it is worth noting that this shift is almost half the resonance achieved in the case of the previously studied system with two holes. The total channel length of the two-coiled structure with one hole is almost double that in a single-coil structure in the case of the single hole which shows that extreme low-frequency absorption can be achieved by increasing the propagation channel length. The corresponding acoustic pressure profile is shown at 65Hz in Fig. 3.4(c). The acoustic pressure is higher inside the deeper region (coil without hole) as compared to the coil with a hole.

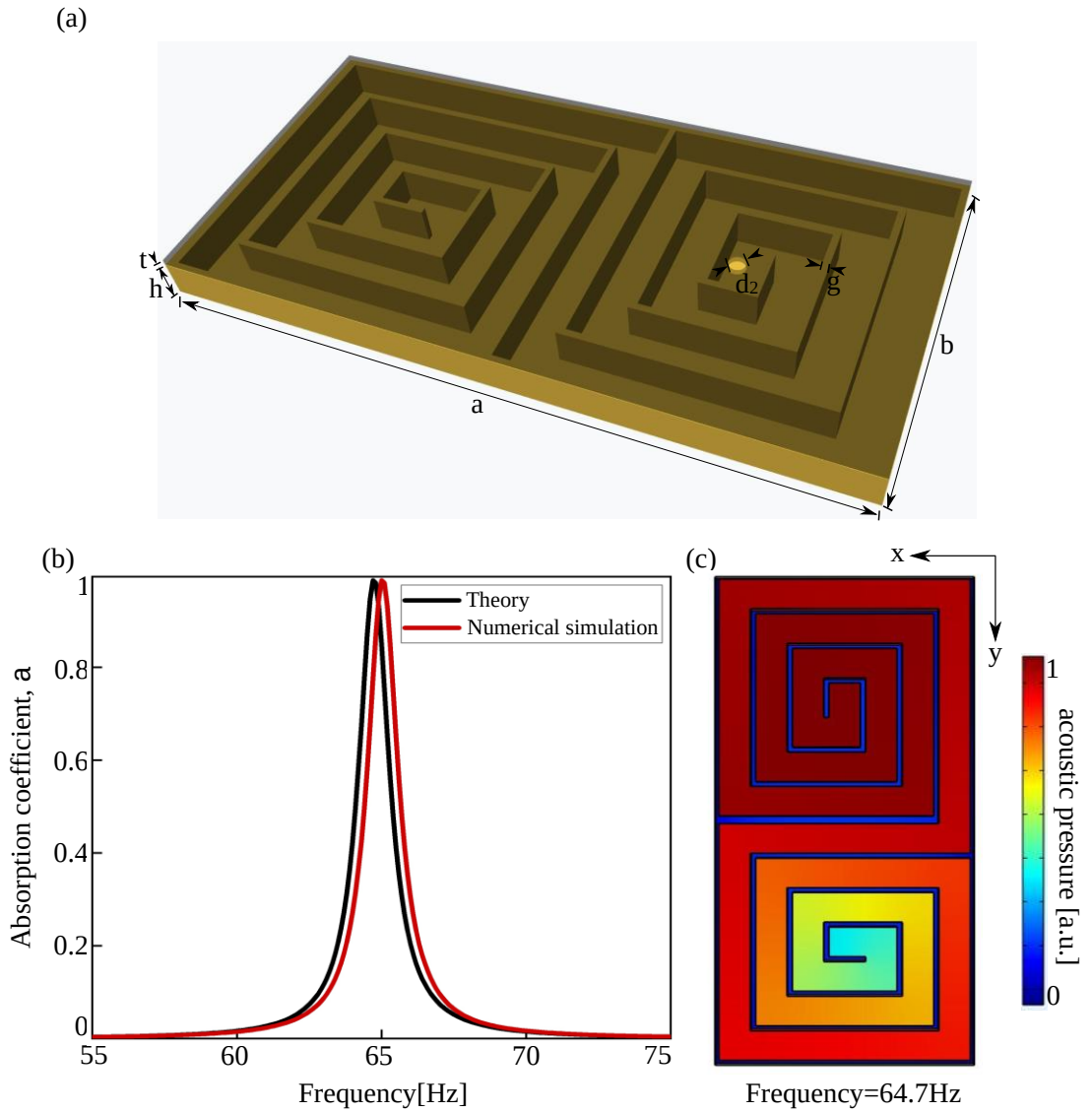

Figure 3.4- (a) Schematic illustration of the two-coiled metasurface absorber with a single hole (diameter d_2). (b) The absorption spectrum of the two-coiled metasurface absorber with a single hole (d_2=4.5mm). The geometrical parameters are, a=200mm, b=100mm, t=0.2mm, h=12mm, g=2mm. Total absorption is achieved at 65Hz in the case of the numerical simulation and 64.7Hz in theoretical calculations. (c) Simulated sound pressure profile at 65Hz.

We further analyze the balance by adjusting the geometrical parameters of a two-coiled system with a single hole and their absorption spectra. Figure 3.5(a) shows absorption spectrum as a function of diameter of holes, d_2 with the other parameters constant: a=200mm, b=100mm, t=0.2mm, h=12mm, g=2mm. It is found that by increasing the d_2, the resonance frequency increases, and perfect absorption is achieved when d_2=4.5mm which is shown in Fig.3.4(b). We may be found some absorption peaks with other parameter combinations, but the perfect absorption is not fully reached due to impedance mismatch. Further, we investigate the effect of the thickness of the perforated plate (or the thickness of the hole, t) on the absorption performance of the given metasurface structure. Figure 3.5(b) illustrates the absorption

coefficient as a function of the thickness of the hole, t keeping d_2=4.5mm fixed. When we increase the thickness, the absorption peak shifts to the lower frequencies. Almost perfect absorption is realized for a certain range of the hole thickness (t=0.2 to 2.2mm) due to the insensitivity concerning t.

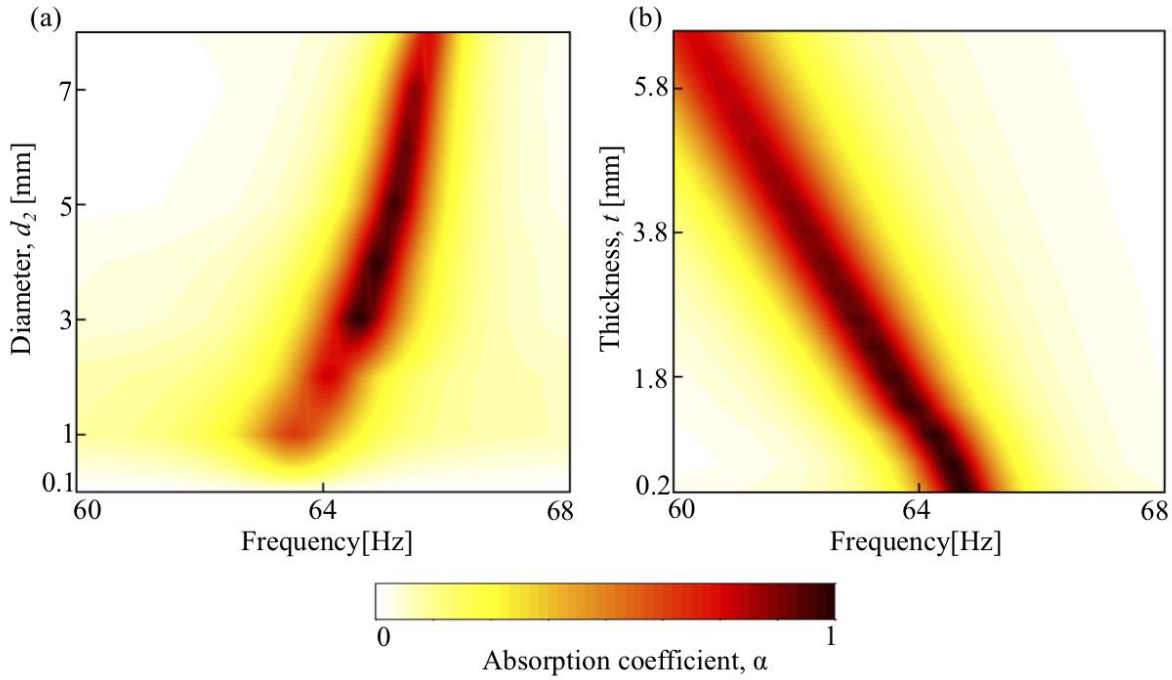

Figure 3.5- The absorption spectrum of the two-coiled metasurface with a single hole as a function of (a) the diameter d_2 with fixed parameters (a=200mm, b=100mm, t=0.2mm, h=12mm, g=2mm, w=12mm) and (b) the thickness of hole, t with fixed parameters (a=200mm, b=100mm, d_2=4.5mm, h=12mm, g=2mm, w=12mm).

In general, a balance between scattering and dissipation can be achieved by adjusting the geometrical size of the holes, allowing to build the perfect acoustic absorber. The perfect absorption is achieved at 65Hz with the total thickness of the structure, $(h+t)$ is 12.2mm. It is only 1/433 of the working wavelength.

3.2.2 Three-coiled Structure

We further extend our study to the three-coiled as shown in Fig.3.6. The system consists of three coiling structures (thickness h, width w) and the perforated plate (thickness t) with three holes (diameter d_1, d_2, and d_3, thickness t) in the center of each coiling structure. The propagation channel of all three structures is connected. However, this structure is different than the previous two-coiled structure as the propagation channel is not continuous. We implement the numerical model for the three-coiled structure with the same simulation settings in the COMSOL Multiphysics v5.4 as discussed in section 3.2.1.

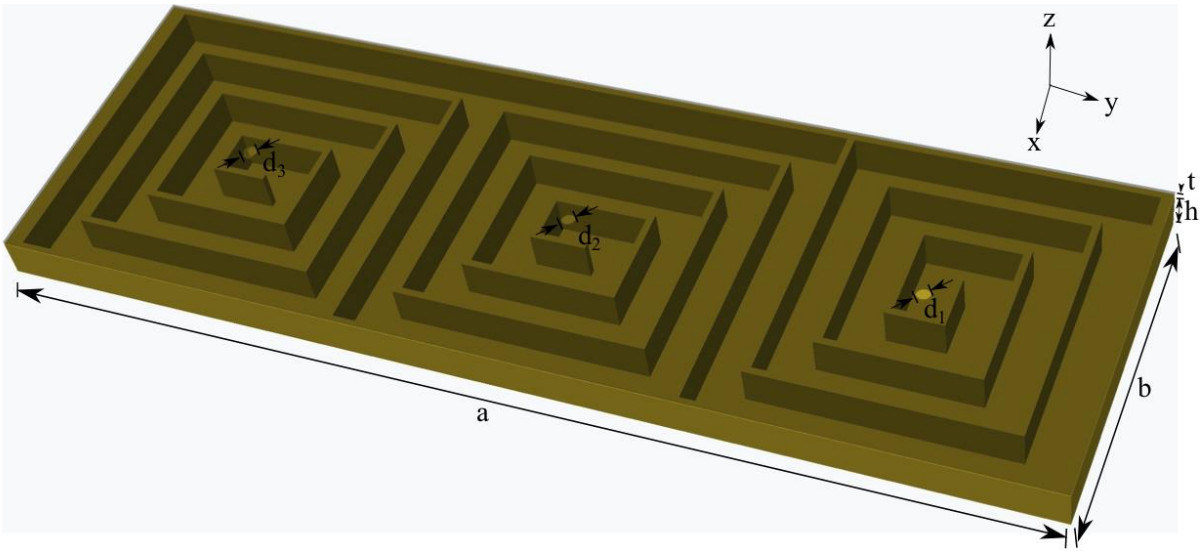

Figure 3.6- Schematic illustration of three-coiled metasurface absorber (cross area $a \times b$, total thickness $h+t$) composed of three coiled channels (channel thickness h, width w) (yellow color) connected with each other and perforated plate (thickness t) with three holes (thickness t, diameters d_1, d_2, and d_3) (transparent black color). The normal incidence wave propagates along the z-axis enters the system through the perforated holes and penetrates the coiling chambers.

To evaluate the performance of the three-coiled metasurface, first, we simulate the structure with the same diameters of all three holes. The diameters are optimized at $d_1=d_2=d_3$=4mm to obtain full absorption. Other geometrical parameters are kept as, a=300mm, b=100mm, t=0.2mm, h=12mm, g=2mm. Figure 3.7(a) shows the absorption coefficient, α, of the presented case with an absorption peak at 126.7Hz. The acoustic pressure distribution in the different parts of the coiling channel is shown in Fig. 3.7(b). For all three coils, the acoustic pressure is higher in the deeper region of the coiling channels as compared to the opening area. Further, we remove two holes, d_2 and d_3 to study the three-coiled system with a single hole. The resulted absorption spectra and acoustic pressure distribution are shown in Figs. 3.8(a) and (b), respectively. The full absorption is achieved at an extreme low-frequency of 46.6Hz with the total thickness of the system, $(h+t)$ =12.2mm, which is 1/603 of the working wavelength. However, the total cross-area ($a \times b$) is significantly increased. Further, we did not analyze the other geometrical parameters for this structure.

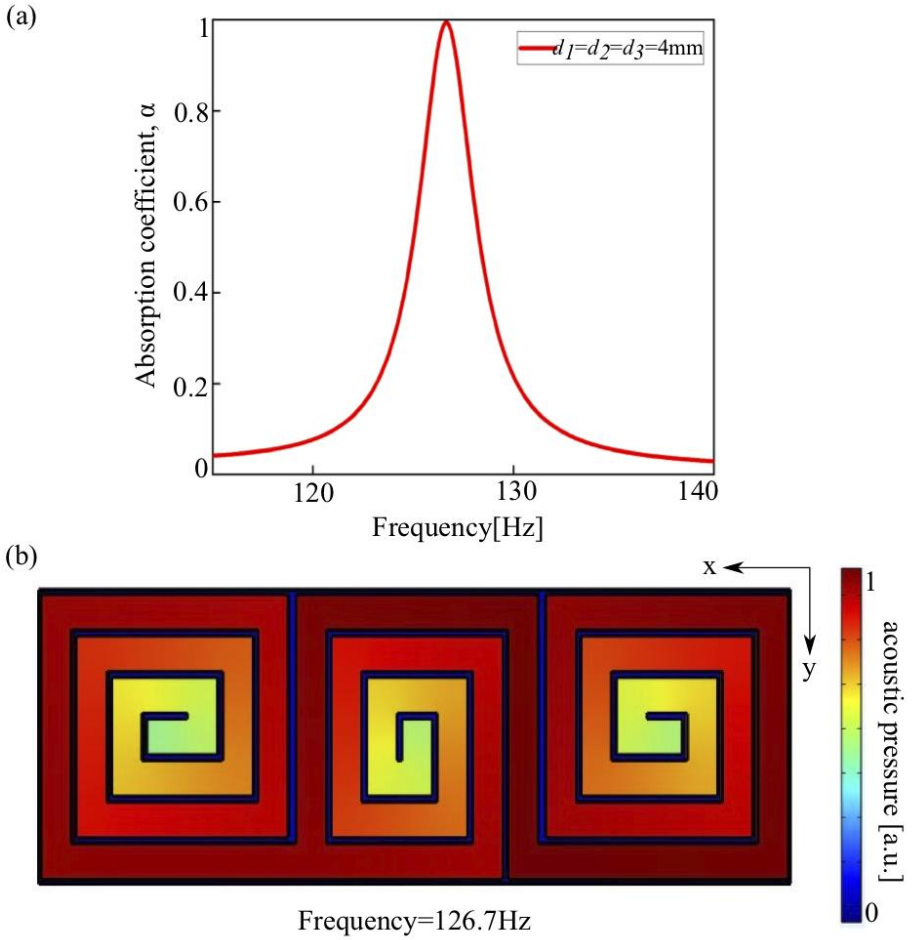

Figure 3.7- (a) Numerically obtained absorption spectrum of the three-coiled metasurface absorber with the diameters, $d_1=d_2=d_3$=4mm. The geometrical parameters are, a=300mm, b=100mm, t=0.2mm, h=12mm, g=2mm. Total absorption is achieved at 126.7Hz. (b) Corresponding simulated sound pressure profile at 126.7Hz.

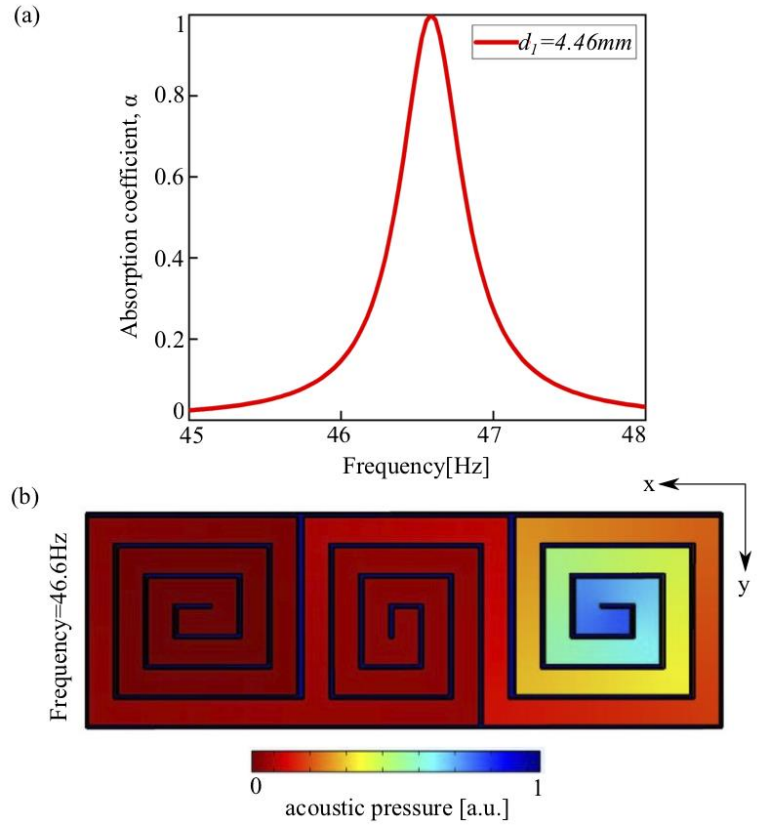

Figure 3.8- (a) Absorption spectrum of the three-coiled metasurface absorber with single hole (d_3=4.46mm). The geometrical parameters are, a=200mm, b=100mm, t=0.2mm, h=12mm, g=2mm. Total absorption is achieved at 46.6Hz. (b) Simulated sound pressure profile at 46.6Hz.

3.3 Multi-coiled Structure

The results of the two-coiled and three-coiled metasurface absorber systems with a single hole show that the perfect absorption can be achieved at extreme low frequency at 65Hz and 46.6Hz, respectively with the same thickness of the single-coil (12.2mm) [47]. However, due to the significantly large cross-section area, these systems are not desirable for practical applications. From Eq. (3.6), it can be observed that the length of the propagation channel, l in the cotangent function, plays a major role in determining the resonant frequency and the absorption peak rather than the cross-section area of the metasurface. Consequently, to further shrink the total area while increasing the channel length, we propose a multi-coiled metasurface absorber which is composed of a perforated plate, circular aperture, and several labyrinth structures inside the single-coiled channel [143]. The advantages of this concept are first, to fully use the space inside the coiled chamber, and second to have an additional degree of freedom which helps to shift the resonance towards extreme low-frequency without increasing the total thickness or the area of the metasurface absorber. The implementation of the proposed MCM is explained in the

following subsection which is followed by theoretical analysis and absorption measurement using two-microphone methods.

3.3.1 Implementation of the MCM

Before implementing the full MCM system, first, we briefly evaluate the effect of a circular aperture on the absorption performance without introducing the labyrinth structures. The single-coiled metasurface structure (without labyrinth structure) is shown in Fig.3.9(a). It consists of a circular aperture (height h_a and diameter d) which is fixed with the perforated plate at the opening of the coiled channel. The incident acoustic wave ($\lambda >> a$) along the z-direction enters into the coiled chamber via the aperture. Due to the energy dissipation, sound energy can be highly absorbed at the resonant frequency. The embedded circular aperture enables the tunable perfect absorption performance with a constant length of the coiled channel which helps to shift the absorption peak towards the lower frequencies. The concept of the embedded aperture was theoretically investigated and experimentally validated in Ref.[50] and Ref.[48] for the Helmholtz resonator and the spiral metasurface, respectively. The reported results in these works show that embedded apertures, indeed, offer an additional degree of freedom to tune the acoustic impedance powerfully, thereby exhibiting superior capability and tunability for achieving desired absorption performances without increasing total thickness and the cross-section area of the system.

In our study, the width of the metasurface is kept as, a=100mm and the thickness of the coiling channel as, h=12mm. The thickness of the perforated plate is kept as, t=1mm due to the fabrication constraint. The thickness of the propagation channel wall is g=2mm which is thick enough to provide sound insulation. For the given combination of the geometrical parameters, we tune the diameter of the aperture as, d=3mm to achieve full absorption. The acoustic absorption spectra of the coiled metasurface with an embedded circular aperture can be obtained numerically as a function of aperture height, h_a and frequency as shown in Fig.3.9(b). The absorption spectrum is calculated for the different heights of the aperture varied from 3mm to 11mm. It also illustrates the case without including the aperture. For all the cases, nearly perfect absorption is achieved which shows a good surface impedance matching with the surrounding air medium. The thickness of the aperture wall is kept as, t_d=1mm. Without including the aperture, the resonance is found to be at 122Hz for the given geometrical parameters. It is observed that as the height of the aperture increases, the absorption peak is significantly shifted

to the lower frequencies with nearly perfect absorption for all the cases with fixed coiled channel. This shows the improved capability of the absorber system offered by the embedded aperture. The maximum shift is observed with h_a=11mm, i.e., the resonance frequency is shifted to 92Hz. However, due to the fabrication constraint, we choose h_a=9mm as optimum height which illustrates the perfect absorption at 97.2Hz.

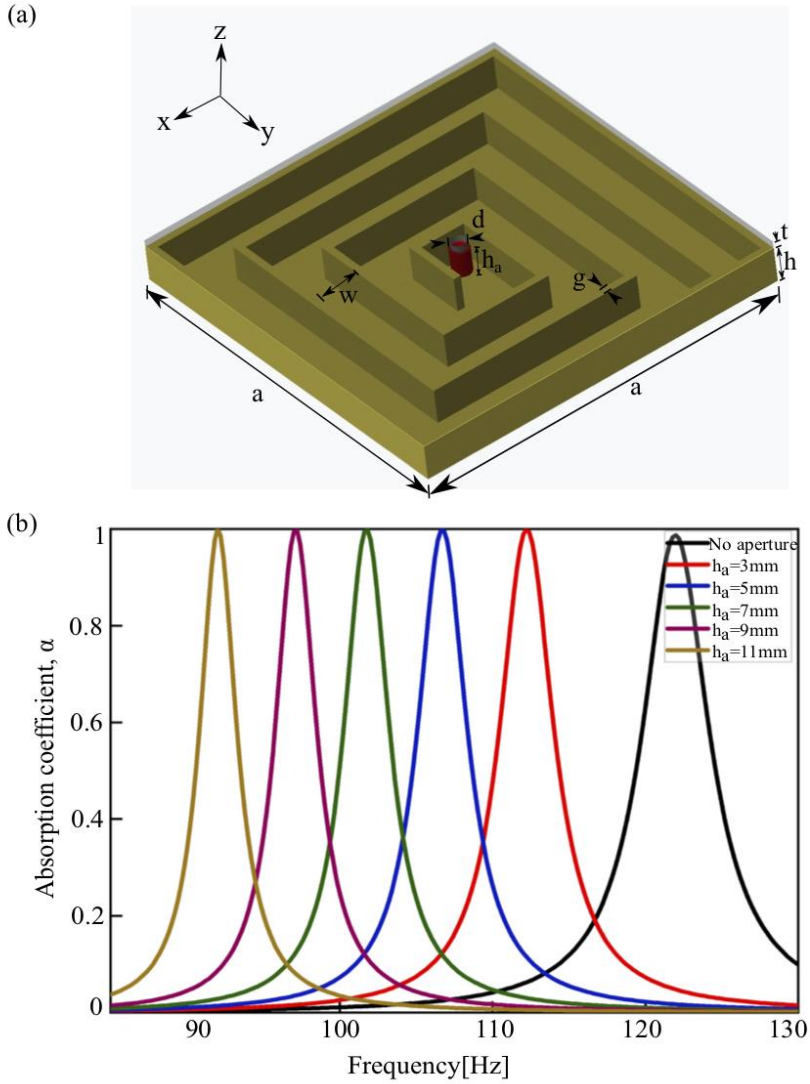

Figure 3.9- (a) Schematic illustration of the single coiled metasurface absorber (width a and whole thickness h+t) consist of a perforated plate (thickness t), a coiling chamber (width w, thickness h), and a circular aperture (height h_a, wall thickness t_d). (b) The absorption spectrum as function of the height of the circular aperture, h_a and frequency. The other geometrical parameters are fixed: a=100mm, t=1mm, h=12mm, w=12mm, t_a=1mm, d=3mm, g=2mm.

That being said, there is a trade-off between the low absorption frequency and the bandwidth of the absorption curve for the absorbing metasurface with a constant external configuration. It can be seen that when the absorption peak shifts to the lower frequencies, the bandwidth decreases. Perfect absorption at low-frequency with broad bandwidth can be

achieved by changing the external configuration of the metasurface structure. It is observed that large absorption bandwidth can be achieved by increasing the thickness of the structure [48]. One more way to improve the bandwidth is to use the supercell approach. Results in Fig.3.9(b) show a promising prospect to realize the broadband absorption by making use of super-cells by combining several unit-cells with different h_a or d. We implement the supercell approach to enlarge the bandwidth by combining metasurfaces with different values of d in the next part of this work.

Regarding now the design of the full MCM system, we have carried out a systematic and optimization study to conceive an efficient labyrinthine ultrathin metasurface. Here, I only delineate the final structure we have conceived and created. In fact, the proposed absorbing metasurface we have achieved is composed of a total of 11 labyrinthine passages of different sizes into the coplanar chamber which essentially force incoming waves to propagate through passages that are much longer than their external dimension. Figure 3.10(a) shows the structural assembly of the coplanar chamber, embedded circular aperture, and labyrinthine structures, while Fig. 3.10(b) illustrates the detailed view of the MCM. The labyrinthine structures divide the whole coiling channel into labyrinthine structure and cavities (area between two passages). Total 12 cavities are created inside the coiling channel. To analyze the MCM shown in Fig. 3.10(a), we simulate it using COMSOL Multiphysics v5.4. To check the effectiveness of this rigid boundary treatment at very low frequencies, we verify the numerical simulation with the real PLA material properties.

The labyrinthine structures are made of solid rectangle beams of width w_l =2mm and length, l_l=10mm. We achieve the full absorption at extreme low frequency with the MCM, while keeping the geometrical parameters as, a=100mm, h=12mm, t=1mm, h_a=9mm, d=3mm. Figure 3.11(a) shows the numerically obtained absorption curve exhibiting an absorption peak at 50Hz. The perfect absorption is achieved with the total thickness of the MCM system, h+t=13mm, which is 1/527 of the working wavelength. The obtained thickness is significantly smaller than the one reported in the previous works [47,48,73]. It is even smaller than our two-coiled and three-coiled metasurface absorbers discussed in sections 3.2.1 and section 3.2.2, respectively. This shows the effectiveness of the implemented labyrinthine structures inside the single-coil to increase the propagation path length without increasing the total area to achieve extreme low-frequency absorption.

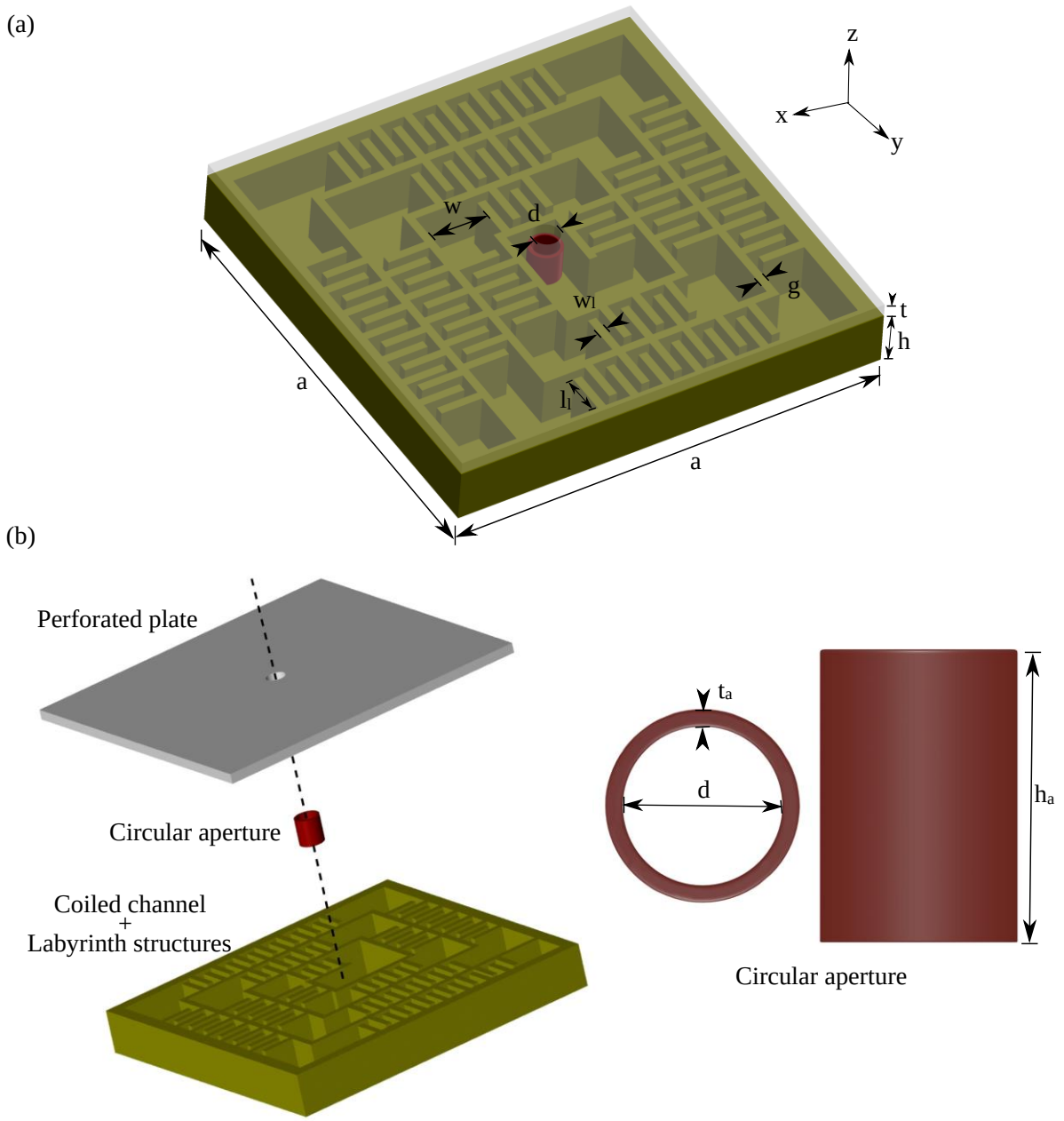

Figure 3.10- Schematic of a multi-coiled metasurface absorber (cross area $a \times a$) composed of a coiled channel, labyrinthine passages, aperture, and perforated plate. (a) The structural assembly of the coplanar channel (width of channel *w*, height of the coiled chamber *h*, thickness of the wall *g*), embedded aperture (height h_a, thickness of wall t_a and diameter *d*), labyrinthine passages, and perforated plate (hole diameter *d*, thickness *t*). (b) Detailed view of the structure.

To understand the absorption physical mechanism, acoustic pressure distribution inside the metasurface is shown at the resonant frequency, 50Hz, in Fig. 3.11(b). The acoustic pressure is higher in deeper regions of the multi-coiled structure at the resonance frequency. Acoustic pressure amplitude difference between different coiled passages drives the air-flows in the coiled passage, making the whole channel strongly rubbed by the acoustic wave so that the incident acoustic energy is rapidly attenuated inside and gets absorbed.

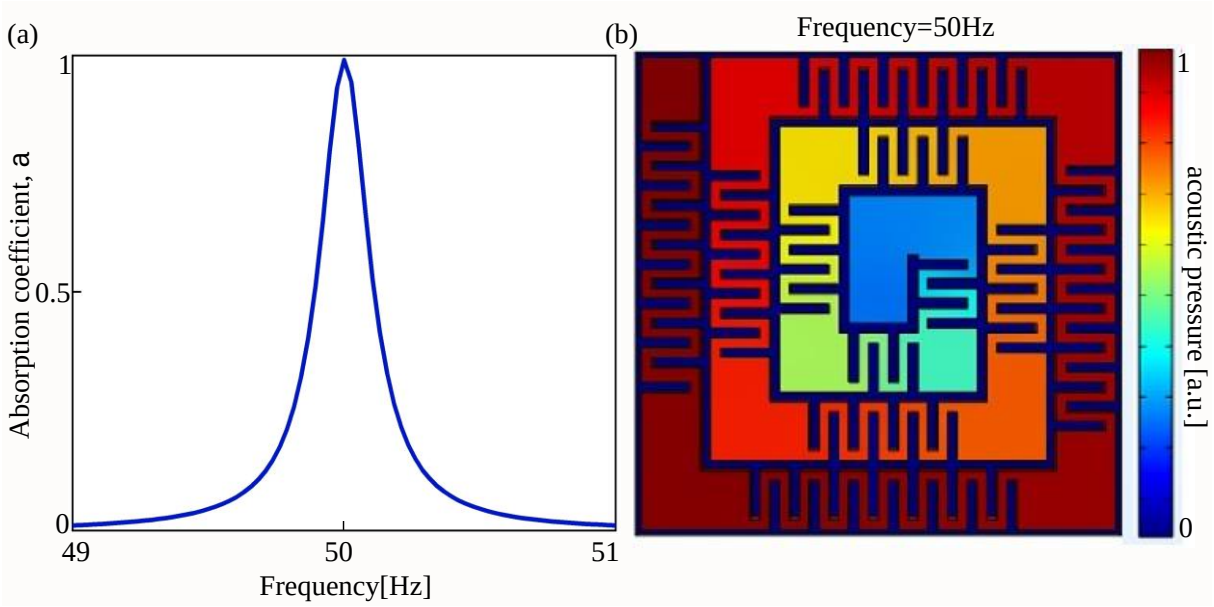

Figure 3.11- (a) The absorption coefficients of the presented metasurface with geometrical parameters: a=100mm, d=3mm, h_a=9mm, h=12mm, w=12mm, t=1mm. g=2mm. (b) Simulated sound pressure profile at 50Hz.

The MCM can be theoretically analyzed using a lumped RLC circuit model. The equivalent electrical circuit of the system is shown in Fig. 3.12. The circular aperture, perforated plate, and labyrinthine structures contribute essentially to the acoustic resistance and inductance of the structure, while the cavities (gaps between two labyrinthine passages) contribute essentially to acoustic capacitance. Herein, we give the analytical derivations of the total acoustic impedance of the MCM system.

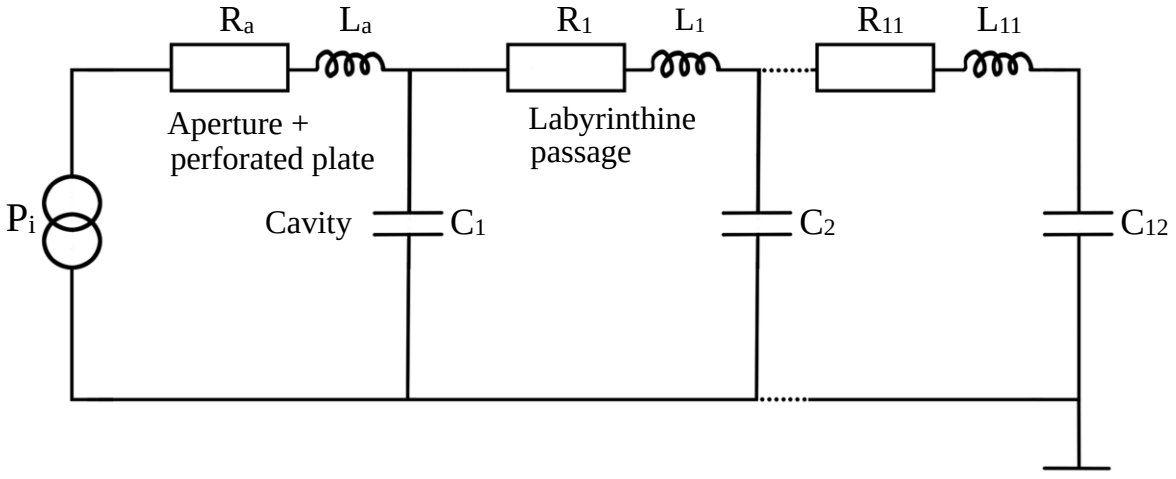

Figure 3.12- The effective circuit model of the MCM. The circular aperture, perforated plate, and labyrinthine structures contribute essentially to the acoustic resistance and inductance of the structure, while the cavities (gaps between two labyrinthine passages) contribute essentially to acoustic capacitance.

Acoustic impedance per unit length of an infinite aperture can be calculated from the Crandall's theory [154]. In our case, the aperture is relatively long with height, $h_a = 9mm$. Thus, the thermal-viscous loss needs to be considered. Considering the effect of thermal-viscous loss, the acoustic resistance R_a and inductance M_a provided by the long circular aperture contributing to the MCM can be given by [48],

$$R_a = \sqrt{2\omega\rho_0\eta} \tag{3.9}$$

$$M_a = \frac{4A}{\pi d^2}\left[\sqrt{2\omega\rho_0\eta} - \frac{2\rho_0 c\, sin\left(\frac{k_c h_a}{2}\right)}{\omega(\gamma-(\gamma-1)\Psi_t)\Psi_v}\right] \tag{3.10}$$

where, ω is the angular frequency, η is dynamic viscosity of the air, k_c is the complex wave number, h_a is the height of aperture, Ψ_t and Ψ_v are the functions of thermal and viscous fields in the aperture, respectively. $A = a^2$ is the area of the integral metasurface and δ_i is the end correction. In our case, top part of the aperture is attached with the perforated plate and embedded inside the coiled channel. Then, the end correction δ_i can be given by, $\delta_i = [1 + (1 - 1.25\epsilon)] \times \delta_0/2$, where $\epsilon = d/min(w,h)$ and δ_0=0.85d. The function of thermal, Ψ_t and viscous field, Ψ_v can be derived as [155],

$$\Psi_t = \frac{J_2\left(\frac{k_t d}{2}\right)}{J_0\left(\frac{k_t d}{2}\right)} \tag{3.11}$$

$$\Psi_v = \frac{J_2\left(\frac{k_v d}{2}\right)}{J_0\left(\frac{k_v d}{2}\right)} \tag{3.12}$$

Where, k_t and k_v are the thermal and viscous wave number which can be expressed as [50],

$$k_t^2 = -j\omega\frac{\rho_0 C_p}{K} \tag{3.13}$$

$$k_v^2 = -j\omega\frac{\rho_0}{\eta} \tag{3.14}$$

Where J_n is the Bessel function of the first kind and order n. C_p is the specific heat at constant pressure, η is the dynamic viscosity, and K is the thermal conductivity. As discussed earlier, the introduction of labyrinthine structures divides the whole channel geometry into several narrow-coiled passages and cavities. The acoustic resistance and inductance for these passages are calculated by [156],

$$R = \frac{h}{\pi d^3}\sqrt{2\mu\omega\rho_0} + 2\frac{\sqrt{2\mu\omega\rho_0}}{\pi d^2} + \frac{\rho_0 c_0}{\pi d^2}\left[1 - \frac{2J_1\,(2kd)}{2kd}\right] \tag{3.15}$$

$$M = \frac{l_b \rho_0}{S} \tag{3.16}$$

where l_b is the total length and S is the total area of the channel, the air density is ρ_0=1.21kg/m^3, J_1 is the Bessel function of the first kind, the sound speed is c_0=343m/s and ω=2πf is the angular frequency. The volumes of all 12 cavities are different and their acoustic capacitance is given as [80],

$$C = \frac{V}{\rho_0 c_0^2} \tag{3.17}$$

where V is the volume of the cavity. Since the resistor and inductor are connected in series and capacitor is in parallel and connected to the ground, the total acoustic impedance, Z of the MCM can be expressed by,

$$Z = \frac{1}{\frac{1}{\left(Z_{R_a} + Z_{L_a}\right)} + \frac{1}{Z_{C_1}}} + \frac{1}{\frac{1}{\left(Z_{R_1} + Z_{L_1}\right)} + \frac{1}{Z_{C_2}}} + \sum_{i=2}^{10} \frac{1}{\frac{1}{Z_{R_i} + Z_{L_i}} + \frac{1}{Z_{C_i}}} + \left(Z_{R_{11}} + Z_{L_{11}} + Z_{C_{12}}\right) \tag{3.18}$$

The acoustic absorption coefficient, α of MCM can be determined by its normal acoustic impedance, Z and this relationship can be given by,

$$\alpha = 1 - \left|\frac{Z - \rho_0 c_0}{Z + \rho_0 c_0}\right|^2 \tag{3.19}$$

Equation (3.19) indicates that perfect absorption requires the impedance matching between the air and the metasurface. i.e., $Re(Z) = \rho_0 c_0$ and $Im(Z) = 0$.

3.3.2 Experimental Measurements

Regarding the experiments to measure the absorption coefficients of the designed MCM, first, we fabricate the absorbing metasurface from polylactic acid (PLA) material by 3D printing technology. The sound speed and the density of the used PLA are c=1200m/s and ρ=2700kg/m^3, respectively. Photographs of the fabricated MCM are shown in Fig.3.13. Figure 3.13(a) shows the internal structure of the MCM with coiling channel and labyrinthine passages. Figure 3.13(b) and (c) show the side and top views of the full MCM system. During 3D printing, it is difficult to fabricate the circular aperture and the perforated plate without support. After, some trials, we were able to print the desired quality sample. One possible solution is to use water dissolvable polyvinyl alcohol which can be removed after the printing process. However, in the case of the MCM, it is difficult to remove the dissolved PVA from the coiling channels through such a small hole.

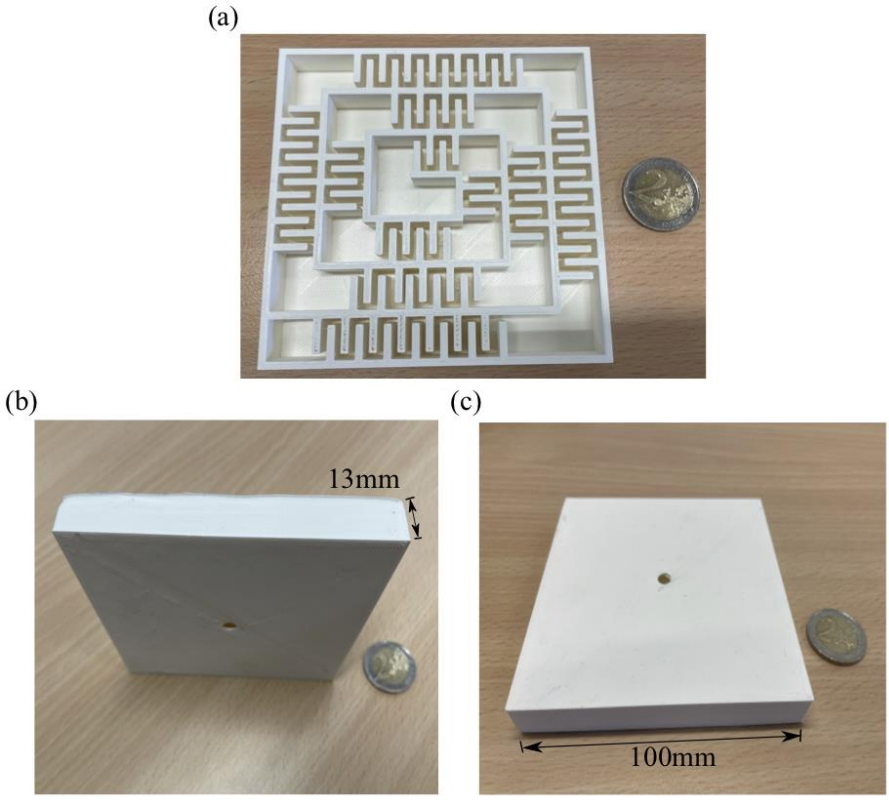

Figure 3.13- (a) Internal structure of the experiment sample. (b), (c) Photographs of experimental sample with geometrical parameters: a=100mm, d=3mm, h_a=9mm, h=12mm, w=12mm, t=1mm.

The measurement of the absorption coefficient is carried out using two-microphone method. We use the experiment setup which is shown in Fig.2.5, chapter 2. Figure 3.14 shows the comparison of the absorption coefficients of the MCM obtained by the theoretical analysis, numerical simulation, and experiments. It can be observed that the absorption coefficients obtained by the theoretical analysis and numerical simulation present an excellent agreement with the experimental measurement.

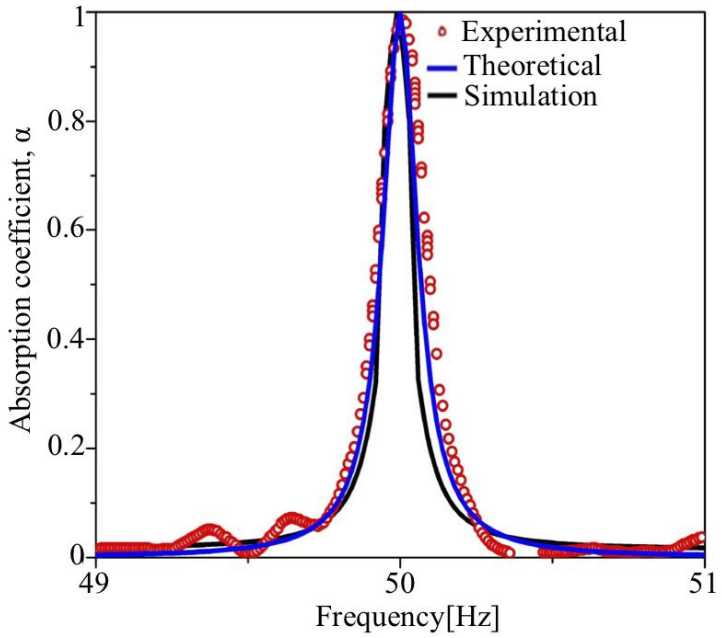

Figure 3.14- The absorption coefficients of the presented metasurface with geometrical parameters: a=100mm, d=3mm, h_a=9mm, h=12mm, t=1mm, w=12mm, g=2mm. The solid black line, blue line, and red dots represent the numerical simulation, theoretical and experimental results, respectively.

3.3.3 Bandwidth Improvement

As the bandwidth is a highly desired feature when it comes to absorption in general, and especially in low-frequency regimes, we, in follow, introduce an approach by which we can provide broadband absorbing metasurface operating around a frequency of 50Hz. For this aim, we design a supercell consisting of 9-unit cells (3×3) resonating at different frequencies and having different size aperture diameters as shown in Fig. 3.15(a). The total thickness of the supercell is still 13mm and the side length of the square supercell is 30cm. Figure 3.15(b) shows the equivalent electrical circuit for the super cell. As the unit cell are arranged in parallel, the total impedance of this super cell is given by,

$$Z_{total}^{-1} = Z_1^{-1} + Z_2^{-2} + \cdots + Z_9^{-1} \tag{3.20}$$

The equivalent acoustic impedance Z_{total} at the surface of the sample must be equal to the impedance of the air to achieve full absorption ($Z_{total}=Z_0=\rho_0 c_0$). Further, end correction is considered here, that for the supercell, the end correction is about 1.414 times of the single unit cell. Figure 3.15(c) shows the comparison of the absorption coefficient of the broadband metasurface obtained by theoretical calculations and numerical simulations. The difference between simulation and analytical calculations is due to the nonlocal effect and it has resulted from the coupling effect between the unit cells with different parameters [157].

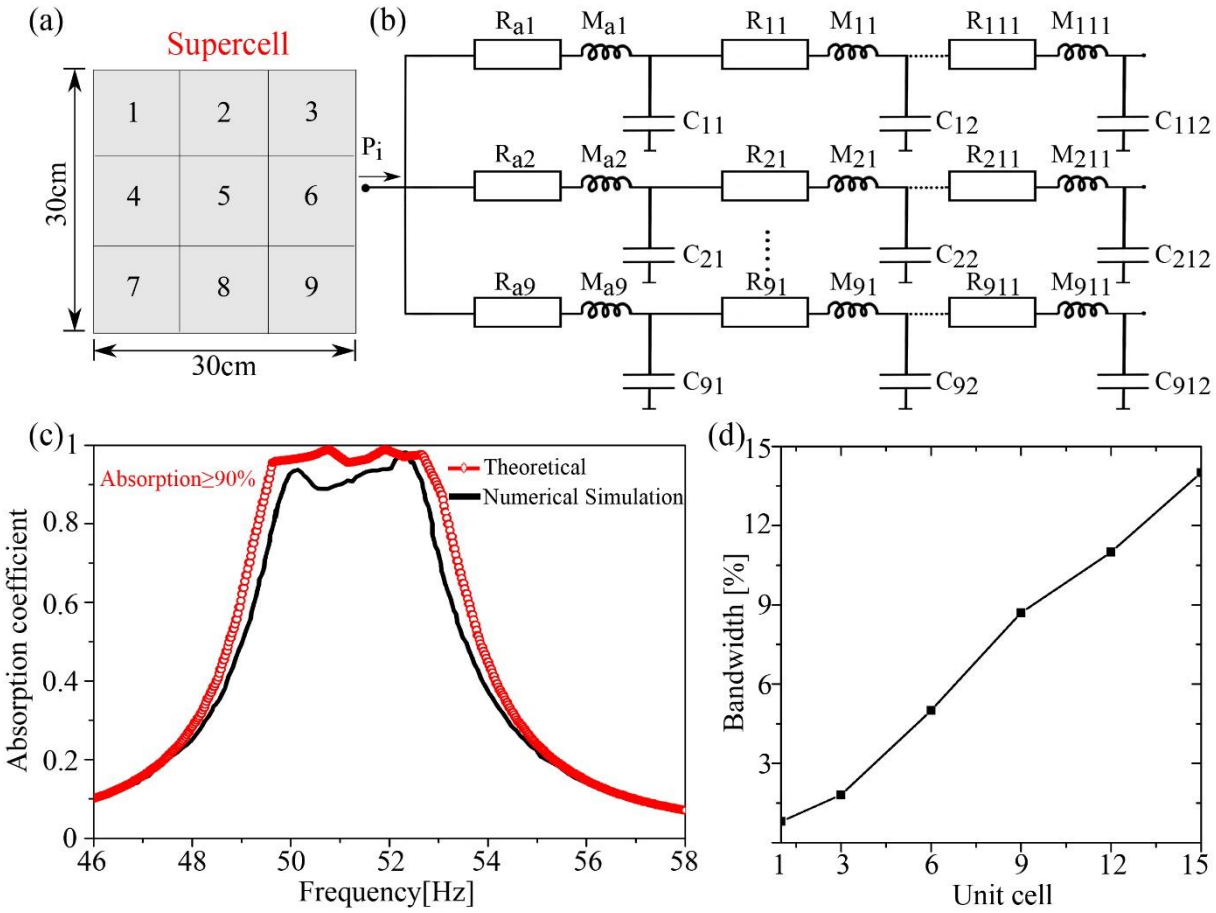

Figure 3.15- (a) The supercell consists of 3×3-unit cells denoted as 1-9. The side length of the supercell is 30cm. (b) Equivalent circuit of the supercell. (c) The absorption for the frequency range of 45-56Hz. 8.7% bandwidth is achieved while preserving the absorption higher than 90% for 3×3-unit cells. The solid black line and red dots represent the numerical simulation and theoretical results, respectively. (d) Relationship between bandwidth and the number of unit cells in the supercell.

Here, the average absorption is higher than 90% for the given frequency range, but does not reach the perfect absorption. This is due to the fact that the structure still has a small impedance mismatching, making the effective acoustic impedance at the surface slightly deviates from $\rho_0 c_0$. The bandwidth can be further improved by adding more unit cells. The relation between the bandwidth and the number of the unit cells is given in Fig. 3.15(d), showing almost a linear dependence.

3.3.4 Temperature Effects on the MCM

The desired unusual properties of acoustic metasurface absorbers strongly depend on the operating temperature. In this subsection, we systematically study the effect of temperature on the absorption performance of the MCM. The method for analyzing how temperature affects

acoustic properties is a major challenge for this multi-field coupling problem. Therefore, the temperature-dependent parameters of the surrounding medium are used to characterize the change in the acoustic properties due to the temperature variation as a substitute approach [145,146,152]. In this case, the parameters describing the physical properties of the surrounding medium play a key role rather than the structural materials.

Based on Fig. 3.12, the theoretical model of the MCM was implemented in section 3.3.2 with the structure considered as acoustically rigid. There is no heat transfer between the air and boundaries. The temperature-dependent variables of air, such as dynamic viscosity η, sound speed *c*, and mass density ρ have a significant impact on the sound absorption performance of the MCM. To study the temperature effect, we introduce the temperature dependent parameters of the air to predict the absorption spectrum at a given temperature. T (in Kelvin) is the surrounding temperature, the dynamic viscosity of air is $\eta = \eta_0(T/T_0)^2(C_0 + T_0)/(C_0 + T)$, where $\eta_0 = 1.827 \times 10^{-5}\ Pa\ s$, $T_0 = 291.15K$, and $C_0 = 120K$. As a vital property of the air, η dramatically change with the temperature. It almost doubles when the temperature rises from 300K to 700K which profoundly alters the velocity distribution for a given pressure gradient. As a result, the temperature has a significant impact on the surface impedance, which is closely related to velocity and pressure fields [158]. Consequently, the sound absorption performance will show a noticeable peak shift. Another important property is the sound speed $c = \sqrt{\gamma RT/M}$ where, γ the heat capacity ratio (1.4 for air), $R = 8.314$J/mol-K is the universal gas constant, and $M = 0.029kg/mol$ is the molecule mass. Finally, the density of the air in case of temperature change can be written as, $\rho = P_0 R^{-1} T^{-1}$ where $P_0 = 101.325$ kPa is the standard atmospheric pressure.

To explore the underlying physics, we implement a temperature-dependent numerical model of the MCM in COMSOL Multiphysics using the Acoustic-thermoacoustic module. We derive simulation parameters from the aforementioned equations to make those temperature dependents. The thickness of the viscous boundary layer is set as, $\delta_v = \sqrt{2\,\eta/\omega\rho}$ which indicates that δ_v is in proportion to the square root of the dynamic viscosity. This equation depicts a direct relationship between the thickness of the viscous boundary layer and the frequency, as well as an indirect relationship between the thickness of the viscous boundary layer and the frequency. The thickness of the viscous boundary layer decreases as the frequency rises, but increases as the temperature rises, resulting in strengthened viscous effects [158].

The comparison of sound absorption coefficients of the MCM obtained via simulation and analytical model are presented in Fig. 3.16(a) for different temperature cases: -100 ℃, 100℃, 300℃, 500℃, and 700℃. The analyzed MCM has the following geometrical parameters: a=100mm, h=12mm, h_a=9mm, d=3mm, t=1mm. It is optimized to have the perfect absorption at 50Hz at room temperature as shown in Fig.3.11. The theoretical predictions match well with the numerical simulation results at all temperatures. It can be observed that the as the temperature rises, the absorption peaks move to a higher frequency [151,152,158,164]. Here, we also consider -100℃ case to see the effect of the temperature lower than the room temperature on the absorption coefficient. At -100℃, the absorption peak is shifted to the lower frequency reaching 36.1Hz with the maximum absorption coefficient value 0.85. Perfect absorption is maintained up to 100°C. Further rise in temperature diminishes the peak value of the absorption curve.

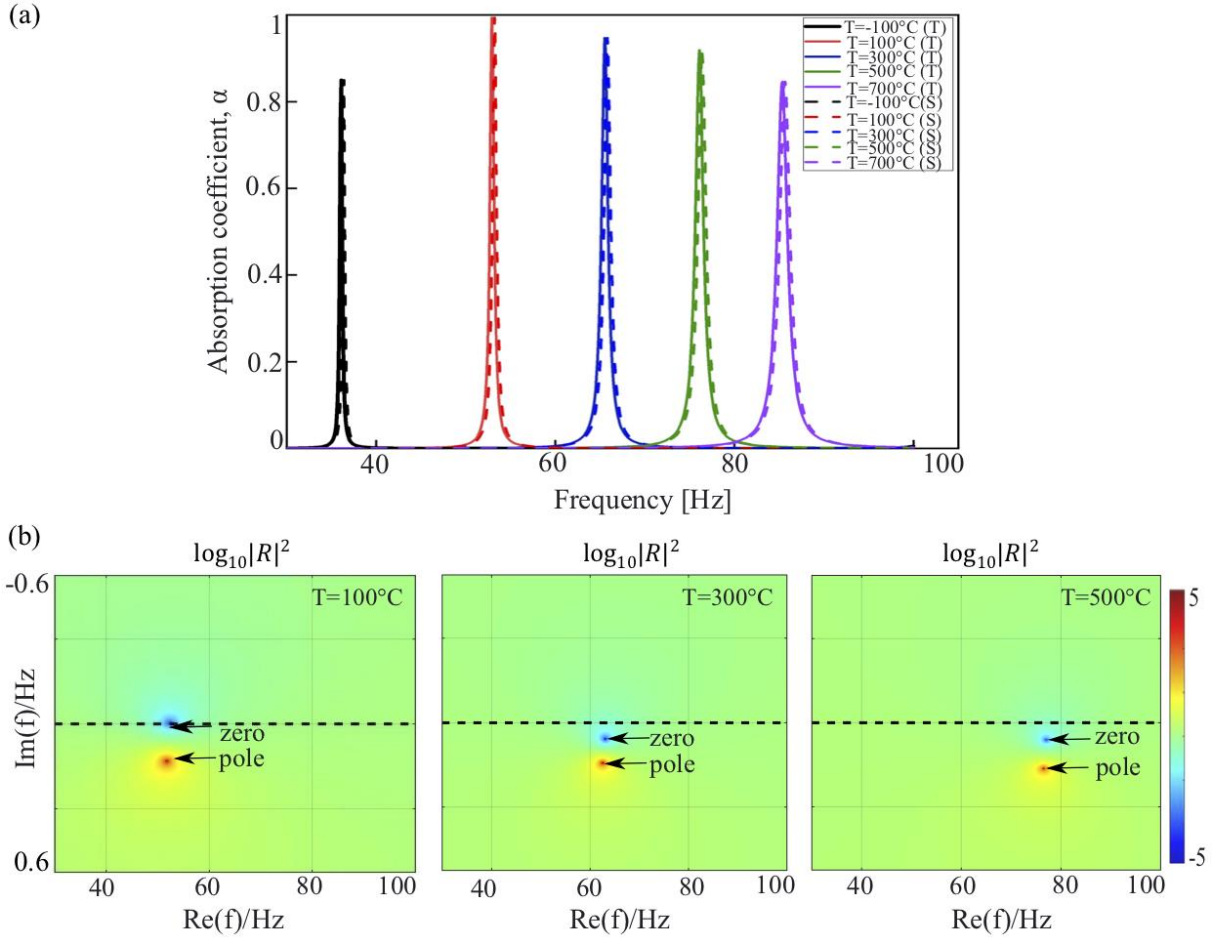

Figure 3.16- (a) Sound absorption predicted by the theoretical (dashed line) and numerical (solid lines) methods at -100°C to 700°C. The analyzed MCM has the following geometrical parameters: a=100mm, h=12mm, h_a=9mm, d=3mm, t=1mm. (b) Representation of the reflection coefficient in the complex frequency plane at the three different temperatures at 100°C, 300°C and 500°C.

Figure 3.16(b) illustrates the distributions of $\log_{10}|R|^2$ in the complex frequency plane at the three different temperatures at 100 ℃, 300 ℃ and 500 ℃. By replacing the frequency f with a complex frequency $f' = f_{re} + jf_{im}$ in the theoretical model, the reflection coefficient can be represented in the plane of the complex frequency considering f_{re} and f_{im} as variables. Here, the f_{re} and f_{im} are real and imaginary frequency, respectively. The zero and pole in the complex frequency plane indicates the minimum and the maximum value of the reflection coefficient, respectively [159]. The distance of the zero from the real axis corresponds to the amplitude of the absorption peak at a given resonant frequency. The closer the position of zero to the real frequency axis, the higher absorption amplitude is achieved. In all plots in Fig.3.16(b), the pole-zero pair can be found at the corresponding resonant frequency. For the perfect absorption condition in the case of 100℃, the zero can be found on the real axis whereas, for other cases, the zero is downshifted from the real axis.

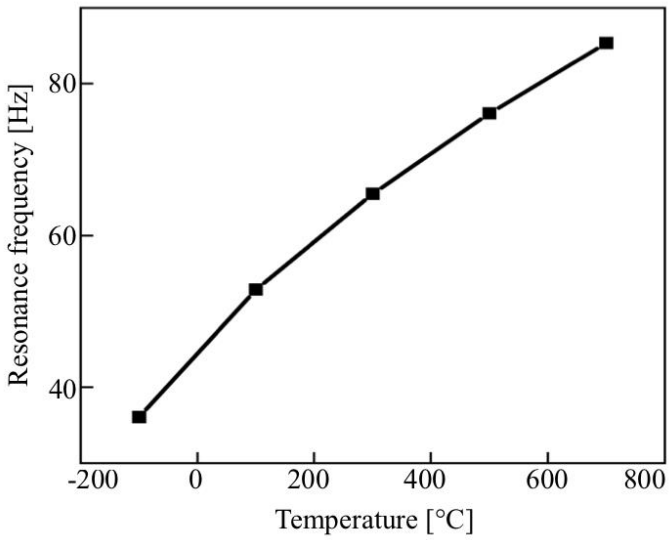

Figure 3.17- Variations in resonance frequency of the MCM as a function of temperature.

The sound absorption peak is mainly affected by the sound speed *c* when the temperature increases. For the temperature variation from -100°C to 700°C, the plot of resonance frequency as a function of the temperature is shown in Fig. 3.17. It shows the resonant frequency is proportional to the sound speed of air. The resonant frequency for the -100℃ and 100℃ cases are found at 36.1Hz and 52.9Hz, respectively. For the given temperature change, relative change in the resonant frequency can be given by, |36.1-52.9.1|/52.9=31.76% which is approximately equal to the relative change of the sound speed (|263.72-387.14|/387.14=31.88%) at corresponding temperature. Table 3.1 shows the relative variation of the resonant frequency and the sound speed for the given variation in the temperature for the range -100℃-700℃. It

shows that relative shift in resonant frequency of the MCM is proportional to the relative change in the sound speed in air for the given temperature variation. Therefore, the resonant frequency of the MCM simultaneously increases with the increasing in the temperature of air. Figure 3.18 shows the acoustic pressure intensity maps for four different temperature profile: -100°C, -100°C, 300°C, and 500°C. The effect of temperature is not apparent for the -100°C to 100°C, but there is a distinct pressure gap between -100°C and 500°C. Such kind of behavior is also observed in Ref. [152].

Temperature (°C)	Relative variation in resonance frequency of MCM	Relative variation in sound speed
-100-100	31.76%	31.88%
100-300	19.24%	19.31%
300-500	13.93%	13.90%
500-700	10.89%	10.87%

Table 3.1- Comparison of relative variations in resonance frequency of the MCM and relative variation in sound speed with for the given temperature variations from -100°C to 700°C.

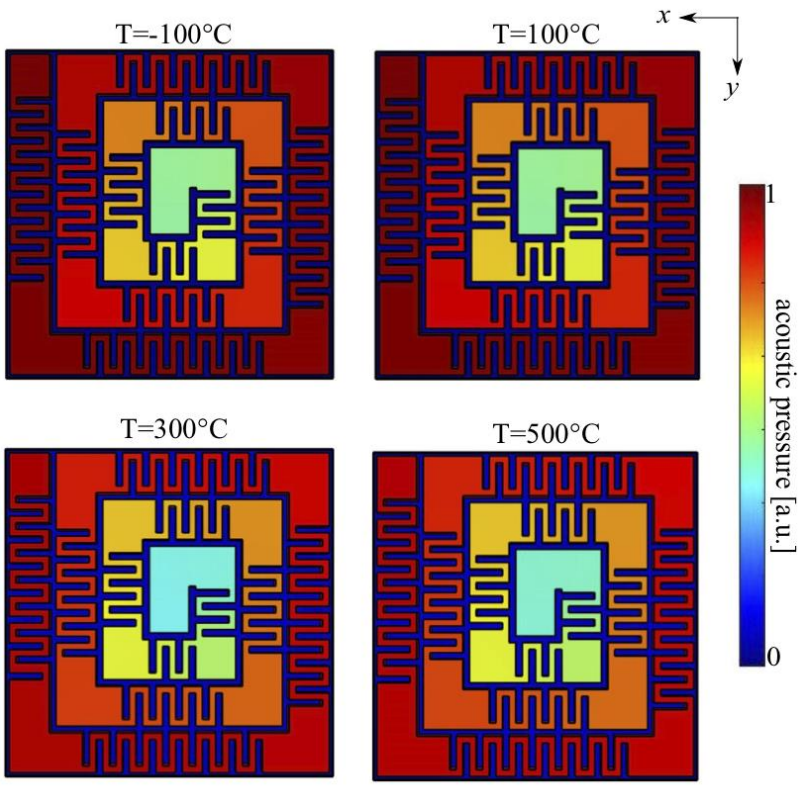

Figure 3.18- Simulated acoustic pressure intensity maps of the MCM at the corresponding resonance peaks for the different temperatures (-100°C, 100°C, 300°C and 500°C).

Our study shows that the sound absorption performance of the present MCM is greatly influenced by the temperature-dependent variable of air including dynamic viscosity, sound speed, and mass density. High temperature partially deteriorates the absorption performance of the MCM. The absorption peak is achieved at 50Hz at room temperature, which is shifted to 85.4Hz at 700℃. Potentially, the absorption performance of the MCM can be improved using constant temperature control methods such as the conventional PID control technique and the adaptive neural technique [158]. However, such type of behavior opens the venue to design temperature tunable metasurface to achieve the perfect absorption at the desired frequency.

3.4 Conclusions

In this chapter, first, we investigated two-coiled and three-coiled metasurface structures to achieve the perfect absorption at extremely low frequencies (<100Hz) keeping the total thickness of the structure the same as the single coiled structure (12.2mm) [47]. From the results, it can be observed that the length of the propagation channel plays a major role in determining the resonant frequency and the absorption peak rather than the cross-section area of the unit cell. To further shrink the total area while increasing the channel length, we proposed a multi-coiled metasurface absorber structure which consists of a coplanar coiling chamber with 11 labyrinthine passages, embedded aperture, and a perforated plate. This design offers two main advantages. First, it fully uses the space inside the coiled chamber, and second, it has an additional degree of freedom which helps to shift the resonance towards extreme low-frequency without increasing the total thickness and the lateral dimension of the metasurface. We analytically, numerically, and experimentally demonstrated the effectiveness of this physical mechanism and its real added value compared to the previous works. The presented multi-coiled metasurface is capable of fully absorb acoustic energy in the low-frequency regime with a deep sub-wavelength thickness. The full absorption is achieved at 50Hz with the thinnest metasurface achieved until now, 13mm ($\lambda/527$), overcoming the major obstacles related to the intrinsically physical dissipation mechanism and to the huge size of classical absorbers when it comes to absorbing very large wavelengths. Moreover, the length of the propagation channel of this structure is $\lambda/4.7$, which breaks the quarter-wavelength resonator theory. To achieve a superior capability of acoustic absorption and broadband feature, we have used a super-cell approach. This proposed metasurface concept introduces a real leap towards pragmatic applications in extreme low-frequency acoustic absorption and presents a genuine breakthrough to develop ultra-thin, lightweight, and efficient meta-absorbers.

Further, we also investigated theoretically and numerically the effect of temperature on the absorption performance of the MCM for practical applications. From the results, it can be observed that the temperature of the surrounding medium significantly affects the performance of the MCM. Rising in the temperature shifts the absorption curves to higher frequencies as well as diminishes the peak absorption value. However, the shift of the absorption peaks with the rise in temperature indicates that the acoustic wave propagation can be effectively tuned by changing the temperature. As a result, the proposed metasurface structure can be used to flexibly absorb the sound at the desired frequency.

Chapter 4

Ultrathin Acoustic Absorbing Metasurface Based on Deep Learning Approach

In this chapter, we propose a deep neural network architecture to design an ultrathin absorbing metasurface for an extreme low-frequency regime. The conventional design method of acoustic metasurface absorbers typically relies on the theoretical approach or is based on numerical simulations. It is often inefficient and requires significant efforts to investigate the enormous number of possible structures with different physical and geometric parameters, which demands huge computational resources. This is especially when modeling narrow cavities using FEM software, and where thermoviscous loss has to be considered. In this chapter, a deep learning-based acoustic metasurface absorber design approach is introduced to significantly reduce the characterization time while maintaining accuracy. Based on a convolutional neural network, the proposed network can model a wide absorption spectrum response in a timescale of milliseconds after the training phase. The performance of the implemented network is compared with other classical machine learning methods to show its efficacy to build complex input-output relations. Using CNN, we have simulated an ultrathin metasurface absorber having perfect absorption at an extremely low frequency of 38.6Hz and featuring simultaneously an ultrathin thickness down to $\lambda/684$ (1.3cm) which is the thinnest metasurface achieved until now. The network prediction is validated using experimental measurements to demonstrate the effectiveness of this physical mechanism. Furthermore, we have proposed a broadband low-frequency metasurface absorber by coupling unit cells exhibiting different properties based on the supercell concept. Our implemented deep learning approach is attractive for applications necessitating fast on-demand design and optimization of an acoustic absorbing metasurfaces.

4.1. Introduction

To design the acoustic metasurface absorbers, various reliable and efficient tools are being used and deeply investigated. One way is to use a theoretical approach using impedance analysis techniques. Using this method, acoustic metasurface absorbers were designed based on the coiling up structures as discussed in chapter 1, section 1.2 [47,48]. In this approach, the

metasurface is designed to satisfy two conditions to achieve perfect or nearly perfect absorption: a resonant state and impedance matching with the background medium [47]. Another efficient theoretical tool to design the perfect metasurface absorbers is by introducing a complex frequency plane of reflection coefficients [67,68]. This method is based on the analysis of the reflection coefficient in the complex frequency plane. It aids in obtaining the critical coupling condition to achieve the perfect absorption. In all these theoretical methods, acoustic wave theory is the design basis, designers are required to have strong expertise in this field. It prevents layman users from designing metasurface according to actual demands. Besides, a widely adopted way in acoustic metasurface design is to use iterative numerical full-wave simulations like finite-element method, using the commercial software COMSOL Multiphysics. Here, the all-over design time depends on the simulation time of each trial design and the number of design degrees of freedom (DOFs). Thus, exploration of the whole parameter space is unrealistic when there are massive design DOFs need to be considered for example, in case of the free-form device design. One more approach is to use various optimization strategies based on the concept of the adjoint variable method [106] or evolutionary algorithms [105]. These methods can quickly generate non-intuitive metasurface designs in less time compared to direct brute-force searching approaches. However, their local optimizers still rely on simulation software for verifications and can be computationally expensive, depending on the performance of initial distributions of the generated metasurface designs.

To overcome these obstacles, we consider a data-driven approach based on machine learning methods. It offers a solution to significantly reduce time-consuming calculations with limited computational resources. Among all ML methods, deep learning has emerged as a very promising method for solving non- institutional problems. Over the last few decades, substantial research in artificial intelligence and the latest advances in GPU computing have resulted in a tectonic shift in the performance of deep learning networks. Inspired by this, several deep learning-based architectures that connect electromagnetic metasurface structures to their EM responses are developed and then trained with a large amount of pre-simulated data calculated by full-wave simulations [112-115]. The reported studies to date mostly emphasize solving electromagnetic problems [160-164], while robust deep learning models for acoustic problems are yet to be developed.

Because deep learning has inherent advantages and superiorities in automatically mining undefined rules, we linked deep learning theory to our metasurface absorber design. This could lead to a subversive breakthrough in the field of acoustic metasurface design,

allowing fast and efficient designs. In this chapter, we have introduced a deep learning model based on two-dimension CNN as a practical tool to model acoustic metasurface absorbers for low-frequency applications. In classification and pattern recognition challenges in computer vision, CNN designs have outperformed competing approaches. The input image/data is convoluted using kernels of different dimensions, and their output is then pooled using pooling layers, processed via a nonlinear activation function, and directed to further convolutional layers [165,166]. During the 1990s and the first decade of the twenty-first century, CNNs were widely used in a variety of applications, but they quickly fell out of favor, especially with the introduction of new generation ML algorithms such as Support Vector Machines. There were two main factors for this, it was difficult to achieve superior generalized capability by training the deep CNN using small or medium-sized datasets. Second is that the training of a deep CNN is computationally very costly and feasible only with the modern graphical processors present today. In comparison, SVMs have fewer parameters that may be fine-tuned, especially over small to medium-sized datasets and regardless of image resolution. In 2012, for the first time, Krizhevsky et al. introduced the deep CNN model, known as AlexNet [167], which is the ancestor of the deep learning model. This model consists of 8-layers (five convolutional-pooling layers and three fully connected layers). It achieved a 16.4% error rate in the ImageNet benchmark database [168] which is about 10% lower than the second top method that uses a traditional ML approach, i.e., SVM. The era of deep CNNs has begun with the successful introduction of AlexNet, which quickly supplanted traditional machine learning classification and identification methods. We implement the custom architecture of CNN with 2-3 convolutional layers to connect the metasurface structure with its acoustic properties through deep learning methods. We also compare its performance with traditional MLs.

In our work, the implemented metasurface absorber structure solves two key challenges of the previous work [47]. The first one is to remove the dependency of absorption on the length of the coiled channel. Indeed, in a coiled structure of metasurface, the length of the coiled channel strictly requires a quarter wavelength channel to achieve perfect absorption, creating difficulties in adjusting the absorption frequency and bandwidth. As a solution to this problem, a multi-coiled metasurface with an embedded aperture and the labyrinthine structure was proposed and demonstrated [143]. Second, one does not need to create a specific design of the channel for acoustic wave propagation to tune the desired resonance frequency. Using the implemented concept, as we will demonstrate, full absorption at 38.6Hz with a total thickness

down to λ/684 is achieved. To validate the predicted results by CNN, we perform experimental measurements using two microphone methods.

4.2 Structure of the Metasurface Absorber

To design our metasurface, first, we consider a resonant absorber system composed of a cavity with a free-form propogation channel, covered by a plate with a circular opening hole as shown in Fig.4.1(a). An incident acoustic wave travel along *z*-direction normally impinges the system and penetrates the hole (diameter *d* and thickness *t*) to the back cavity (thickness *h*). As a result of the energy dissipation, sound energy can be highly absorbed at the resonant frequency. We use the fixed width of the unit cell, *a*=100mm. The thickness of the outer walls is 2mm, therefore the lateral dimension of the square cavity is 96mm. Here, the thickness of the cavity is *h*=11mm, diameter of hole *d*=6mm, and the perforated plate is *t*=2mm. These parameters are also fixed. Initially, we choose the position of the hole in the center, $(a/2, a/2)$ of the plate. We further change the position of the hole to $(a/4, a/4)$, $(a/6, a/6)$, and $(a/8, a/8)$. We get the maximum shift of the absorption peak towards the lower frequency for the hole position at $(a/8, a/8)$. However, we are restricted to choose this optimum position, as it is very near to the boundary of the plate and it may cause an isolation problem during the experiment. Therefore, we decide to choose the second-best optimized hole position viz $(a/6, a/6)$ in our case.

To further tune the resonance frequency, we add a free-form propagation channel inside the cavity. The propagation channel, indeed, offers a degree of freedom to tune the acoustic impedance powerfully, thereby exhibiting superior capability and tunability for shifting resonance at extremely low frequency. We consider such structures to solve using deep learning algorithms. To set up the deep learning model, we decompose the cavity into square lattice sites of 2×2mm^2 as shown in Fig.4.1(b). It can be presented as a 48×48 lattice mesh marked with '.' or blank. Blank lattice site means that the area is filled up by air, and '.' lattice site means the area is filled up with PLA (density, ρ=2700kg/m^3). In our study, we choose the square lattice sites of size 2×2mm^2 to create the propagation channel with a wall thickness of 2mm which is enough thick to provide sound insulation.

It is worth to mention that decreasing the lattice mesh increases the size of the lattice site, but prevents designing long channels and achieving resonance at the lower frequencies. On the other side, increasing the size of lattice mesh decreases the size of the lattice site. This

helps to create long propagation channels that shift the resonance to lower frequency range, while it also increases a large number of variables to train the CNN which increases the computation cost. The current lattice mesh is sufficient to tune the resonance at any frequency of our range of interest viz 30-70Hz. Figure 4.2(a) and (c) shows examples of metasurface absorber patterns decomposed into lattice sites consisting of propagation channels of varying size. The corresponding absorption spectrum calculated using FEM method in shown in Figs.4.2(b) and (d), respectively. It can be observed that with the longer propagation channel, perfect absorption is achieved at lower frequencies.

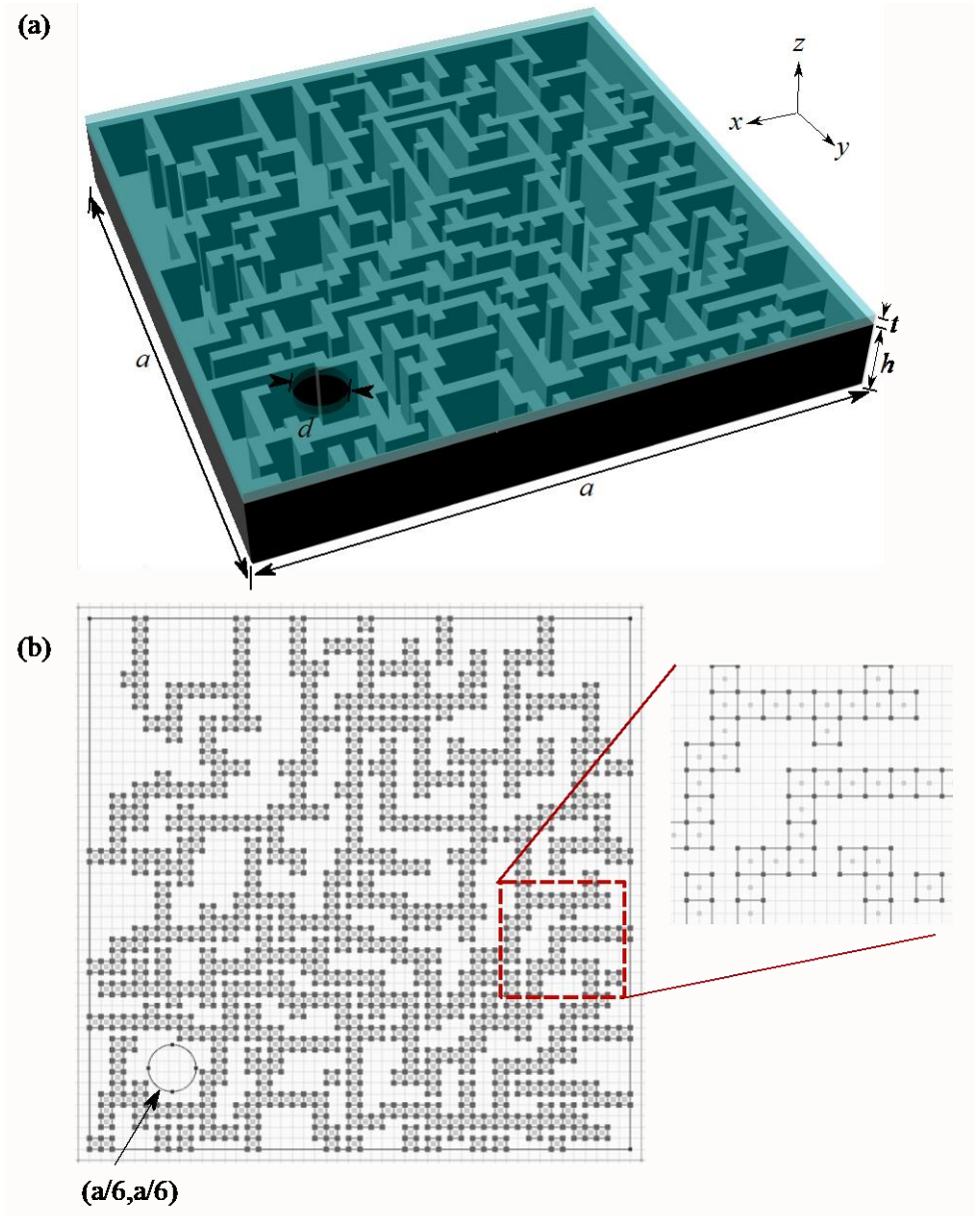

Figure 4.1- (a) Metasurface absorber unit cell (cross-area=$a\times a$) consists of a free-form propagation channel inside the cavity. The normal incident wave propagates along the z-direction and penetrates the channel from the through-hole the perforated plate. (b) Illustration of the metasurface absorber decomposed into square lattice sites of $2\times2mm^2$ to create the propagation channel inside the cavity. Here,

blank lattice site means that area is filled up by air, and '.' lattice site means the area is filled up with PLA.

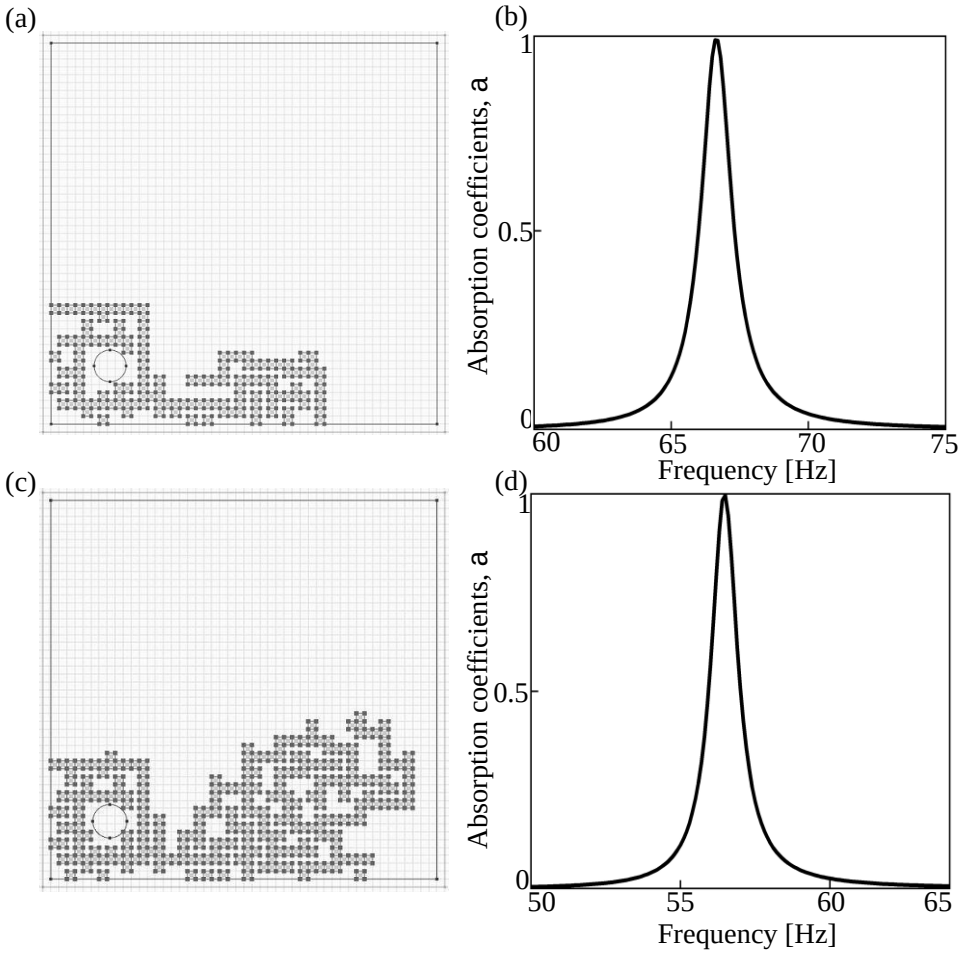

Figure 4.2- (a)-(d) Illustration of the metasurface absorbers structures encoded into lattice mesh and their corresponding simulated absorption spectrum.

To get the dataset to train the deep learning model, metasurface structures are regarded as input data, while the corresponding absorption coefficients are taken as the output data. To obtain the absorption coefficients, numerical simulations are conducted with the preset thermoviscous module of COMSOL Multiphysics v5.5 as the metasurface absorbers consist of narrow propagation channels. Sound hard boundaries are imposed on the interfaces between air and solid due to the huge impedance mismatch between air and structure. For the meshing of geometry, a predefined finer mesh element size is used. The spectra of interest are set to be from 30 to 70Hz. We generate 10,000 pairs of metasurface structures with free-form propagation channels and absorption coefficients to form our dataset to train the CNN. For the dataset generation, numerical simulations are performed in batch mode without the graphical user interface on three servers working in parallel. Each metasurface is subjected to a sound

wave of a given frequency range, and we obtain the value of the absorption coefficient at each frequency that forms a continuous absorption spectrum for the given frequency band. The metasurface structures are randomly split into the training and test data sets, with 80% used to train the network while the remaining 20% are used to evaluate network performance after training. Normally, in terms of the volume of training data in deep learning, we are more concerned with the ratio of the number of samples to the number of features for each sample than with the total number of samples [164].

4.3 Forward Design

In this section, an efficient deep learning-based framework is implemented to simulate acoustic metasurfaces for very low frequency absorption. To start with the less complex architecture, first, we implement the one-dimensional architecture of the CNN. In the later part, we implement two-dimensional CNN. Both types have similar characteristics and use the same methodology. The main difference is the input data's dimensionality and how the feature detector (or filter) moves across it. For both cases, we first present network architecture, followed by the aspect of training and generating spectral responses. Here, implemented CNNs are trained for various shapes of freeform propagation channels keeping other geometrical parameters constant. To train the network with other properties, the presented model has to be modified and needs to add a merging layer like concatenation or averaging after the input layer. It also requires a good proportion of data for each different geometrical parameter like aperture size, lattice size, thickness, etc. which is time-consuming under current conditions. Moreover, by just tuning or changing the propagation channel we can tune the desired resonance frequency for the given frequency range.

4.3.1 1D Convolutional Neural Network

For the 1D CNN, the input data should be one dimensional. To implement it, first we convert the total lattice mesh into the form of a 1D vector,

$$m = \{r_1, x_{1,} y_1, r_2, x_2, y_2, \dots, y_{48}\} \tag{4.1}$$

where r_i = 0 and 1 if the lattice site is filled with air and PLA, respectively. x_i and y_i are the x and y coordinates of the lattice site i, respectively. To maintain the spatial information, we use

1D CNN with the lattice site coordinates. The pattern is encoded into the vector m^a and the input of the 1D CNN comprises all vectors m for all the patterns considered.

4.3.1.1 Network Architecture

The overall 1D CNN design we use is illustrated in Fig.4.3. The objective of the whole process is to achieve total absorption at low frequencies, while other geometrical parameters are kept constant. The neural architecture consists of three 1D convolutional layers along with two fully connected layers. In our case, the shape of the input layer is (6912,1). Here, 6912 are the total number of features in the input vector m defined by Eq. (4.1). The network starts with three convolutional layers named as $l^{(1)}$, $l^{(2)}$, $l^{(3)}$. These layers are used to extract the latent features from the input as illustrated in Fig.4.3. Each convolutional layer consists of a set of filters, which are applied over the input to the layer. The operation of the first 1D convolutional layer, $l^{(1)}$ can be explained by the schematic as illustrated in Fig.4.4. Here, the neurons $r_1, x_1, y_1, \dots, y_{48}$ in the input layer indicate the features of the input vector m^a. b is the bias term. The filters of the size (4,1) are applied on the input layer which slides over the input features. We use total 128 filters of the same filter size (4,1) in our model. The bias 'b' is added over every output of the convolution operation which allows the activation function to better fit the data. The output of the first convolutional layer, $l^{(1)}$ is fed to the next convolutional layer, $l^{(2)}$.

The last convolutional layer $l^{(3)}$ is followed by a max-pooling layer $l^{(4)}$. This layer down-samples the input representation, reducing its dimensionality. Applying directly fully connected layers after convolutional ones without applying pooling or max-pooling layer makes the process computationally expensive, which is not desirable. That is why the pooling layer is the only option to reduce the computation cost. Here, we use a pool size of (2,1). This reduces the size of the input features by half. As such, there is a significant reduction in the number of parameters or weights. This phenomenon lowers the computational cost and mitigates over-fitting. A non-linear activation function using the Rectified Linear Units (ReLU) is applied to each layer.

The output of the pooling layer is then flattened using the flattening layer $l^{(5)}$ and is passed through two fully connected layers $l^{(6)}$ and $l^{(7)}$ of sizes DS= {500,100}. The output of the fully connected layer $l^{(7)}$ is calculated by,

$$l_j^{(7)} = \sum_{i=1}^{500} w_{ji}^{l^{(7)}} l_i^{(6)} + b_j^{(7)} \tag{4.2}$$

where, $w_{ji}^{l^{(7)}}$ is the trainable matrix corresponds to the layer $l^{(7)}$. i and j represents the neurons in layers $l^{(6)}$ and $l^{(7)}$, respectively. The bias term b_j^7 represents the bias associated with a neuron j present in the layer $l^{(7)}$. Finally, the sigmoid function is used to obtain the predicted output from the model. It is given by,

$$S(x) = \frac{1}{1 + e^{-x}} \tag{4.3}$$

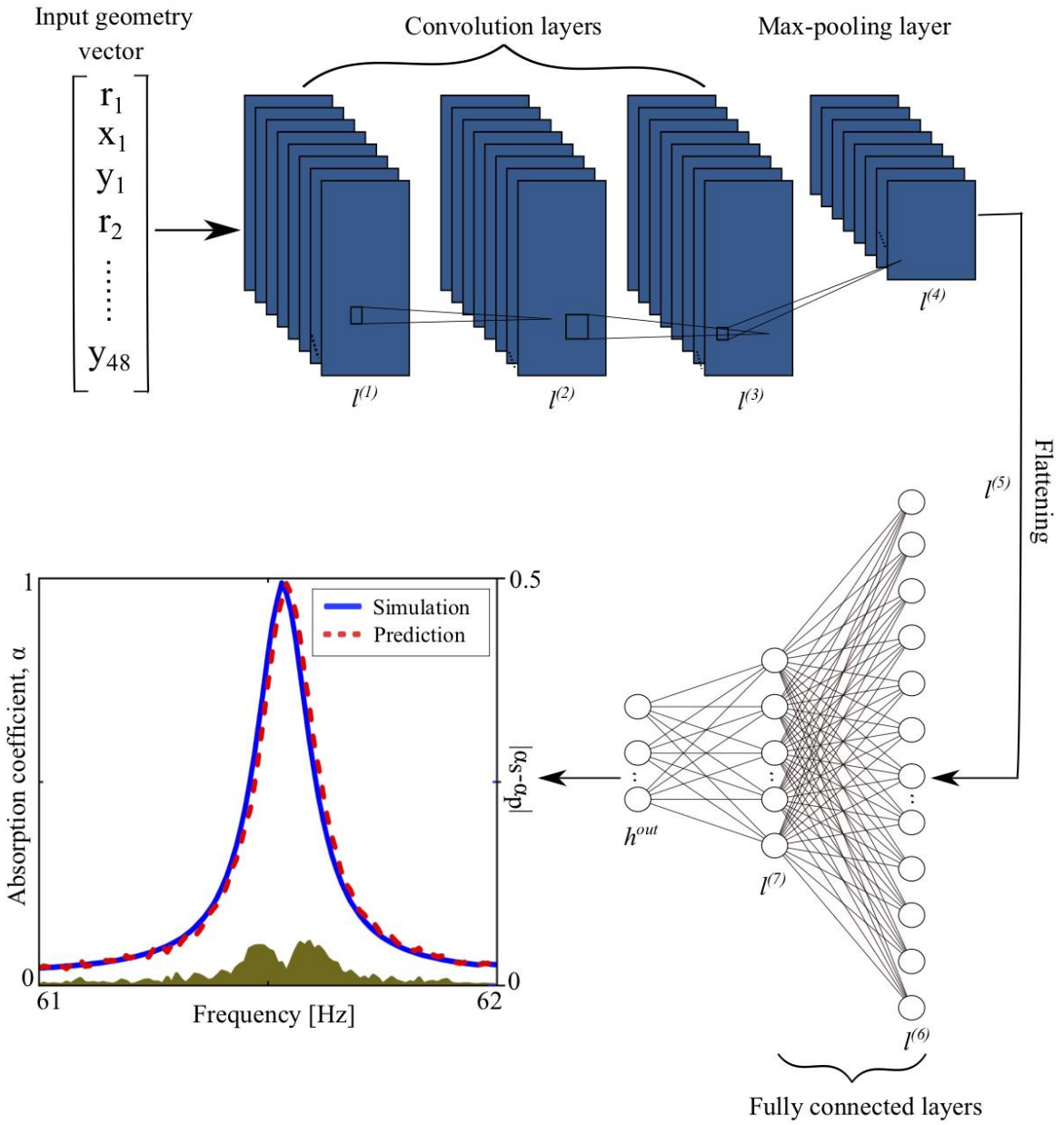

Figure 4.3- An illustration of the one-dimensional convolutional neural network architecture for the metasurface absorber design. It consists of three convolutional layers followed by a pooling layer. The output of the pooling layer is flattened before feeding to the fully connected layer. After being processed with three dense layers, the absorption spectra are ready for evaluation. The output of CNN is fed to the

fully connected layers which produce a predicted spectrum (red dashed curve) compared to the ground truth (blue curve).

The sigmoid function is able to deal with any output in range of (0,1). *S(x)* returns 0 for large negative inputs and 1 for large positive inputs. It is also easier to calculate the sigmoid derivative, which makes the weight coefficient updating process easier. The final output can be restricted to a value between 0 and 1. The output of the final layer, l_{out}^{k} is calculated by,

$$l_{out}^{k} = \sum_{k=1}^{N=51} w_{kj}^{h^{out}} h^{(7)} + b_{k}^{out} \tag{4.4}$$

Where N=51 is total number of neurons in the output layer and $w_{kj}^{h^{out}}$ is the trainable weight matrix for the output layer and b_{k}^{out} is the bias associated with a neuron k present in the layer h^{out}.

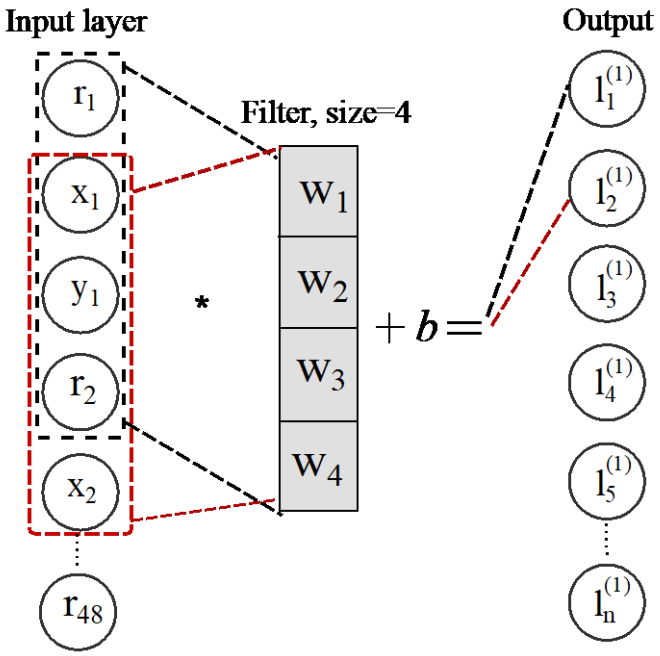

Figure 4.4- Schematic of the 1D convolutional operation with the filter size, *k*=4. Here, *b* is a bias number.

4.3.1.2 Training and Result Analysis

The error is extracted by comparing the absorption spectral response predictions generated by the CNN, which are minimized during the training process. The network performance is quantified in terms of mean squared error. The optimization of the hyperparameters is a crucial step in the implementation of convolutional neural networks as the accuracy and performance

of these networks are entirely reliant on the hyperparameters. The number of convolutional layers, number of fully connected dense layers and neurons, probability of dropout implementation, and learning rate are all hyperparameters that affect this multilayered architecture. As a result, searching for hyperparameters in hyperparameter space is extremely difficult when constructing such a complex hierarchical architecture. The grid search method is a widely used optimization algorithm. In this, the model is trained over a range of hyperparameters, and the values that best perform on the test data are chosen. Table 4.1 shows the optimum values for the hyperparameters used in the training of 1D CNN. For the training, we use Adam optimizer which is a stochastic gradient descent method based on adaptive estimation of first-order and second-order moments [169].

Hyperparameters	**Values**
Optimizer	Adam
Epochs	200
Learning rate	0.2
Momentum	0
Dropout rate	0
Weight initialization	Random initiative
Time taken	5.3hrs

Table 4.1- Hyperparameters used in the training of 1D CNN.

We predict the absorption spectrum for testing data using the trained network and compare the results with those obtained by COMSOL Multiphysics. As can be observed in Fig.4.5, the predicted frequency-dependent absorption spectra (red dashed curves) match the simulated spectra (blue curves) well for different geometries from the test data. The predicted absorption spectra (α_p) and simulated absorption (α_s) overlap almost perfectly. The corresponding mean square value for each case is shown in the inset. There is a very small difference between the absorption coefficient values obtained by the CNN and those obtained by the simulation results. To show this difference clearly, the absolute value of the difference in absorption, defined as $|\alpha_s - \alpha_p|$ is shown on the right axis. More importantly, once trained with enough data, the proposed CNN can generate the predictions in milliseconds, which is four orders of magnitude faster than the conventional FEM-based software.

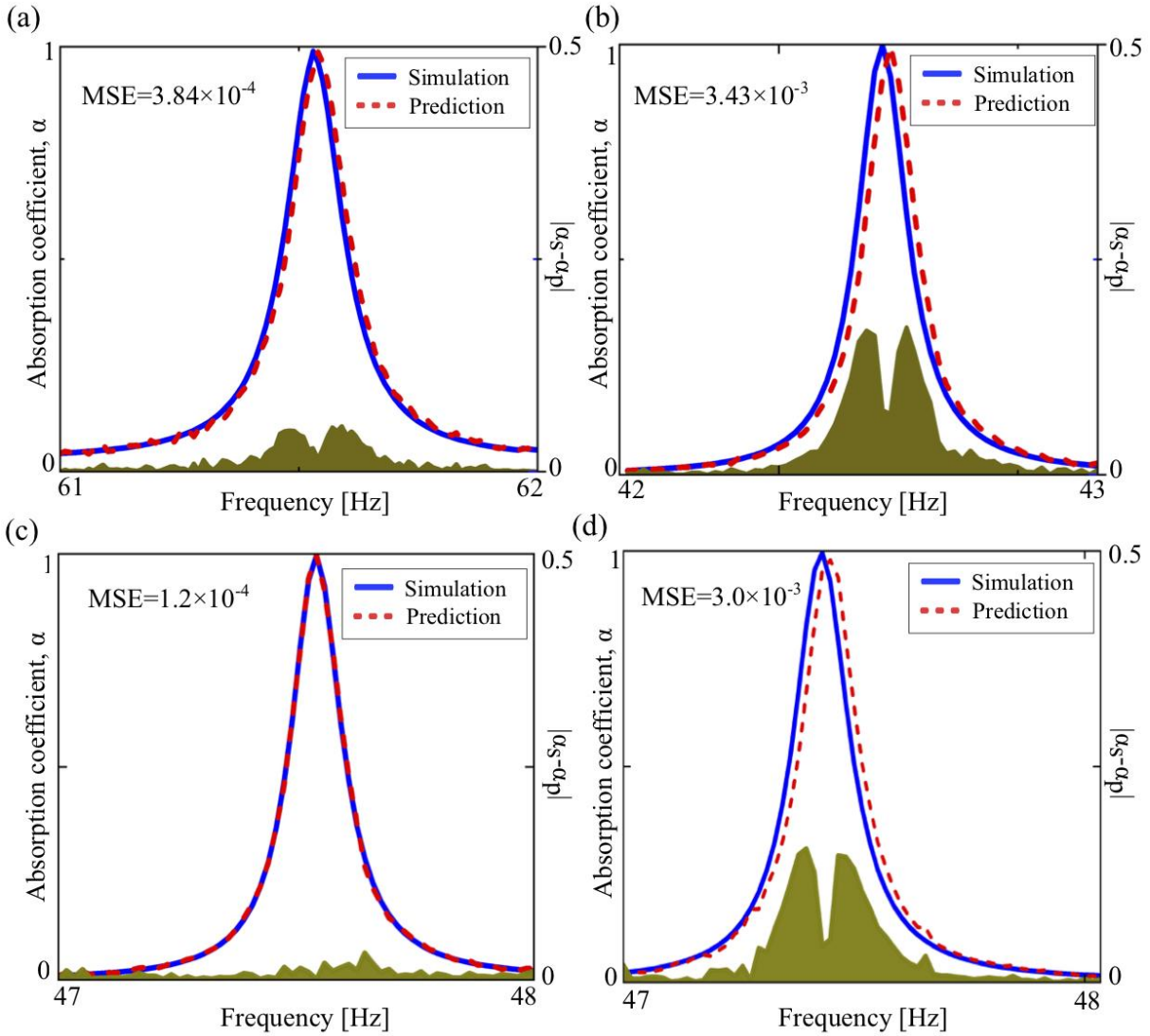

Figure 4.5- Network predictions of the frequency-dependent absorption (red dashed curves) and simulated spectra (blue curves) demonstrating excellent prediction accuracy for a variety of spectral features and input geometric parameters. The shaded gray area shows the absolute value of the difference in predicted and simulated absorption, i.e. $|\alpha_s - \alpha_p|$, shown on the right vertical axis.

4.3.2 2D Convolutional Neural Network

To take better advantage of the spatial information and translational invariance, we further implement a 2D convolutional neural network. As, the input to the 2D CNN is two dimensional, first, we encode the total lattice mesh into a pattern matrix a,

$$a = \begin{bmatrix} r_{1,1} & \cdots & r_{1,48} \\ \vdots & \ddots & \vdots \\ r_{48,1} & \cdots & r_{48,48} \end{bmatrix} \tag{4.5}$$

where $r_{i,j}$ = 0 and 1 if the lattice site is filled with air and PLA, respectively. These pattern matrices are then input to our 2D CNN. Here, each pattern matrix corresponds to a set of absorption coefficients. For our case, the total number of lattice sites is 2304. The possible numbers of pattern matrices are 2^{2304}. Using such matrices, huge numbers of free-form channels can be created. Ideally, it takes millions of years for the calculation of all data, which is an impossible task under current calculation conditions. Therefore, the use of deep learning networks is advantageous here to find optimum value while reducing computational time.

4.3.2.1 Network Architecture

The operation of the first 2D convolutional layer with the filter size (2,2) can be illustrated as shown in Fig.4.6. For our 2D CNN, the stride of (2,2) and the filters of the size (2,2) are applied on the input layer which slides over the input features. The 2D CNN architecture we use is illustrated in Fig.4.7 which consists of a sequence of convolutional and pooling layers. Here, the neural architecture consists of two 2D convolutional layers along with two max-pooling layers. The shape of the input layer is (48, 48, 1) because the input 2D pattern matrix (Eq. (4.5)) consists of 48 elements (lattice sites) in row and columns. The network starts with a convolutional layer named as $h^{(1)}$.

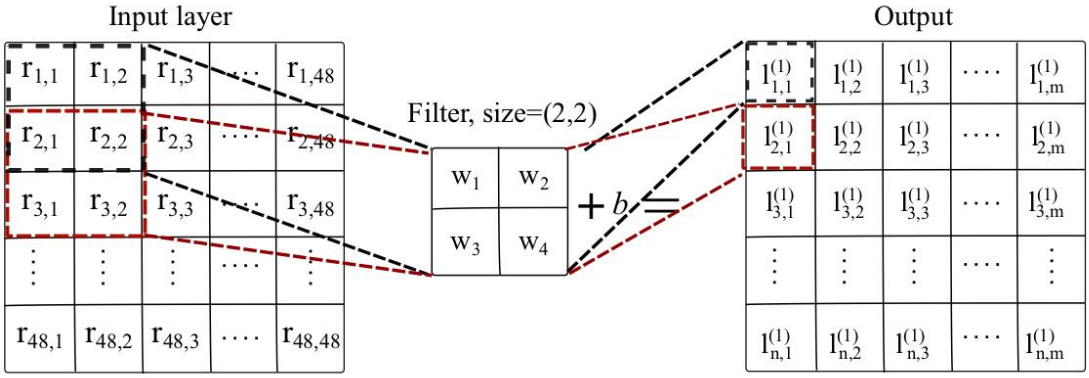

Figure 4.6- Schematic of the 2D convolution operation with the kernel size, (2,2).

The output of the $h^{(1)}$ layer is fed to the max pool layer, $h^{(2)}$. Here, we use a pool size of (2,2) and the stride of (2,2). The stride parameter determines how much the filter is moved at each step. As such, there is a significant reduction in the number of parameters or weights. This phenomenon lowers the computational cost and mitigates over-fitting. Similarly, another

convolutional layer, $h^{(3)}$ is used which followed by a pooling layer, $h^{(4)}$ with the same filter size. The bias is added over every output of the convolutional operation. Here, we use multiple pooling layers that helps to increase the size of the receptive field of the convolutions in later layers. A batch normalization layer and a non-linear activation function ReLU are applied to the output of all layers except for the last one. The output of the pooling layer, $h^{(4)}$ is then flattened using a flattening layer, $h^{(5)}$ which converts the output data of convolutional layers into a 1D array. Here, we flatten the output to create a single long feature vector and passed through two fully connected layers, $h^{(6)}$ and $h^{(7)}$ of sizes DS= {500,100}. In Fig. 4.7, h^{out} represents the absorption coefficients for the given frequency range.

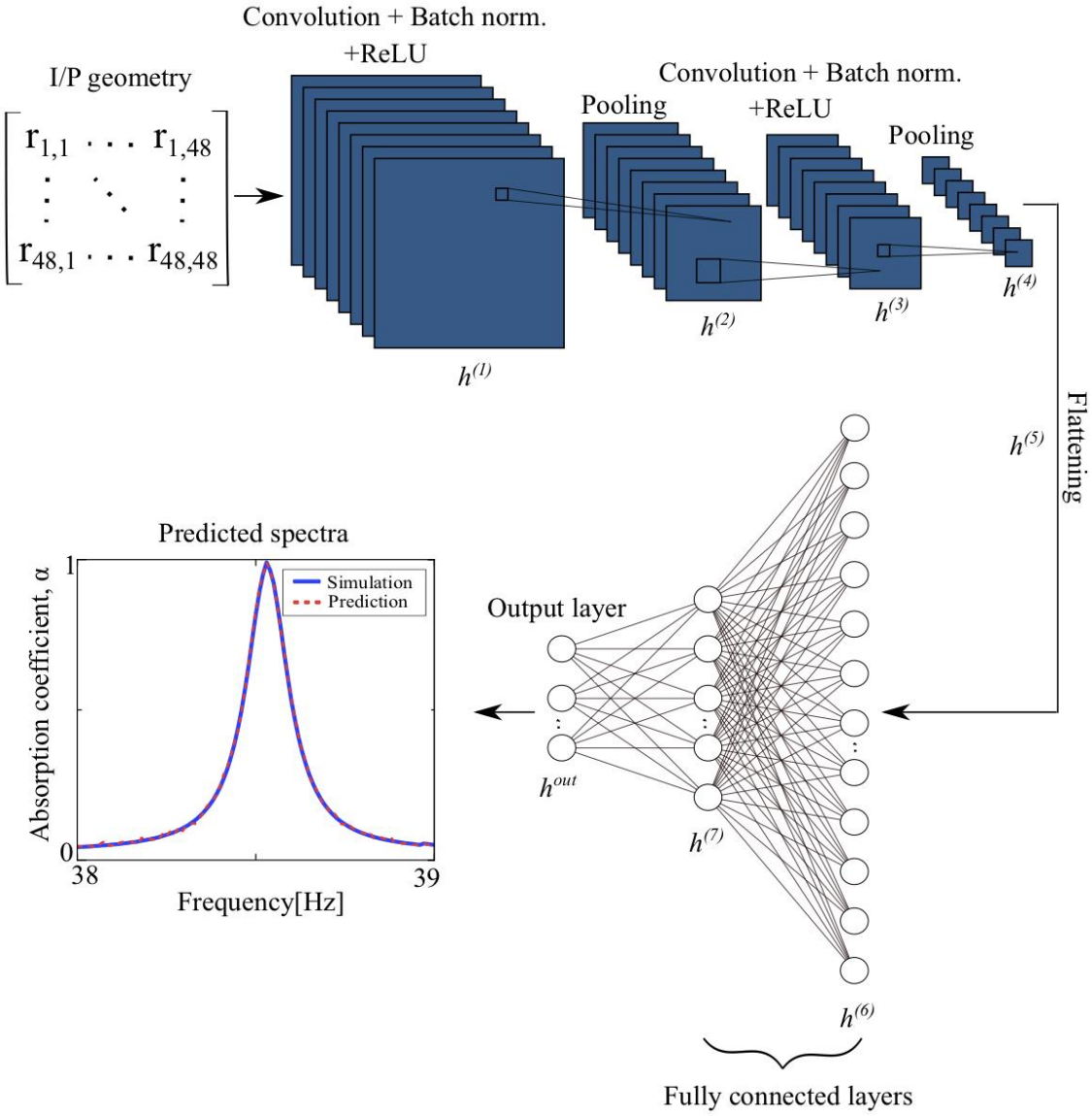

Figure 4.7- An illustration of the 2D CNN based deep learning network architecture for the metasurface absorber design. A set of geometric input is fed to 2D CNN which makes data smoothed and up sampled in a learnable manner. Here, the input geometric matrix is passed through two convolutional layers and pooling layers then flattened into a 1D array. After being processed to two fully connected layers, the

absorption spectrum over the 30-70Hz is ready to evaluate. A predicted spectrum (red dashed curves) is compared to the ground truth (blue curves).

4.3.2.2 Training and Result Analysis

To get the optimum value of hyperparameters for 2D CNN, we perform optimization search over them: number of epochs from [10, 20, 50, 100], learning rate from [0.001, 0.1, 0.2, 0.3], dropout for the dense layers from [0.0, 0.1, 0.2, 0.3], optimizer from [‘SGD’, 'RMSprop', 'Adagrad', 'Adadelta', 'Adam', 'Adamax'], weight initialization from ['uniform', 'normal', 'glorot_normal', 'glorot_uniform', 'he_normal', 'he_uniform']. The list of hyperparameters and their values used in the train is given in Table 4.2.

Hyperparameters	**Values**
Optimizer	Adam
Batch Norm.	Yes
Batch size	64
Epochs	100
Learning rate	0.2
Momentum	0
Dropout rate	0
Weight initialization	Random initiative
Time taken	6hrs

Table 4.2- Hyperparameters used in the training of 2D CNN.

We predict the absorption spectrum for testing data using the trained network and compare the results with those obtained by the COMSOL Multiphysics. Figure 4.8 depicts the spectral response of four representative cases from the testing data that indicate that the predicted frequency-dependent absorption spectra (red dashed curves) match the simulated one (blue curves) well for different curves. The predicted absorption spectra (α_p) and simulated absorption (α_s) overlap almost perfectly such that we plot on the right axis (shaded dark green area), the absolute value of the difference in absorption, defined as $|\alpha_s - \alpha_p|$. We have shown the comparison only for narrow frequency range to clearly show the difference between simulated and predicted results around the absorption peak.

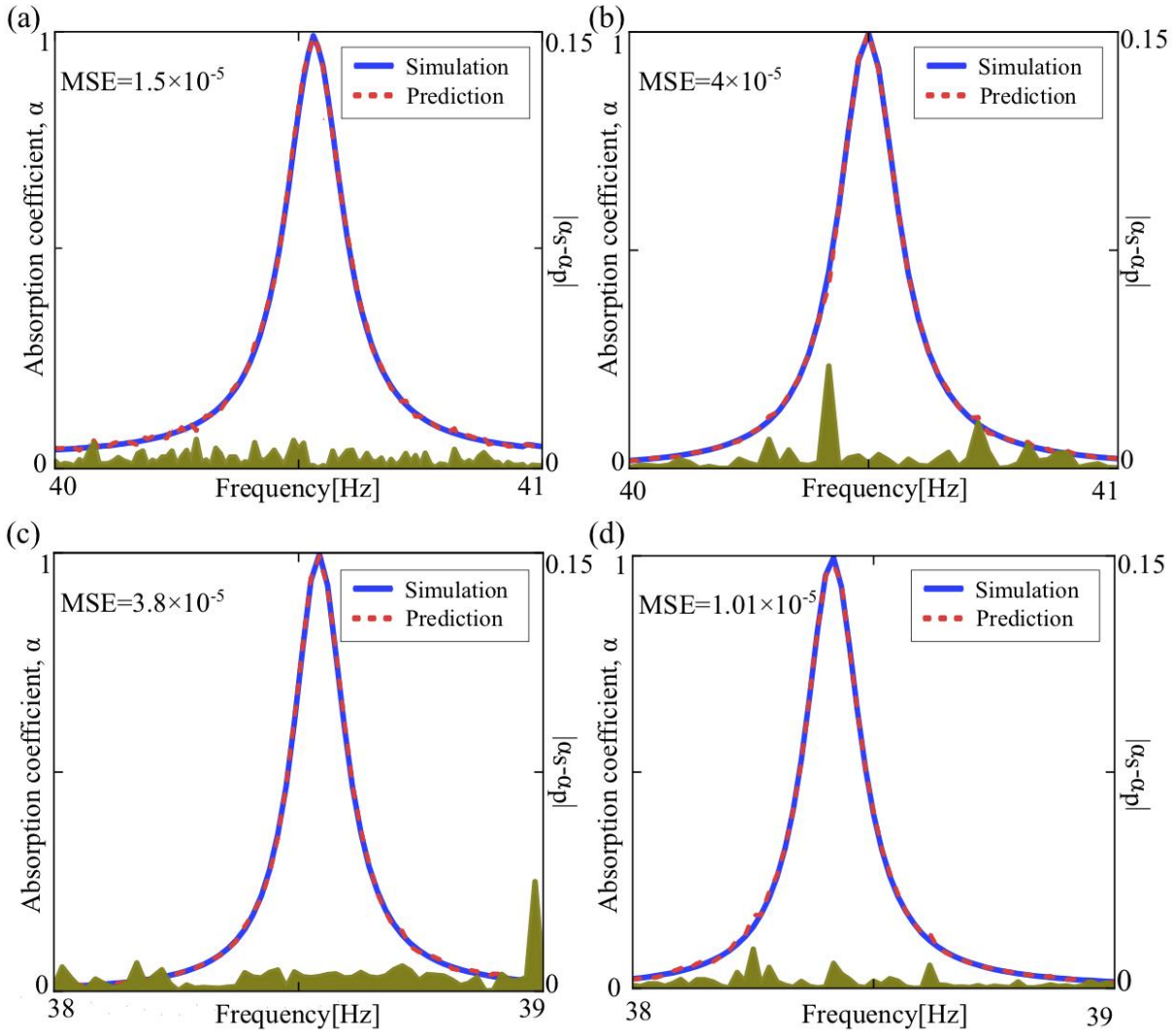

Figure 4.8- Examples of 2D CNN network predictions of the frequency dependent absorption (red dashed curve) and simulated spectra (blue curves) demonstrating excellent prediction accuracy for a variety of input geometries. The shaded green area shows the absolute value of the difference in predicted and simulated absorption, i.e. $|\alpha_s - \alpha_p|$, shown on the right vertical axis.

Comparison of the plots of Fig.4.5 and Fig.4.8 shows that better accuracy is achieved using the 2D CNN as compared to the 1D CNN. The problem setup of a 2D lattice lends itself to 2D convolutions over the lattice sites as they would be able to better take advantage of the spatial information and translational invariance compared to the 1D CNN. Also, we use two max-pooling layers in the case of 2D CNN that helps to increase the size of the receptive field of the convolutions in later layers. We believe that this accuracy can be further improved using more training data with increased diversity.

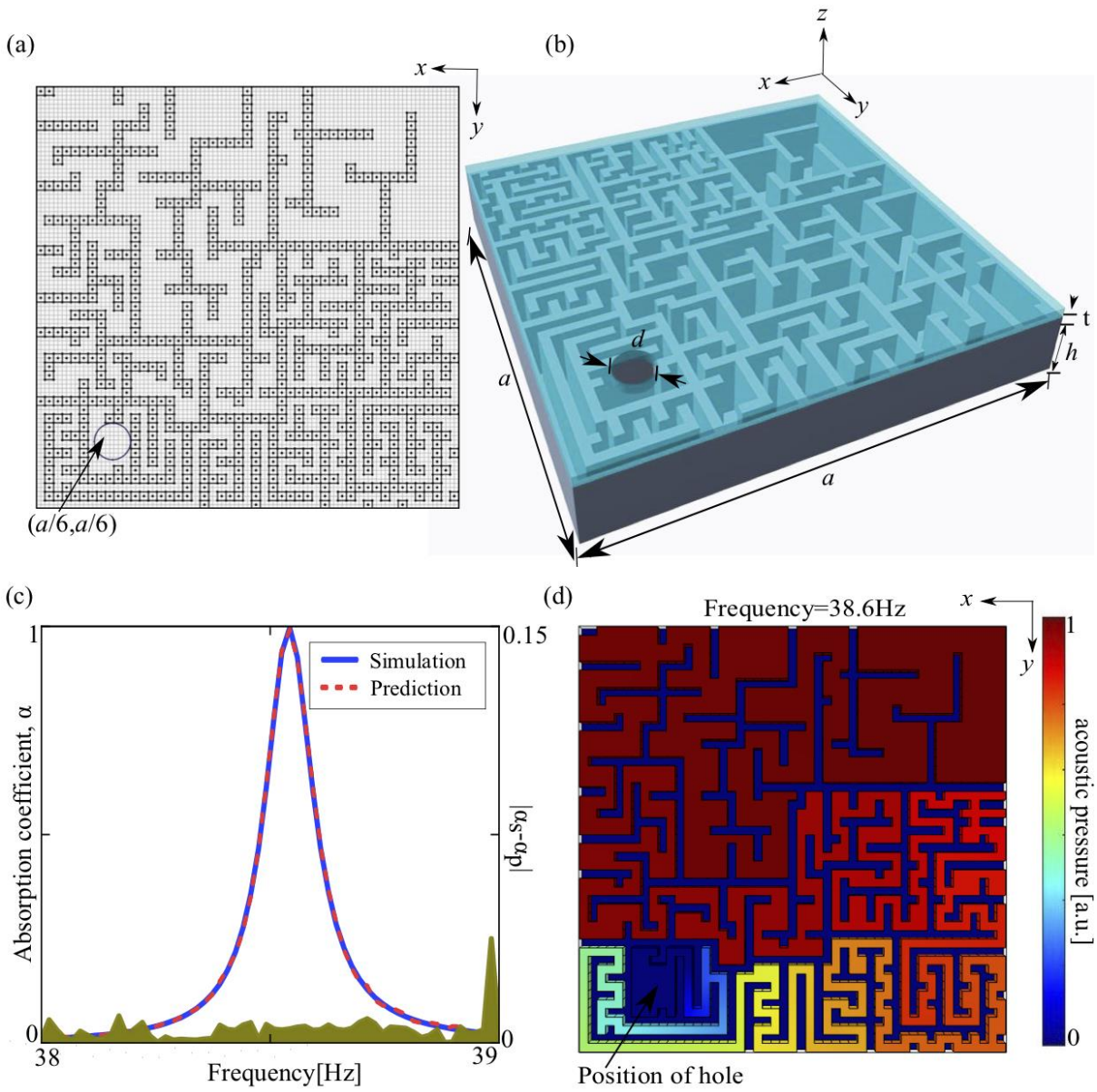

Figure 4.9-(a) Schematic illustration of matrix encoding for optimized achieving perfect absorption at 38.6Hz. (b) Corresponding 3D structure of the metasurface absorber (c) Comparison of the CNN predicted and simulated absorption curve of the optimized structure. (d) Sound pressure profile inside the structure at 38.6Hz.

Based on all the precedent developments and optimizations, in Fig.4.9, we provide and demonstrate an example of an ultrathin metasurface absorber achieving total absorption at an extremely low frequency of 38.6Hz. Figure 4.9(a) shows the simulated metasurface absorber encoded into lattice mesh and corresponding to the 3D structure shown in Fig. 4.9(b). The network predicted absorption spectra are compared with the simulation in Fig. 4.9(c). The total thickness (h+t) of the structure is 1.3cm ($\lambda/684$) which is the thinnest achieved metasurface ever [170]. Here, one thing worth noting is that the total path for the propagating waves inside

the channel is about λ/5.7 which is quite smaller than the length required by the quarter-wavelength resonator approach. For the further analysis of the metasurface absorber, we simulate the pressure profile at the resonance frequency of 38.6Hz using the FEM software as shown in Fig.4.9(d). It can be observed that the acoustic pressure is higher in "deeper" regions of the structure at the resonance frequency, whose distribution is similar to previous metasurface absorber designs with a gradient channel. When the wave passes through the channel at the resonant frequency, it is being absorbed due to thermoviscous loss and its energy is dissipated into heat.

4.4. Comparison with Classical Machine Learning Techniques

We compare the performance of our implemented 2D CNN with three classical machine learning techniques: KNN, SVM, and RF. Before feeding the data to the machine learning algorithms, we preprocess them. Using the MinMaxScaler function defined in the scikit learn library, the input data is scaled to be within the provided input range (default feature range = {0,1}). Such scaling of data is an important preprocessing step for most of machine learning algorithms. This transformation is given by,

$$X_{scaled} = X_{std} \times (max - min) + min \tag{4.6}$$

where $X_{std} = (X - X_{\min(axis=0)} / (X_{\max(axis=0)} - X_{\min(axis=0)})$. Here, for any data point X,

$X_{min(axis=0)}$ = Minimum value in the particular column

$X_{max(axis=0)}$ = Maximum value in the particular column

max = maximum possible value post scaling (defined during function call - default value being 1)

min = minimum possible value post scaling (defined during function call - default value being 0)

As the number of input features for any machine learning algorithms increases, the number of calculations to be performed also increases and it leads to an increase in both the computation time as well as the required computational resources. To overcome this issue, we have applied PCA keeping the number of components considered to 30. Thus, we reduce the feature space from 200 to 30. After the data preprocessing, the train_test_split function defined in the scikit learn library is used to split the scaled dataset into train and test sets for training the

model and evaluating the performance of the trained model respectively. A ratio of 0.33 has been used to split the data into 67% data as training set and 33% as test dataset. ‘random_state’ has been defined for reproducibility i.e. for ensuring that the function gives the same fractions in each run. For all three machine learning algorithms, we optimize the hyperparameters. Final optimized values are listed in Table 4.3.

Machine learning technique	**Hyperparameters**	**Value**	**Description**
KNN	n_neighbors	2	Number of neighbors
	weight initialization	uniform	Weight initialization
SVM	kernel	RBF	Type of kernel
	gamma	0.1	Kernel coefficient for 'rbf'
	C	100	Regularization parameter
Random Forest	n_estimators	10	Number of estimators
	maximum depth	default	Maximum depth of the tree

Table 4.3- Hyperparameters of classical machine learning techniques and corresponding values which are used to train the algorithms.

We are using mean square error which helps to determine the relative accuracy of the absorption coefficients against expected values. Here, after predicting the estimated values of absorption coefficients, we further choose a threshold (10^{-4}) to judge if the prediction is accurate up to certain limits or not. Hence, the accuracy metric is used to estimate the effectiveness of the model to predict absorption coefficients with a certain precision. Other ML methods can have similar (or lower) MSE than the 2D CNN, but after testing over 12 examples, CNN seems to be the most reliable method with an average accuracy of 86%. As shown in Fig.4.10, it can be observed that 2D CNN outperforms these classical techniques with an average accuracy of 86%. Practically, deep learning models are not precise enough to reach 100% accuracy, it only shows probabilities. To improve efficiency, further optimization may be needed. Even after optimization, the prediction value can be achieved to be close to the optimal value, which also speeds up the modeling process.

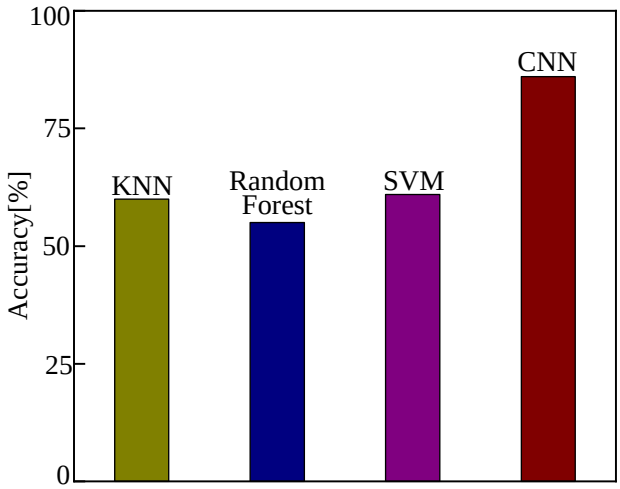

Figure 4.10- The comparison between 2D CNN and other classical machine learning techniques in terms of accuracy.

4.5 Acoustic Absorption Measurement

To test our procedure for the application phase, we compare the experimental absorption coefficients to the ones predicted by our implemented CNN architecture. First, we fabricate the sample having the perfect absorption at 38.6Hz. The fabricated sample is shown in Fig.4.11. However, the operating frequency bandwidth of our measurement setup starts around 50Hz. So, it is not possible to measure absorption for this sample. Therefore, we have opted to model an absorber with the CNN algorithm operating at 66Hz to allow reliable comparison with the experimental results. Also, we slightly modified the design having the hole in the center.

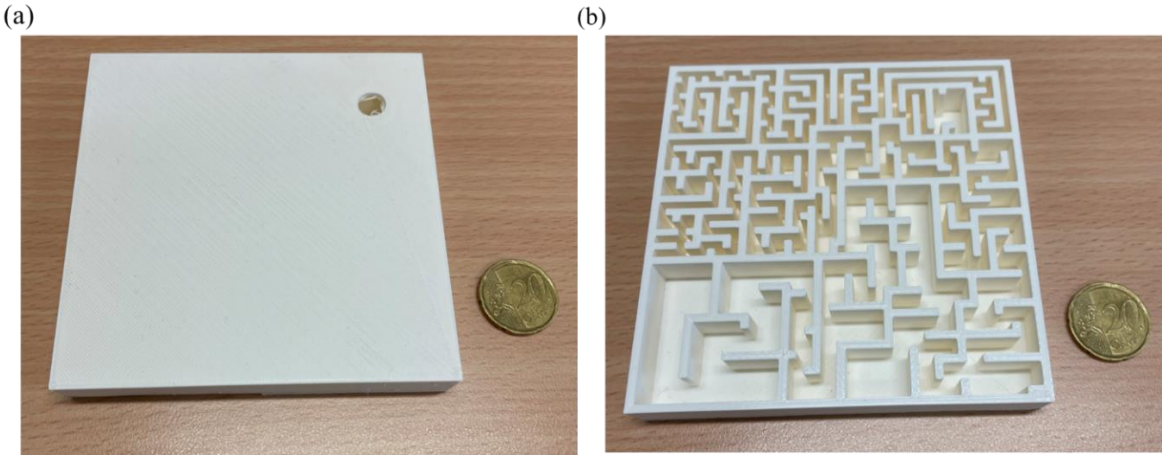

Figure 4.11- (a) Fabricated sample having the full absorption at 38.6Hz. (b) Internal view of the structure.

Figure 4.12(a)-(c) shows the fabricated sample using 3D printing to having absorption at 66Hz. Fig. 4.12(b) shows the internal structure of the fabricated sample and Figs. 4.12(b)-(c) shows the vertical and horizontal view of the sample. The obtained results show a good agreement, validating the procedure using the CNN program to predict acoustic absorption properties. It demonstrates the efficacy of this physical mechanism as well as its true added value.

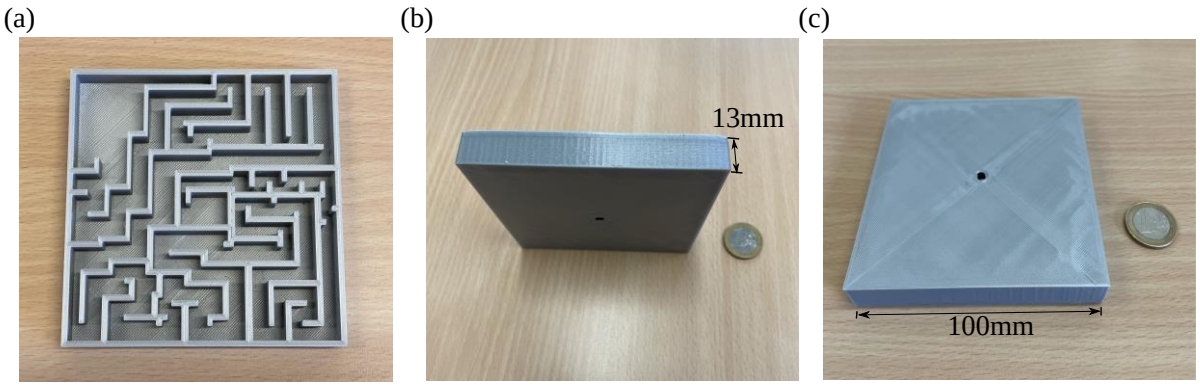

Figure 4.12- Fabricated sample having absorption at 66Hz. (a) Internal structure of the experiment sample. (b)-(c) Photographs of experiment sample with geometrical parameters: a=100mm, d=7mm, w=h+t=13mm.

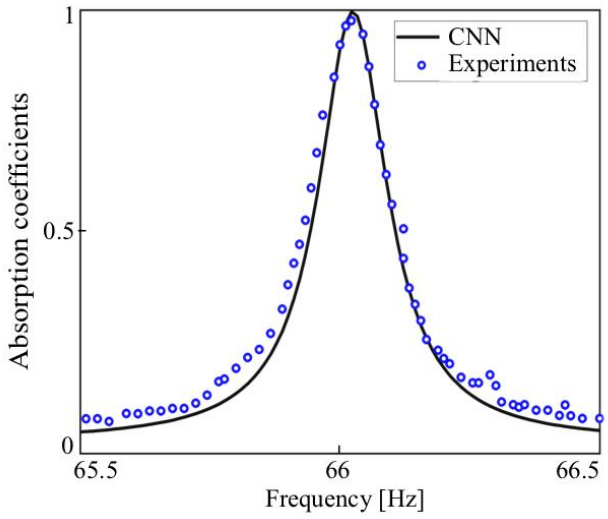

Figure 4.13- Comparison of the absorption coefficients obtained via 2D CNN (black curve) and experimental measurement (blue circles).

4.6 Bandwidth Improvement

As the bandwidth is a highly desired feature when it comes to the absorption in general, and specifically in the low-frequency regime, we, in follow, describe an approach by which we can achieve a broadband ultrathin absorbing metasurface. Here, our objective is to design the

metasurface around 38.6Hz which is the lowest resonance frequency where the full absorption is achieved. For this aim, we design a supercell consisting of 25 unit-cells (5×5) resonating at different frequencies and having a different hole diameter of the perforated plate as shown in the inset in Fig.4.14(b). It can be achieved by overlapping the resonances for each metasurface in the supercell. Fig.4.14(a) shows the relation between the diameter of the hole and corresponding resonance frequency for the considered designs. The hole diameters of the different metasurface are tuned between 1.5mm to 4.5mm to get overlapped resonances. The total thickness of the supercell is still 13mm, and the side length of the square supercell is 50cm. Achieving simultaneously broad bandwidth and thin metasurface is contradictory. Current bandwidth can be further improved by increasing the thickness of the metasurface. Here, the average absorption is higher than 95% for the given frequency range but does not reach the perfect absorption as shown in Fig.4.14(b). This is because the hybrid structure still has a small impedance mismatching, making the effective acoustic impedance at the surface slightly deviate from the impedance of the air, q_0c_0.

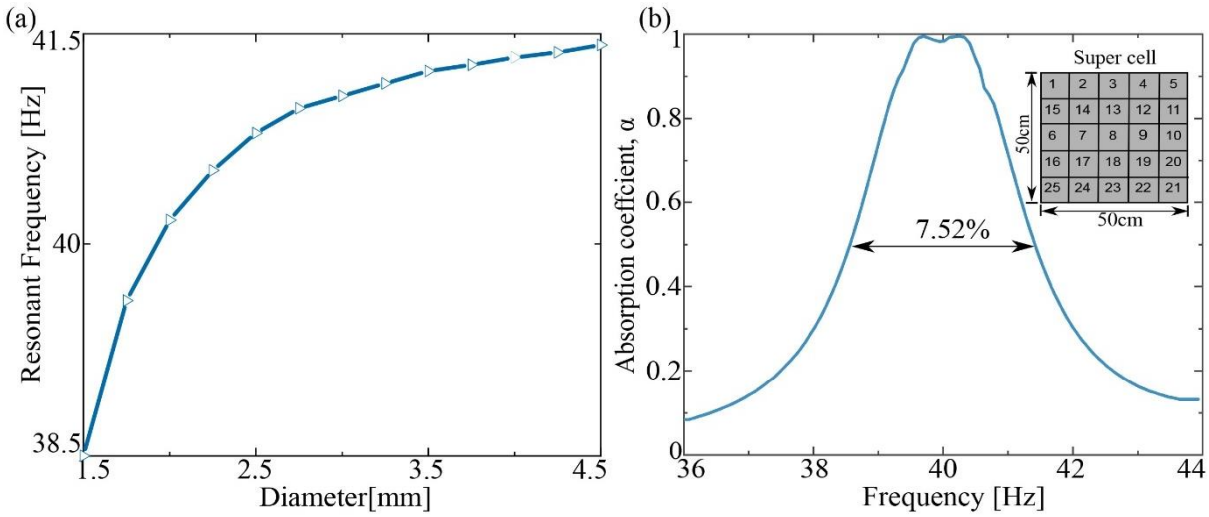

Figure 4.14- (a) Relation between the diameter of the holes of given metasurface and the resonant frequency (b) Bandwidth improvement using the supercell. The supercell consists of 5×5-unit cells denoted as 1–25 in the inset photo.

4.7 Conclusions

In this chapter, we have proposed a deep learning-based simulation approach for acoustic metasurface absorbers to solve the key limitations of existing design methods. Accurate absorption spectrum responses of metasurface absorbers have been derived using 1D and 2D CNN-based network structure in the timescale of milliseconds, which is over four orders of magnitude faster than conventional FEM simulation software. Implemented 2D CNN is more

accurate as compared to the 1D CNN as it takes the advantage of spatial information. We have further compared the performance of the implemented 2D CNN with popular classical machine learning techniques like KNN, RF, and SVM. Implemented 2D CNN outperformed these classical techniques with an average accuracy of 86%. It shows efficacy of deep learning methods as compared to the classical machine learning techniques to build complex input-output relationships. We believe that with more training data, this accuracy can be improved. Further, we have performed experimental measurements and validated the network predictions which demonstrate the effectiveness of this physical mechanism and its real added value compared to the previous works. Using CNN, an ultrathin metasurface absorber is modeled having perfect absorption at extremely low 38.6Hz with the ultrathin thickness down to $\lambda/684$ (1.3cm) which is the thinnest achieved metasurface ever. The total path for the propagating waves inside the channel is about $\lambda/5.7$ which breaks the quarter-wavelength resonator approach. We also have designed a broadband low-frequency metasurface absorber by coupling unit cells exhibiting different properties based on the supercell concept. The bandwidth can be further improved by connecting more unit cells with different geometrical parameters.

In our implemented CNN, we have kept other geometrical parameters constant as by tuning the length of propagation channel only, ample samples can be generated to have absorption resonance for the given frequency range. To train the network with other parameters, the presented model can be modified by adding a merging layer like concatenation or averaging after the input layer. Such kind of network is implemented and discussed in chapter 5 to design a metasurface absorber with high degrees of freedom. Our implemented method provides laypeople, engineers as well as scientists with a powerful design tool that allows them to focus solely on their design goals. We envision that our method can be generically utilized for fast and accurate modeling of acoustic metasurface devices with minimum human intervention.

Chapter 5

Forward and Inverse Design of Metasurface Absorber for Oblique Wave Incidence

In this chapter, we demonstrate the forward and inverse design of complex metasurface absorber structure for the oblique wave incidence using the two-dimensional convolutional neural network (2D CNN) and conditional generative adversarial network (CGAN), respectively. The proposed forward deep learning network is capable of modeling a metasurface absorber for very low-frequency absorption using 2D images of nearly freeform propagation channels and concatenating with other geometric properties. It significantly reduces the characterization time (four orders of magnitude faster than conventional FEM calculations) while maintaining high accuracy. Compared to the previous neural network-based acoustic designs, our implemented network offers high degrees of freedom to solve complex metasurface structures. Further, we have implemented a CGAN to solve the inverse design problem. When an input set of predefined absorption spectra is fed to the CGAN, it produces on-demand candidate metasurface patterns. Such an approach could open new venues for neural networks in acoustic metasurface designs to automate the design process. We demonstrate the capability of the implemented network architecture by designing a metasurface absorber operating at 82Hz for the oblique wave incidence with a thickness of $\lambda/64$. The presented approaches of the metasurface design enable a much more generalized and broader scope of the optimal designs that go beyond acoustics applications.

5.1 Introduction

The unprecedented functionalities of the acoustic metasurface absorbers come at the cost of tremendous difficulty in finding individual metasurface structures based on specific criteria. It makes the design and optimization of the metasurface a key challenge in the acoustic field. Inverse design problems are even more difficult because they require direct retrieval of the proper structure for the desired acoustic performance, which requires a much larger number of DOFs in the design space. Such designs are usually based on either optimization methods: gradient-based or evolutionary-based. This approach enables researchers to discover non-intuitive and freeform acoustic structures which outperform empirically designed structures.

These algorithms, on the other hand, are driven by rules that have iterative searching steps in a case-by-case manner and frequently rely on numerical simulations to generate intermediate results that aid in the modification of the searching strategy. The converging speed using this approach depends on the solver which is connected to the optimizer. As a result, modeling and characterization tools play an important role in all current design processes. In this context, precise and time-efficient design tools must be thoroughly investigated in order to facilitate the design of next-generation acoustic metasurface absorbers, which are frequently characterized by large numbers of design DOFs and multifunctionalities.

Other than the traditional design methods, deep learning methods have been adopted as a radically new design tool to address forward and inverse acoustic problems, recently. In the field of acoustics, this approach has been applied for the acoustic cloaks design [117], object recognition [118], regional control of sound fields [122], far-field subwavelength acoustic imaging [121], and extreme low-frequency acoustic absorption [170]. Various deep learning-based models are proposed to solve inverse acoustic problems [117,122,171]. Once properly trained with the sufficient data, such deep learning models are very accurate and capable of generating desired acoustic responses within very fast. Despite such development in this field, there are still issues with the existing networks specially built using FCLs. These works primarily deal with simple acoustic structures with a limited number of parameters, severely limiting the accessible acoustic design DOF and because of this, current deep learning models are insufficient as a general design scheme.

In this chapter, we present forward and inverse deep learning models for simulating and designing metasurface absorbers. The implemented approach addresses the issues and limitations to deal with large number of parameters. To expand the design space, this approach considers high DOFs and accounts for the 2D geometrical pattern with complex freeform propagation channels, as well as properties like the thickness of the structure, and angle of the incidence. Once fully trained with a sufficient amount of data, the proposed forward prediction network can generate accurate absorption coefficients of complex metasurface absorber structures for the given frequency. Practical applications of the metasurface absorber demand acoustic absorption effect at a particular frequency, which needs to realize design parameters that produce the customer-defined spectral response defined at the input. The goal of inverse design is to generate a working structure directly from the desired acoustic responses, eliminating the need for lengthy parameter scans or trial-and-error methods. Due to the enormous degrees of freedom in typical metasurface patterns, the CNN scheme, such as

backpropagation in trained simulator networks, is ineffective in the inverse design of metasurface. Furthermore, the trained simulator defines the problem as a deterministic system, which means that a single simulator will always produce a fixed result for a given input condition. Meanwhile, multiple solutions may exist for the same target spectra fed to the simulator. To overcome these challenges, we implement a conditional generative adversarial network.

Using the proposed deep learning architectures, we demonstrate a metasurface absorber operating at 82Hz with nearly omnidirectional performance with a subwavelength thickness of λ/64. The performance of the produced metasurface absorber prototypes corroborates that the network achieves two important goals for designing absorbing metasurface: (1) fast and accurate performance evaluation of complex structures for the oblique wave incidence at very low frequency; and (2) finding non-institutive device designs based on predetermined acoustic response requirements. It is envisioned that the proposed approach also validates the feasibility of object-driven 3D acoustic device design which can be easily extended and generalized to many other acoustic device designs.

5.2 Structure Design of Acoustic Metasurface Absorber

The metasurface under evaluation is composed of a resonant cavity, free-form propagation channel, and cylindrical aperture covered by a perforated plate of thickness, t=1mm as shown in Fig.5.1(a). The embedded aperture is appended to the opening of the propagation channel. Such aperture and the propagation channel provide a feasible approach to tune the acoustic impedance powerfully, thereby exhibiting superior capability and tunability for achieving desired absorption performances. The lattice size is fixed at a=58mm and the thickness of the outer wall of the cavity is 2mm. Thus, the lateral dimension of the square cavity is 54mm. The whole area of the square cavity is then decomposed into the square lattice sites of $2\times2mm^2$ to construct the propagation channel made of PLA (density, ρ = 2700 kg m^{-3}) with a thickness of 2mm.

The absorption responses of these structures are then calculated with the preset thermoviscous module of COMSOL Multiphysics v5.6. Sound hard boundary conditions are imposed on the air-structure interface due to huge impedance mismatch. For the meshing of geometry, we use finer mesh in maximum element size. Over the 9000 metasurface structures with different propagation channel shapes, the diameter of the holes, incidence angles, and thicknesses are generated within the following ranges (all dimensions are in mm and angles are

in degree): thickness, $h \in [65,75]$, incidence angle $\theta \in [0,60]$, diameter of hole, $d \in [10,12]$ since this range includes ample samples generating absorption resonance for the given frequency range. Height of the circular aperture is selected as $h_a = (h - 2)$ mm to take full advantage of the resonance to achieve a lower frequency absorption. The spectra of interest are chosen as 80-100Hz for the purpose of demonstration. The whole spectrum is down-sampled into 201 frequency points with a frequency step of 0.1Hz as the absorption bandwidth is very narrow at a very low frequency. For the dataset generation, numerical simulations were performed using COMSOL Multiphysics in batch mode without the graphical user interface on three servers working in parallel. The spectral response for the normal incidence is not influenced by the rotation of the structure. Hence, data augmentation is used by rotating the 2D images and keeping their spectral response constant to generate more training data. Before feeding the network, the image data, associated properties, and corresponding response are cleaned and preprocessed which is explained in the subsequent section.

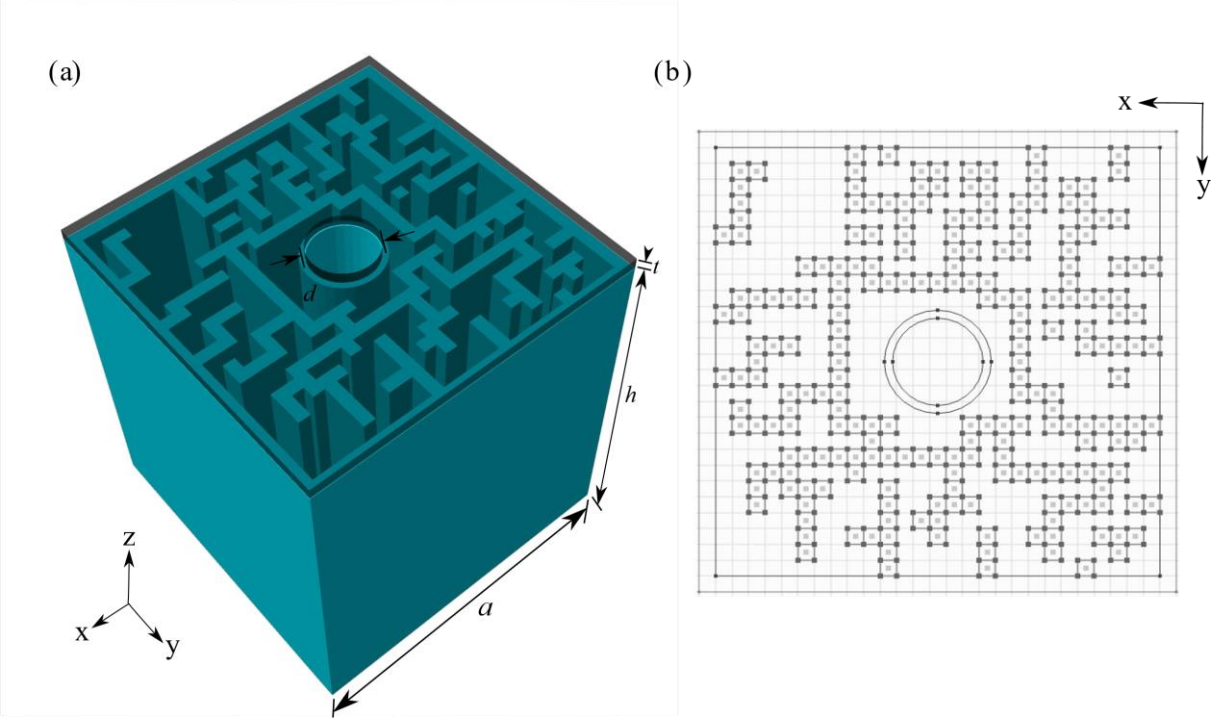

Figure-5.1 (a) Schematic of metasurface absorber (cross-area=$a \times a$ and whole thickness $h+t$) for the oblique angle incidence. The full system consists of a plate with a centered hole (diameter d) with thickness t, circular aperture, freeform propagation channel (thickness h). The perforated plate is given a transparent effect to display the details of the back chamber. (b) Top view of the system.

5.3 Data Augmentation and Preprocessing

Here, the training data is generated from the numerical simulation and the size of which is limited. As compared to the modern neural network architecture, which are in order of the millions, the training data size is very small which may result in the overfitting of the network. Thus, some data augmentation technique should be use to avoid this problem. To increase the quantity and diversity of the training data, we use the image augmentation using the rotation. This technique synthetically expands the dataset by applying various transformations on the existing training data. The convolutional neural networks trained with data augmentation can more easily adapt to different architectures compared to the weight decay and dropout [172]. For our metasurface structure, the spectral response for the normal incidence is not influenced by the rotation of the structure perpendicular to the *z*-axis. Hence, we use data augmentation by rotating the structure by random rotations, keeping the spectral response constant as shown in Fig.5.2. Here, for a given input sample x, transformed samples $T_1(x)$, $T_2(x)$, and $T_3(x)$ are shown. The output spectral response is independent of sample rotation for the normal incidence. This process not only increases the dataset size, but it also increases the diversity in the training data. Consequently, it makes the network model more robust to the input data variations.

In the next steps, the image data, associated properties, and corresponding response are cleaned and preprocessed. We save the absorption responses in the form of a '.csv' file. The top five rows of these '.csv' files are skipped while loading as they consist of non-numerical irrelevant data for our use. Also, the values in the spectral responses are converted to float values using double-precision floating-point format (also, known as FP64 or float64). All the 2D images are rescaled by dividing each pixel intensity by 255 for rescaling the pixel values from 0 to 1. In addition, we reduce the image size to 64×64 (i.e. 64 pixels as height and width). The images are converted into grayscale images to make the process computationally less expensive. Whenever we work with a color image, the image is made up of multiple pixels, each of which contains three different RGB channel values i.e. red, green, and blue. The problem with images with multiple color channels is that we have enormous amounts of data to work with, making the process computationally intensive. In our case, multiple colors in the images do not have significance, therefore we convert them into grey scale images that consist of only one channel.

As compared to total variables for our case, the training dataset is smaller, and hence to help the neural network to learn the patterns more easily, principal components analysis (PCA) is implemented using the 'scikit-learn' library. PCA is a statistical method that allows to

significantly lower the dimensionality of data without a significant loss of information in the process. It performs mean centering followed by identifying the principal components which can be used to represent the data. For our data, we use the first 20 components which explain 96.5% variance thus enabling us to reduce the dimensionality of the target from 201 to 20 i.e. 90% reduction.

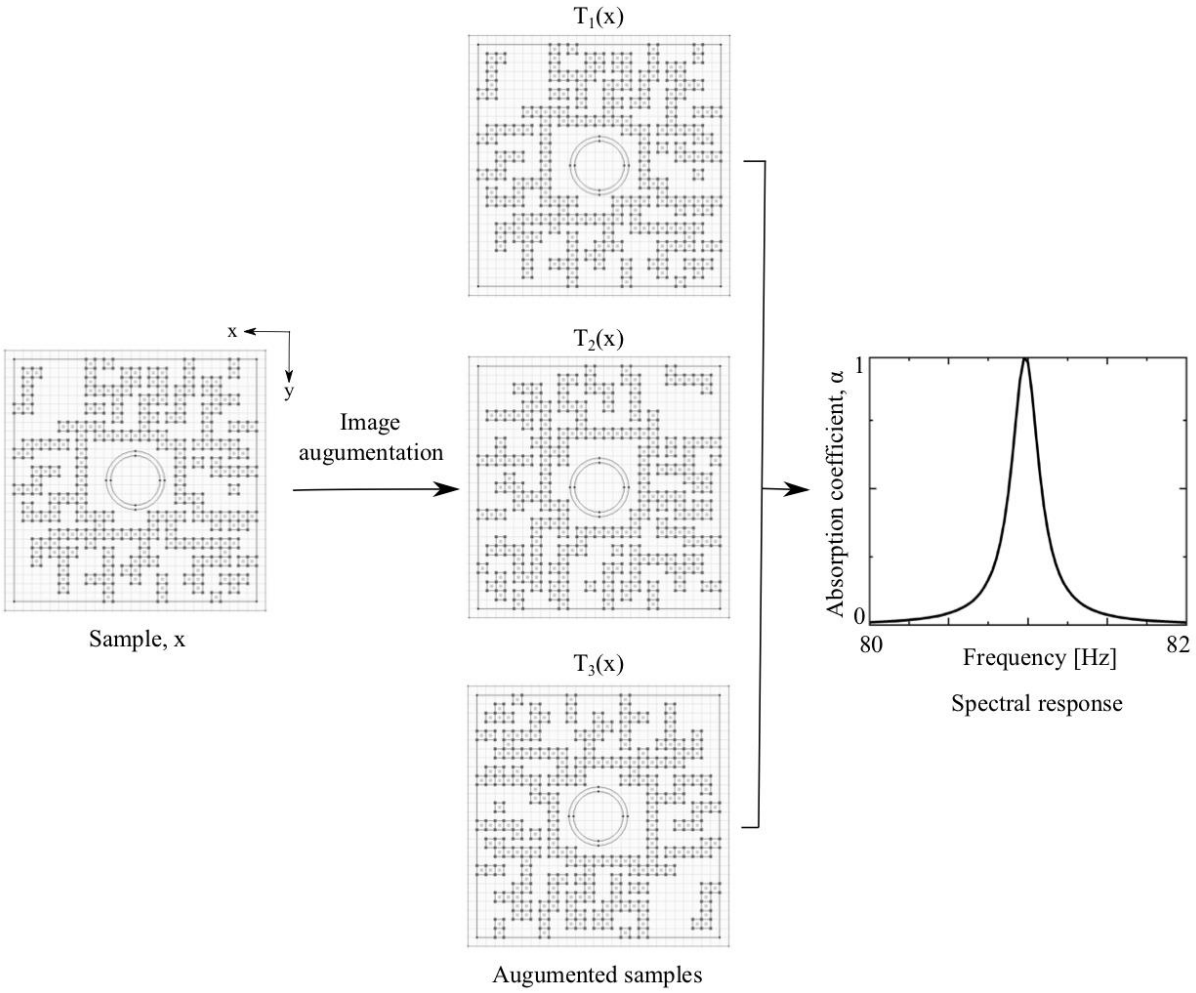

Figure 5.2- Illustration of data augmentation process for the normal incidence case. $T_1(x)$, $T_2(x)$, and $T_3(x)$ are the transformed of the sample, x.

5.4 Forward design: Convolutional Neural Network

We first construct forward neural networks based on 2D CNN architecture that aims to reveal the hidden relationship between the metasurface absorbers and corresponding spectral response and thus accurately predict absorption responses for the given metasurface design. To prove the proposed approach is not limited to certain shapes and normal incidence only, we parameterized each metasurface structure's top view (a 2D pattern that includes the propagation channel and

hole diameter), thickness, and incidence angle. Later, they are concatenated as an input to the PNN. For feeding the input data to the predicting neural network (PNN), a batch generator is used that considerably lowers the RAM requirements. For any data, it randomly picks *n* rows (*n* is the batch size), and preprocesses them following which batch input is fed to the network.

We implement two different approaches to combine metadata with the images: (1) Processing 2D image and other 1D properties independently and concatenate the results at some point followed by further processing of the combined data, (2) Adding additional information as additional channels to the image, and processing them together. This can be done by giving part or all the pixels in the additional channel the property value. In prior work on electromagnetic metasurface design, good results have been obtained using the first approach [115]. First, we have implemented such kind of forward prediction network which is discussed in section 5.4.1. However, in our case, we found that the network shows overfitting when processing both properties separately. Therefore, we propose PNN that processes both in the same network by adding 1D properties into 2D properties as additional channels which is discussed in section 5.4.2.

5.4.1 Convolutional Neural Network (Processing 1D and 2D properties separately)

Figure 5.3 shows the proposed CNN architecture with the data flow details included. The input metasurface structure is decomposed into 2D image tensors (64×64) and a 1D property tensor (1×2). Both are processed through different networks for further feature extraction. First, we pass the 1D input properties through a dense layer having 64 neurons post which is reshaped and duplicated along the axis (using tile function in TensorFlow and lambda layer). Afterward, it is passed through a convolutional layer, h_7 having 64 filters and 3 as kernel size. In this subnetwork, the input properties are processed and converted to a shape that can be concatenated with an image network output. The image subnetwork is mainly a CNN network. Here, the input image (64×64) is passed sequentially through three combinations of convolutional and max-pooling layers (h_1-h_6). The output tensors of both networks are then stacked using a concatenate layer with the dimensions of 8×8×64 and pass through a combination of a convolutional, h_8 and max-pooling layer, h_9 followed by a batch normalization. The convolutional, h_8 consists of 128 filters and 3 as kernel size. The pool size of max-pooling, h_9 is 2. The output is then flattened (layer h_{10}) and passed through a dense layer (FCL), h_{10}, having 512 neurons followed by the output layer, h_{12}. ReLU activation function is applied to

the output tensor of each layer. The output ‘ReLU’ is chosen as the activation rather than linear as we know that the responses cannot be negative.

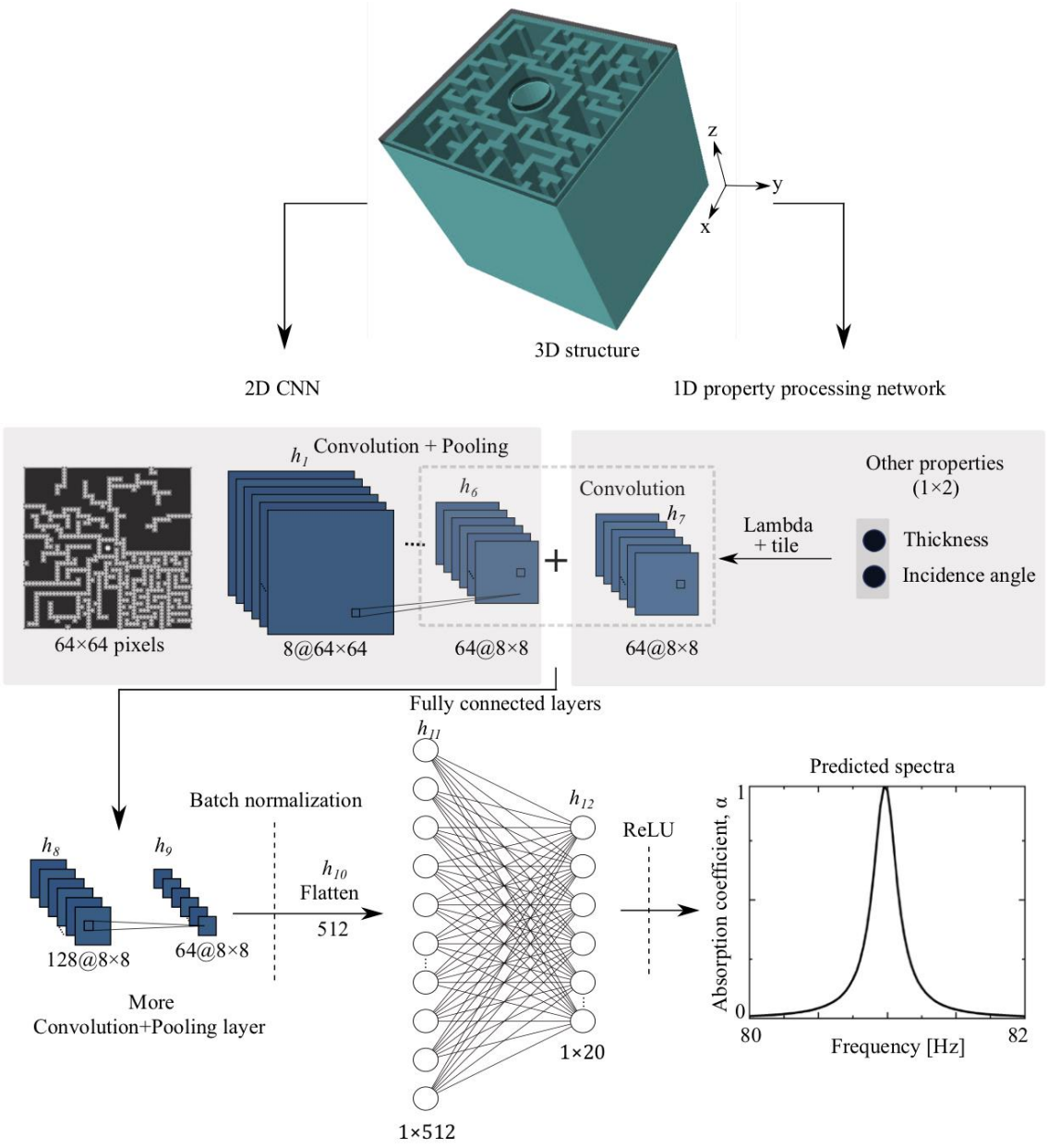

Figure 5.3- An illustration of the predicting network architecture for the metasurface absorber design for the oblique wave incidence. Design parameters are processed through separate neural networks: 2D image processing network and 1D property processing network. 2D images are processed with a set of convolutional layers and pooling layers, and then combined with the 1D design properties. Combined results are further processed with convolutional and pooling layer then flattened into a 1D array before feeding to the FCLs. After being processed, the absorption spectra over the given frequency range is ready for evaluation.

For the training process, generated datasets are split into training, validation, and test datasets. Owing to the paucity of data and the fact that the validation set is used for decision

making, 10% data is used as validation data, 2% is used as test files and the rest 88% is used as training data. Equitable distribution in all the sets ensures that the model is generalized and is not tuned to any particular class while ignoring the others. Figure 5.4 shows the learning curves for the training and validation data as a function of the epoch. It can be observed that around 40 epochs the architecture begins to overfit the training data resulting in divergence from the training loss. Overfitting occurs when a model learns the details of the training data so well that it results in poor generalization to the new unseen samples. The hyperparameters used in the training of this architecture are listed in Table 5.1.

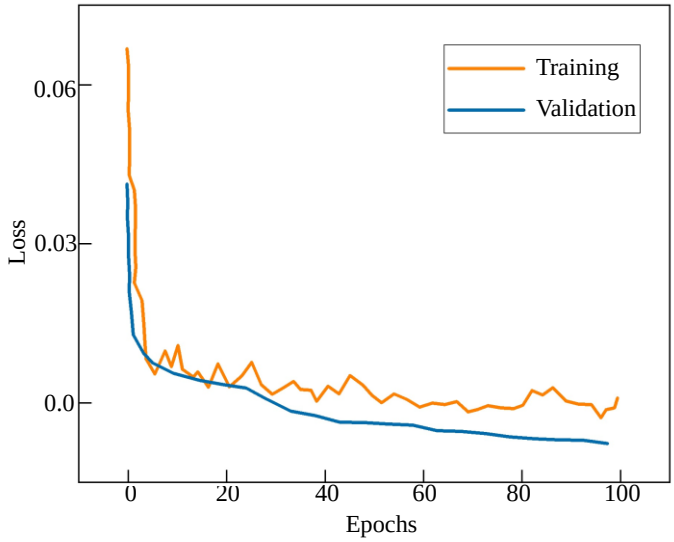

Figure 5.4 -Learning curves for training and validation datasets as a function of epochs.

Hyperparameters	Value
Optimizer	Adam
Learning rate	10^{-6}
Dropout rate	0.2
Epochs	100
Patience	200
Nonlinear activations	ReLU
Batch size (training)	64
Batch size (validation)	8
Batch Norm.	Yes
Time taken	2.5hrs

Table 5.1- Hyperparameters used in the training of the network.

5.4.2 Modified Convolutional Neural Network

To resolve the issue of overfitting of the previously implemented architecture, we propose the prediction neural network in which 1D properties are added to the 2D images and then processed together which is discussed in this section.

5.4.2.1 Network Architecture

As illustrated in Fig.5.5, 1D properties (i.e. thickness, angle of incidence) are added to the 2D images (in this case, a binary image composed of 64×64 pixels) as additional channels. i.e., each 1D property is given a size of $64 \times 64 \times 1$ and is combined with the 2D image. The combined input of size $64 \times 64 \times 3$ is then fed to the PNN.

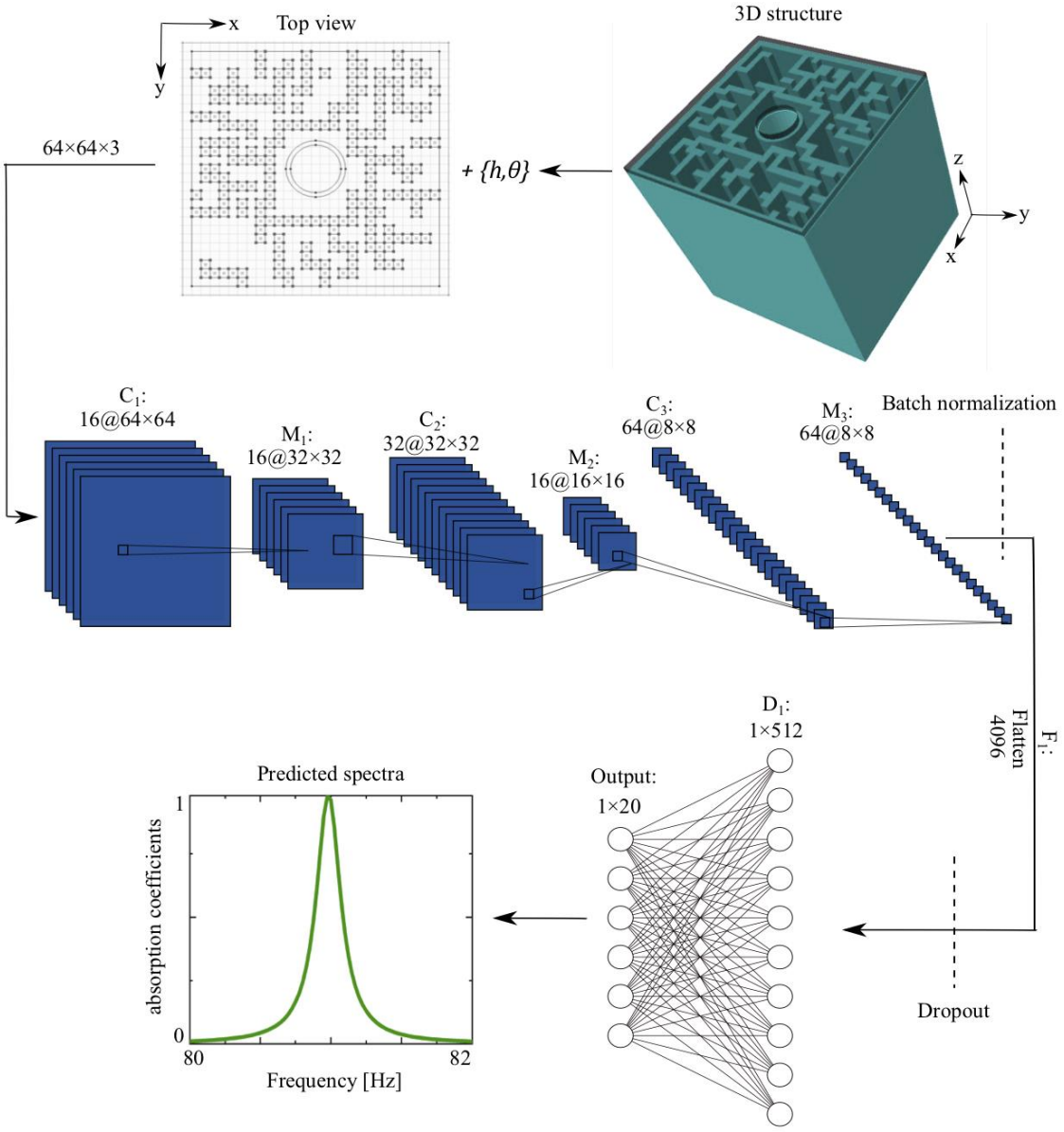

Figure 5.5- An illustration of the predicting network architecture (PNN) for the metasurface absorber design for oblique wave incidence. The input structure is divided into 1D properties and 64×64 pixels 2D images. 1D properties are added to the 2D images as additional channels and both are processed through the same network. The output of the last max-pool layer, M_3 is followed by a batch normalization layer before flattening. After being processed with two dense layers (D_1 and output), the absorption spectra are ready for evaluation.

The input is passed sequentially through three combinations of convolutional and max-pooling layers (C_1-M_1-C_2-M_2-C_3-M_3), each convolutional layer having a kernel size of 3 and max-pooling having the pool size of 2. The total number of filters used in the convolutional layers are 16, 32, and 64 respectively. The output of layer M_3 is passed through the batch normalization layer and flattened (F_1), after which it is passed through a dense layer D_1 having 512 neurons followed by the output layer with 20 neurons corresponding to components post PCA. A nonlinear activation function ReLU is applied to the output to introduce the nonlinearity. Summary of all the layers of modified CNN architecture is included in the additional documents section (Table A1).

5.4.2.2 Training Process and Result Analysis

Similar to the first network, generated datasets are split into training, validation, and test datasets, with 88% are used during the training process, 10% for the validation, and the remaining 2% are used to evaluate the trained network. After finalizing the architecture through a series of experiments (modifying the number of neurons in each layer along with the depth of the network), selected hyperparameters are tuned to further improve the performance of the model. A batch size of 32 is used for the training data and a batch size of is used for the validation data. To determine the optimum number of epochs, ModelCheckpoint callback is used which saves the model weights for the best performing model using the validation loss as the basis. A sufficiently large number of epochs are used (500) relying on the callback to store the weights for the best performing model. Also, ReduceLROnPlateau callback is used to reduce the learning rate in case the validation loss doesn't improve further. A patience value of 20 is used i.e. after 20 epochs if the loss doesn't reduce the learning rate is reduced by a factor of 0.8. To reduce overfitting, the dropout value is used in both architectures. The fraction is determined based on experiments using validation loss as the criterion. Figure 5.6 shows the learning curves (for the training and validation data), as a function of epochs. During the training phase, both the training and validation errors decreased and converged after 500 epochs. When the training was completed, the average MSE was 0.00904 for the predicted absorption

coefficients in the validation data. During the training process, the weights are continuously optimized to minimize the validation loss. The hyperparameters used in the training are given in Table 5.2.

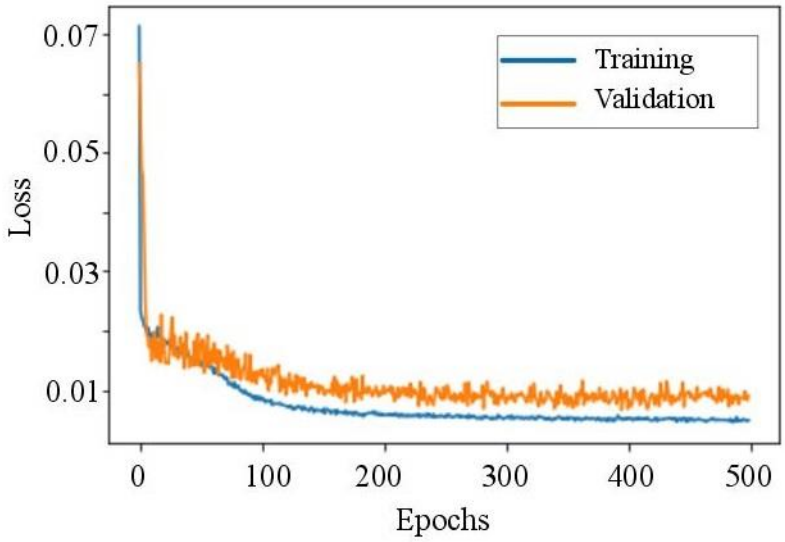

Figure 5.6- Learning curves of PNN for training and validation datasets as a function of epochs.

Hyperparameters	Values
Optimizer	Adam
Learning rate	10^{-4}
Dropout rate	0.5
Epochs	500
Nonlinear activations	ReLU
Patience	20
Batch size (training)	32
Batch size (validation)	8
Batch Norm.	Yes
Error (training)	0.018
Error (validation)	0.009
Time taken	8hrs

Table 5.2- Hyperparameters used in the training of PNN.

We then calculate the predicted spectra and compare the results to numerical simulations to extract the prediction error. The default mean squared error loss defined in the TensorFlow library is modified to give the loss value considering the column index in the data. PCA components for target data (after transforming the acoustic responses) are ordered in terms of

explained variances i.e. 1st column explains the most variance in the data and so on. Hence, the loss function is modified to similarly give more weightage to the columns with the lower index values. To check the prediction accuracy of the trained model, we have evaluated it on the test dataset. Figure 5.7 (a)-(f) displays the example of some best fits in order to show the capability of the network. The result comparison is shown for two different metasurface structures with different shapes of the propagation channel (inset in plot (a) and (d)). For both cases, the results are shown for three different angles of incidence. For each case, the mean square error is listed in the inset. As indicated by the MSE, the absorption spectra predicted by the PNN (red dashed curves) agreed well with the FEM simulations (blue curves) for the variety of different propagation channels and different incidence angles. It can be observed that the resonance frequency is nearly unchanged. The absorption for both the structure is about 86% at θ=60° which shows overall good performance at large angles incidence. Figure 5.7(a) shows the resonance at 82Hz with the thickness of 65mm ($\lambda/64$). The thickness can be further optimized by adjusting the lateral dimensions.

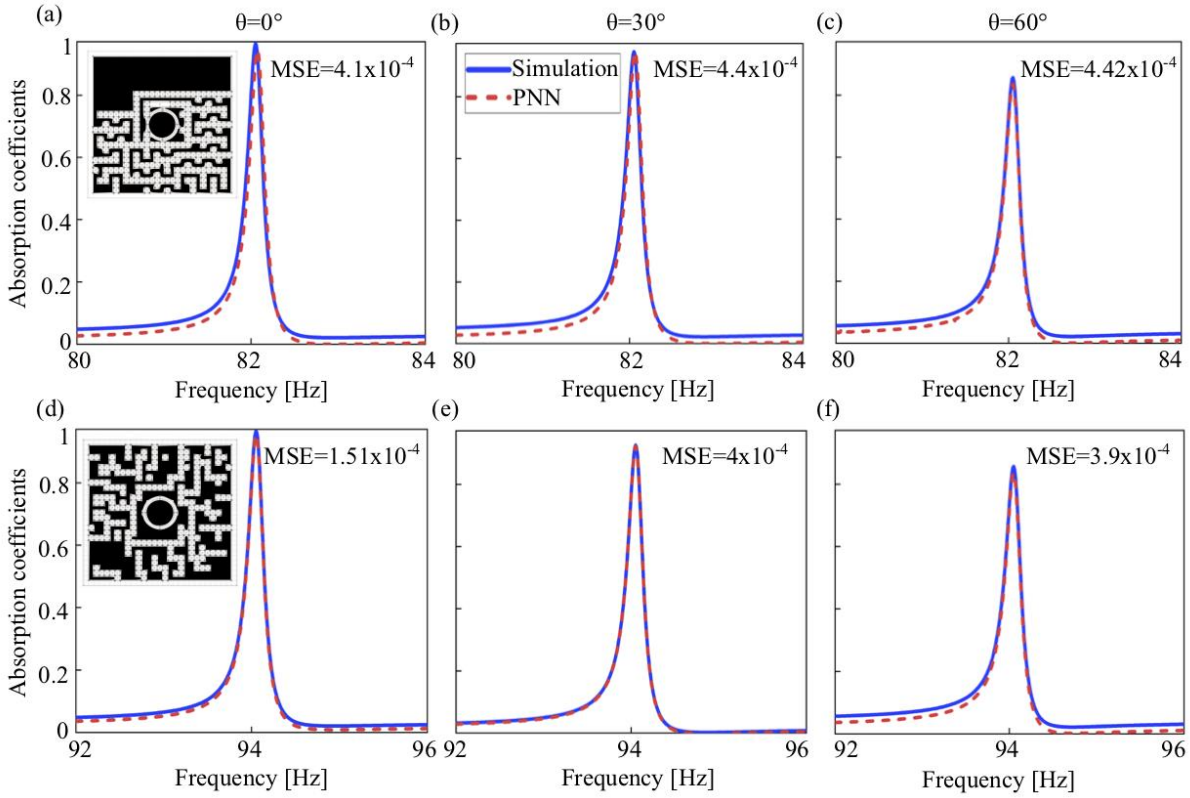

Figure 5.7- 5(a)-(f) Comparison of PNN predicted absorption spectra (red dashed curves) with the simulated one (blue curves) for two different example metasurface structures with different shapes of the propogation channel (inset in plot (b) and (d)). For each example, the comparison is shown 0°, 30°, and 60°. MSE of each case is included as insets.

5.4.2.3 Ablation Analysis

A deep learning network has a multitude of elements which when modified give very different results. Ablation analysis is carried out to understand the impact major configuration changes have on the performance of the network by modifying only one parameter at a time. In our experiments, to justify the usage of batch normalization layer, and flatten layer. During training, we construct four different network configurations each having one configuration modified or removed. The training is carried out for 500 epochs for each network configuration and mean absolute error is used as the metric. The mean absolute error is calculated for the unseen data or the test set during training the network for each epoch to compare the performance of the different configurations.

As evident in Fig.5.8, the chosen network configuration offers the best performance in terms of faster convergence and the mean absolute error during training. Using Flatten layer (to convert 4d tensor to 2d tensor and feed to subsequent fully connected layers for prediction) instead of Global Average pooling offers a significantly better performance both in terms of error rate and stability during training. Though the time taken per epoch is significantly lower for the global average pooling layer but the performance deficit is huge and thus the flatten layer is used in the final network configuration. Without batch normalization, it can be observed that convergence is much slower as compared to the network architecture with batch normalization.

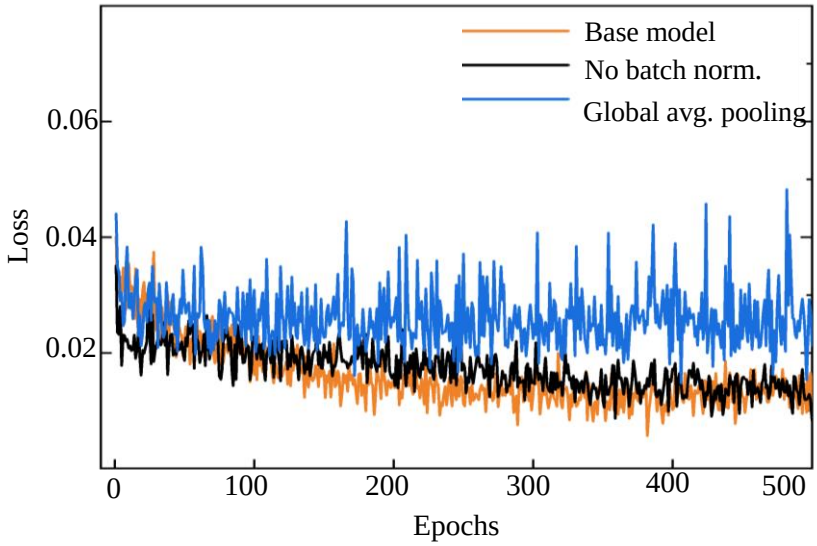

Figure 5.8- Ablation analysis with three different network configurations.

5.5 Inverse Design: Conditional Generative Adversarial Network

Practical applications of the metasurface absorber demand the perfect absorption at a particular frequency or frequency range which needs to generate design parameters to produce the desired absorption response using the inverse design. Once properly trained, the inverse network should be able to unearth the best possible metasurface absorber pattern that yields absorption spectra with minimum deviation from the input spectra. The development of such inverse design using deep neural networks significantly reduces the computational time for design optimization.

5.5.1 Network Architecture

To realize the inverse design, we have constructed the network architecture based on conditional GAN as shown in Fig.5.9(a). The aim of this network is to predict the metasurface structure for the prescribed absorption spectra and the thickness for the given incidence angle, θ. The network is divided into two parts: a generator (G) and a discriminator (D). Both are convolutional neural networks with delicate differences in their detailed architecture. The generator is conditioned to produce images of new structures as a function of angle of incidence, thickness, and desired absorption spectra. The inputs to the generator are the incidence angle θ, thickness h, desired absorption spectra A, and latent input space, z. Before feeding to the generator, the inputs are concatenated and passed through the dense layer for reshaping. The detailed architecture of the generator is shown in Fig.5.9(b). The reshaped input is passed through four transpose convolutional layers CT_1, CT_2, CT_3, CT_4 with varying numbers of filters 128,32,16,1 and strides of 2,2,1,1 respectively. Such layers can be understood as the opposite of a pooling layer i.e. it increases the dimensions of the input and performs convolution after that to learn appropriate weights. Nonlinear activation function ReLU is applied after each the output of layers CT_1, CT_2, CT_3, and sigmoid activation function is applied at the output of the layer CT_4. A sigmoid activation is appropriate at the output of the layer as we want the discriminator's output to be 1 or 0. Summary of all the layers in the Generator architecture is listed in the additional document section (Table A2).

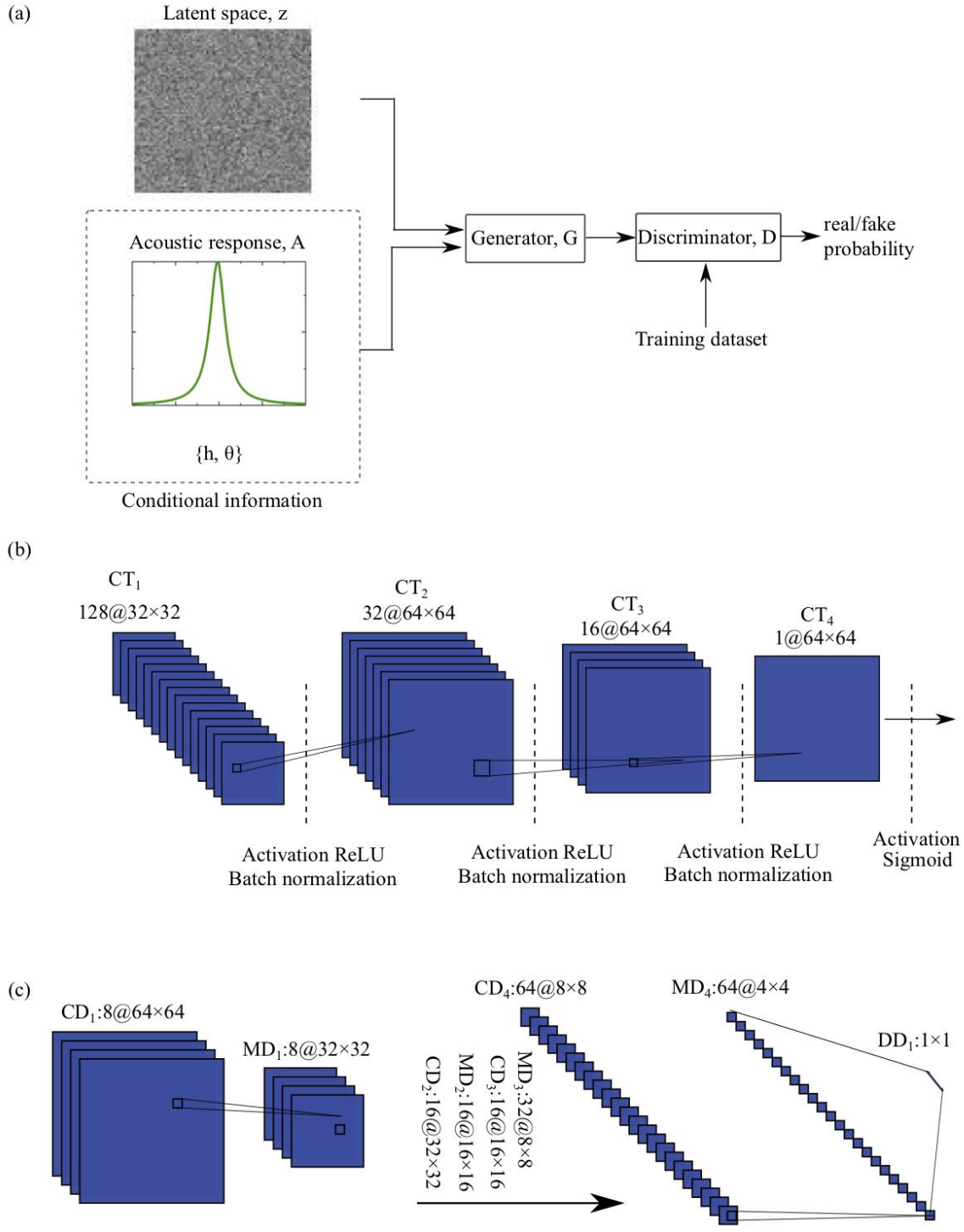

Figure 5.9: An illustration of the conditional generative adversarial network for the inverse metasurface absorber design for oblique wave incidence. (a) Schematic of the implemented network. (b) Detailed structure of the Generator (G). (c) Detailed structure of the Discriminator (D).

The input to the discriminator is the absorption spectra, the associated properties and the images generated by the generator. Before feeding to the discriminator, the absorption spectra and the properties are passed through dense layers individually and reshaped as an

additional channel for the 2D image. These label inputs (absorption spectra and properties) are then concatenated with the image and passed through the first layer of the discriminator. Our discriminator model is a convolutional neural network consisting of four convolutional layers CD_1, CD_2, CD_3, and CD_4 with the kernel size of 3 as shown in Fig.5.9(c). Each convolutional layer uses 8, 16, 32, and 64 filters respectively with the stride of 1. Here, each convolutional layer is followed by a max pool layer (M_1, M_2, M_3, M_4) with the pooling size 2. We applied LeakyRELU activation functions in the layers of the discriminator network except for the final layer which is activated by a sigmoid function. The output of the last max-pool layer, M_4 is flattened and fed to a fully connected layer having 1 neuron to generate the output i.e. 0 - image is fake, 1 - image is real. To prevent the networks from overfitting, a dropout layer is used in both the architectures. Latent space, used as an input to the generator, comprises the number (latent size) of randomly chosen values between -1 to 1. Summary of all the layers in the Discriminator architecture is listed in the additional document section (Table A3). The discriminator, which is a classification network, learns to distinguish between image samples that come from the training dataset and those that come from the generator. It accepts both the 2D images from the training dataset and the images generated from the generator.

5.5.2 Training Process and Result Analysis

The generator and discriminator are trained alternately by competing against each other during the training process. As a result, both networks improve their predictions until the related counterpart can no longer recognize the proposed data. The training process of the whole network for the one epoch can be explained as follows. To begin the training process, a small subset of the dataset, known as a batch, is created. It includes the latent space, the absorption spectra and other properties from the training set. The generator creates the corresponding images based on the information in the batch. One thing to keep in mind is that because the inputs come from the randomized latent space, the early image generations are likely to be extremely noisy. Also, the generator network parameters (weights and biases) are randomly initialized. Next, the same number of 2D structure images and corresponding absorption spectra are chosen from the training dataset. This selection is then mixed with the generator's predictions while keeping the labels to identify the source of data. Using this mixed subset, the discriminator learns to distinguish between images predicted by the generator and images from the training dataset. When the discriminator's output predicts either "fake" for a generator input (fake $\widehat{=}$ 0) or "real" for a training dataset input (real $\widehat{=}$ 1), it is considered true. The

discriminator's parameters are updated and frozen after this step. This is critical because the discriminator has already been trained for the current epoch, and the generator's training phase should not affect its parameters. Both the generator and discriminator are trained using the binary cross entropy loss which can be given by,

$$E = -\frac{1}{N}\sum_{k=1}^{N} y_k \cdot \log(p(y_k)) + (1 - y_k) \cdot \log\big(1 - p(y_k)\big) \tag{5.1}$$

where y_k is the label and $p(y_k)$ is the predicted probability of for all N points. Once the training of the GAN is completed, the trained generator network is extracted from it. The generator expects a prescribed absorption spectra, thickness, and angle of incidence as its input. Based on the desired input characteristics, appropriate metasurface absorber structure can be tailored by the generator network. Table 5.3 shows the optimized hyperparameters of CGAN network.

Hyperparameters	**Values**
Optimizer	Adam
Latent size	100
Batch size	64
Learning rate	10^{-4}
Decay	6×10^{-8}
Training steps	20,000

Table 5.3- Hyperparameters used in the training of CGAN.

As a demonstration of the proposed framework's overall competence, we use the absorption spectra, *A*, and other properties; thickness *h*, and angle of incidence θ, randomly selected from the test data as input and ask the network to look for proper metasurface patterns based on these spectra. We denote this test set as *s*, the absorption spectra of each s as A. Once these spectra and other properties passed through the network, a 2D pattern is retrieved which is denoted by s'. To verify the result, we simulate the generated set s′ in COMSOL Multiphysics and denote the output spectra as A′. In Fig.5.10(a), the first row shows the sample from the test data, s and the second row show the corresponding samples s′ generated by the CGAN. Each pair in two rows matches very well. Figure 5.10(b)-(d) show some best fits in order to demonstrates the capability of the network. Target designs of various metasurface absorbers and the corresponding suggested designs show good agreement.

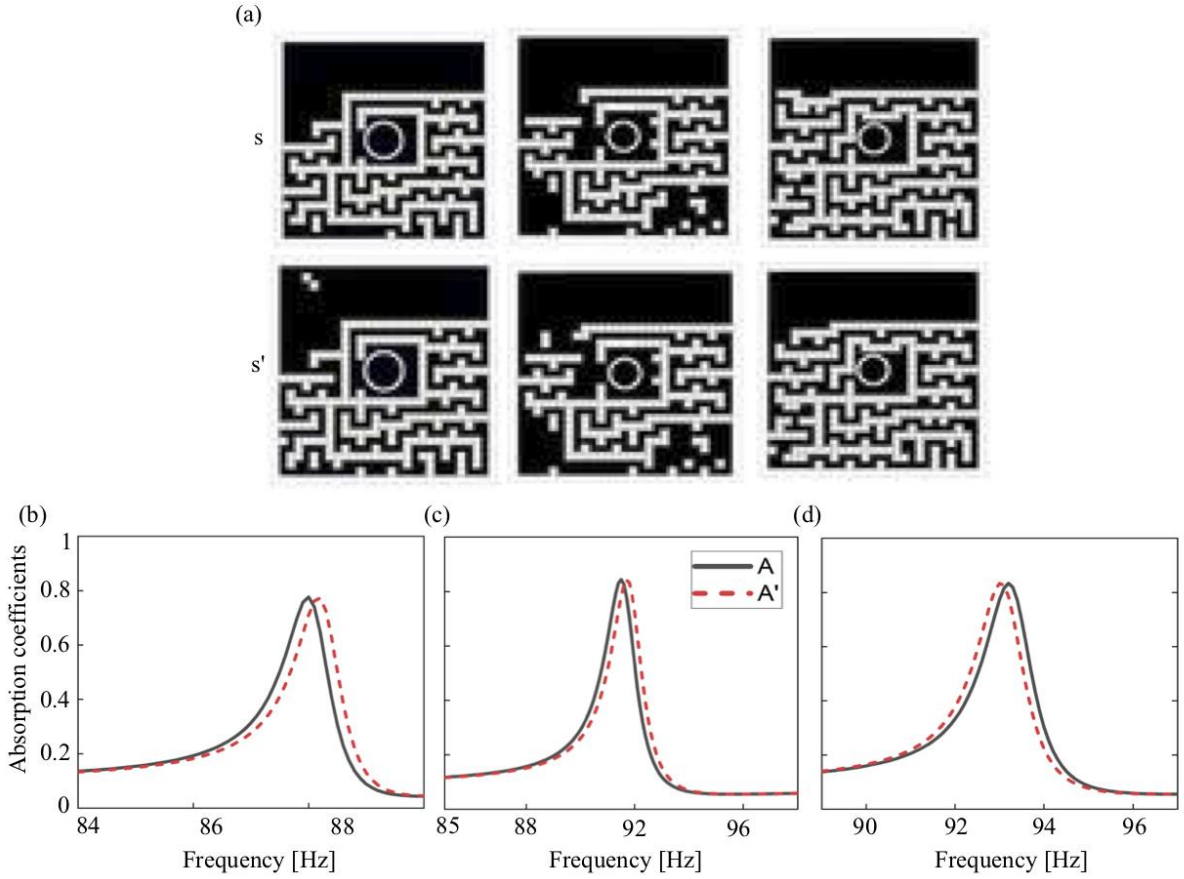

Figure 5.10- (a) 2D patterns s from the test dataset are shown in the top row and the corresponding generated patterns by CGAN are shown in the second row. (b)-(d) Comparison of the absorption spectra, A from the test set (black curve) and FEM simulated absorption spectra, A′ of the retrieved pattern s′ shown in the second row.

5.6 Acoustic Absorption Measurements

In most cases in acoustic, absorption coefficients are measured in reverberation rooms (ISO 354) [173] or using the impedance tubes according to ISO 10534 [101]. Because these methods are only useful for measuring the random or normal incidence absorption coefficients, there is a growing demand for absorption coefficient measurement techniques of finite absorbers at oblique incidence. With the assumption of the diffused sound field, the room method is based on the reverberation time measurements and it is only appropriate for describing absorber properties in the case of random sound incidence. Due to the so-called edge diffraction effect, the absorption coefficient determined by the chamber method can surpass unity for the finite-sized samples [174]. To carry out the absorption measurement, we consider the adaption of the classical impedance tube. Such an experimental system was theoretically and numerically studied to determine the transmission loss of materials under oblique wave incidence [175].

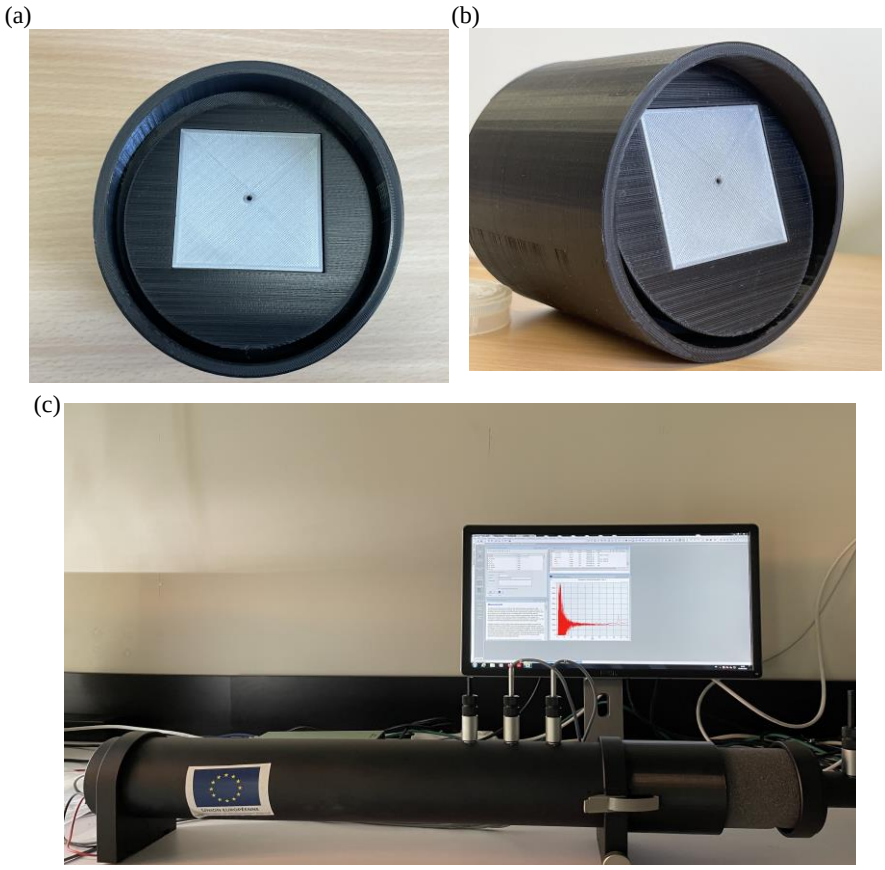

Figure 5.11- (a)-(b) Photographs of the designed sample holder. (c) Experimental setup for measuring absorption using the two-microphone method.

The sample (lateral dimension=58mm×58mm) under the consideration is designed to have the resonance at 96Hz at an incidence angle of a 15degree. For the measurement, we fabricate a holder using 3D printing to fix the sample at 15degree angle as shown in Fig. 5.11(a)-(b). The outer dimension of the holder is kept such that the holder can be fixed with the opening of the impedance tube. The absorption coefficient is measured with the impedance tube from Bruel & Kjaer using a fitting connection from the fabricated holder to the circular shape of the impedance tube as shown in Fig 5.11(c). The experimental and numerically simulated absorption curves are plotted in Fig.5.12. It can be observed that the resonance is achieved at the same frequency as in numerical simulation but, the absorption performance is not good. This may arise due to the imperfect sound insulation. Also, the size of the sample is much smaller than the tube. This difference may lead to lower absorption because of the acoustic impedance mismatch.

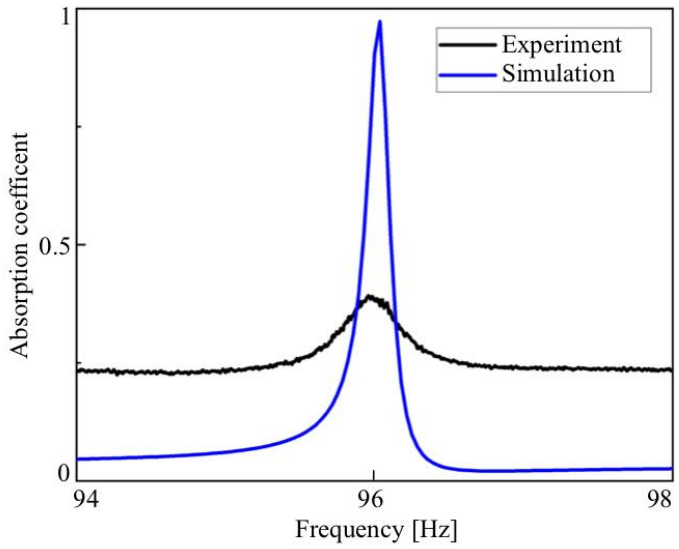

Figure 5.12- Comparison of the absorption coefficients obtained via numerical simulation and experiment.

5.7 Conclusions

In this work, a deep neural network based metasurface absorber designing approach for the oblique wave incidence is proposed and demonstrated. In particular, we implement CNN and CGAN for accurate forward and inverse design respectively. Compared to the previous work, our approach can handle a large set of input parameters, including 2D patterns that include free-form propagation channel and hole diameter, and other properties like thickness and angle of incidence for the complex metasurface absorber structure. Accurate absorption spectrum responses of metasurface absorbers were derived using a 2D CNN-based network structure in the timescale of milliseconds, which is over four orders of magnitude faster than conventional FEM simulation software. Using the presented CNN approach, we have demonstrated a metasurface absorber having nearly omnidirectional absorption at 82Hz with a thickness of $\lambda/64$. Using the proposed metasurface absorber structure, about 86% absorption is achieved at θ=60° which shows overall good performance at large angles incidence. We have further implemented conditional GAN which can be adapted for the designing metasurfaces with prescribed absorption spectra. The proposed deep learning approaches can be generically utilized for fast and accurate modeling and design process of the complex physical systems with minimum human intervention. We envision widespread and increasing use of deep learning technology in the field of physics, allowing scientists and engineers to focus more on truly

creative ideas to solve the complex design problems that have yet to be explored by the machine, rather than on tedious trial and error processes.

General Conclusions and Perspectives

In this dissertation, we developed acoustic metasurface absorbers for extreme low frequencies (<100Hz). We first introduced a multicoiled metasurface absorber design via numerical, theoretical, and experimental approaches. Next, we presented the development of deep-learning-based strategies for the simulation and inverse design of acoustic metasurface absorbers. For the forward design of acoustic metasurface absorbers, we proposed convolutional neural networks. Such kind of deep learning network takes benefit of local spatial coherence which makes them highly efficient to extract the relevant information from the input structures with low computational cost. Then, we implemented a generative model based on the conditional generative adversarial network for the inverse design for oblique wave incidence. Based on the input customer-defined absorption spectra, the CGAN can predict the optimal metasurface absorber structure in a fast way.

More relevant literature on acoustic metamaterials, acoustic metasurfaces, specifically for the low-frequency absorption have been sufficiently reviewed in chapter 1. Moreover, the fundamental of acoustics is outlined to support the explanation of the thermoviscous loss mechanisms. Chapter 2 presents a detailed overview of the methodologies used throughout the thesis. A detailed explanation of deep learning strategies implemented in this dissertation and related state of art is also included.

An acoustic metasurface absorber based on the multicoiled structure has been proposed and analyzed in chapter 3. The proposed MCM structure is composed of a perforated plate, a coplanar coiled chamber with an aperture, and labyrinthine passages. This design offers two advantages; first, it uses the space inside the coiling channel, and second, the aperture and labyrinthine passages offer an extra degree of freedom which helps to shift the resonance towards extreme low-frequency. We implemented this concept using numerical simulation and theoretical method using an equivalent circuit model. The perfect absorption was achieved at extreme low-frequency of 50Hz with a metasurface design simultaneously featuring an ultrathin thickness down to $\lambda/527$ (1.3cm). The total propagation path is about $\lambda/4.7$ which indicates that the underlying physical mechanism of the MCM is not based on the classical quarter wavelength concept, it is instead based on the hybrid resonance of the coiling up geometries and the resonance due to cavities between the labyrinthine passages. The implemented structure

solves the key limitation of previous works on the coiling up structure in which the resonant frequency is restricted to a quarter wavelength making it difficult to realize the full absorption at a target frequency. Regarding the experiments, we fabricated the sample using 3D printer in our lab and measured the absorption coefficients using the two-microphone method. The absorption coefficients obtained by experimental measurement present an excellent agreement with the analytical and numerical results. Further, we implemented the supercell approach to achieve broadband performance. The tunable performance of the circular aperture shows a promising prospect to realize broadband performance using the supercell approach. This can be achieved either by changing the height or by changing the diameter of the aperture. We designed a supercell by coupling 9-unit cells with different diameters and resonating at different frequencies. Using this approach, an absorption higher than 90% was achieved for the given frequency range. However, achieving simultaneously broad bandwidth and thin metasurface is contradictory. Current bandwidth can be further improved by increasing the thickness of the structure.

In chapter 4, we implemented a deep learning-based metasurface absorber modeling approach which significantly reduces the characterization time while maintaining high accuracy. The metasurface absorber structure under the consideration consists of a perforated plate and free-form propagation channel. Based on the convolutional neural network, proposed networks can simulate the metasurface absorber structure with a nearly freeform propagation channel in the time scale of milliseconds. We kept the other geometrical parameters constant as ample samples can be generated by tuning the length of the propagation channel only to have absorption resonance in the given frequency range. The performance of the implemented CNN was compared with three classical machine learning techniques (KNN, SVM, RF). The accuracy metric is used to estimate the effectiveness of the model to predict the absorption coefficient with a certain precision. The 2D CNN outperformed the machine learning methods with 86% accuracy which shows the efficacy of deep learning methods as compared to the classical machine learning techniques to build complex input-output relationships. Using the 2D CNN, an ultrathin metasurface absorber is simulated having perfect absorption at extremely low 38.6Hz with the ultrathin thickness down to $\lambda/684$ (1.3cm) which is the thinnest achieved absorbing acoustic metasurface ever. Further, the network predictions were validated by the experimental measurements which demonstrate the effectiveness of the implemented approach. The presented CNN model can be trained with other geometrical parameters by adding a merging layer or averaging after the input layer. Such kind of deep learning network has been

implemented and discussed in chapter 5 to design metasurface absorbers with high degrees of freedom.

For designing acoustic metasurface absorbers for the oblique wave incidence, we proposed forward and inverse design framework using the 2D convolutional neural network and conditional generative neural network, respectively, as we reported in chapter 5. The inverse design can be understood as generating the acoustic structure for the desired absorption spectra given in the input. The metasurface structure under consideration is composed of a perforated plate, circular aperture, and a cavity with a free-form propagation channel. In our research, we represented the structure in 2D binary images along with other one-dimensional properties like the height of the structure and the angle of incidence. However, simply feeding data to the deep learning networks led to the overfitting issue due to a large number of parameters of the network architectures. To alleviate this problem, we augmented the data through rotation of the 2D patterns to increase the diversity in the training dataset. Rotating the 2D structure patterns does not affect the acoustic response for the case of the normal wave incidence. Using this approach, we essentially generated a significantly large number of the training data, and thus greatly reduced the overfitting issue. For the forward design, we implemented two different approaches. In the first approach, 2D and 1D properties are processed through two separate networks and later combined and passed through the rest of the network. However, it has shown network overfitting issue in our case. In the second approach, both properties were combined in the same network by adding 1D properties into 2D properties as additional channels. Using the presented 2D CNN, we have demonstrated a metasurface absorber having nearly omnidirectional absorption at 82Hz with a thickness of $\lambda/64$. For the given metasurface absorber structure, about 86% absorption is achieved at θ=60° which shows overall good performance at large angles of incidence. When the DOFs of the acoustic structures are large, it may be difficult to obtain a solution using the traditional optimization approaches as it may be stuck in local minima or may not converge at all. In this case, it is required to find an alternative encoding approach that can represent the structure in a continuous space. In our case, we used CGAN to encode the input 2D binary images and one-dimensional properties which represent the metasurface absorber structure into a low-dimensional latent space. The implemented CGAN includes two components- a generator and a discriminator. The generator produces candidates of the metasurface structure, while the discriminator guides the generator to yield a metasurface structure that satisfies the design objective. Using the CGAN,

metasurface absorber structures that are not in the dataset were generated according to the prescribed absorption spectra in the input.

Challenges and Future Perspective

In the past few years, many promising schemes have been proposed and implemented to design efficient acoustic metasurface for very low-frequency absorption. Various concepts have been developed to design such metasurfaces with simple structures and deep subwavelength thickness. Despite significant advancement in this field, there are remaining many challenges. The main issue is the narrow bandwidth specially design the metasurface absorbers below 100Hz. To improve their performance over the broad bandwidth, the supercell approach is used consisting of many unit cells with different working frequencies. However, this approach increases the size of the overall design and defeats the purpose of acoustic metasurfaces. It is even more challenging to achieve omnidirectional performance with broadband absorption response.To design the compact acoustic absorbing metasurface that can operate over broadband, new design principles are required to develop.

Recently, machine learning has gained a tremendous amount of attention due to its potential to design and solve complex physical systems accurately with minimum human intervention. However, deep learning approaches require a large amount of training data to understand the latent patterns of data as compared to the classical machine learning techniques. For designing the complex acoustics devices, the generation of the training dataset is usually dependent on the numerical simulations which leads to a substantial computational burden. It is extremely challenging to generate high-quality annotated data on a large scale using numerical simulations. This is a major concern especially for the low-frequency three-dimensional (3D) acoustic calculations because, at low frequencies, the narrow bandwidth requires sufficiently high resolution to sweep the frequencies for accurate calculations which is a time-consuming process. This becomes even more challenging when designing large structures, for example, acoustic metasurface absorbers for broadband design. The tradeoff between the size of the training dataset and the model accuracy is a critical factor to be considered. This problem can be partly solved by incorporating transfer learning or data augmentation techniques. Recently, many methods have been investigated to mitigate data dependency. For example, by combining advanced machine learning algorithms with the physical methods, the prediction accuracy can be improved with a small dataset. Also, as

proposed for the photonics devices, an effective way to accelerate the deep-learning-driven acoustic design process is to generate the large and versatile dataset collectively with the effort of the acoustic community. The established dataset for various acoustic designs could eliminate the need for repeated data generation processes and shorten the implementation cycle of new deep learning models. Using recent advancements in transfer learning approaches, such a large and generic dataset can prove beneficial for any acoustic design in low dataset scenarios. Because of the strict geometric and physical constraints, acoustic designs in modern applications are heavily reliant on numerical simulations and optimization algorithms nowadays. We anticipate that the progressive incorporation of state-of-the-art deep learning approaches should bring the performance closer to the limit bound by physics. Such approaches in combination with traditional methods should significantly accelerate the discovery and development of advanced acoustic metasurface devices.

References

[1] C. Shi, *Acoustic Metamaterials and The Angular Momentum of Sound*, 136 (n.d.).

[2] N. I. Zheludev, *The Road Ahead for Metamaterials APPLIED PHYSICS*.

[3] V. M. Shalaev, *Optical Negative-Index Metamaterials*, Nat. Photonics **1**, 41 (2007).

[4] M. Caleap and B. W. Drinkwater, *Metamaterials: Supra-Classical Dynamic Homogenization*, New J. Phys. **17**, (2015).

[5] A. Elayouch, M. Addouche, and A. Khelif, *Extensive Tailorability of Sound Absorption Using Acoustic Metamaterials*, J. Appl. Phys. **124**, 155103 (2018).

[6] E. Yablonovitch, *Inhibited Spontaneous Emission in Solid-State Physics and Electronics*, Phys. Rev. Lett. **58**, 2059 (1987).

[7] M. I. Hussein, M. J. Leamy, and M. Ruzzene, *Dynamics of Phononic Materials and Structures: Historical Origins, Recent Progress, and Future Outlook*, Appl. Mech. Rev. **66**, (2014).

[8] MA, Guancong et SHENG, Ping. Acoustic metamaterials: From local resonances to broad horizons. *Science advances*, vol. 2, **2**, p. e1501595, (2016).

[9] S. H. Lee, C. M. Park, Y. M. Seo, Z. G. Wang, and C. K. Kim, *Acoustic Metamaterial with Negative Density*, Phys. Lett. A **373**, 4464 (2009).

[10] S. A. Cummer, J. Christensen, and A. Alù, *Controlling Sound with Acoustic Metamaterials*, Nat. Rev. Mater. **1**, 1 (2016).

[11] H. H. Huang, C. T. Sun, and G. L. Huang, *On the Negative Effective Mass Density in Acoustic Metamaterials*, Int. J. Eng. Sci. **47**, 610 (2009).

[12] J. Mei, G. Ma, M. Yang, Z. Yang, W. Wen, and P. Sheng, *Dark Acoustic Metamaterials as Super Absorbers for Low-Frequency Sound*, Nat. Commun. **3**, 756 (2012).

[13] C. Liu, J. Luo, and Y. Lai, *Acoustic Metamaterials with Broadband and Wide-Angle Impedance Matching*, Phys. Rev. Mater. **2**, 045201 (2018).

[14] M.-H. Lu, L. Feng, and Y.-F. Chen, *Phononic Crystals and Acoustic Metamaterials*, Mater. Today **12**, 34 (2009).

[15] L. Fok, M. Ambati, and X. Zhang, *Acoustic Metamaterials*, MRS Bull. **33**, 931 (2008).

[16] F. Zangeneh-Nejad and R. Fleury, *Active Times for Acoustic Metamaterials*, Rev. Phys. **4**, 100031 (2019).

[17] P. M. Morse and K. U. Ingard, *Theoretical Acoustics* (Princeton University Press, 1986).

[18] Z. Liu, X. Zhang, Y. Mao, Y. Y. Zhu, Z. Yang, C. T. Chan, and P. Sheng, *Locally Resonant Sonic Materials*, Science **289**, 1734 (2000).

[19] Z. Yang, J. Mei, M. Yang, N. H. Chan, and P. Sheng, *Membrane-Type Acoustic Metamaterial with Negative Dynamic Mass*, Phys. Rev. Lett. **101**, 204301 (2008).

[20] J. Christensen, Z. Liang, and M. Willatzen, *Metadevices for the Confinement of Sound and Broadband Double-Negativity Behavior*, Phys. Rev. B **88**, 100301 (2013).

[21] J. Christensen, L. Martín-Moreno, and F. J. García-Vidal, *All-Angle Blockage of Sound by an Acoustic Double-Fishnet Metamaterial*, Appl. Phys. Lett. **97**, 134106 (2010).

[22] J. Li, K. H. Fung, Z. Y. Liu, P. Sheng, and C. T. Chan, *Generalizing the Concept of Negative Medium to Acoustic Waves*, in *Physics of Negative Refraction and Negative Index Materials: Optical and Electronic Aspects and Diversified Approaches*, edited by C. M. Krowne and Y. Zhang (Springer, Berlin, Heidelberg, 2007), pp. 183–215.

[23] Z. Liang and J. Li, *Extreme Acoustic Metamaterial by Coiling Up Space*, Phys. Rev. Lett. **108**, 114301 (2012).

[24] Y. Xie, B.-I. Popa, L. Zigoneanu, and S. A. Cummer, *Measurement of a Broadband Negative Index with Space-Coiling Acoustic Metamaterials*, Phys. Rev. Lett. **110**, 175501 (2013).

[25] Z. Liang, T. Feng, S. Lok, F. Liu, K. B. Ng, C. H. Chan, J. Wang, S. Han, S. Lee, and J. Li, *Space-Coiling Metamaterials with Double Negativity and Conical Dispersion*, Sci. Rep. **3**, 1614 (2013).

[26] J. Christensen and F. J. G. de Abajo, *Anisotropic Metamaterials for Full Control of Acoustic Waves*, Phys. Rev. Lett. **108**, 124301 (2012).

[27] V. M. García-Chocano, J. Christensen, and J. Sánchez-Dehesa, *Negative Refraction and Energy Funneling by Hyperbolic Materials: An Experimental Demonstration in Acoustics*, Phys. Rev. Lett. **112**, 144301 (2014).

[28] S. Guenneau, A. Movchan, G. Pétursson, and S. A. Ramakrishna, *Acoustic Metamaterials for Sound Focusing and Confinement*, New J. Phys. **9**, 399 (2007).

[29] S. Zhang, L. Yin, and N. Fang, *Focusing Ultrasound with an Acoustic Metamaterial Network*, Phys. Rev. Lett. **102**, 194301 (2009).

[30] X. Su, A. N. Norris, C. W. Cushing, M. R. Haberman, and P. S. Wilson, *Broadband Focusing of Underwater Sound Using a Transparent Pentamode Lens*, J. Acoust. Soc. Am. **141**, 4408 (2017).

[31] H. Jia, M. Ke, R. Hao, Y. Ye, F. Liu, and Z. Liu, *Subwavelength Imaging by a Simple Planar Acoustic Superlens*, Appl. Phys. Lett. **97**, 173507 (2010).

[32] B. D. F. Casse, W. T. Lu, Y. J. Huang, E. Gultepe, L. Menon, and S. Sridhar, *Super-Resolution Imaging Using a Three-Dimensional Metamaterials Nanolens*, Appl. Phys. Lett. **96**, 023114 (2010).

[33] K. Deng, Y. Ding, Z. He, H. Zhao, J. Shi, and Z. Liu, *Theoretical Study of Subwavelength Imaging by Acoustic Metamaterial Slabs*, J. Appl. Phys. **105**, 124909 (2009).

[34] D. Torrent and J. Sánchez-Dehesa, *Acoustic Cloaking in Two Dimensions: A Feasible Approach*, New J. Phys. **10**, 063015 (2008).

[35] Y. Cheng, F. Yang, J. Y. Xu, and X. J. Liu, *A Multilayer Structured Acoustic Cloak with Homogeneous Isotropic Materials*, Appl. Phys. Lett. **92**, 151913 (2008).

[36] M. Farhat, S. Enoch, S. Guenneau, and A. B. Movchan, *Broadband Cylindrical Acoustic Cloak for Linear Surface Waves in a Fluid*, Phys. Rev. Lett. **101**, 134501 (2008).

[37] S. H. Lee, C. M. Park, Y. M. Seo, and C. K. Kim, *Reversed Doppler Effect in Double Negative Metamaterials*, Phys. Rev. B **81**, 241102 (2010).

[38] S. L. Zhai, X. P. Zhao, S. Liu, F. L. Shen, L. L. Li, and C. R. Luo, *Inverse Doppler Effects in Broadband Acoustic Metamaterials*, Sci. Rep. **6**, 32388 (2016).

[39] H. Esfahlani, S. Karkar, H. Lissek, and J. R. Mosig, *Acoustic Dispersive Prism*, Sci. Rep. **6**, 18911 (2016).

[40] C. J. Naify, J. S. Rogers, M. D. Guild, C. A. Rohde, and G. J. Orris, *Evaluation of the Resolution of a Metamaterial Acoustic Leaky Wave Antenna*, J. Acoust. Soc. Am. **139**, 3251 (2016).

[41] Y. Wu and J. Li, *Total Reflection and Cloaking by Zero Index Metamaterials Loaded with Rectangular Dielectric Defects*, Appl. Phys. Lett. **102**, 183105 (2013).

[42] A. Alù, M. G. Silveirinha, A. Salandrino, and N. Engheta, *Epsilon-near-Zero Metamaterials and Electromagnetic Sources: Tailoring the Radiation Phase Pattern*, Phys. Rev. B **75**, 155410 (2007).

[43] N. Fang, D. Xi, J. Xu, M. Ambati, W. Srituravanich, C. Sun, and X. Zhang, *Ultrasonic Metamaterials with Negative Modulus*, Nat. Mater. **5**, 452 (2006).

[44] S. H. Lee, C. M. Park, Y. M. Seo, Z. G. Wang, and C. K. Kim, *Acoustic Metamaterial with Negative Modulus*, J. Phys. Condens. Matter **21**, 175704 (2009).

[45] B. Assouar, B. Liang, Y. Wu, Y. Li, J.-C. Cheng, and Y. Jing, *Acoustic Metasurfaces*, Nat. Rev. Mater. **3**, 460 (2018).

[46] Y. Zhu and B. Assouar, *Multifunctional Acoustic Metasurface Based on an Array of Helmholtz Resonators*, Phys. Rev. B **99**, 174109 (2019).

[47] Y. Li and B. M. Assouar, *Acoustic Metasurface-Based Perfect Absorber with Deep Subwavelength Thickness*, Appl. Phys. Lett. **108**, 063502 (2016).

[48] S. Huang, X. Fang, X. Wang, B. Assouar, Q. Cheng, and Y. Li, *Acoustic Perfect Absorbers via Spiral Metasurfaces with Embedded Apertures*, Appl. Phys. Lett. **113**, 233501 (2018).

[49] MA, Guancong, YANG, Min, XIAO, Songwen, *et al.* Acoustic metasurface with hybrid resonances. *Nature materials*, vol. 13, no 9, p. 873-878 (2014).

[50] S. Huang, X. Fang, X. Wang, B. Assouar, Q. Cheng, and Y. Li, *Acoustic Perfect Absorbers via Helmholtz Resonators with Embedded Apertures*, J. Acoust. Soc. Am. **145**, 254 (2019).

[51] J. Mei and Y. Wu, *Controllable Transmission and Total Reflection through an Impedance-Matched Acoustic Metasurface*, New J. Phys. **16**, 123007 (2014).

[52] F. Ju, Y. Tian, Y. Cheng, and X. Liu, *Asymmetric Acoustic Transmission with a Lossy Gradient-Index Metasurface*, Appl. Phys. Lett. **113**, 121901 (2018).

[53] M. Molerón, M. Serra-Garcia, and C. Daraio, *Acoustic Fresnel Lenses with Extraordinary Transmission*, Appl. Phys. Lett. **105**, 114109 (2014).

[54] Y. Cheng, C. Zhou, B. G. Yuan, D. J. Wu, Q. Wei, and X. J. Liu, *Ultra-Sparse Metasurface for High Reflection of Low-Frequency Sound Based on Artificial Mie Resonances*, Nat. Mater. **14**, 1013 (2015).

[55] N. Yu, P. Genevet, M. A. Kats, F. Aieta, J.-P. Tetienne, F. Capasso, and Z. Gaburro, *Light Propagation with Phase Discontinuities: Generalized Laws of Reflection and Refraction*, Science **334**, 333 (2011).

[56] L. Huang, X. Chen, H. Mühlenbernd, H. Zhang, S. Chen, B. Bai, Q. Tan, G. Jin, K.-W. Cheah, C.-W. Qiu, J. Li, T. Zentgraf, and S. Zhang, *Three-Dimensional Optical Holography Using a Plasmonic Metasurface*, Nat. Commun. **4**, 2808 (2013).

[57] Y. Li, X. Jiang, B. Liang, J. Cheng, and L. Zhang, *Metascreen-Based Acoustic Passive Phased Array*, Phys. Rev. Appl. **4**, 024003 (2015).

[58] R. Baron John William Strutt, *The Theory of Sound.* (Macmillan and co., London, 1877).

[59] K. Tang, C. Qiu, M. Ke, J. Lu, Y. Ye, and Z. Liu, *Anomalous Refraction of Airborne Sound through Ultrathin Metasurfaces*, Sci. Rep. **4**, 6517 (2014).

[60] F. C. Sgard, X. Olny, N. Atalla, and F. Castel, *On the Use of Perforations to Improve the Sound Absorption of Porous Materials*, Appl. Acoust. **66**, 625 (2005).

[61] J. P. Arenas and M. J. Crocker, *Recent Trends in Porous Sound-Absorbing Materials*, 7 (n.d.).

[62] W. Frank and J. F. Irregeher, *Foam Material Sound Absorption*, US4584232A (22 April 1986).

[63] MAA, Dah-You. Theory and design of microperforated panel sound-absorbing constructions. Sci. Sin. **18**, 55 (1975).

[64] Z. Yang, H. M. Dai, N. H. Chan, G. C. Ma, and P. Sheng, *Acoustic Metamaterial Panels for Sound Attenuation in the 50–1000 Hz Regime*, Appl. Phys. Lett. **96**, 041906 (2010).

[65] C. J. Naify, C.-M. Chang, G. McKnight, F. Scheulen, and S. Nutt, *Membrane-Type Metamaterials: Transmission Loss of Multi-Celled Arrays*, J. Appl. Phys. **109**, 104902 (2011).

[66] M. Badreddine Assouar, M. Senesi, M. Oudich, M. Ruzzene, and Z. Hou, *Broadband Plate-Type Acoustic Metamaterial for Low-Frequency Sound Attenuation*, Appl. Phys. Lett. **101**, 173505 (2012).

[67] N. Jiménez, W. Huang, V. Romero-García, V. Pagneux, and J.-P. Groby, *Ultra-Thin Metamaterial for Perfect and Quasi-Omnidirectional Sound Absorption*, Appl. Phys. Lett. **109**, 121902 (2016).

[68] V. García, V., G. Theocharis, O Richoux, V. Pagneux. "Use of complex frequency plane to design broadband and sub-wavelength absorbers." *The Journal of the Acoustical Society of America* **139** (2016): 3395-3403.

[69] L. Liu, H. Chang, C. Zhang, and X. Hu, *Single-Channel Labyrinthine Metasurfaces as Perfect Sound Absorbers with Tunable Bandwidth*, Appl. Phys. Lett. **111**, 083503 (2017).

[70] C. Zhang and X. Hu, *Three-Dimensional Single-Port Labyrinthine Acoustic Metamaterial: Perfect Absorption with Large Bandwidth and Tunability*, Phys. Rev. Appl. **6**, 064025 (2016).

[71] D. Li, D. Chang, and B. Liu, *Enhancing the Low Frequency Sound Absorption of a Perforated Panel by Parallel-Arranged Extended Tubes*, Appl. Acoust. **102**, 126 (2016).

[72] T. Yasuda, C. Wu, N. Nakagawa, and K. Nagamura, *Studies on an Automobile Muffler with the Acoustic Characteristic of Low-Pass Filter and Helmholtz Resonator*, Appl. Acoust. **74**, 49 (2013).

[73] F. Simon, *Long Elastic Open Neck Acoustic Resonator for Low Frequency Absorption*, J. Sound Vib. **421**, 1 (2018).

[74] V. Leroy, A. Strybulevych, M. Lanoy, F. Lemoult, A. Tourin, and J. H. Page, *Superabsorption of Acoustic Waves with Bubble Metascreens*, Phys. Rev. B **91**, 020301 (2015).

[75] T. Lee and H. Iizuka, *Heavily Overdamped Resonance Structurally Engineered in a Grating Metasurface for Ultra-Broadband Acoustic Absorption*, Appl. Phys. Lett. **113**, 101903 (2018).

[76] S. Kim, Y.-H. Kim, and J.-H. Jang, *A Theoretical Model to Predict the Low-Frequency Sound Absorption of a Helmholtz Resonator Array*, J. Acoust. Soc. Am. **119**, 1933 (2006).

[77] N. Jiménez, V. Romero-García, V. Pagneux, and J.-P. Groby, *Rainbow-Trapping Absorbers: Broadband, Perfect and Asymmetric Sound Absorption by Subwavelength Panels for Transmission Problems*, Sci. Rep. **7**, 13595 (2017).

[78] J. Li, W. Wang, Y. Xie, B.-I. Popa, and S. A. Cummer, *A Sound Absorbing Metasurface with Coupled Resonators*, Appl. Phys. Lett. **109**, 091908 (2016).

[79] M. Yang, S. Chen, C. Fu, and P. Sheng, *Optimal Sound-Absorbing Structures*, Mater. Horiz. **4**, 673 (2017).

[80] L. E. Kinsler, A. R. Frey, A. B. Coppens, and J. V. Sanders, *Fundamentals of Acoustics* (John Wiley & Sons, 2000).

[81] D. R. Raichel, *The Science and Applications of Acoustics*, 2nd ed (Springer, New York, 2006).

[82] E. W. Lemmon, R. T. Jacobsen, S. G. Penoncello, and D. G. Friend, *Thermodynamic Properties of Air and Mixtures of Nitrogen, Argon, and Oxygen From 60 to 2000 K at Pressures to 2000 MPa*, J. Phys. Chem. Ref. Data **29**, 331 (2000).

[83] G. P. Ward, *The Manipulation of Sound with Acoustic Metamaterials*, (2017).

[84] *Fundamentals of Physical Acoustics | Wiley*, https://www.wiley.com/en-us/Fundamentals+of+Physical+Acoustics-p-9780471319795.

[85] T. Yazaki, Y. Tashiro, and T. Biwa, *Measurements of Sound Propagation in Narrow Tubes*, Proc. R. Soc. Math. Phys. Eng. Sci. **463**, 2855 (2007).

[86] H. Tijdeman, *On the Propagation of Sound Waves in Cylindrical Tubes*, J. Sound Vib. **39**, 1 (1975).

[87] D. E. Weston, *The Theory of the Propagation of Plane Sound Waves in Tubes*, Proc. Phys. Soc. Sect. B **66**, 695 (1953).

[88] G. Kirchhoff. Ueber den einfluss der wärmeleitung in einem gase auf die schallbewegung. Annalen der Physik, 210:177 – 193, (2006).

[89] L. Rayleigh. The Theory of Sound—Volume 2. Macmillan, London, 2nd edition, 1877.

[90] Y. Aurégan, R. Starobinski, and V. Pagneux, *Influence of Grazing Flow and Dissipation Effects on the Acoustic Boundary Conditions at a Lined Wall*, J. Acoust. Soc. Am. **109**, 59 (2001).

[91] G. Kooijman, A. Hirschberg, and J. Colliard, *Acoustical Response of Orifices under Grazing Flow: Effect of Boundary Layer Profile and Edge Geometry*, J. Sound Vib. **315**, 902 (2008).

[92] G. P. Ward, R. K. Lovelock, A. R. J. Murray, A. P. Hibbins, J. R. Sambles, and J. D. Smith, *Boundary-Layer Effects on Acoustic Transmission Through Narrow Slit Cavities*, Phys. Rev. Lett. **115**, 044302 (2015).

[93] M. Molerón, M. Serra-Garcia, and C. Daraio, *Visco-Thermal Effects in Acoustic Metamaterials: From Total Transmission to Total Reflection and High Absorption*, New J. Phys. **18**, 033003 (2016).

[94] X. Olny and C. Boutin, *Acoustic Wave Propagation in Double Porosity Media*, J. Acoust. Soc. Am. **114**, 73 (2003).

[95] Multiphysics, C. O. M. S. O. L. "Introduction to comsol multiphysics®." *COMSOL Multiphysics, Burlington, MA, accessed Feb* 9 (1998).

[96] Zienkiewicz, Olgierd Cecil, Robert Leroy Taylor, and Jian Z. Zhu. *The finite element method: its basis and fundamentals*. Elsevier, (2005).

[97] J. Beadle, *Exploration of Acoustic Metasurfaces*, (2020).

[98] Bathe, Klaus-Jürgen. "Finite element method." *Wiley encyclopedia of computer science and engineering* (2007): 1-12.

[99] G. Dhatt, E. Lefrançois, and G. Touzot, *Finite Element Method* (John Wiley & Sons, 2012).

[100] A. Rodríguez-Panes, J. Claver, and A. M. Camacho, *The Influence of Manufacturing Parameters on the Mechanical Behaviour of PLA and ABS Pieces Manufactured by FDM: A Comparative Analysis*, Materials **11**, 8 (2018).

[101] ISO 10534-2:1998, "Acoustics-Determination of the sound absoprtion coefficient and impedance in the impedance tube-Part 2: Transfer-function method."

[102] A. Merkel, G. Theocharis, O. Richoux, V. Romero-García, and V. Pagneux, *Control of Acoustic Absorption in One-Dimensional Scattering by Resonant Scatterers*, Appl. Phys. Lett. **107**, 244102 (2015).

[103] Romero-García, V., et al. "Perfect and broadband acoustic absorption by critically coupled sub-wavelength resonators." *Scientific reports* 6.1 (2016): 1-8.

[104] V. M. García-Chocano, L. Sanchis, A. Díaz-Rubio, J. Martínez-Pastor, F. Cervera, R. Llopis-Pontiveros, and J. Sánchez-Dehesa, *Acoustic Cloak for Airborne Sound by Inverse Design*, Appl. Phys. Lett. **99**, 074102 (2011).

[105] P. Cobo, E. Moraes, and F. Simón, *Inverse Estimation of the Non-Acoustical Parameters of Loose Granular Absorbers by Simulated Annealing*, Build. Environ. **94**, 859 (2015).

[106] J. Dong, K. K. Choi, and N. H. Kim, *Design Optimization for Structural-Acoustic Problems Using FEA-BEA With Adjoint Variable Method*, J. Mech. Des. **126**, 527 (2003).

[107] S. S. Girija, *TensorFlow: Large-Scale Machine Learning on Heterogeneous Distributed Systems*, 25 (n.d.).

[108] A. Paszke, S. Gross, F. Massa, A. Lerer, J. Bradbury, G. Chanan, T. Killeen, Z. Lin, N. Gimelshein, L. Antiga, A. Desmaison, A. Kopf, E. Yang, Z. DeVito, M. Raison, A. Tejani, S. Chilamkurthy, B. Steiner, L. Fang, J. Bai, and S. Chintala, *PyTorch: An Imperative Style, High-Performance Deep Learning Library*, in *Advances in Neural Information Processing Systems*, Vol. 32 (Curran Associates, Inc., 2019).

[109] V. Nair and G. E. Hinton, *Rectified Linear Units Improve Restricted Boltzmann Machines*, in (2010).

[110] N. Srivastava, G. Hinton, A. Krizhevsky, I. Sutskever, and R. Salakhutdinov, *Dropout: A Simple Way to Prevent Neural Networks from Overfitting*, 30 (n.d.).

[111] S. Ioffe and C. Szegedy, *Batch Normalization: Accelerating Deep Network Training by Reducing Internal Covariate Shift*, in *Proceedings of the 32nd International Conference on Machine Learning* (PMLR, 2015), pp. 448–456.

[112] W. Ma, Z. Liu, Z. A. Kudyshev, A. Boltasseva, W. Cai, and Y. Liu, *Deep Learning for the Design of Photonic Structures*, Nat. Photonics **15**, 77 (2021).

[113] J. Jiang, M. Chen, and J. A. Fan, *Deep Neural Networks for the Evaluation and Design of Photonic Devices*, Nat. Rev. Mater. **6**, 679 (2021).

[114] S. An, C. Fowler, B. Zheng, M. Y. Shalaginov, H. Tang, H. Li, L. Zhou, J. Ding, A. M. Agarwal, C. Rivero-Baleine, K. A. Richardson, T. Gu, J. Hu, and H. Zhang, *A Deep Learning Approach for Objective-Driven All-Dielectric Metasurface Design*, ACS Photonics **6**, 3196 (2019).

[115] An, Sensong, Bowen Zheng, Mikhail Y. Shalaginov, Hong Tang, Hang Li, Li Zhou, Jun Ding et al. "Deep learning modeling approach for metasurfaces with high degrees of freedom." *Optics Express* 28, no. 21 (2020): 31932-31942.

[116] Y. Zhang, A. Mesaros, K. Fujita, S. D. Edkins, M. H. Hamidian, K. Ch'ng, H. Eisaki, S. Uchida, J. C. S. Davis, E. Khatami, and E.-A. Kim, *Machine Learning in Electronic-Quantum-Matter Imaging Experiments*, Nature **570**, 484 (2019).

[117] W. W. Ahmed, M. Farhat, X. Zhang, and Y. Wu, *Deterministic and Probabilistic Deep Learning Models for Inverse Design of Broadband Acoustic Cloak*, Phys. Rev. Res. **3**, 013142 (2021).

[118] WENG, Jingkai, DING, Yujiang, HU, Chengbo, *et al.* Meta-neural-network for real-time and passive deep-learning-based object recognition. *Nature communications*, vol. 11, no 1, p. **1-8** (2020).

[119] G. Genty, L. Salmela, J. M. Dudley, D. Brunner, A. Kokhanovskiy, S. Kobtsev, and S. K. Turitsyn, *Machine Learning and Applications in Ultrafast Photonics*, Nat. Photonics **15**, 91 (2021).

[120] C. Gurbuz, F. Kronowetter, C. Dietz, M. Eser, J. Schmid, and S. Marburg, *Generative Adversarial Networks for the Design of Acoustic Metamaterials*, J. Acoust. Soc. Am. **149**, 1162 (2021).

[121] B. Orazbayev and R. Fleury, *Far-Field Subwavelength Acoustic Imaging by Deep Learning*, Phys. Rev. X **10**, 031029 (2020).

[122] T. Zhao, Y. Li, L. Zuo, and K. Zhang, *Machine-Learning Optimized Method for Regional Control of Sound Fields*, Extreme Mech. Lett. **45**, 101297 (2021).

[123] I. Goodfellow, Y. Bengio, and A. Courville, *Deep Learning* (MIT Press, Cambridge, MA, USA, 2016).

[124] D. Guest, K. Cranmer, and D. Whiteson, *Deep Learning and Its Application to LHC Physics*, Annu. Rev. Nucl. Part. Sci. **68**, 161 (2018).

[125] S. Kullback, *Information Theory and Statistics* (Courier Corporation, 1997).

[126] J. Lin, *Divergence Measures Based on the Shannon Entropy*, IEEE Trans. Inf. Theory **37**, 145 (1991).

[127] R. Bro and A. K. Smilde, *Principal Component Analysis*, Anal. Methods **6**, 2812 (2014).

[128] J. Wu, X.-Y. Chen, H. Zhang, L.-D. Xiong, H. Lei, and S.-H. Deng, *Hyperparameter Optimization for Machine Learning Models Based on Bayesian Optimizationb*, J. Electron. Sci. Technol. **17**, 26 (2019).

[129] H.-P. Nguyen, J. Liu, and E. Zio, *A Long-Term Prediction Approach Based on Long Short-Term Memory Neural Networks with Automatic Parameter Optimization by Tree-Structured Parzen Estimator and Applied to Time-Series Data of NPP Steam Generators*, Appl. Soft Comput. **89**, 106116 (2020).

[130] P. Liashchynskyi and P. Liashchynskyi, *Grid Search, Random Search, Genetic Algorithm: A Big Comparison for NAS*, ArXiv191206059 Cs Stat (2019).

[131] I. Goodfellow, J. Pouget-Abadie, M. Mirza, B. Xu, D. Warde-Farley, S. Ozair, A. Courville, and Y. Bengio, *Generative Adversarial Nets*, in *Advances in Neural Information Processing Systems*, Vol. 27 (Curran Associates, Inc., 2014).

[132] M. Mirza and S. Osindero, *Conditional Generative Adversarial Nets*, (2014).

[133] P. Cunningham and S. J. Delany, *K-Nearest Neighbour Classifiers: 2nd Edition (with Python Examples)*, ACM Comput. Surv. **54**, 1 (2021).

[134] T. K. Ho, *Random Decision Forests*, in *Proceedings of 3rd International Conference on Document Analysis and Recognition*, Vol. 1 (1995), pp. 278–282 vol.1.

[135] M. A. Hearst, S. T. Dumais, E. Osuna, J. Platt, and B. Scholkopf, *Support Vector Machines*, IEEE Intell. Syst. Their Appl. **13**, 18 (1998).

[136] C. Shorten and T. M. Khoshgoftaar, *A Survey on Image Data Augmentation for Deep Learning*, J. Big Data **6**, 60 (2019).

[137] L. Perez and J. Wang, *The Effectiveness of Data Augmentation in Image Classification Using Deep Learning*, ArXiv171204621 Cs (2017).

[138] J. Lemley, S. Bazrafkan, and P. Corcoran, *Smart Augmentation Learning an Optimal Data Augmentation Strategy*, IEEE Access **5**, 5858 (2017).

[139] L. Taylor and G. Nitschke, *Improving Deep Learning with Generic Data Augmentation*, in *2018 IEEE Symposium Series on Computational Intelligence (SSCI)* (2018), pp. 1542–1547.

[140] Y. Zhu, A. Merkel, K. Donda, S. Fan, L. Cao, and B. Assouar, *Nonlocal Acoustic Metasurface for Ultrabroadband Sound Absorption*, Phys. Rev. B **103**, 064102 (2021).

[141] Y. Li, C. Shen, Y. Xie, J. Li, W. Wang, S. A. Cummer, and Y. Jing, *Tunable Asymmetric Transmission via Lossy Acoustic Metasurfaces*, Phys. Rev. Lett. **119**, 035501 (2017).

[142] Y. Zhu, K. Donda, S. Fan, L. Cao, and B. Assouar, *Broadband Ultra-Thin Acoustic Metasurface Absorber with Coiled Structure*, Appl. Phys. Express **12**, 114002 (2019).

[143] K. Donda, Y. Zhu, S.-W. Fan, L. Cao, Y. Li, and B. Assouar, *Extreme Low-Frequency Ultrathin Acoustic Absorbing Metasurface*, Appl. Phys. Lett. **115**, 173506 (2019).

[144] J. Hui Wu, Z. P. Hu, and H. Zhou, *Sound Absorbing Property of Porous Metal Materials with High Temperature and High Sound Pressure by Turbulence Analogy*, J. Appl. Phys. **113**, 194905 (2013).

[145] Z. Li, Z. Wang, Z. Guo, X. Wang, and X. Liang, *Ultra-Broadband Sound Absorption of a Hierarchical Acoustic Metamaterial at High Temperatures*, Appl. Phys. Lett. **118**, 161903 (2021).

[146] W. Xu, D. Yu, and J. Wen, *Simple Meta-Structure That Can Achieve the Quasi-Perfect Absorption throughout a Frequency Range of 200–500 Hz at 350 °C*, Appl. Phys. Express **13**, 047001 (2020).

[147] W. Wang, M. Jia, W. Jiang, B. Lou, W. Jiao, D. Yuan, X. Li, and Z. Liu, *High Temperature Property and Modification Mechanism of Asphalt Containing Waste Engine Oil Bottom*, Constr. Build. Mater. **261**, 119977 (2020).

[148] L. C. Sutherland and R. D. Horonjeff, *Impact of Low-frequency Sound on Historic Structures*, J. Acoust. Soc. Am. **118**, 1850 (2005).

[149] M. Mizokami and Y. Kurosaki, *Noise Variation by Compressive Stress on the Model Core of Power Transformers*, J. Magn. Magn. Mater. **381**, 208 (2015).

[150] F. Sun, H. Chen, J. Wu, and K. Feng, *Sound Absorbing Characteristics of Fibrous Metal Materials at High Temperatures*, Appl. Acoust. **71**, 221 (2010).

[151] D. R. A. Christie, *Measurement of the Acoustic Properties of a Sound Absorbing Material at High Temperatures*, J. Sound Vib. **46**, 347 (1976).

[152] B. Xia, N. Chen, L. Xie, Y. Qin, and D. Yu, *Temperature-Controlled Tunable Acoustic Metamaterial with Active Band Gap and Negative Bulk Modulus*, Appl. Acoust. **112**, 1 (2016).

[153] D.-Y. Maa, *Potential of Microperforated Panel Absorber*, J. Acoust. Soc. Am. **104**, 2861 (1998).

[154] M. R. Stinson and E. a. G. Shaw, *Acoustic Impedance of Small, Circular Orifices in Thin Plates*, J. Acoust. Soc. Am. **77**, 2039 (1985).

[155] M. R. Stinson, *The Propagation of Plane Sound Waves in Narrow and Wide Circular Tubes, and Generalization to Uniform Tubes of Arbitrary Cross-sectional Shape*, J. Acoust. Soc. Am. **89**, 550 (1991).

[156] G.-S. Liu, Y.-Y. Peng, M.-H. Liu, X.-Y. Zou, and J.-C. Cheng, *Broadband Acoustic Energy Harvesting Metasurface with Coupled Helmholtz Resonators*, Appl. Phys. Lett. **113**, 153503 (2018).

[157] Y. Zhu, A. Merkel, K. Donda, S. Fan, L. Cao, and B. Assouar, *Nonlocal Acoustic Metasurface for Ultrabroadband Sound Absoprtion, Phys. Rev. B 103,064102 (2021).*

[158] Y. Tang, F. Xin, and T. J. Lu, *Sound Absorption of Micro-Perforated Sandwich Panel with Honeycomb-Corrugation Hybrid Core at High Temperatures*, Compos. Struct. **226**, 111285 (2019).

[159] M. Duan, C. Yu, Z. Xu, F. Xin, and T. J. Lu, *Acoustic Impedance Regulation of Helmholtz Resonators for Perfect Sound Absorption via Roughened Embedded Necks*, Appl. Phys. Lett. **117**, 151904 (2020).

[160] M. V. Zhelyeznyakov, S. Brunton, and A. Majumdar, *Deep Learning to Accelerate Scatterer-to-Field Mapping for Inverse Design of Dielectric Metasurfaces*, ACS Photonics **8**, 481 (2021).

[161] V. Puzyrev, *Deep Learning Electromagnetic Inversion with Convolutional Neural Networks*, Geophys. J. Int. **218**, 817 (2019).

[162] Z. Liu, *Algorithmic Design of Photonic Structures with Deep Learning*, (2021).

[163] T. Shan, X. Pan, M. Li, S. Xu, and F. Yang, *Coding Programmable Metasurfaces Based on Deep Learning Techniques*, IEEE J. Emerg. Sel. Top. Circuits Syst. **10**, 114 (2020).

[164] QIU, Tianshuo, SHI, Xin, WANG, Jiafu, *et al.* Deep learning: a rapid and efficient route to automatic metasurface design. *Advanced Science*, 2019, vol. 6, no 12, p. 1900128.

[165] S. Kiranyaz, O. Avci, O. Abdeljaber, T. Ince, M. Gabbouj, and D. J. Inman, *1D Convolutional Neural Networks and Applications: A Survey*, Mech. Syst. Signal Process. **151**, 107398 (2021).

[166] C. SZEGEDY, L. Wei, Y.JIA, *et al.* Going deeper with convolutions. In : *Proceedings of the IEEE conference on computer vision and pattern recognition*. 2015. p. 1-9..

[167] A. Krizhevsky, I. Sutskever, and G. E. Hinton, *ImageNet Classification with Deep Convolutional Neural Networks*, Commun. ACM **60**, 84 (2017).

[168] J. Deng, W. Dong, R. Socher, L.-J. Li, K. Li, and L. Fei-Fei, *ImageNet: A Large-Scale Hierarchical Image Database*, in *2009 IEEE Conference on Computer Vision and Pattern Recognition* (2009), pp. 248–255.

[169] D. P. Kingma and J. Ba, *Adam: A Method for Stochastic Optimization*, ArXiv14126980 Cs (2017).

[170] K. Donda, Y. Zhu, A. Merkel, S.-W. Fan, L. Cao, S. Wan, and B. Assouar, *Ultrathin Acoustic Absorbing Metasurface Based on Deep Learning Approach*, Smart Mater. Struct. **30**, 085003 (2021).

[171] Gurbuz, C., Kronowetter, F., Dietz, C., Eser, M., Schmid, J., & Marburg, S. (2021). Generative adversarial networks for the design of acoustic metamaterials. *The Journal of the Acoustical Society of America, **149**,1162-1174 (2021).*

[172] HERNÁNDEZ-GARCÍA, Alex et KÖNIG, Peter. Further advantages of data augmentation on convolutional neural networks. In : *International Conference on Artificial Neural Networks*. Springer, Cham, 2018. p. 95-103.

[173] STANDARD, British. BS EN ISO 354: 2003. *Acoustics-Measurement of sound absorption in a reverberation room* (2003).

[174] M. Ottink, J. Brunskog, C.-H. Jeong, E. Fernandez-Grande, P. Trojgaard, and E. Tiana-Roig, *In Situ Measurements of the Oblique Incidence Sound Absorption Coefficient for Finite Sized Absorbers*, J. Acoust. Soc. Am. **139**, 41 (2016).

[175] E. Sadoulet-Reboul, M. L. Bourles, and K. Verdiã, *Investigations of an Impedance Tube Technique to Determine the Transmission Loss of Materials under Angular Incidence*, **6** (2015).

Vita

My name is Krupali. I was born in May 1991 at Bhavnagar, India. I completed my master's in Electronics and Communication from Gujarat Technological University in 2015, later I joined Indian Institute of Technology, Gandhinagar as a Junior Research Fellow. My area of research was designing Electromagnetic metasurface-based devices for the visible frequency range. Two and half years later, I moved to Nancy, France to pursue my Ph.D. degree. My research interests are in the inter-disciplinary field of acoustic metasurface designs and deep learning applications. The acquired research results during my Ph.D. career in the form of papers and conference presentation are listed below.

List of Publications

Journal papers

1. **K. Donda**, Y. Zhu, A. Merkel, S.-W. Fan, L. Cao, S. Wan, and B. Assouar, *Ultrathin Acoustic Absorbing Metasurface Based on Deep Learning Approach*, Smart Mater. Struct. 30, 085003 (2021).

2. **K. Donda**, Y. Zhu, S.-W. Fan, L. Cao, Y. Li, and B. Assouar, *Extreme Low-Frequency Ultrathin Acoustic Absorbing Metasurface*, Appl. Phys. Lett. 115, 173506 (2019).

3. **K. Donda**, Y. Zhu, and B. Assouar, Deep Learning Approach for Acoustic AbsorbingMetasurface: Design with High Degrees of Freedom. *(In preparation).*

4. Y. Zhu, A. Merkel, **K. Donda**, S. Fan, L. Cao, and B. Assouar, *Nonlocal Acoustic Metasurface for Ultrabroadband Sound Absorption*, Phys. Rev. B 103, 064102 (2021).

5. Y. Zhu, S.-W. Fan, L. Cao, **K. Donda**, and B. Assouar, *Acoustic Meta-Equalizer*, Phys. Rev. Appl. 14, 014038 (2020).

6. Y. Zhu, **K. Donda**, S. Fan, L. Cao, and B. Assouar, *Broadband Ultra-Thin Acoustic Metasurface Absorber with Coiled Structure*, Appl. Phys. Express 12, 114002 (2019).

7. Y. Zhu, F. Fei, S. Fan, L. Cao, **K. Donda**, and B. Assouar, *Reconfigurable Origami-Inspired Metamaterials for Controllable Sound Manipulation*, Phys. Rev. Appl. 12, 034029 (2019).

Conference Proceeding

1. **K. Donda**, Y. Zhu, A. Merkel, S. Wang and B. Assouar, *Deep learning modeling approach for ultrathin acoustic metasurface absorber for extremely low frequencies*, METAMATERIALS 2021: 15th International Congress on Artificial Materials for Novel Wave Phenomena (2021).

Additional Documents

A1. Summary of the Modified CNN

Layer (type)	Output Shape	Param#
conv_1(Conv2D)	(None,64,64,16)	448
max_pooling2d (Maxpooling2D)	(None,32,32,16)	0
conv_2 (Conv2D)	(None,16,16,32)	4640
max_pooling2d_1(Maxpooling2D)	(None,16,16,64)	0
conv_3 (Conv2D)	(None,16,16,64)	18496
max_pooling2d_2(Maxpooling2D)	(None,8,8,64)	0
batch_normalization	(None,8,8,64)	256
flatten (Flatten)	(None,4096)	0
dense (Dense)	(None,512)	2097664
dropout (Dropout)	(None,512)	0
dense_1 (Dense)	(None,20)	10260

A2. Summary of the Generator Model

Layer	Shape	Param#	Connected to
z_shape	(None, 100)	0	-
class_label1s(InputLayer)	(None, 201)	0	-
class_label2s (InputLayer)	(None, 2)	0	-
concatenate_1 (Concatenate)	(None, 303)	0	z_input[0][0] class_label1s[0][0] class_label2s[0][0]
dense_3	(None, 32768)	9961472	concatenate_1[0][0]
reshape_2	(None, 16,16,128)	0	dense_3[0][0]
Batch_normalization	(None, 16,16,128)	512	reshape_2[0][0]
Activation_1	(None, 16,16,128)	0	batch_normalization[0][0]
Dropout_4	(None, 16,16,128)	0	activation_1[0][0]
conv2d_transpose	(None, 32,32,128)	147584	dropout_4[0][0]
Batch_normalization_1	(None, 32,32,128)	512	conv2d_transpose [0][0]
Activation_2	(None, 32,32,128)	0	batch_normalization_2[0][0]
Dropout_5	(None, 32,32,128)	0	activation_3[0][0]
conv2d_transpose_1	(None,64,64,32)	36896	dropout_5[0][0]
Batch_normalization_2	(None,64,64,32)	128	conv2d_transpose_1[0][0]
Activation_3	(None,64,64,32)	0	batch_normalization_2[0][0]

Dropout_6	(None,64,64,32)	0	activation_3[0][0]
conv2d_transpose_2	(None,64,64,16)	4624	dropout_6[0][0]
Batch_normalization_3	(None,64,64,16)	64	conv2d_transpose_2[0][0]
Activation_4	(None,64,64,16)	0	batch_normalization_3[0][0]
Dropout_7	(None,64,64,16)	0	activation_4[0][0]
conv2d_transpose_3	(None,64,64,1)	145	dropout_7[0][0]
Activation_5	(None,64,64,1)	0	conv2d_transpose_3[0][0]

A3. Summary of the Discriminator Model

Layer (type)	**Output Shape**	**Param#**	**Connected to**
class_label1s (InputLayer)	[(None,201)]	0	-
class_label2s (InputLayer)	[(None,2)]	0	-
dense_8 (Dense)	(None,4096)	827392	class_label1s[0][0]
dense_9 (Dense)	(None,4096)	12288	class_label2s[0][0]
discriminator_input (InputLayer)	[(None,64,64,1)]	0	-
reshape_6 (Reshape)	[(None,64,64,1)]	0	dense_8[0][0]
reshape_7 (Reshape)	(None,64,64,1)	0	dense_9[0][0]
concatenate_4 (Concatenate)	(None,64,64,3)	0	discriminator_input[0][0] reshape_6[0][0] reshape_7[0][0]
leaky_re_lu_8 (LeakyReLU)	(None,64,64,3)	0	concatenate_4[0][0]
dropout_16 (Dropout))	(None,64,64,3)	0	leaky_re_lu_8[0][0]
Conv2d_8 (Conv2D)	(None,64,64,8)	224	dropout_16[0][0]
leaky_re_lu_9 (LeakyReLU)	(None,64,64,8)	0	conv2d_8[0][0]
dropout_17 (Dropout)	(None,64,64,8)	0	leaky_re_lu_9[0][0]
conv2d_9 (Conv2D)	(None,64,64,16)	1168	dropout_17[0][0]
leaky_re_lu_l0 (LeakyReLU)	(None,64,64,16)	0	conv2d_9[0][0]
dropout_18 (Dropout)	(None,64,64,16)	0	leaky_re_lu_10[0][0]
conv2d_10 (Conv2D)	(None,64,64,32)	4640	dropout_18[0][0]
leaky_re_lu_l1 (LeakyReLU)	(None,64,64,32)	0	conv2d_10[0][0]
dropout_19 (Dropout)	(None,64,64,32)	0	leaky_re_lu_11[0][0]
conv2d_11 (Conv2D)	(None,64,64,32)	18496	dropout_19[0][0]
max_pooling2d_3 (MaxPooling2D)	(None,32,32,64)	0	conv2d_11[0][0]
flatten_2 (Flatten)	(None,65536)	0	max_pooling2d_3[0][0]
dense_10 (Dense)	(None,1)	65537	flatten_2[0][0]
activation_12 (Activation)	(None,1)	0	dense_10[0][0]

Métasurfaces acoustiques absorbantes pour le régime basses fréquences: Approche en deep-learning et démonstration expérimentale

Résumé

En raison de la forte augmentation de la population urbaine, la pollution sonore est devenue un problème majeur dans notre vie quotidienne et a un impact négatif sur la santé et la qualité de vie. En particulier, l'existence de niveaux élevés de bruit basse fréquence d'origine humaine a été signalée dans de nombreux environnements. Dans le paysage sonore urbain, les principales sources de ces bruits sont les transports, les compresseurs, les turbines, les chaudières, les moteurs d'automobiles, les moteurs d'avions, la musique amplifiée, etc. Diverses expériences sur des animaux montrent que l'exposition au bruit à long terme provoque des changements vasculaires permanents et des altérations du muscle cardiaque. Plusieurs rapports montrent de nombreux impacts dangereux du bruit à basse fréquence sur la santé humaine. Chez l'homme, l'exposition à long terme au bruit de la circulation routière peut provoquer du stress, perturber les habitudes de sommeil, augmenter la pression artérielle, modifier la variabilité du rythme cardiaque et, finalement, entraîner des maladies chroniques comme l'athérosclérose, l'hypertension et les cardiopathies ischémiques. Une étude expérimentale sur des personnes en bonne santé montre que l'exposition au bruit du trafic routier résidentiel augmente les niveaux d'expression des gènes biomarqueurs du stress oxydatif et de la réparation de l'ADN. En 2011, l'Organisation mondiale de la santé (OMS) a considéré le bruit comme l'un des facteurs les plus cruciaux qui affectent négativement la santé publique et a publié plusieurs rapports indiquant l'impact négatif du bruit sur les êtres humains. Dans cette perspective, il est essentiel de trouver des moyens efficaces pour contrôler le bruit de manière effective.

Au cours des 40 à 50 dernières années, l'utilisation et la variété des matériaux insonorisant disponibles a considérablement augmenté. Cette évolution est principalement due à l'amélioration de la technologie et aux préoccupations du public concernant le bruit dans la vie quotidienne. Pour réduire le niveau de bruit, on utilise une variété de matériaux traditionnels tels que les fibres naturelles (laine, kenaf, coton naturel, etc.), les matériaux granulaires (béton poreux, asphalte et argiles granulaires), les matériaux cellulaires synthétiques (laine de verre inerte, mousses de mélamine, polyuréthane et polyester), etc. Ces matériaux peuvent être

utilisés pour développer des systèmes et des structures d'absorption des bruits à haute fréquence. Malgré leur simplicité, les approches visant à contrôler le bruit à l'aide de matériaux que l'on trouve facilement dans la nature sont soumises à des restrictions drastiques, en particulier pour l'absorption des basses fréquences en raison de leur fort pouvoir de pénétration. Sur la base de la loi masse-densité, les spectres d'absorption ne peuvent être ajustés qu'en modifiant l'épaisseur, pour un matériau classique dense donné, ce qui donne des absorbeurs volumineux. Pour absorber les sons de basse fréquence, de nombreuses structures composites ont été proposées, telles que des matériaux à gradient d'indice, des absorbeurs basés sur des panneaux microperforés, des matériaux poreux, etc. Ces structures sont capables d'atténuer le bruit dans la gamme des moyennes et hautes fréquences. Ces structures sont capables d'atténuer le bruit dans la gamme des moyennes et hautes fréquences. Cependant, l'atténuation des sons à basse fréquence reste un défi en raison de la faible dissipation intrinsèque des matériaux homogènes traditionnels dans le régime des basses fréquences.

En 20 ans, l'avènement des métamatériaux/métasurfaces acoustiques a bouleversé les moyens conventionnels dans tous les aspects de la propagation et de la manipulation du son. Plus précisément, il a offert une expansion sans précédent de notre capacité à atténuer le son au-delà de la loi masse-densité. Le concept de métasurfaces a été introduit dans les communautés de la science des matériaux et de la physique pour les ondes optiques en utilisant la loi de Snell généralisée. Il a ouvert de nombreuses possibilités pour la manipulation de l'onde optique et a conduit à de nouvelles applications. Grâce à ce travail de pionnier et parce que les ondes acoustiques suivent également la loi de Snell, une vague d'activité a révélé que les métasurfaces acoustiques étaient des matériaux appropriés pour la manipulation du son et a conduit à de nouvelles applications en acoustique. Les métasurfaces sont uniques en ce qu'elles peuvent adapter librement les champs d'ondes, permettant un contrôle complet de la phase et/ou de l'amplitude. Le concept de métasurface acoustique est basé sur des réseaux d'unités sub-longueur d'onde qui peuvent être utilisés pour réaliser des fonctionnalités fascinantes telles que les faisceaux auto-fléchissants, la transmission asymétrique, la réflexion diffuse, la focalisation des faisceaux, les résonances de Mie artificielles et l'absorption quasi parfaite. Au cours des dernières années, nous avons assisté à des progrès considérables dans le développement de divers concepts basés sur les métasurfaces acoustiques pour absorber les ondes sonores à basse fréquence avec des caractéristiques sub-longueur d'onde, ce qui sera l'aspect principal discuté dans cette thèse. Les démonstrations sont principalement basées sur les métasurfaces d'adaptation d'impédance avec des résonances hybrides ou des géométries spatiales

d'enroulement. En raison de la possibilité d'utiliser n'importe quel matériau acoustiquement rigide, la mise en œuvre de métasurfaces absorbantes enroulées est simple. Cependant, il reste difficile d'obtenir une absorption extrême à basse fréquence (<100Hz) car, dans ces conceptions, l'absorption est contrôlée par la longueur du canal enroulé, ce qui rend difficile l'ajustement de la fréquence de résonance.

Pour la conception des absorbeurs acoustiques métasurface, la conception des structures joue un rôle clé. Ces approches de conception, à ce jour, reposent sur une expertise en acoustique pour mettre en œuvre les modèles théoriques ou pour guider la progression des simulations numériques basées sur la méthode des éléments finis (FEM). Les approches théoriques comprennent des méthodes basées sur la physique, comme l'analyse d'impédance, le plan de fréquence complexe, etc. Bien que ces approches fournissent des lignes directrices utiles, trouver les bonnes structures pour réaliser la réponse acoustique souhaitée n'est pas une tâche facile, surtout dans le cas de géométries complexes dans un problème à contraintes multiples. Dans de tels cas, nous nous appuyons sur des simulations numériques. Si nécessaire, par exemple dans des cavités étroites, le module "Thermoviscous-Acoustic" doit être utilisé. Ce système d'équations a beaucoup plus de degrés de liberté que le module "Pressure-Acoustics", ce qui augmente le temps de calcul. De plus, ce module utilise un maillage plus fin que le module pression-acoustique car il y a tellement de mécanismes à petite échelle, en particulier dans les espaces confinés tels que les espaces acoustiques étroits/cavités, où l'interaction complexe du son avec les couches limites visqueuses et thermiques doit être prise en compte. En partant de la condition initiale et en établissant des conditions aux limites appropriées, la solution peut être obtenue en résolvant les équations de Navier-Stokes linéarisées. Avec des maillages suffisants et de nombreuses itérations, une réponse acoustique précise peut être dérivée pour une structure donnée. Néanmoins, il est souvent nécessaire d'affiner la géométrie et d'exécuter des simulations de manière itérative pour s'approcher de la réponse acoustique souhaitée. Comme pour les approches théoriques, cette procédure nécessite également une expérience et des connaissances en acoustique. En raison de la puissance de calcul et des contraintes de temps, cette approche ne permet d'explorer qu'un espace de conception limité pour trouver la meilleure structure. C'est une préoccupation majeure, en particulier pour les calculs tridimensionnels (3D) à basse fréquence, car, à basse fréquence (<50Hz), la bande passante étroite nécessite une résolution suffisamment élevée pour balayer les fréquences afin d'obtenir des calculs précis. Dans cette thèse, nous identifions des solutions pour contourner ces approches de conception conventionnelles en utilisant des architectures modernes de deep-

learning. Récemment, le deep-learning est apparu comme une méthode très prometteuse, notamment pour résoudre des problèmes non institutionnels, et s'est avéré très efficace pour découvrir des structures complexes dans des données à haute dimension. Il offre une nouvelle perspective pour résoudre les problèmes directs et inverses grâce à sa capacité à imiter la relation physique non linéaire entre un grand nombre de variables interdépendantes, telles que celles entre la structure acoustique et sa réponse spectrale. En outre, il est désormais possible de concevoir et d'entraîner des réseaux de neurones plus avancés capables d'exploiter des ensembles de données plus importants avec des performances supérieures grâce à l'introduction de nouvelles techniques d'entraînement et de régularisation telles que la fonction d'activation "ReLU" (unités linéaires rectifiées), le dropout et la normalisation par lots.

L'objectif principal de cette thèse est de concevoir des absorbeurs acoustiques métasurface ultrafins pour un régime d'extrême basse fréquence (<100Hz). Pour cela, nous avons d'abord proposé le concept d'absorbeur métasurface multicoiled (MCM) qui permet d'atteindre les limites basse fréquence des concepts précédemment mis en œuvre. Les systèmes acoustiques sont généralement étudiés en fonction de deux problèmes : (1) Problème direct : étant donné une structure acoustique, quelle est la réponse acoustique ? (2) Problème inverse : étant donné une réponse acoustique prescrite, comment concevoir et dessiner la structure et la géométrie acoustiques appropriées ? Pour établir le cadre basé sur le deep-learning, nous adoptons des architectures basés sur les réseaux de neurones convolués (CNN) et les réseaux adverses génératifs conditionnels (CGAN) pour les conceptions avant et inverse, respectivement. Dans le contexte des conceptions acoustiques inverses, un simulateur avant basé sur les CNN permet d'accélérer le processus de simulation, ce qui se traduit par une convergence plus rapide pendant le processus d'optimisation. Basé sur les deux propriétés essentielles de l'espace latent : la compacité et la continuité, le CGAN peut identifier les topologies plus efficacement que les algorithmes de recherche traditionnels, et peut également produire la structure de métasurface qui n'est pas dans l'ensemble de données. En tant que tel, le schéma de conception inverse mis en œuvre représente une méthode efficace et automatisée pour la conception d'absorbeurs acoustiques à métasurface pour l'incidence des ondes obliques avec des caractéristiques sub-longueur d'onde. Ces méthodes ont fourni une plateforme prometteuse pour apprendre la relation intrinsèque entre divers paramètres structurels et leurs réponses spectrales de manière intelligente. Une fois la phase d'apprentissage terminée, elles offrent une solution pour réduire considérablement les calculs fastidieux avec des ressources informatiques limitées. En outre, ces méthodes sont largement accessibles. Des logiciels libres

allant de TensorFlow à PyTorch sont disponibles gratuitement pour mettre en œuvre et entraîner le réseau.

La thèse commence par le chapitre 1, qui présente un bref état de l'art et une revue de la littérature sur les métamatériaux et métasurfaces acoustiques. Il passe en revue quelques travaux pertinents de la littérature sur la conception de métasurfaces acoustiques pour l'absorption de très basses fréquences. Dans la deuxième partie du chapitre 1, les équations fondamentales de l'acoustique sont exposées. L'importance des propriétés thermodynamiques du milieu de propagation du son, en particulier la présence de couches limites visqueuses et thermiques à l'interface entre le fluide et une frontière rigide, est discutée.

Dans le chapitre 2, un aperçu détaillé des méthodologies importantes utilisées tout au long du travail de thèse est présenté. Tout d'abord, la simulation numérique utilisant la méthode des éléments finis qui est utilisée pour analyser toutes les conceptions tout au long du travail de thèse est discutée. Lorsque le son se propage à travers les régions étroites de la structure, les pertes se produisent dans les couches limites près des parois qui doivent être considérées pour construire un modèle précis. Pour cela, les modèles de simulation sont implémentés en utilisant l'interface Thermoviscous Acoustics qui est discutée. Pour les mesures, de multiples échantillons expérimentaux ont été fabriqués à l'aide de l'impression 3D qui sera discutée. Ensuite, la méthode à deux microphones pour la mesure de l'absorption acoustique est présentée avec le processus de calibration associé. Dans la dernière partie du chapitre, les méthodes d'apprentissage automatique utilisées pour concevoir les absorbeurs métasurface sont discutées. Tout d'abord, les réseaux de neurones de type discriminateur et générateur sont présentés ainsi que leur processus de formation. Cela inclut l'explication de chaque couche de l'architecture du réseau et des hyperparamètres importants. Une brève explication des techniques classiques d'apprentissage automatique telles que le k-plus proche voisin (KNN), la forêt aléatoire (RF), la machine à vecteur de support (SVM) utilisée pour comparer les performances du réseau de deep-learning mis en œuvre est fournie. Plusieurs techniques qui atténuent la fiabilité des grands ensembles de données d'entraînement et la réduction de la dimensionnalité sont également discutées. Comme l'ensemble de données d'entraînement est généré par la simulation numérique, sa taille est plus petite. Pour augmenter la diversité de l'ensemble de données et éviter les problèmes de sur-adaptation du réseau, nous utilisons la technique d'augmentation des données qui est discutée brièvement.

Dans le chapitre 3, le concept de l'absorbeur métasurface multi-coiled pour l'absorption des fréquences extrêmement basses est démontré. La dérivation analytique, la simulation numérique et les démonstrations expérimentales sont fournies et le mécanisme physique associé est discuté. Contrairement à l'état de l'art, cette métasurface multi-enroulée de conception originale offre des degrés de liberté supplémentaires pour régler efficacement l'impédance acoustique sans augmenter l'épaisseur totale. L'absorption totale est atteinte à 50Hz avec la métasurface la plus fine réalisée jusqu'à présent, 13mm (λ/527), surmontant les obstacles majeurs liés au mécanisme de dissipation intrinsèquement physique et à la taille énorme des absorbeurs classiques lorsqu'il s'agit d'absorber de très grandes longueurs d'onde. En outre, la longueur du canal de propagation de cette structure est de λ/4,7, ce qui rompt avec la théorie du résonateur à quart de longueur d'onde. En outre, sur la base de la même approche conceptuelle, l'approche supercellulaire est présentée pour élargir la bande passante en couplant des cellules unitaires présentant des propriétés différentes. Ce concept de métasurface proposé introduit un véritable saut vers des applications pragmatiques dans l'absorption acoustique à basse fréquence extrême et présente une véritable percée pour développer des méta-absorbeurs ultra-minces, légers et efficaces. Dans la dernière partie de ce chapitre, l'effet de la température sur les performances du MCM est étudié via des approches numériques et théoriques. D'après les résultats, on peut observer que la température du milieu environnant affecte significativement la performance du MCM. L'augmentation de la température déplace les courbes d'absorption vers des fréquences plus élevées et diminue la valeur du pic d'absorption. Cependant, le déplacement des pics d'absorption avec l'augmentation de la température indique que la propagation des ondes acoustiques peut être efficacement réglée en changeant la température. Par conséquent, la structure métasurface proposée peut être utilisée pour absorber de manière flexible le son à la fréquence souhaitée.

Le chapitre 4 présente un cadre basé sur un réseau de neurones convolués pour la conception avancée d'un absorbeur acoustique à métasurface. Nous avons mis en œuvre une architecture CNN personnalisée avec deux couches de convolution et deux couches de mise en commun. L'efficacité du réseau mis en œuvre est démontrée par quelques exemples. Pour comparer la performance du CNN 2D, trois algorithmes classiques d'apprentissage automatique : KNN, RF, et SVM sont implémentés et entraînés sur le même jeu de données. Le CNN 2D implémenté a surpassé ces techniques classiques avec une précision moyenne de 86%. Cela montre l'efficacité des méthodes de deep-learning par rapport aux techniques classiques d'apprentissage automatique pour construire des relations entrée-sortie complexes. Nous

pensons qu'avec plus de données d'entraînement, cette précision peut être améliorée. De plus, nous avons effectué des mesures expérimentales et validé les prédictions du réseau qui démontrent l'efficacité de ce mécanisme physique et sa réelle valeur ajoutée par rapport aux travaux précédents. En utilisant CNN, un absorbeur métasurface ultra-mince est modélisé ayant une absorption parfaite à 38.6Hz extrêmement faible avec une épaisseur ultra-mince jusqu'à $\lambda/684$ (1.3cm) qui est la métasurface la plus fine jamais réalisée. Le chemin total pour les ondes de propagation à l'intérieur du canal est d'environ $\lambda/5.7$, ce qui rompt avec l'approche du résonateur à quart de longueur d'onde. La stratégie de conception avancée proposée, basée sur le deep-learning, peut être utilisée de manière générique pour une modélisation rapide et précise des dispositifs de métasurface acoustique avec une intervention humaine minimale. Nous avons également conçu un absorbeur métasurface basse fréquence à large bande en couplant des cellules unitaires présentant des propriétés différentes sur la base du concept de supercellule. La bande passante peut être encore améliorée en connectant plus de cellules unitaires avec des paramètres géométriques différents.

Dans le chapitre 5, la conception directe et inverse d'un absorbeur métasurface pour des incidences de vagues obliques est présentée en se basant respectivement sur un réseau de neurones convolués bidimensionnel (2D CNN) et un réseau adverse génératif conditionnel. Le réseau de deep-learning avancé proposé est capable de simuler un absorbeur métasurface pour l'absorption de très basses fréquences en utilisant des images 2D de la structure concaténées avec d'autres propriétés géométriques (hauteur, angle d'incidence, etc.). Les données sont prétraitées en utilisant plusieurs stratégies de transformation des données comme la normalisation des données, l'analyse en composantes principales (ACP), etc. qui sont discutées. Nous avons également introduit le concept d'augmentation des données pour accroître la diversité de l'ensemble de données. Pour les structures acoustiques complexes, les données d'apprentissage sont normalement générées par la simulation, et la taille d'un tel ensemble de données est plus petite par rapport au nombre de paramètres dans les architectures modernes de réseaux de deep-learning (généralement de l'ordre de millions). Dans un tel cas, le modèle a tendance à être sur-ajusté. Ainsi, l'augmentation des données réduit considérablement ce problème et rend le modèle plus robuste. En utilisant l'approche CNN présentée, nous avons démontré un absorbeur métasurface ayant une absorption presque omnidirectionnelle à 82Hz avec une épaisseur de $\lambda/64$. En utilisant la structure d'absorbeur métasurface proposée, environ 86% d'absorption est atteint à $\theta=60°$, ce qui montre une bonne performance globale à de grands angles d'incidence. En outre, nous proposons le CGAN pour la conception inverse. L'idée de la

conception inverse est de générer une structure métasurface directement à partir des spectres d'absorption acoustique souhaités, éliminant ainsi le besoin de longs balayages de paramètres ou de méthodes d'essais et erreurs. Nous envisageons une utilisation généralisée et croissante de la technologie de deep learning dans le domaine de la physique, permettant aux scientifiques et aux ingénieurs de se concentrer davantage sur des idées réellement créatives pour résoudre les problèmes de conception complexes qui doivent encore être explorés par la machine, plutôt que sur des processus d'essais et d'erreurs fastidieux.

Enfin, un résumé des conceptions d'absorbeurs acoustiques de métasurface et des stratégies de deep-learning mises en œuvre dans cette thèse est présenté. Les défis de la conception des absorbeurs acoustiques métasurface pour les applications basse fréquence et les futures directions de recherche utilisant les approches d'apprentissage profond sont également discutés.

Mots clés: métasurfaces et métamatériaux acoustiques, absorption basses fréquences, deep-learning, réseaux de neurones convolués, réseaux adverses génératifs, design inverse.

LOW FREQUENCY ABSORBING ACOUSTIC METASURFACES: DEEP-LEARNING APPRAOCH AND EXPERIMENTAL DEMONSTRATION

Abstract

The advent and development of acoustic metamaterials/metasurfaces in recent years has overturned conventional means in all aspects of acoustic waves propagation and manipulation. In the context of the sound absorption, it has offered an unprecedented expansion of our ability to attenuate the low-frequency sound beyond the classical physical limits. The main aim of this dissertation is to conceive and design acoustic metasurfaces for extreme low-frequency absorption (<100Hz). First, the concept of multicoiled metasurface absorber (MCM) is proposed. The effectiveness of its physical mechanism is theoretically, numerically, and experientially demonstrated. The presented MCM is capable of fully absorbing acoustic energy at extreme low-frequency of 50Hz with a deep subwavelength thickness ($\lambda/527$). To circumvent the conventional physics- and rule-based approaches and accelerate the design process, novel deep learning-based framework is introduced in this dissertation. Specifically, the convolutional neural network (CNN) and conditional generative adversarial networks (CGAN) are implemented to simulate and optimize complex metasurface absorber structures. The developed deep learning-based framework for the acoustic metasurface absorber can be potentially extended to the design and optimization of other acoustic devices. This dissertation provides a new way for deep learning-enabled acoustic metasurface designs that will allow acoustics community to focus more on truly creative ideas. This will be led to solving complex design problems that have yet to be explored by the machine, rather than on tedious trial and error processes.

Keywords: acoustic metasurfaces and metamaterials, low-frequency absorption, deep learning, convolutional neural network, conditional generative adversarial network, inverse design.

Résumé

L'avènement et le développement des métamatériaux/métasurfaces acoustiques au cours des dernières années ont bouleversé les approches conventionnels concernant de la propagation et de la manipulation des ondes acoustiques et même au-delà. Dans le contexte de l'absorption acoustique, ces structures artificielles ont ouvert des possibilités et des opportunités sans précédent pour s'atteler aux problèmes de l'absorption acoustique et du bruit en très basses fréquences défiant les limitations physiques classiques . L'objectif principal de cette thèse est de concevoir et réaliser des métasurfaces acoustiques pour l'absorption acoustique en extrême basses fréquences (<100Hz). Tout d'abord, le concept de métasurface absorbante à enroulement d'espace (MCM) est proposé. L'efficacité de son mécanisme physique associé est démontré théoriquement, numériquement et expérimentalement. Le MCM présenté est capable d'absorber entièrement l'énergie acoustique à une fréquence extrêmement basse de 50 Hz avec une épaisseur ultrasub-longueur d'onde ($\lambda/527$). Pour contourner les approches conventionnelles basées sur des méthodes et formalismes de simulation classiques, de nouvelles approches basées sur le deep-learning est introduit dans ce travail de thèse. En particulier, le réseau de neurones convolutif (CNN) et les réseaux adverses génératifs conditionnels (CGAN) sont mis en œuvre pour simuler et optimiser les structures complexes de métasurfaces absorbantes. Le cadre développé basé sur l'apprentissage profond pour ces métasurfaces absorbantes peut être potentiellement étendu à la conception et à l'optimisation d'autres dispositifs acoustiques. Cette thèse fournit de nouvelles méthodes et outils pour la conceptions de métasurfaces acoustiques basées sur le deep-learning qui pourrait permettre à la communauté acoustique de se concentrer davantage sur des idées vraiment créatives pour résoudre les problèmes de conception complexe qui doivent encore être explorés par la machine, plutôt que sur des processus fastidieux d'essais et d'erreurs

Mots clés : métasurface et métamatériaux acoustiques, absorption basse fréquence, deep-learning, réseaux de neurones convolutifs, réseaux adverses génératifs conditionnels, problème inverse.